UNIVERSITY OF SOUTHAMPTON

Spatial Modulation Aided Non-Orthogonal Multiple Access

by

Yusha Liu

Supervisors:

Prof. Lajos Hanzo and Prof. Lie-Liang Yang

A thesis submitted in partial fulfillment for the degree of Doctor of Philosophy

in the

Faculty of Engineering and Physical Sciences

School of Electronics and Computer Science

November 2020

UNIVERSITY OF SOUTHAMPTON

ABSTRACT

FACULTY OF ENGINEERING, SCIENCE AND MATHEMATICS
SCHOOL OF ELECTRONICS AND COMPUTER SCIENCE

Doctor of Philosophy

by Yusha Liu

For easing the burden on the heavily-loaded communication systems, high-throughput spatial modulation-aided non-orthogonal multiple access (SM-NOMA) schemes are proposed and investigated. Firstly, SM-aided sparse code-division multiple access (SM-SCDMA) is conceived, which exploits the joint benefits of SM and SCDMA. Furthermore, the advantages of multicarrier (MC) signalling and SM-SCDMA are amalgamated to conceive a SM/MC-SCDMA transceiver. Sparse frequency-domain spreading is utilized for mitigating the peak-to-average power ratio of MC signalling, as well as for facilitating low-complexity detection using the message passing-aided detection (MPAD). Furthermore, grant-free access is designed for SM-NOMA in order to support large-scale access for devices transmitting in a sporadic pattern at a low rate. Explicitly, a pair of compressive sensing-based low-complexity detectors are conceived for jointly detecting the identity of the active users and their transmitted data.

Additionally, a reduced-complexity hybrid detector and decoder (HDD) is conceived for turbo-coded sparse code multiple access (SCMA) by analysing its convergence behavior using EXtrinsic Information Transfer (EXIT) charts. Furthermore, we propose an adaptive turbo-coded SCMA system for mitigating the influence of multipath propagation so that the system's bits per symbol throughput may be improved under favorable channel conditions by using the most appropriate operational mode in the light of the near-instantaneous user load, modulation order and coding rate.

Furthermore, space-time coded generalized SM-aided SCDMA (STC/GSM-SCDMA) is proposed, which exploits the benefits of multi-dimensional transmit diversity in the context of multiple-input multiple-output systems. As an additional solution, a generalised SM-aided sparse space-time-frequency spreading (GSM/SSTFS) scheme is also proposed for supporting large-scale access at a high normalized user-load in the context of next-generation systems by simultaneously exploiting the transmit diversity in the spatial-, time- and frequency-domain, which outperforms conventional multiple-input multiple-output NOMA systems.

Dedicated to my beloved family and friends ...

Contents

Acknowledgements **xiii**

1 Introduction **1**
1.1 Spatial Modulation . . . 2
1.2 Spatial Modulated-Aided Orthogonal Multiple Access . . . 3
1.3 Spatial Modulation-Aided Non-Orthogonal Multiple Access . . . 5
1.4 Grant-Free Multiple Access . . . 6
1.5 Outline and Contributions . . . 10

2 Spatial Modulation-Aided Sparse Code Division Multiple Access **17**
2.1 Introduction . . . 18
2.2 System Model . . . 19
2.2.1 Transmitter Model . . . 19
2.2.2 Receiver Model . . . 21
2.3 Signal Detection . . . 21
2.3.1 Maximum-Likelihood Detection . . . 22
2.3.2 Maximum *A-Posteriori* Detection . . . 23
2.3.3 Message Passing Algorithm Aided Detection . . . 24
2.4 Performance Analysis . . . 25
2.4.1 Analysis of Single-User Average Bit Error Rate . . . 26
2.4.2 Analysis of Approximate Bit Error Rate . . . 29
2.5 Performance Results . . . 35
2.6 Chapter Summary and Conclusions . . . 42

3 Spatial Modulation-Aided Multicarrier Sparse Code-Division Multiple Access **45**
3.1 Introduction . . . 45
3.2 System Model . . . 47
3.2.1 Transmitter Model . . . 48
3.2.2 Receiver Model . . . 49
3.3 Signal Detection . . . 50
3.3.1 Maximum-Likelihood Detection . . . 51
3.3.2 Maximum *A-Posteriori* Detection . . . 52
3.3.3 Message Passing Algorithm Aided Detection . . . 53
3.4 Analysis of the Single-User Performance and its Discussion . . . 55
3.4.1 Analysis of Single-User Average Bit Error Rate . . . 55
3.4.2 Discussions . . . 60

3.5 Performance Results . . . 61
3.6 Chapter Summary and Conclusions . . . 70

4 Joint User-Activity and Data Detection for Grant-Free Spatial-Modulated Multi-Carrier Non-Orthogonal Multiple Access 73
4.1 Introduction . . . 74
4.2 System Model . . . 77
4.2.1 Transmitter Model . . . 77
4.2.2 Receiver Model . . . 78
4.3 Overview of Compressive Sensing-Based Detectors . . . 79
4.4 Joint Multiuser Matching Pursuit Detection . . . 81
4.4.1 Description of our Joint Multiuser Matching Pursuit detection . . . 81
4.4.2 Termination Criteria for Joint Multiuser Matching Pursuit Detection 86
4.5 Adaptive Multiuser Matching Pursuit Detection . . . 87
4.5.1 Description of the Adaptive Multiuser Matching Pursuit Detector . 87
4.5.2 Termination Criteria of the Adaptive Multiuser Matching Pursuit Algorithm . . . 89
4.6 Performance Results and Discussion . . . 91
4.6.1 Bit Error Rate Performance . . . 91
4.6.2 Complexity . . . 94
4.7 Chapter Summary and Conclusions . . . 98

5 Hybrid Iterative Detection and Decoding of Near-Instantaneously Adaptive Turbo-Coded Sparse Code Multiple Access 99
5.1 Introduction . . . 100
5.2 System Model . . . 103
5.2.1 Transmitter Model . . . 103
5.2.2 Receiver Model . . . 104
5.3 Signal Detection and Decoding . . . 105
5.3.1 Separate Signal Detection and Decoding . . . 105
5.3.2 Joint Signal Detection and Decoding . . . 109
5.4 System Performance and Hybrid Detection and Decoding . . . 110
5.4.1 Capacity . . . 110
5.4.2 Error Correction Performance . . . 111
5.4.3 EXtrinsic Information Transfer Chart Analysis . . . 114
5.4.4 Improved Scheduling of Detection and Decoding . . . 115
5.4.5 Complexity Analysis . . . 119
5.5 Adaptive Turbo-Coded Sparse Code Multiple Access System . . . 119
5.5.1 Adaptive System Design . . . 120
5.5.2 Performance of the Adaptive Turbo-Coded Sparse Code Multiple Access System . . . 121
5.6 Chapter Summary and Conclusions . . . 123

6 Space-Time-Coded Generalized Spatial Modulation for Sparse Code Division Multiple Access 125
6.1 Introduction . . . 125
6.2 System Model . . . 128
6.2.1 Transmitter Model . . . 128

6.2.2 Receiver Model . . . 130
6.3 Detection Algorithms . . . 132
6.3.1 Message Passing-Aided Detection . . . 132
6.3.1.1 Initialisation . . . 133
6.3.1.2 Variable Node Update . . . 133
6.3.1.3 Check Node Update . . . 134
6.3.1.4 Symbol Mapping . . . 135
6.3.2 Approximated Message Passing Detection . . . 135
6.3.2.1 Initialisation . . . 136
6.3.2.2 Variable Node Update . . . 136
6.3.2.3 Check Node Update . . . 137
6.3.2.4 Final Iteration . . . 139
6.3.2.5 Symbol Mapping . . . 140
6.4 Single-User Performance Analysis . . . 141
6.5 Performance Results . . . 143
6.5.1 Bit Error Rate Performance . . . 143
6.5.2 Complexity . . . 147
6.6 Chapter Summary and Conclusions . . . 149

7 Sparse Space-Time-Frequency-Domain Spreading for Large-Scale Non-Orthogonal Multiple Access 151
7.1 Introduction . . . 151
7.2 System Model . . . 153
7.2.1 Transmitter Model . . . 153
7.2.2 Receiver Model . . . 156
7.3 Joint Message Passing-Aided Detection . . . 157
7.3.1 Factor Graph Design . . . 157
7.3.2 Joint Message Passing-Aided Detection . . . 158
7.4 Performance Results . . . 160
7.5 Conclusions . . . 163

8 Conclusions and Future Research 165
8.1 Chapter Conclusions . . . 165
8.1.1 Chapter 1 . . . 165
8.1.2 Chapter 2 . . . 166
8.1.3 Chapter 3 . . . 167
8.1.4 Chapter 4 . . . 167
8.1.5 Chapter 5 . . . 168
8.1.6 Chapter 6 . . . 169
8.1.7 Chapter 7 . . . 170
8.2 Design Guidelines . . . 170
8.3 Future Work . . . 172
8.3.1 Non-Coherent Detection of Spatial Modulation-Aided Non-Orthogonal Multiple Access . . . 172
8.3.2 Physical-Layer Security Design of Spatial Modulation-Aided Non-Orthogonal Multiple Access . . . 173
8.3.3 Deep-Learning-Aided Grant-Free Non-Orthogonal Multiple Access 173

Bibliography **179**

Subject Index **195**

Author Index **197**

List of Publications

1. **Y. Liu**, L.-L. Yang and L. Hanzo, "Joint User-Activity and Data Detection for Grant-Free Spatial-Modulated Multi-Carrier Non-Orthogonal Multiple Access," *IEEE Transactions on Vehicular Technology*, Accepted, 2020, Early Access.

2. **Y. Liu**, L.-L. Yang and L. Hanzo, "Sparse Space-Time-Frequency-Domain Spreading for Large-Scale Non-Orthogonal Multiple Access," *IEEE Transactions on Vehicular Technology*, Accepted, 2020, Early Access.

3. **Y. Liu**, L.-L. Yang, P. Xiao, H. Haas and L. Hanzo, "Spatial Modulated Multicarrier Sparse Code-Division Multiple Access," *IEEE Transactions on Wireless Communications*, vol. 19, no. 1, pp. 610-623, 2020.

4. **Y. Liu**, L.-L. Yang and L. Hanzo, "Spatial Modulation Aided Sparse Code-Division Multiple Access," *IEEE Transactions on Wireless Communications*, vol. 17, no. 3, pp. 1474-1487, 2018.

5. **Y. Liu**, L.-L. Yang and L. Hanzo, "Hybrid Iterative Detection and Decoding of Near-Instantaneously Adaptive Turbo-Coded Sparse Code Multiple Access," *IEEE Transactions on Vehicular Technology*, under review.

6. **Y. Liu**, Y. Yang, L.-L. Yang and L. Hanzo, "Physical Layer Security of Spatially Modulated Sparse-Code Multiple Access in Aeronautical Ad-Hoc Networking," *IEEE Transactions on Vehicular Technology*, under review.

7. **Y. Liu**, L. Xiang, R. G. Maunder, L.-L. Yang and L. Hanzo, "Space-Time Coded Generalized Spatial Modulation for Sparse Code Division Multiple Access," *IEEE Transactions on Wireless Communications*, under review.

8. L. Xiang, **Y. Liu**, Z. Kaykac, R. G. Maunder, L.-L. Yang and L. Hanzo, "Soft List Decoding of Polar Codes," *IEEE Transactions on Vehicular Technology*, Accepted, 2020, Early Access.

9. L. Xiang, **Y. Liu**, C. Xu, R. G. Maunder, L.-L. Yang and L. Hanzo, "Iterative Receiver Design for Polar-Coded SCMA System Under Imperfect CSI," *IEEE Transactions on Communication*, under review.

10. L. Xiang, **Y. Liu**, T. V. Luong, R. G. Maunder, L.-L. Yang and L. Hanzo, "Deep-Learning-Aided Joint Channel Estimation and Data Detection for Spatial Modulation," *IEEE Access*, under review.

11. L. Xiang, **Y. Liu**, L.-L. Yang and L. Hanzo, "Low Complexity Detection for Spatial Modulation Aided Sparse Code Division Multiple Access," To submit.

12. L. Xiang, **Y. Liu**, R. G. Maunder, L.-L. Yang and L. Hanzo, "Soft Successive Cancellation Stack Polar Decoder," To submit.

13. J. An, C. Xu, **Y. Liu**, L. Gan, L.-L. Yang and L. Hanzo, "Improved-Throughput Generalised Spatial Modulation: Bit-to-symbol Mapping, Detection and Performance Analysis," To submit.

14. J. An, C. Xu, **Y. Liu**, L. Gan, L.-L. Yang and L. Hanzo, "Weighted Space Shift Keying for MIMO Channels," To submit.

DECLARATION OF AUTHORSHIP

I, **Yusha Liu**, declare that the thesis entitled **Spatial Modulation Aided Non-Orthogonal Multiple Access** and the work presented in the thesis are both my own, and have been generated by me as the result of my own original research. I confirm that:

- This work was done wholly or mainly while in candidature for a research degree at this University;
- Where any part of this thesis has previously been submitted for a degree or any other qualification at this University or any other institution, this has been clearly stated;
- Where I have consulted the published work of others, this is always clearly attributed;
- Where I have quoted from the work of others, the source is always given. With the exception of such quotations, this thesis is entirely my own work;
- I have acknowledged all main sources of help;
- Where the thesis is based on work done by myself jointly with others, I have made clear exactly What was done by others and what I have contributed myself;
- Parts of this work have been published in the provided list of publications.

Signed: .....

Date: 28/09/2020

Acknowledgements

I would like to first express my deepest gratitude to my supervisors Prof. Lajos Hanzo and Prof. Lie-Liang Yang for their continuous generous support and guidance throughout my time at Southampton. Since the very first day of my PhD, they offered professional and personal advice for my PhD and research career. Since then, they encouraged me to discover my potential at research.

I sincerely appreciate the supervision Lajos has generously offered, not only as a supervisor but also as a life mentor. I am deeply impressed and completely influenced by his passion towards research. I will always remember the Christmas parties at Rita and Lajos' house.

I would also like to express my sincere gratitude to Lie-Liang for his patient guidance as a tutor during my MSc study and as a supervisor during my PhD. His inspiring ideas and encouragements has always kept me on the right track, while his rigorous attitude towards research built my academic perception.

I am also heartily grateful to Dr. Yuli Yang, who helped me to widen my research and offered her professional insight through our collaborative work. Through our regular meetings during the past months, I learned a lot from her and appreciated all her suggestions on my academic research and on career plan.

I would like to express my appreciation to the Next Generation Wireless Research Group, School of Electronics and Computer Science, University of Southampton for offering financial support of my PhD study.

I would also like to express my heartfelt gratitude to all the staffs of the Next Generation Wireless Research Group for their useful discussions and comments throughout my research. Sincere thanks to Prof. Sheng Chen, Prof. Robert G. Maunder, Dr. Soon X. Ng, Dr. Mohammed El-Hajjar, for their constructive suggestions, technical support and collaborative work.

Special thanks to my best friend Miss Jiadong Yu, for her support and stimulating ideas over the past three years. I will always cherish this lifelong friendship built during my PhD.

Many thanks to my colleagues Mr. Yanqing Zhang, Mr. Shuai Shao, Mr. Jiancheng An, Mr. Shuai Wang, Miss Jue Chen, Mr. Kunlun Li, Mr. Haochen Liu, Mr. Bohan Li, Mr. Mingze Zhang, Dr. Luping Xiang, Dr. Xiaoyu Zhang, Dr. Siyao Lu and Dr. Simeng Feng for their constructive comments and suggestions.

I would also like to express my warmest gratitude to my parents, Mr. Xiuzhi Liu and Mrs. Junrong Wang, as well as my grandparents, Mr. Xiujin Wang and Mrs. Aiying Li for their unconditional love, understanding and support.

Finally, many thanks to my better half, Dr. Luping Xiang, for his unfailing companionship and support throughout my PhD journey.

List of Symbols

General notation

- The superscript $(\cdot)^{-1}$ represents matrix inversion.
- The superscript $(\cdot)^{*}$ represents complex conjugate.
- The superscript $(\cdot)^{T}$ represents matrix transpose.
- The superscript $(\cdot)^{H}$ represents Hermitian transpose
- The operation $\| \cdot \|_n$ represents ℓ_n-norm.

Special symbols

K	The number of users
N	The number of subcarriers
U	The number of receive antennas
γ_0	SNR per symbol
γ_b	SNR per bit
j	Variable node (VN) j
i	Check node (CN) i
$\mathcal{C}_i$	VNs that have connections to CN i
$\mathcal{X}_j$	CNs that have connections to VN j
$\eta_{i,j}^{a_m,t}$	The information sent from VN j to CN i in the t-th iteration
$\delta_{i,j}^{a_m,t}$	The information sent from CN i to VN j in the t-th iteration
ε	The normalisation factor
d_x	The maximum number of subcarriers that a user's signal spread over
d_c	The maximum number of users sharing one of the N subcarriers

L	The number of resolvable time-domain paths
M_1	SSK modulation order
M_2	APM/QAM modulation order
b_1	The number of bits of a single SSK symbol
b_2	The number of bits of a single APM/QAM symbol
$\mathcal{S}_1$	The SSK symbol set
$\mathcal{S}_2$	The APM/QAM symbol set
$\mathcal{S}$	The super constellation set for SSK and APM
b	The total number of bits for a single SSK-APM/QAM symbol
$\boldsymbol{c}_k$	The spreading sequence for user k
$\boldsymbol{h}_{s_{k1}}$	Channel impulse response (CIR) between the s_{k1}-th TA of user k and the U receive antennas (RAs) at the base station (BS)
$\hat{\boldsymbol{h}}_{s_{k1}}$	The frequency-domain CIR between the s_{k1}th TA of user k and the U RAs at the BS
$\boldsymbol{n}_u$	Additive white Gaunssian noise (AWGN) at the u-th RA
$\boldsymbol{y}_u$	The received signal at the u-th RA
$\bar{P}_{bS}$	The average bit error rate (BER)
$\bar{P}_{sS}$	The average symbol error rate
P_{EP}	The pairwise error probability
$\boldsymbol{I}_U$	Identity matrix with a size U
$e_{j,i}$	The connection between VN j to CN i
$\boldsymbol{R}$	The covariance matrix of $\boldsymbol{h}$
$\boldsymbol{V}$	The indicator matrix
$\mathcal{O}(\cdot)$	Complexity order

Chapter 4

p	Activation probability
K_a	The actual number of acitve users
K_e	The estimated number of acitve users
$\boldsymbol{r}^{(i)}$	The residual signal at ith iteration
z	The search step size
$\boldsymbol{t}^{(i)}$	Received signal after the matched filtering (MF) at the i-th iteration
$\mathcal{T}^{(i)}$	Index set of selected candidate users at the i-th iteration

$\mathcal{M}^{(i)}$	Index set of selected candidate users at the i-th iteration
$\mathcal{F}^{(i)}$	Index set of final candidate users at the i-th iteration
$\hat{\boldsymbol{x}}_k$	The detected symbol of user k

Chapter 5

F	Frame length
A	Information frame length
R	Coding rate
$\mathcal{S}_k$	SCMA codebook for user k
$\boldsymbol{u}_k$	Information bits of user k
$\boldsymbol{b}_{1,k}^{(u)}$	*Parity bits* of user k
$\boldsymbol{b}_{2,k}^{(u)}$	*Systematic bits*
$\boldsymbol{b}_k$	Turbo encoded bits of user k
M	SCMA cosntellation size
γ_i	Instantaneous SNR
L^e	The *extrinsic* LLR
L^a	The *a priori* LLR
$\bar{\boldsymbol{\alpha}}$	The forward state metrics
$\bar{\boldsymbol{\beta}}$	The backward state metrics
C	The DCMC capacity
I	The mutual information (MI)
T	The number of iterations
$\mathcal{C}$	The number of floating point operations (FLOPs)

Chapter 6, Chapter 7

$\mathcal{G}_{k,2}$	Alamouti's code for user k
$\boldsymbol{X}_k$	The transmit signal matrix
$\boldsymbol{y}_u^{(t)}$	The received signal at u-th receiver t-th time slot
$\boldsymbol{z}$	The super constellation
N_T	Number of TAs
N_A	Number of active TAs

Chapter 1

Introduction

Next generation communication systems aim for supporting large-scale access for myriads of devices in the Internet-of-Things (IoT) and in massive Machine-Type Communications (mMTC) [1–3]. However, facilitating large-scale access is challenging owing to the severe multi-user interference (MUI), especially for short packets. As a promising technique for addressing this challenge, non-orthogonal multiple access (NOMA) has been proposed for rank-deficient scenarios. In contrast to the orthogonal multiple access (OMA) schemes [4], where users are supported by the orthogonal resources of the time, frequency or code domain, NOMA schemes rely on non-orthogonal resource allocation, where more users can be supported than the number of resource-units [5–8], albeit at the cost of requiring more complex receivers for mitigating the inter-user interference (IUI). In this context, numerous NOMA schemes have been investigated, which can be classified into numerous categories [9]. Perhaps the most popular ones are the power-domain [10–14] and code-domain NOMA solutions [15, 16]. While the power-domain NOMA exploits the user-power difference and separates them by successive interference cancellation (SIC) at the receiver, code-domain NOMA schemes assign different non-orthogonal codes to users.

In parallel with the development of NOMA schemes, spatial modulation (SM) [17–22] has distinguished itself as a promising low-complexity single-radio frequency (RF)-chain based multiple-input multiple-output (MIMO) technique relying on a single activated antenna. This unique transmit antenna (TA) activation scheme allows the transmitter to implicitly convey additional information bits 'hidden' in the active TA index patterns, hence achieving energy-efficient modulation.

The application of SM to different NOMA schemes has been investigated in [23–34], demonstrating significant complexity reductions compared to the conventional MIMO-NOMA systems, owing to its reduced number of RF chains in SM-NOMA. The benefit of SM-NOMA may be further enhanced in the context of mMTC and IoT scenarios, where data are transmitted sporadically and at a relatively low rate.

Against this backdrop, this thesis details the design considerations of several SM-NOMA schemes capable of supporting the mMTC and IoT operational modes of the next generation communications.

1.1 Spatial Modulation

For coping with the dramatically increasing data traffic, novel transmission schemes are in urgent demand for improving the throughput, while minimizing the deployment complexity. Among numerous cutting-edge techniques, SM [17–22, 35] has been envisioned as a promising scheme, which reduces the number of RF chains and mitigates the interference between antennas.

To be more specific, by activating a single TA or a subset of TAs, various SM schemes have been proposed in the past two decades [17, 18, 35–48], as summarized in Table 1.1. The pioneering contribution on SM can be traced back to 2001, when Chau *et al.* [35] proposed *space-shift keying (SSK)*, which was further investigated in [36]. While SSK [35, 36] only conveys information by the activated TA indices, the *SM* [17, 18] activates a single TA, which transmits a single amplitude-phase modulation (APM) symbol, rather than simply being energized. Following this, SM was combined with Trellis coding (TC) in [37] and with space-time block coding (STBC) [38] for exploiting the advantages of both. An alternative way of combining STBC with SM was proposed in [39], referred to as *space-time shift keying (STSK)*, which applied the SSK/SM concept to both the space and time domain upon combing SSK/SM with STBC. As a further development, Yang [40] proposed the *precoded SM (PSM)* philosophy, also known as *receive SM (RSM)*, which activated a single receive antenna (RA) for detection by relying on the employment of precoding at the transmitter.

A subsequent SM development relied on activating a fraction of TAs, which was termed as *generalised SM (GSM)* [41], which simultaneously activates a group of TAs to convey multiple APM symbols, etc. Further refinements of the SM techniques include *quadrature SM (QSM)* [44], which extends the real-valued SM constellation to in-phase and quadrature dimensions, and spatial multiplexing aided SM [49], which activates multiple TAs by antenna grouping. Additionally, Xiao *et al.* [47] investigated the integration of STBC and QSM, proposing the STBC-QSM concept.

Noncoherent detection was achieved for the first time by the employment of *differential SM (DSM)* proposed in [43]. The differential transmission approach has been further investigated by *differential QSM (DQSM)* [45], *rectangular DSM (RDSM)* [46] and *STBC-RDSM* [48].

Additionally, the activated TA(s) convey the classically modulated information bits using conventional APM, which belongs to the family of bandwidth-efficient modulation

TABLE 1.1: Summary of research contributions on SM.

Year	Author(s)	Scheme
2001	Chau *et al.* [35]	SSK
2006	Mesleh *et al.* [17, 18]	SM
2010	Mesleh *et al.* [37]	TC-SM
2010	Basar *et al.* [50]	STBC-SM
2010	Sugiura *et al.* [39]	STSK
2011	Yang *et al.* [40]	PSM
2012	Wang *et al.* [41]	GSM
2013	Zhang *et al.* [42]	GPSM
2014	Mesleh *et al.* [44]	QSM
2014	Bian *et al.* [43]	DSM
2017	Mesleh *et al.* [45]	DQSM
2017	Ishikawa *et al.* [46]	RDSM
2018	Xiao *et al.* [47]	STBC-QSM
2019	Wu *et al.* [48]	STBC-RDSM

schemes. As an additional benefit, again, either one or a low number of RF-chains can be used, which results in lower detection complexity in terms of matrix multiplications at the receiver, when compared to conventional MIMO systems [17]. Hence, SM strikes a flexible trade-off among the spectral efficiency, energy efficiency and complexity.

1.2 Spatial Modulated-Aided Orthogonal Multiple Access

SM-aided multiuser communications are achieved by sharing the resources using either orthogonal or nonorthogonal approaches. For SM-aided orthogonal multiple access (SM-OMA) [51–65], as summarized in Table 1.2, each user occupies a single resource in the time/ frequency or code domain.

Specifically, the bit error ratio (BER) performance of SSK-aided multiuser communications over fading channels was initially analysed in [51], followed by the multiuser SM system proposed in [52] for the first time. Later, Narasimhan *et al.* [53] conceived a large-scale multiuser SM-MIMO system, which was later generalised to the GSM-MIMO by Narasimhan *et al.* [56]. Additionally, Wang *et al.* [54] investigated multiuser SM-MIMO systems in the presence of low-resolution analog-to-digital convertors (ADCs).

Table 1.2: Summary of research contributions on SM-OMA.

Year	Author(s)	Contributions
2011	Di Renzo *et al.* [51]	Performed performance analysis for multiuser SSK.
2012	Serafimovski *et al.* [52]	Proposed multiuser SM for the first time.
2014	Narasimhan *et al.* [53]	Conceived large-scale multiuser SM-MIMO systems.
2014	Wang *et al.* [54]	Investigated multiuser SM-MIMO systems with low-resolution ADCs for the first time.
2014	Narayanan *et al.* [55]	Proposed a novel precoding scheme for multiuser SM-MIMO.
2015	Narasimhan *et al.* [56]	Applied GSM technique in the large-scale multiuser MIMO systems.
2015	Garcia-Rodriguez *et al.* [57]	Proposed CS-based detection for the multiuser SM-MIMO system.
2015	Gao *et al.* [58]	Investigated CS-based detection for the uplink large-scale SM-MIMO system.
2016	Maleki *et al.* [59]	Proposed layered SM for multiuser communications.
2016	He *et al.* [60]	Proposed the multi-cell massive SM-MIMO system for multiuser communications.
2016	Meng *et al.* [61]	Proposed structured approximate message passing (AMP) for multiuser SM
2018	Rajashekar *et al.* [62]	Proposed TAS for single and multiuser SM.
2019	Maleki *et al.* [63]	Investigated precoding for multiuser RSM.
2019	Pan *et al.* [64]	Investigated SM for CDMA system.
2020	Castillo-Soria *et al.* [65]	Proposed multiuser QSM-MIMO transmission.

Furthermore, Narayanan *et al.* [55] proposed a novel precoding scheme for multiuser SM-MIMO.

Compressive sensing-based detection algorithms have been investigated in [57,58], which achieved low-complexity detection by refining the orthogonal matching pursuit (OMP) algorithm. Furthermore, Maleki *et al.* [59] proposed the layered SM for multiuser communications. He *et al.* [60] proposed the multi-cell massive SM-MIMO system for multiuser communications. Further improvements of multiuser SM-MIMO solutions include low-complexity detection [61], transmit antenna selection (TAS) [62] and precoding [63].

Finally, Pan *et al.* [64] investigated SM for heavily-loaded code division multiple access (CDMA) systems, whereas SM multiuser communications employing QSM was recently investigated in [65].

1.3 Spatial Modulation-Aided Nonorthogonal Multiple Access

As a promising solution to pervasive connectivity, the NOMA concept [5, 66–69], has found applications in next-generation massive mMTC and IoT [70–72] systems. For accommodating a high number of device connections, code-domain [10–14] and power-domain NOMA [9, 15, 16, 73] techniques have been proposed by adopting nonorthogonal power allocation and by enabling resource sharing, respectively.

In contrast to the OMA concept, which has a hard-limited user-capacity owing to its non-overlapping nature, NOMA is capable of supporting multiple users within a single resource unit. In uplink power-domain NOMA scenarios, users can be separated by creating a power-difference between paired users through a predefined power allocation pattern [9, 15, 16, 73]. By contrast, code-domain NOMA schemes assign different non-orthogonal codes to users. In this way, a 'massive' number of connections can be supported by a limited number of resources. For example, a low density signature (LDS) based technique has been proposed in [10] to exploit the beneficial properties of sparse signatures for approaching the optimum single-user performance in systems supporting a high user-load by relying on the massage passing algorithm (MPA) [74,75]. Further studies include the design of sparse code multiple-access (SCMA) [13], which amalgamates modulation, spreading as well as constellation shaping into a single codebook. Explicitly, the data are no longer carried only by the APM symbols, but by specifically designed multi-dimensional codewords. Hence, an improved coding gain becomes achievable by the proposed design of the code books, mapping the data to the codewords. We also note that powerful yet low-complexity receiver designs based on the MPA have been proposed in [76–81], which are capable of reducing the detection complexity at the cost

of a modestly degraded BER performance in comparison to the optimum detection based on maximum likelihood detection (MLD).

On the other hand, for SM-NOMA [23–34], where each of the orthogonal time, frequency or code domain resources are shared by more than a single user, a higher normalised user load can be supported. This demonstrates the potential of its applications in heavily loaded communications environments, where the system has to support ultra-dense deployment of numerous devices, such as in IoT [82] and mMTC [83, 84]. However, designing and implementing affordable-complexity detection is challenging for various SM-NOMA systems, which is the focus of this thesis.

The research contributions on SM-NOMA are summarized in Table 1.3 at a glance. Firstly, a series of treatises on SM-NOMA have been published in 2017 [23–26]. In more detail, a cooperative vehicle-to-vehicle power-domain NOMA scheme combined with SM has been introduced in [23] and its performance has been comprehensively investigated. In [24], the authors have proposed a general NOMA-based downlink scheme relying on SM. Additionally, a SM-assisted two-user NOMA uplink scheme based on space division multiple access (SDMA) principles has been studied in [25]. By contrast, we have investigated the integration of code-domain NOMA with SM in [26] and proposed the SM-SCDMA scheme for supporting heavily loaded mMTC scenarios.

Later, Zhong *et al.* [27] introduced the idea of SM-assisted multi-antenna NOMA for avoiding the SIC at the receiver. Furthermore, Pan *et al.* [28] extended our SM-SCDMA system to SCMA and proposed an uplink SM-SCMA system. We then extended the SM-SCDMA system concept to support multicarrier (MC) transmission by proposing the SM/MC-SCDMA arrangement in [29]. Following this, the low-complexity detection of SM-SCMA was studied in [30].

Additionally, the application of SM-NOMA systems has been investigated in [31, 32]. Specifically, Li *et al.* [31] proposed a novel cooperative relaying system for Rayleigh flat-fading channels using SM-NOMA and Si *et al.* analysed the system performance of SM-NOMA both in coordinated direct and relay-aided transmission.

More recently, we proposed the sparse space-time-frequency-domain spreading (SSTFS) for uplink SM-NOMA, facilitating multiple active TAs, while Hong *et al.* [34] investigated user grouping and resource allocation for downlink QSM-NOMA.

1.4 Grant-Free Multiple Access

Although SM-NOMA is a promising solution to the massive connectivity problem, another challenge encountered in the mMTC scenario is its low-latency requirement and the sporadic transmission pattern of the uplink tele-traffic. While a 'massive' number of devices on the order of say a million or so may connect to the base station (BS), they

TABLE 1.3: Summary of research contributions on SM-NOMA.

Year	Work	Contributions
2017	[23]	Analysed the system performance of SM-NOMA in the context of vehicle-to-vehicle communication scenario.
2017	[24]	Investigated SM-NOMA for downlink transmission.
2017	[25]	Investigated an SM-assisted two-user NOMA uplink scheme based on SDMA principles.
2017	[26]	Proposed and analysed the uplink SM-SCDMA system for flat Rayleigh fading channels.
2018	[27]	Provided general analysis of SM-NOMA.
2018	[28]	Proposed an uplink SM-SCMA system.
2019	[29]	Proposed and analysed the uplink SM/MC-SCMA system for frequency-selective Rayleigh fading channel.
2019	[30]	Proposed a low-complexity detection for SM-SCMA.
2019	[31]	Proposed a novel cooperative relaying system for Rayleigh flat-fading channels using SM-NOMA.
2020	[32]	Analysed the system performance of SM-NOMA for the coordinated direct and relay transmission.
2020	[33]	Proposed SSTFS for uplink NOMA
2020	[34]	Investigated user grouping and resource allocation for downlink QSM-NOMA.

tend to transmit their signals to the BS at a low activity rate and at a low data rate for each active user [85].

In this case, the classic grant-based legacy access schemes, require extra resources, such as time-slots for requesting access grant, which imposes extra latency. This is clearly undesirable for mMTC. Hence, grant-free access schemes are more promising in terms of satisfying the stringent low-latency requirements, whilst simultaneously supporting sporadic uplink transmissions without imposing any overhead. However, when incorporating grant-free transmissions, the receiver has to promptly detect both the user activity and the transmitted data.

In most mMTC scenarios, only a very small fraction of user devices is active at a time. This activity sparsity of grant-free NOMA systems inspired the application of compressive sensing (CS) algorithms [86], leading to the design of a range of low-complexity multi-user detectors [87–94], as summarized in Table 1.4. In these CS-based detectors, the OMP [95], subspace pursuit (SP) [96] and compressive sampling matching pursuit (CoSaMP) [97] have been adopted.

Initially, Zhu *et al.* [87] proposed three CS-based detectors for exploiting the sparsity of user activity in CDMA systems, whereas Bockelmann *et al.* [88] proposed a greedy CoSaMP-based algorithm, facilitating joint user activity and data detection. Additionally, the correlation of user activities over consecutive time slots was exploited in [89,90,93]. In particular, Wang *et al.* [89] proposed a dynamic CS (DCS)-based multiuser detection for grant-free NOMA to realize both user activity and data detection in several consecutive time slots by exploiting the temporal correlation of active user sets. For further improving the detection performance, Du *et al.* [90] proposed a prior-information-aided adaptive subspace pursuit (SP) algorithm, which was then enhanced in [93]. The channel estimation problem of grant-free NOMA systems was considered in [90], which jointly performed channel estimation and multiuser detection for frame-based multiuser transmission scenarios, where the users are (in)active for the duration of a frame.

Furthermore, Wang *et al.* [91] investigated a grant-free GSM-NOMA scenario relying on a terrestrial return channel. Zhang *et al.* [94] proposed user activity and signal detection for orthogonal frequency division multiplexing (OFDM) systems relying on LDS, where the signal spreading across the frequency domain (FD) resulted in beneficial frequency diversity gain, since the individual LDS-chips experienced independent fading. As a further advance, Zhang *et al.* [98] proposed an information-enhanced adaptive matching pursuit (MP) algorithm, which exploits both the frame-wise user sparsity and the unique nature of the transmit signal. More recently, Jiang *et al.* [99] developed joint user identification, channel estimation and signal detection based on the AMP algorithm.

Recently, machine learning-aided approaches have been proposed for solving the joint user and data detection problem [99–101], as also summarized in Table 1.4, where deep learning [100, 101] or reinforcement learning [99] techniques were adopted.

TABLE 1.4: Summary of research contributions on joint user activity and data detection for grant-free multiple access.

Year	Work	Contributions
2013	[88]	Proposed a greedy CS-based algorithm to facilitate the joint user activity and data detection.
2016	[89]	Proposed a DCS-based multiuser detection to realize both user activity and data detection in several continuous time slots.
2017	[90]	Proposed a prior-information-aided adaptive SP algorithm.
2017	[91]	Proposed a joint user activity and signal detection scheme based on the block-sparse CS in the terrestrial return channel.
2018	[92]	Proposed a novel joint channel estimation and multiuser detection for the frame based multiuser transmission scenario.
2018	[93]	Proposed a pair of enhanced block CS-based greedy algorithm for frame-based multiuser uplink scenarios.
2018	[94]	Investigated the joint user activity detection and channel estimation and extracted the necessary information for data detection.
2019	[100]	Employed deep learning for random user activation and symbol spreading in grant-free NOMA.
2019	[98]	Proposed the information-enhanced adaptive MP, which exploits both the frame-wise user sparsity and the ternary nature of transmit signal.
2020	[99]	Developed a joint user identification, channel estimation, and signal detection based on the AMP algorithm.
2020	[102]	A deep reinforcement learning-based algorithm is proposed for reducing collision in grant-free NOMA.
2020	[101]	Proposed a deep learning-based algorithm for active user detection.

Additionally, among the above-mentioned research publications, only [91] exploits the SM-NOMA philosophy. Hence, further investigation of grant-free access-based SM-NOMA will be performed in this thesis.

1.5 Outline and Contributions

This thesis is mainly focused on providing practical solutions for dense mMTC scenarios and it is based on six submitted or published journal papers. The outline of this thesis is portrayed in Fig. 1.1.

Specifically, we commence by proposing and analysing the SM-SCDMA scheme in Chapter 2, which adopts nonorthogonal techniques for supporting SM-aided multiuser communications. The novel contributions of Chapter 2 are summarized as follows:

- A SM-SCDMA scheme is proposed for supporting a high normalized user-load in uplink communications. We assume that each user employs several TAs for supporting SM, while the BS employs several RAs for enhancing the detection reliability, where multiple access is achieved with the aid of SCDMA. Since our SM-SCDMA relies on the principle of NOMA, it has the potential of supporting the MA transmission, where the number of (active) users is higher than the total number of chips in the spreading codes.
- It has been widely recognized that employing SM is beneficial for the implementation of MIMO using a low number of RF transceivers, since it provides low-complexity receiver implementation options [18,20]. However, when there is a high number of users sharing the resources based on SCDMA, the design of relatively low-complexity detectors that are capable of achieving near-ML performance is challenging. In this chapter, we first consider the classic MLD in order to quantify the best possible potential of the SM-SCDMA scheme. Then, we derive a maximum *a-posteriori* detector (MAPD), based on which we develop a reduced-complexity message passing-aided detector (MPAD) that is suitable for SM-SCDMA systems, which employs SM and exploits receiver diversity.
- In most of the code-domain NOMA references [10–14], the performance study mainly relies on simulations, which can only deal with a rather limited number of users. However, it is hard to simulate the performance of a multiple access system supporting hundreds or even thousands of users, even though it is of practical interest to predict the achievable performance of such large-scale multiple access systems. Given this motivation, in this chapter, we mathematically analyze the performance of SM-SCDMA systems by first deriving the single-user BER bound and then analyzing the approximate BER of multi-user SM-SCDMA systems. By exploiting the specific structure of SM-SCDMA, a range of formulas are derived, which allow

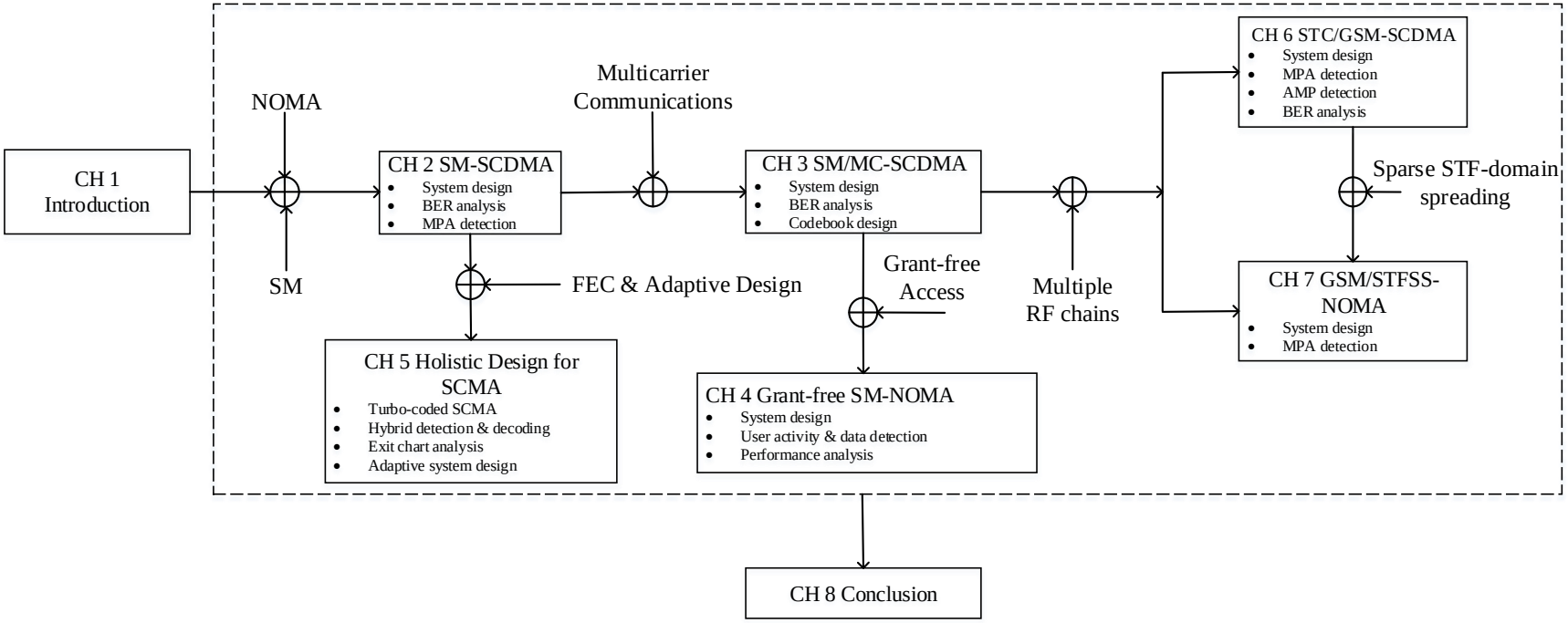

FIGURE 1.1: Outline of the thesis.

us to estimate the BER performance of SM-SCDMA systems having an arbitrary user population.

- The performance of SM-SCDMA systems is investigated both by Monte-Carlo simulations and by evaluating our mathematical formulas derived. Based on the SM-SCDMA systems of relatively small size, we verify the accuracy of formulas derived with the aid of simulations. Then, the performance of relatively large-scale SM-SCDMA systems is investigated based on the numerical evaluation of our formulas derived. Furthermore, we address the impact of the associated parameters on the BER performance attained, and demonstrate the efficiency of the MPAD.

- Finally, we propose a novel 8QAM scheme. When communicating over Gaussian channels, this scheme outperforms all the existing 8QAM schemes in the relatively low signal-to-noise (SNR) (≤ 10 dB) region, while achieving a similar BER performance to the best existing 8QAM schemes in the relatively high-SNR region. By contrast, when communicating over Rayleigh fading channels, it outperforms all the existing 8QAM schemes within the SNR region considered.

However, the SM-SCDMA scheme proposed in Chapter 2 relies on the assumption of having frequency-flat fading channels. When practical frequency-selective fading channels are considered, SM-SCDMA will suffer from severe inter-symbol interference (ISI), hence the complexity of the MPAD is exponentially increased with the number of paths of the frequency-selective fading channels.

Fortunately, an effective technique of combatting frequency-selective fading is to employ FD-spreading aided MC signalling [103], which is capable of exploiting the energy scattered across the frequency-domain by combining the signals gleaned from the different subcarriers. However, conventional MC signalling employing all subcarriers for each user has the disadvantage of high peak-to-average power ratio (PAPR), requiring the employment of high-linearity power-hungry class-A amplifiers, which becomes excessively costly in the uplink of device-centric communications [103, 104]. By contrast, for SCDMA-assisted MC systems activating only a small fraction of subcarriers for each user, the PAPR problem of conventional MC systems can be mitigated. Against this backdrop, Chapter 3 extends our solution developed in Chapter 2 to MC communications and proposes a SM/MC-SCDMA system. The associated novel contributions are summarized as follows.

- A SM/MC-SCDMA system is proposed for supporting massive uplink connectivity. In the proposed system, SM is employed for reducing the number of RF chains. In contrast to the SM-SCDMA system proposed in [26], which assumes flat fading, the SM/MC-SCDMA employs MC signalling to combat frequency-selective fading. Sparse spreading is employed for the sake of facilitating low-complexity detection, whilst significantly alleviating the PAPR problem of MC systems. Furthermore, a

MPAD is developed for the SM/MC-SCDMA system for low-complexity detection, even in the face of a high normalized user-load.

- Since our proposed SM/MC-SCDMA system is designed for operation in practical frequency-selective fading channels, which result in correlated fading in the frequency-domain, the single-user BER bounds derived in [105–108] cannot be directly exploited, since all of them assume independent flat Rayleigh fading. Therefore, we analyze the single-user BER bound of the SM/MC-SCDMA system, when assuming that the signals experience frequency-selective fading, whilst taking into account the correlation among the subcarriers.

- Based on the single-user BER bound, we propose the guidelines for sparse code design. Furthermore, we conceive a sparse code allocation technique for achieving a high diversity gain.

- The BER performance of the proposed SM/MC-SCDMA system using MPAD is studied both by Monte-Carlo simulations and by our analytical results. Additionally, the SM/MC-SCDMA scheme is generalized to the SM/MC-SCMA arrangement for the sake of obtaining extra shaping gain. Furthermore, the BER performance of both SM/MC-SCDMA and SM/MC-SCMA is compared to that of other related legacy MIMO schemes.

Another challenge encountered in our mMTC scenario is the low-latency requirement and the sporadic uplink transmission pattern. In this context, grant-free access schemes are promising in terms of satisfying the stringent low-latency requirements, whilst simultaneously supporting sporadic uplink transmissions without imposing any overhead. Hence, in Chapter 4, we relax the assumption of Chapters 2 and 3, which assume all users to be active within each symbol duration in the system, and propose an uplink grant-free SM/MC-NOMA scheme, where the users transmit in a sporadic pattern at a low rate. The novel contributions of Chapter 4 are as follows.

- We propose an uplink SM/MC-NOMA scheme for supporting massive grant-free multiple access for next-generation wireless communications. The proposed SM/MC-NOMA scheme gleans diversity gains from the often independently-fading frequency- and spatial-domains. SM is employed for reducing the number of RF chains, while non-orthogonal FD spreading attains FD diversity gains for MC transmission over frequency-selective fading channels. In contrast to the existing research on SM-NOMA uplink transmissions [23, 26, 27, 109], which assumes that all users are active all the time and transmit their data to the BS, we assume grant-free uplink transmission, where each user only becomes active at a small activation probability.

- In order to identify the active users and detect their transmitted data, an iterative Joint Multiuser Matching Pursuit (JMuMP) detector is proposed based on the SP

algorithm of [96], which exploits the sparsity existing in both the user activity and in the SM antenna domain. In contrast to the original SP detector of [96], which recovers the user signals by exploiting the known activity at the receiver, the number of active users is estimated by our JMuMP detector before the detection of data conveyed by the classic SSK and APM symbols, with the SSK information detection being intrinsically integrated into the active user identification process. Meanwhile, a more accurate symbol mapping approach is proposed and integrated in JMuMP detector.

- We also conceive an Adaptive MuMP (AMuMP) detector, which does not require the *a priori* knowledge of the user activity at the receiver, and yet further improves the BER performance of the SM/MC-NOMA system employing the JMuMP detector. Naturally, this is achieved at the cost of a higher detection complexity and latency. In the proposed AMuMP detector, both the active users as well as their data are iteratively detected, until both the active users and their data are deemed to be reliably detected. This is more realistic, but also more challenging than the JMuMP philosophy of assuming that the number of users identified in each iteration remains unchanged. We demonstrate that the AMuMP scheme provides more reliable detection than the JMuMP detector, even when the user activation probability is as high as $p = 0.3$.

- The BER vs complexity trade-off of our SM/MC-NOMA system employing the JMuMP and AMuMP detectors is demonstrated by simulation results.

The previous chapters only consider the performance of uncoded systems. Therefore, in Chapter 5, we extend our focus to the holistic design of the SCMA system, and conceive an EXtrinsic Information Transfer (EXIT)-chart-aided hybrid detection and decoding (HDD) algorithm for turbo-coded SCMA systems, which reduced the complexity of the conventional joint detection and decoding (JDD), without degrading the BER performance. The novel contributions of Chapter 5 are as follows.

- Firstly, we investigate the impact of the iterative extrinsic logarithmic likelihood ratio (LLR) exchange between the MPA detector and the Logarithmic Bahl-Cocke-Jelinek-Raviv (Log-BCJR) turbo decoder by comparing the BER of separate detection and decoding (SDD) to that of the JDD scheme in each iteration. The significant BER improvement of JDD shows the advantage of iterative extrinsic information exchange.

- Secondly, by analysing the convergence behaviour by EXIT charts, we propose an HDD algorithm, which maintains the BER performance compared to the conventional JDD, but achieves a beneficial complexity reduction. To be more specific, we optimize the activation order of detection and decoding scheduling for achieving early termination with the aid of EXIT chart analysis. In this way, the detection

and decoding latency can be significantly reduced at a similar BER to that of HDD. Additionally, by exploiting the resultant early-termination property, the proposed HDD achieves a complexity reduction of up to 25%.

- Finally, we propose a near-instantaneously adaptive turbo-coded SCMA system, where the transmitter selects the most appropriate transmission mode according to the prevalent near-instantaneous channel conditions. Our adaptive turbo-coded SCMA system configures itself in the most appropriate mode of operation by jointly selecting the user load, coding rate as well as modulation order by maintaining the data rate at the target BER. Our adaptive system design principle can be readily extended to SCMA systems in combination with other channel coding schemes, such as LDPC codes and polar codes, just to name a few.

From Chapter 6, we further expand our scope to the exploitation of the transmit diversity for the SM-NOMA systems investigated in the previous chapters. In this chapter, we propose a space-time-coded generalized SM-aided SCDMA (STC/GSM-SCDMA) system, which achieves transmit diversity in both spatial- and frequency-domain (SFD). The novel contributions of Chapter 6 are as follows.

- Firstly, we propose a STC/GSM-SCDMA system for supporting the heavily-loaded multiuser (MU) multicarrier (MC) uplink, while achieving a beneficial transmit diversity gain both in the spatial- and in the FD. In our STC/GSM-SCDMA system, GSM is employed both for reducing the number of RF chains and for transmitting extra information bits via the activated TA indices, while STC is employed for exploiting spatial domain diversity. Meanwhile, by adopting the LDS concept in the FD, MC signalling can also be activated for mitigating the deleterious effects of frequency-selective fading. Furthermore, in contrast to the conventional orthogonal MU systems, where 'only' up to 100% normalized user-load can be attained, each orthogonal FD resource unit in the proposed STC/GSM-SCDMA system is capable of supporting more than 'just' a single user. Hence, our solution supports a high normalized user-load.

- Secondly, we design a joint factor graph for representing the connections of the proposed STC/GSM-SCDMA system, which combines the GSM symbols with the quadrature amplitude modulation (QAM) symbols and aggregates all observations at all RAs of each subcarrier. Then bespoke MPA detection is conceived based on the proposed joint factor graph.

- Thirdly, a 3-dimensional (3D) factor graph is designed, where the connections between users and TAs as well as those between subcarriers and RAs are separately illustrated, based on which a low-complexity AMP detector is proposed. The AMP detector conceived in this chapter imposes 1000 times lower computational complexity than the MPA detector, at the cost of a modest 2 dB BER SNR increase.

- Finally, the theoretical single-user performance bound is derived for the proposed STC/GSM-SCDMA system for transmission over frequency-selective Rayleigh fading channels, which is employed as the benchmark of the multiuser STC/GSM-SCDMA systems. Our simulation results also demonstrate that our STC/GSM-SCDMA system outperforms the MIMO-NOMA systems of [29, 110].

Chapter 7 provides an alternative way for achieving the transmit diversity to that of Chapter 6 and proposes the generalized spatial modulation-aided sparse space-time-frequency spreading (GSM/SSTFS) for NOMA systems. The novel contributions of Chapter 7 are as follows.

- Firstly, we propose a GSM/SSTFS system for supporting large-scale access at a high normalized user-load by achieving the STF-domain spreading for the first time. Specifically, in the GSM/SSTFS system relying on two active TAs, each user spreads its signal over two symbol durations, two active TAs, and multiple subcarriers by a unique pre-assigned sparse code, before transmitting the signal over the channel. Furthermore, with the aid of GSM, extra information bits are embedded in the TA indices.
- Secondly, a joint factor graph is designed for signal detection, which is eminently suitable for visualizing the message-propagation by the STF-domain spreading. Based on the connections of the proposed joint factor graph, a joint message passing-aided (JMPA) detector is conceived for attaining a near-single-user BER at a low complexity.
- Finally, our BER performance results have demonstrated that the proposed GSM/SSTF-S scheme achieves superior BER, compared to that of conventional MIMO-NOMA schemes at the same data rate in terms of bits per symbol (BPS).

Finally, Chapter 8 summarises the main conclusions of the thesis and suggests potential research ideas for multiuser MC next-generation communications.

Chapter 2

Spatial Modulation-Aided Sparse Code Division Multiple Access

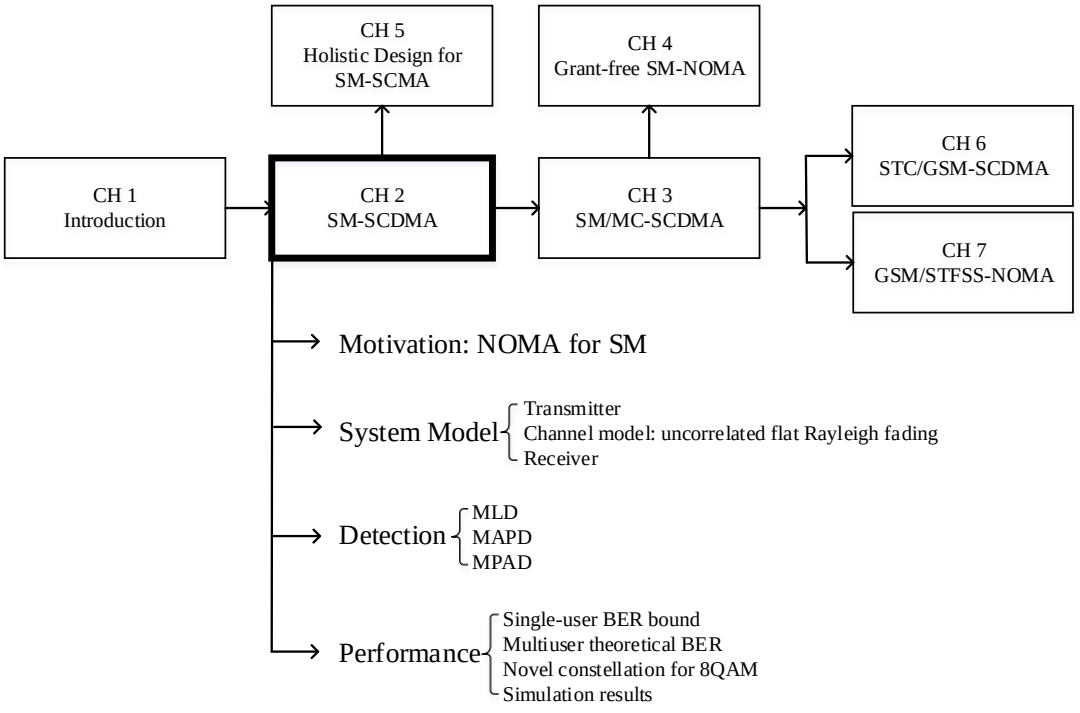

FIGURE 2.1: The relationship of Chapter 2 with the rest of the thesis.

2.1 Introduction

As discussed in Section 1.2, the spatial modulation-aided orthogonal multiple-access (SM-OMA) schemes summarized in Table 1.2 are only capable of supporting a normalized user load up to 100%, which prevents their application in next-generation massive machine-type communications (mMTC) or in the Internet-of-Things (IoT), which typically have to support more users/nodes than the number of resource slots. With the motivation of supporting these demanding scenarios, non-orthogonal multiple-access (NOMA) [73,111] is capable of of supporting a higher number of users (or devices) than that of the number of resource units available.

Therefore, in this chapter, we exploit the properties of both SM as well as NOMA, and propose a spatial-modulated sparse code division multiple access (SM-SCDMA) scheme, in order to support these demanding mMTC and IoT scenarios. In summary, the contributions of this chapter are as follows.

- A SM-SCDMA scheme is proposed for supporting a normalized user-load up to 200% in uplink communications. We assume that each user employs a few transmit antennas (TAs) for supporting the SM, while the base station (BS) employs several receive antennas for enhancing the detection reliability, where MA is achieved with the aid of SCDMA. Since our SM-SCDMA relies on the principle of NOMA, it has the potential of supporting the MA (multiple access) transmission, where the number of (active) users is higher than the total number of chips in the spreading codes.

- It has been recognized that employing SM is beneficial for the implementation of multiple-input multiple-output (MIMO) using a low number of radio-frequency (RF) transceivers, and provides lower complexity receiver implementation options [18, 20]. However, when there is a high number of users sharing the resources based on SCDMA, the design of relatively low-complexity detectors that are capable of achieving near-optimum performance is challenging. In this chapter, we first consider the classic maximum-likelihood detection (MLD) in order to study the best possible potential of the SM-SCDMA scheme. Then, we derive a maximum *a-posteriori* detector (MAPD), based on which we develop a reduced complexity message passing-aided detector (MPAD) that is suitable for SM-SCDMA systems, which employs SM and exploits receiver diversity.

- In most existing references on code-domain NOMA [10–14], the performance study depends mainly on simulations, which can typically deal with tens of users. However, it is hard to simulate the performance of a MA system supporting hundreds or even thousands of users. However, future NOMA systems are expected to support a huge number of users, hence it is interesting to predict the achievable performance

of such large-scale MA systems. With this motivation, in this chapter, we mathematically analyze the error performance of SM-SCDMA systems by first deriving the single-user bit error rate (BER) bound and then analyzing the approximate BER of multi-user SM-SCDMA systems. By exploiting the specific structure of SM-SCDMA, a range of formulas are derived, which allow us to estimate the BER performance of the SM-SCDMA systems of arbitrary size.

- The performance of SM-SCDMA systems is investigated both by Monte-Carlo simulations and by the evaluation of the formulas derived. Based on the SM-SCDMA systems of relatively small size, we verify the formulas derived by simulation and find their valid ranges. Then, the performance of relatively large-scale SM-SCDMA systems is investigated based on the numerical evaluation of our formulas derived. Furthermore, we address the impact of the related parameters on the BER performance attained, and demonstrate the efficiency of the MPAD.

- Finally, we propose a novel 8 quadrature amplitude modulation (8QAM) scheme. When communicating over Gaussian channels, it outperforms all the existing 8QAM schemes in the relatively low signal-to-noise (SNR) ($\leq$ 10 dB) region, while achieving a similar BER performance to the best existing 8QAM schemes in the relatively high-SNR region. By contrast, when communicating over Rayleigh fading channels, it outperforms all the existing 8QAM schemes within the SNR region considered.

The structure of the rest of this Chapter is summarized in Fig. 1.1. Specifically, Section 2.2 describes the proposed SM-SCDMA system model. Then, the detection algorithms are addressed in Section 2.3. Section 2.4 analyzes the BER of the SM-SCDMA system, while the BER performance of SM-SCDMA systems is investigated in Section 2.5. Finally, Section 2.6 summarizes the main conclusions of our research.

2.2 System Model

In this section, we describe the transmitter and receiver models in Sections 2.2.1 and 2.2.2, respectively. Furthermore, our main assumptions and notations are detailed.

2.2.1 Transmitter Model

Let us consider a single-cell wireless uplink, where K users simultaneously transmit their information to a single BS. In order to avoid dealing with the trivial cases, but to focus our attention on the important principles, we assume that all users employ the same M_1 number of TAs satisfying $M_1 = 2^{b_1}$, where b_1 is an integer. We assume that the BS employs U receive antennas (RAs) for attaining receiver diversity. Based on the principles of SM [18], we assume that within a symbol duration of T_s seconds,

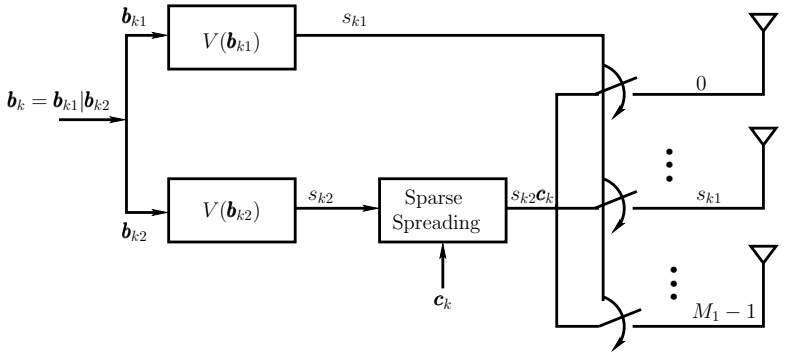

FIGURE 2.2: Transmitter schematic diagram of the kth user in the SM-SCDMA system.

one of the M_1 TAs of a user is activated for transmitting b_1 bits, forming an M_1SSK scheme [36]. Hence, the SSK symbol set can be expressed as $\mathcal{S}_1 = \{0, 1, ..., M_1 - 1\}$ and the corresponding b_1-bit symbols can be their natural binary representations. In addition to the M_1SSK, the SM also uses the activated TA to transmit $b_2 = \log_2 M_2$ bits, relying on a M_2-ary APM (M_2APM), such as M_2-ary QAM (M_2QAM). For convenience, the APM symbol set is expressed as $\mathcal{S}_2 = \{s_{2,0}, s_{2,1}, ..., s_{2,M_2-1}\}$, whose elements satisfy $\sum_{i=0}^{M_2-1} |s_{2,i}|^2/M_2 = 1$. Therefore, when considering both the M_1SSK and M_2APM, $b = (b_1 + b_2)$ bits per symbol can be transmitted by a user to the BS. Note that the SM model considered can be readily extended to the generalized SM model of [20], where multiple TAs are activated for simultaneously transmitting multiple APM symbols.

Fig. 2.2 depicts the transmitter schematic of the kth user of the SM-SCDMA system. During a symbol period, the b-bit symbol $\boldsymbol{b}_k$ of user k is first partitioned into two sub-symbols, the SSK symbol $\boldsymbol{b}_{k1}$ consisting of the first b_1 bits and the APM symbol $\boldsymbol{b}_{k2}$ consisting of the remaining b_2 bits. Let $s_{k1} \in \mathcal{S}_1$ be an integer value obtained from the mapping $V_1(\boldsymbol{b}_{k1})$, which determines the TA activated by user k. Furthermore, let $s_{k2} \in \mathcal{S}_2$ be obtained from the mapping $V_2(\boldsymbol{b}_{k2})$, which is an APM symbol. Following the principles of SCDMA [10], s_{k2} is spread to a maximum of d_x chips ($d_x << N$) using the spreading sequence $\boldsymbol{c}_k = [c_{k0}, c_{k1}, ..., c_{k(N-1)}]^T$ assigned to user k, where $\boldsymbol{c}_k$ is of N-length and has d_x non-zero chips, satisfying $\|\boldsymbol{c}_k\|^2 = 1$. Furthermore, we assume that the maximum number of users sharing any of the N chips is d_c. In the following analysis, for simplicity, we assume that d_x and d_c are constants. The set of sparse codes achieving these are referred to as the regular sparse codes. Finally, as shown in Fig. 2.2, the kth user's SM-SCDMA signal is transmitted from the s_{k1}th TA, following some further transmitter processing that is not shown in the figure.

Therefore, given the SM symbol $s_{k1}|s_{k2}$ of user k, the unity-energy baseband equivalent signal transmitted by user k can be expressed as

$$\boldsymbol{t}_k(s_{k1}) = s_{k2}\boldsymbol{c}_k, \quad k = 1, 2, \cdots, K \tag{2.1}$$

where $\boldsymbol{t}_k(s_{k1})$ indicates that the signal is transmitted by the s_{k1}th antenna. For convenience of description, below we define $\mathcal{S} = \mathcal{S}_1 \otimes \mathcal{S}_2$, which is a set containing the $M(= M_1 M_2)$ combinations of the elements in $\mathcal{S}_1$ with those in $\mathcal{S}_2$.

2.2.2 Receiver Model

Assume that the channel between any user and the BS experiences flat Rayleigh fading[1]. Let the channel impulse response (CIR) between the s_{k1}th TA of user k and the U RAs at the BS be expressed as

$$\boldsymbol{h}_{s_{k1}} = [h_{s_{k1}}^{(0)}, h_{s_{k1}}^{(1)}, \cdots, h_{s_{k1}}^{(U-1)}]^T, \ s_{k1} = 0, \ldots, M_1 - 1 \tag{2.2}$$

where $h_{s_{k1}}^{(u)}$ are independent identically distributed (iid) complex Gaussian random variables with zero mean and a variance of 0.5 per dimension. Therefore, when there are K uplink users, the N-length observation vector received by the uth RA is given by

$$\boldsymbol{y}_u = \sum_{k=1}^{K} h_{s_{k1}}^{(u)} \boldsymbol{t}_k(s_{k1}) + \boldsymbol{n}_u = \sum_{k=1}^{K} h_{s_{k1}}^{(u)} s_{k2} \boldsymbol{c}_k + \boldsymbol{n}_u, \quad u = 0, 1, \cdots, U-1, \tag{2.3}$$

where $\boldsymbol{n}_u$ is the Gaussian noise vector of zero mean and having a covariance matrix of $2\sigma^2 \boldsymbol{I}_N$, expressed as $\mathcal{CN}(0, 2\sigma^2 \boldsymbol{I}_N)$, with $\sigma^2 = 1/(2\gamma_0)$, and $\gamma_0 = b\gamma_b$ being the SNR per symbol, while γ_b the SNR per bit.

Let $\boldsymbol{y} = [\boldsymbol{y}_0^T, \boldsymbol{y}_1^T, \cdots, \boldsymbol{y}_{U-1}^T]^T$ and $\boldsymbol{n} = [\boldsymbol{n}_0^T, \boldsymbol{n}_1^T, \cdots, \boldsymbol{n}_{U-1}^T]^T$. Then, we can express $\boldsymbol{y}$ as

$$\boldsymbol{y} = \sum_{k=1}^{K} (\boldsymbol{I}_U \otimes \boldsymbol{c}_k) \boldsymbol{h}_{s_{k1}} s_{k2} + \boldsymbol{n}, \tag{2.4}$$

where $\otimes$ denotes the Kronecker product [112]. Furthermore, we can rewrite (2.4) in a compact form as

$$\boldsymbol{y} = \boldsymbol{H}(\boldsymbol{s}_1)\boldsymbol{s}_2 + \boldsymbol{n} \tag{2.5}$$

where $\boldsymbol{H}(\boldsymbol{s}_1) = [(\boldsymbol{I}_U \otimes \boldsymbol{c}_1)\boldsymbol{h}_{s_{11}}, (\boldsymbol{I}_U \otimes \boldsymbol{c}_2)\boldsymbol{h}_{s_{21}}, \cdots, (\boldsymbol{I}_U \otimes \boldsymbol{c}_K)\boldsymbol{h}_{s_{K1}}]$, $\boldsymbol{s}_1 = [s_{11}, s_{21}, ..., s_{K1}]^T$ collects the SSK symbols and $\boldsymbol{s}_2 = [s_{12}, s_{22}, ..., s_{K2}]^T$ collects the APM symbols transmitted by the K users.

2.3 Signal Detection

In this section, we address the detection of SM-SCDMA signals. We first consider the optimal maximum likelihood detector (MLD) in Section 2.3.1, whereas Section 2.3.2

[1]Frequency-selective fading may be eliminated by multicarrier SM-SCDMA systems.

derives the maximum *a-posteriori* detector (MAPD). Then, based on this the MPAD is developed in Section 2.3.3.

2.3.1 Maximum-Likelihood Detection (MLD)

Let us express the symbols transmitted by the K users as a vector $\boldsymbol{x} = [x_1, x_2, \cdots, x_K]^T$ and assume that the BS exploits the knowledge of both the channels and of the spreading sequences. Then, the MLD finds the estimate of $\boldsymbol{x}$ by solving the optimization problem of[2]

$$\hat{\boldsymbol{x}} = \arg \min_{\tilde{\boldsymbol{x}} \in \mathcal{S}^K} \left\{ \left\| \boldsymbol{y} - \sum_{k=1}^{K} (\boldsymbol{I}_U \otimes \boldsymbol{c}_k) \boldsymbol{h}_{\tilde{s}_{k1}} \tilde{s}_{k2} \right\|^2 \right\} \tag{2.6}$$

$$= \arg \max_{\tilde{\boldsymbol{x}} \in \mathcal{S}^K} \left\{ \sum_{k=1}^{K} \Re\{\tilde{s}_{k2}^* \boldsymbol{h}_{\tilde{s}_{k1}}^H (\boldsymbol{I}_U \otimes \boldsymbol{c}_k)^H \boldsymbol{y}\} - \frac{1}{2} \sum_{k=1}^{K} \sum_{i=1}^{K} \tilde{s}_{k2}^* \boldsymbol{h}_{\tilde{s}_{k1}}^H (\boldsymbol{I}_U \otimes \boldsymbol{c}_k)^H (\boldsymbol{I}_U \otimes \boldsymbol{c}_i) \boldsymbol{h}_{\tilde{s}_{i1}} \tilde{s}_{i2} \right\} \tag{2.7}$$

where $\tilde{x}_k = \tilde{s}_{k1} | \tilde{s}_{k2}$ determines the term $\boldsymbol{h}_{\tilde{s}_{k1}} \tilde{s}_{k2}$, and $\Re\{x\}$ returns the real part of x. In the above equation, we can show that

$$\boldsymbol{h}_{\tilde{s}_{k1}}^H (\boldsymbol{I}_U \otimes \boldsymbol{c}_k)^H \boldsymbol{y} = \sum_{u=0}^{U-1} (h_{\tilde{s}_{k1}}^{(u)})^* \boldsymbol{c}_k^H \boldsymbol{y}_u \tag{2.8}$$

Furthermore, let $\mathcal{C}_k$ be a set containing the d_x indices of $\boldsymbol{c}_k$ having non-zero entries. Then (2.8) can be further simplified to

$$\boldsymbol{h}_{\tilde{s}_{k1}}^H (\boldsymbol{I}_U \otimes \boldsymbol{c}_k)^H \boldsymbol{y} = \sum_{u=0}^{U-1} \sum_{m \in \mathcal{C}_k} (h_{\tilde{s}_{k1}}^{(u)})^* c_{km}^* y_{um} \tag{2.9}$$

The second term of (2.7) can be simplified as

$$\begin{aligned} \boldsymbol{h}_{\tilde{s}_{k1}}^H (\boldsymbol{I}_U \otimes \boldsymbol{c}_k)^H (\boldsymbol{I}_U \otimes \boldsymbol{c}_i) \boldsymbol{h}_{\tilde{s}_{i1}} &= \boldsymbol{h}_{\tilde{s}_{k1}}^H (\boldsymbol{I}_U \otimes \boldsymbol{c}_k^H \boldsymbol{c}_i) \boldsymbol{h}_{\tilde{s}_{i1}} \\ = \boldsymbol{h}_{\tilde{s}_{k1}}^H (\boldsymbol{I}_U \otimes \sum_{m \in \mathcal{C}_k \cap \mathcal{C}_i} c_{km}^* c_{im}) \boldsymbol{h}_{\tilde{s}_{i1}} &= \left(\sum_{m \in \mathcal{C}_k \cap \mathcal{C}_i} c_{km}^* c_{im} \right) \boldsymbol{h}_{\tilde{s}_{k1}}^H \boldsymbol{h}_{\tilde{s}_{i1}} \end{aligned} \tag{2.10}$$

where $\mathcal{C}_k \cap \mathcal{C}_i$ gives a set containing the indices where both $\boldsymbol{c}_k$ and $\boldsymbol{c}_i$ have non-zero entries. Upon substituting (2.9) and (2.10) into (2.7), we obtain

$$\hat{\boldsymbol{x}} = \arg \max_{\tilde{\boldsymbol{x}} \in \mathcal{S}^K} \left\{ \sum_{k=1}^{K} \sum_{u=0}^{U-1} \sum_{m \in \mathcal{C}_k} \Re\{\tilde{s}_{k2}^* (h_{\tilde{s}_{k1}}^{(u)})^* c_{km}^* y_{um}\} - \frac{1}{2} \sum_{k=1}^{K} \sum_{i=1}^{K} \left(\sum_{m \in \mathcal{C}_k \cap \mathcal{C}_i} c_{km}^* c_{im} \right) \tilde{s}_{k2}^* \boldsymbol{h}_{\tilde{s}_{k1}}^H \boldsymbol{h}_{\tilde{s}_{i1}} \tilde{s}_{i2} \right\} \tag{2.11}$$

[2]Throughout the report, x, $\tilde{x}$ and $\hat{x}$ represent the symbol transmitted, the specific symbol being tested by the search algorithms and the final detected symbol, respectively.

From (2.11) we know that although $\mathcal{C}_k$ has only d_x non-zero elements, which can be exploited for significantly reducing the computation, the MLD's complexity is still $\mathcal{O}(M^K)$. Therefore, the MLD described by (2.11) is impractical, especially, when the SM-SCDMA systems are proposed for supporting numerous users (devices). Next, we consider the symbol-based MAPD, which facilitates the employment of the MPA, as shown in Section 2.3.3.

2.3.2 Maximum *A-Posteriori* Detection (MAPD)

Given the observation of $\boldsymbol{y}$ in (2.4), the symbol-by-symbol based MAPD detects the lth user's symbol via maximizing the posteriori probability as

$$\hat{x}_l = \arg\max_{\tilde{x}_l \in \mathcal{S}} \{P(\tilde{x}_l|\boldsymbol{y})\} = \arg\max_{\tilde{x}_l \in \mathcal{S}} \{P(\tilde{x}_l) p(\boldsymbol{y}|\tilde{x}_l)\} = \arg\max_{\tilde{x}_l \in \mathcal{S}} \left\{ \sum_{\boldsymbol{x}_l \in \mathcal{S}^{K-1}} P(\boldsymbol{x}_l, \tilde{x}_l) p(\boldsymbol{y}|\boldsymbol{x}_l, \tilde{x}_l) \right\} \tag{2.12}$$

where $p(x|a)$ is the conditional probability density function (PDF) of x given a, $P(a)$ is the *a-priori* probability of a, while $\boldsymbol{x}_l$ is a $(K-1)$-element vector obtained from $\boldsymbol{x}$ by removing the lth user's symbol. Since the observations $\{y_{un}\}$ are independent for given $(\boldsymbol{x}_l, \tilde{x}_l)$, (2.12) can be written in detail as

$$\hat{x}_l = \arg\max_{\tilde{x}_l \in \mathcal{S}} \left\{ \sum_{\boldsymbol{x}_l \in \mathcal{S}^{K-1}} P(\boldsymbol{x}_l, \tilde{x}_l) \prod_{u=0}^{U-1} \prod_{n=0}^{N-1} p(y_{un}|\boldsymbol{x}_l, \tilde{x}_l) \right\} \tag{2.13}$$

Let $\mathcal{K}_l$ be a set containing all the interfering users sharing at least one (non-zero) chip with user l. Let furthermore $\boldsymbol{x}_{[n]}$ be a d_c-length vector containing the symbols sent by the users sharing the nth chip of the spreading sequences. Then (2.13) can be further simplified to

$$\hat{x}_l = \arg\max_{\tilde{x}_l \in \mathcal{S}} \left\{ \sum_{\boldsymbol{x}'_l \in \mathcal{S}^{|\mathcal{K}_l|}} P(\boldsymbol{x}'_l, \tilde{x}_l) \prod_{u=0}^{U-1} \prod_{n \in \mathcal{C}_l} p(y_{un}|\boldsymbol{x}_{[n]}) \right\} \tag{2.14}$$

where $|\mathcal{K}_l|$ is the cardinality of $\mathcal{K}_l$, and $\boldsymbol{x}'_l$ is of $|\mathcal{K}_l|$-length. In (2.14), when $\boldsymbol{x}_{[n]}$ is given, the PDF of $p(y_{un}|\boldsymbol{x}_{[n]})$ can be expressed as

$$p(y_{un}|\boldsymbol{x}_{[n]}) = \frac{1}{2\pi\sigma^2} \exp\left(-\frac{\| y_{un} - \sum_{k \in \mathcal{D}_n} h^{(u)}_{s_{k1}} s_{k2} c_{kn} \|^2}{2\sigma^2} \right) \tag{2.15}$$

where we define $\mathcal{D}_n$ the set containing the indices of the users conveying information using the nth chip of the spreading codes.

(2.14) shows that the complexity of detecting user l is $\mathcal{O}(M^{|\mathcal{K}_l|})$. When regular sparse codes are employed, $|\mathcal{K}_l|$ is a constant, which is dependent on both d_x and d_c, and is

usually much smaller than K. Hence, employing sparse codes for spreading is capable of reducing the detection complexity of MAPD. Furthermore, when the MAPD is implemented by an approximated algorithm, the detection complexity can be further reduced [10].

2.3.3 Message Passing Algorithm (MPA)-Aided Detection

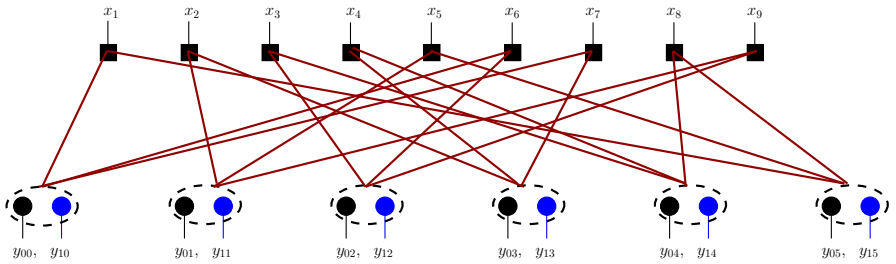

FIGURE 2.3: Factor graph representation of the SM-SCDMA system with the parameters of $U = 2,\ N = 6,\ K = 9$, and $d_x = 2,\ d_c = 3$.

Similar to the classic LDPC codes [113], the input-output relationship in the proposed SM-SCDMA system can be described by a factor graph [10, 74], as shown in Fig. 2.3 for the parameters specified in the caption. In this factor graph, the K symbols of the form $x_k = s_{k1}|s_{k2}$ and sent by K users are represented by K variable nodes, while the UN observations in $\boldsymbol{y}$ act as N function (or check) nodes, with each having U channel inputs provided by the U RAs. As shown in the figure, users 1, 6 and 7 share the 0th function node, which has two observations obtained from the first and second RAs respectively. Hence, while these three users do interfere with each other on the 0th chip, information carried by the different chips activated by the three users can also be transferred from one chip to another via the 0th function node. By doing this, the overall detection performance of SM-SCDMA may be significantly improved. Below we detail the MPAD.

Let us define two sets as

$$\begin{aligned} \mathcal{X}_j &= \{i : 0 \le i \le N-1, e_{j,i} \ne 0\},\ j = 1, 2, \ldots, K \\ \mathcal{C}_i &= \{j : 1 \le j \le K, e_{j,i} \ne 0\},\ i = 0, 1, \ldots, N-1 \end{aligned} \tag{2.16}$$

where we have $|\mathcal{X}_j| = d_x$, representing the d_x connections with the variable node j, and $|\mathcal{C}_i| = d_c$, giving the d_c connections with the function node i.

Let us explicitly express the symbol set as $\mathcal{X} = \{a_0, a_1, \ldots, a_{M-1}\}$, where $M = M_1 M_2$. Let the probability $\eta_{j,i}^{a_m,t}$ be a message sent from the variable node x_j to the function node f_i (corresponding to the ith chip of the spreading sequences) during the tth iteration. Note that here $\eta_{j,i}^{a_m,t}$ is the probability that we have $x_j = a_m$, given all the messages received by x_j from all of its neighboring function nodes, excluding f_i. Similarly, let the probability $\delta_{i,j}^{a_m,t}$ represent a message sent from the function node i to the variable node

j during the tth iteration. Explicitly, this is the probability that $x_j = a_m$, given the specific messages received by f_i from all its neighboring variable nodes, excluding x_j. Then, following [114, 115] and with the aid of Fig. 2.3, the MPAD can be described as follows.

Initially, we set $\eta_{j,i}^{a_m,(0)} = 1/M$ for all $a_m \in \mathcal{X}$ and for any specific (j,i) pairs, where $j \in \mathcal{X}_j$ and $i \in \mathcal{C}_i$. Then, during the tth, $t \geq 0$, iteration, the probability $\delta_{i,j}^{a_m,t}$ can be computed as

$$\delta_{i,j}^{a_m,t} = \sum_{\boldsymbol{x}_{[i]} \in \mathcal{X}^{d_c-1}, x_j = a_m} \left(\prod_{x_v \in \boldsymbol{x}_{[i]} \backslash x_j} \eta_{j,i}^{x_v,t} \right) \prod_{u=0}^{U-1} p(y_{ui} | \boldsymbol{x}_{[i]}, x_j = a_m), \ m = 0, \ldots, M-1 \tag{2.17}$$

for $i \in \mathcal{C}_i$ and $j \in \mathcal{X}_j$, where $\prod_{x_v \in \boldsymbol{x}_{[i]} \backslash x_j} \eta_{j,i}^{x_v,t}$ is the a-priori probability of a given $\boldsymbol{x}_{[i]}$ with $x_j = a_m$, while $p(y_{ui} | \boldsymbol{x}_{[i]}, x_j = a_m)$ is given by (2.15).

Then, during the $(t+1)$st iteration, the values $\delta_{i,j}^{a_m,t}$ for $i \in \mathcal{C}_i$ and $j \in \mathcal{X}_j$ are used to compute $\eta_{j,i}^{a_m,(n+1)}$ for $j \in \mathcal{X}_j$ and $i \in \mathcal{C}_i$, using the formula of

$$\eta_{j,i}^{a_m,(n+1)} = \xi_{j,i} \prod_{v \in \mathcal{X}_j \backslash i} \delta_{v,j}^{a_m,t}, \ m = 0, 1, \ldots, M-1 \tag{2.18}$$

where $\xi_{j,i}$ is applied to make $\sum_{m=0}^{M-1} \eta_{j,i}^{a_m,(n+1)} = 1$.

Finally, when the affordable number of iterations is exhausted, the data symbols sent from the K users are detected as

$$x_j = \arg\max_{a_m} \prod_{v \in \mathcal{X}_j} \delta_{v,j}^{a_m,t}, \ k = 1, 2, \ldots, K \tag{2.19}$$

The complexity of the MPAD is dependent on the number of users sharing a chip. When regular sparse codes are used, the complexity per user can be shown to be $\mathcal{O}(M^{d_c})$ [115]. Hence, provided that $d_x, d_c \geq 2$, the MPAD has a lower complexity than the MAPD considered in Section 2.3.2, which has the complexity of $\mathcal{O}(M^{d_x(d_c-1)})$ per user for regular sparse codes.

2.4 Performance Analysis

This section contributes to the error performance analysis of SM-SCDMA systems. We first analyze the single-user BER performance, which is the lower-bound BER of SM-SCDMA systems. Then, based on the single-user BER, we derive formulas for approximating the BER of SM-SCDMA systems supporting K users.

2.4.1 Analysis of Single-User Average BER

When the SM-SCDMA system supports only a single user, the MLD of (2.7) becomes

$$\hat{x} = \arg\max_{\tilde{x}\in\mathcal{S}} \left\{ \Re\{\tilde{s}_2^* \boldsymbol{h}_{\tilde{s}_1}^H (\boldsymbol{I}_U \otimes \boldsymbol{c}_k)^H \boldsymbol{y}\} - \frac{1}{2}\|\boldsymbol{h}_{\tilde{s}_1}\tilde{s}_2\|^2 \right\} \tag{2.20}$$

where the index k (except $\boldsymbol{c}_k$) is dropped for notational convenience. A detection error occurs, when $\hat{x} \neq x$, which resulted from the event that there is at least one $\tilde{x} \neq x$, yielding

$$\begin{aligned} &\Re\{\tilde{s}_2^* \boldsymbol{h}_{\tilde{s}_1}^H (\boldsymbol{I}_U \otimes \boldsymbol{c}_k)^H \boldsymbol{y}\} - \frac{1}{2}\|\boldsymbol{h}_{\tilde{s}_1}\tilde{s}_2\|^2 \\ &> \Re\{s_2^* \boldsymbol{h}_{s_1}^H (\boldsymbol{I}_U \otimes \boldsymbol{c}_k)^H \boldsymbol{y}\} - \frac{1}{2}\|\boldsymbol{h}_{s_1}s_2\|^2 \end{aligned} \tag{2.21}$$

Let us arrange (2.21) as

$$\begin{aligned} &\Re\{(\boldsymbol{h}_{\tilde{s}_1}\tilde{s}_2 - \boldsymbol{h}_{s_1}s_2)^H (\boldsymbol{I}_U \otimes \boldsymbol{c}_k)^H \boldsymbol{y}\} \\ &> \frac{1}{2}\left(\|\boldsymbol{h}_{\tilde{s}_1}\tilde{s}_2\|^2 - \|\boldsymbol{h}_{s_1}s_2\|^2\right) \end{aligned} \tag{2.22}$$

Then, upon substituting $\boldsymbol{y}$ from (2.4) for $K = 1$ into (2.22), we obtain

$$\Re\left\{(\boldsymbol{h}_{\tilde{s}_1}\tilde{s}_2 - \boldsymbol{h}_{s_1}s_2\|)^H \boldsymbol{n}'\right\} > \frac{1}{2}\left(\|\boldsymbol{h}_{\tilde{s}_1}\tilde{s}_2 - \boldsymbol{h}_{s_1}s_2\|^2\right) \tag{2.23}$$

where $\boldsymbol{n}' = (\boldsymbol{I}_U \otimes \boldsymbol{c})^H \boldsymbol{n}$, which obeys the PDF of $\mathcal{CN}(0, 2\sigma^2\boldsymbol{I}_U)$. Hence, the probability that the transmitted symbol x is detected as $\tilde{x}$, which is usually referred to as the pairwise error probability (PEP), is given by

$$P_{EP}(x \to \tilde{x}) = E_{\boldsymbol{H}}\left[Q\left(\sqrt{\frac{1}{4\sigma^2}\|\boldsymbol{h}_{\tilde{s}_1}\tilde{s}_2 - \boldsymbol{h}_{s_1}s_2\|^2}\right)\right] = E_{\boldsymbol{H}}\left[Q\left(\sqrt{\frac{\gamma_0}{2}\|\boldsymbol{h}_{\tilde{s}_1}\tilde{s}_2 - \boldsymbol{h}_{s_1}s_2\|^2}\right)\right] \tag{2.24}$$

where $Q(x)$ is the Gaussian Q-function defined as $Q(x) = (2\pi)^{-1/2}\int_x^\infty e^{-t^2/2}dt$, and $E_{\boldsymbol{H}}[\cdot]$ denotes the expectation with respect to the MIMO channel $\boldsymbol{H}$ between the user and the BS.

As shown in [116, 117], the average bit error rate (ABER) of SM schemes may be approximately evaluated from the union-bound expressed as

$$\bar{P}_{bS} \leq \frac{1}{M_1 M_2 b}\sum_{m_1=0}^{M_1-1}\sum_{m_2=0}^{M_2-1}\sum_{\tilde{m}_1=0}^{M_1-1}\sum_{\tilde{m}_2=0}^{M_2-1} D\left(\boldsymbol{b}_1^{(m_1)}|\boldsymbol{b}_2^{(m_2)}, \tilde{\boldsymbol{b}}_1^{(\tilde{m}_1)}|\tilde{\boldsymbol{b}}_2^{(\tilde{m}_2)}\right) P_{EP}\left(s_1^{(m_1)}|s_2^{(m_2)} \to \tilde{s}_1^{(\tilde{m}_1)}|\tilde{s}_2^{(\tilde{m}_2)}\right) \tag{2.25}$$

where $D(\cdot,\cdot)$ is the Hamming distance between the two binary entries, and $\boldsymbol{b}_i^{(m)}$, $s_i^{(m)}$ represent the mth realizations in bits and symbols. Furthermore, in [116], the closed-form formulas for the PEP of (2.24) have been derived in the context of different fading channels. Specifically, in this chapter, we are only interested in the iid Rayleigh fading channels. In this case, following the analysis in [116], $P_{EP}(x \to \tilde{x})$ can be analyzed by dividing it into the following three cases:

1. (M_1SSK-Error-Only): $P_{EP}(x \to \tilde{x}) = P_{EP}(s_1|s_2 \to \tilde{s}_1|s_2)$;
2. (M_2APM-Error-Only): $P_{EP}(x \to \tilde{x}) = P_{EP}(s_1|s_2 \to s_1|\tilde{s}_2)$;
3. (Both M_1SSK and M_2APM in Error): $P_{EP}(x \to \tilde{x}) = P_{EP}(s_1|s_2 \to \tilde{s}_1|\tilde{s}_2)$.

Upon invoking the alternative representation for the Q-function [118][3], these probabilities can be explicitly expressed as

$$P_{EP}(s_1|s_2 \to \tilde{s}_1|s_2) = \frac{1}{\pi}\int_0^{\pi/2}\left(\frac{2\sin^2\theta}{2\sin^2\theta+\gamma_0|s_2|^2}\right)^U d\theta \tag{2.26a}$$

$$P_{EP}(s_1|s_2 \to s_1|\tilde{s}_2) = \frac{1}{\pi}\int_0^{\pi/2}\left(\frac{4\sin^2\theta}{4\sin^2\theta+\gamma_0|\tilde{s}_2-s_2|^2}\right)^U d\theta \tag{2.26b}$$

$$P_{EP}(s_1|s_2 \to \tilde{s}_1|\tilde{s}_2) = \frac{1}{\pi}\int_0^{\pi/2}\left(\frac{4\sin^2\theta}{4\sin^2\theta+\gamma_0(|\tilde{s}_2|^2+|s_2|^2)}\right)^U d\theta \tag{2.26c}$$

Equations (2.26a)-(2.26c) show that the fading channel effects have been averaged out in the PEP. This means that the computation of (2.25) does not need to consider the specific M_1SSK symbols, only the M_2APM symbols need to be considered. Therefore, (2.25) can be simplified to [116]

$$\bar{P}_{bS} \le \frac{M_1 b_1}{2M_2 b}\sum_{m_2=0}^{M_2-1} P_{EP}(s_1|s_2^{(m_2)} \to \tilde{s}_1|s_2^{(m_2)}) \tag{2.27a}$$

$$+\frac{1}{M_2 b}\sum_{m_2=0}^{M_2-1}\sum_{\tilde{m}_2\neq m_2}^{M_2-1} D\left(\boldsymbol{b}_2^{(m_2)},\tilde{\boldsymbol{b}}_2^{(\tilde{m}_2)}\right) P_{EP}(s_1|s_2^{(m_2)} \to s_1|\tilde{s}_2^{(\tilde{m}_2)}) \tag{2.27b}$$

$$+\frac{1}{M_2 b}\sum_{m_2=0}^{M_2-1}\sum_{\tilde{m}_2\neq m_2}^{M_2-1}\left[\frac{b_1 M_1}{2}+(M_1-1)D\left(\boldsymbol{b}_2^{(m_2)},\tilde{\boldsymbol{b}}_2^{(\tilde{m}_2)}\right)\right] P_{EP}\left(s_1^{(m_1)}|s_2^{(m_2)} \to \tilde{s}_1^{(\tilde{m}_1)}|\tilde{s}_2^{(\tilde{m}_2)}\right) \tag{2.27c}$$

where the first and third terms at the righthand side are obtained by exploiting the fact that the average number of erroneous bits between a pair of $(\boldsymbol{b}_1,\tilde{\boldsymbol{b}}_1)$ is $b_1 M_1/[2(M_1-1)]$. Furthermore, in $P_{EP}(\cdot)$, $s_i \to \tilde{s}_i$ or $s_i^{(m)} \to \tilde{s}_i^{(\tilde{m})}$ means that the error event corrupts the transmitted s_i (or $s_i^{(m)}$) into $\tilde{s}_i$ (or $\tilde{s}_i^{(\tilde{m})}$).

[3] $Q(x) = \pi^{-1}\int_0^{\pi/2}\exp\left(-\frac{x^2}{2\sin^2\theta}\right)d\theta$

Note first that if we assume that the M_2APM uses Gray coding [118], the ABER of the M_2APM is given by

$$\begin{aligned}\bar{P}_b(M_2\text{APM}) =& \frac{1}{M_2 b_1} \sum_{m_2=0}^{M_2-1} \sum_{\tilde{m}_2 \neq m_2}^{M_2-1} D\left(\boldsymbol{b}_2^{(m_2)}, \tilde{\boldsymbol{b}}_2^{(\tilde{m}_2)}\right) P_{EP}(s_1|s_2^{(m_2)} \to s_1|\tilde{s}_2^{(\tilde{m}_2)}) \\ =& \bar{P}_s(M_2\text{APM})/b_1 \end{aligned} \tag{2.28}$$

where $\bar{P}_s(M_2\text{APM})$ represents the average symbol error probability of M_2APM. For different types of APMs, there are closed-form formulas to evaluate their ABER and average symbol error probability, which can be found in references, such as, [103,118,119]. Hence, we can use the existing formulas for $\bar{P}_b(M_2\text{APM})$ as well as $\bar{P}_s(M_2\text{APM})$, and evaluate (2.27b) as $b_1\bar{P}_b(M_2\text{APM})/b$ or $\bar{P}_s(M_2\text{APM})/b$.

Note secondly that, since U in (2.26) is an integer, according to (64) of [120] or (5A.4b) of [118], the PEPs in (2.26a) - (2.26c) can be expressed in closed form as

$$P_{EP}(x \to \tilde{x}) = \left(\frac{1-\mu}{2}\right)^U \sum_{u=0}^{U-1} \binom{U}{u} \left(\frac{1+\mu}{2}\right)^u \tag{2.29}$$

where μ corresponding to (2.26a), (2.26b) and (2.26c) is respectively defined as

$$\mu = \begin{cases} \sqrt{\dfrac{\gamma_0|s_2|^2}{\gamma_0|s_2|^2+2}}, & \text{if (2.26a) for Case (a)} \\ \sqrt{\dfrac{\gamma_0|\tilde{s}_2 - s_2|^2}{\gamma_0|\tilde{s}_2 - s_2|^2+4}}, & \text{if (2.26b) for Case (b)} \\ \sqrt{\dfrac{\gamma_0(|\tilde{s}_2|^2+|s_2|^2)}{\gamma_0(|\tilde{s}_2|^2+|s_2|^2)+4}}, & \text{if (2.26c) for Case (c)} \end{cases} \tag{2.30}$$

The PEPs can be readily computed with the aid of (2.29).

Equation (2.27) gives a bound for the ABER or the approximate ABER (if the SNR is sufficiently high) of the single-user SM-SCDMA system, without informing us whether the error is dominated by the M_1SSK or the M_2APM. This information is sometimes important in design. For example, if a designer knows that one is more reliable than the other one, the two modulation schemes can be used for unequal protection of multimedia information. Another consideration in the design is that the appropriate M_1SSK and M_2APM may be chosen so that both the modulation schemes give a similar ABER. This is because the overall ABER is always dominated by the less reliable one. In this case, the reliability of the more reliable one may be slightly reduced by transmitting at a higher rate, without unduly increasing the overall ABER.

Similar to the derivation of (2.25) [118], the ABER of the M_1SSK and that of the M_2APM have the following union-bounds:

$$\bar{P}_{bS}(M_1\text{SSK}) \leq \frac{1}{M_1 b_1} \sum_{m_1=0}^{M_1-1} \sum_{m_2=0}^{M_2-1} \sum_{\tilde{m}_1=0}^{M_1-1} \sum_{\tilde{m}_2=0}^{M_2-1} D\left(\boldsymbol{b}_1^{(m_1)}, \tilde{\boldsymbol{b}}_1^{(\tilde{m}_1)}\right) P_{EP}\left(s_1^{(m_1)} | s_2^{(m_2)} \to \tilde{s}_1^{(\tilde{m}_1)} | \tilde{s}_2^{(\tilde{m}_2)}\right) \tag{2.31}$$

$$\bar{P}_{bS}(M_2\text{APM}) \leq \frac{1}{M_2 b_2} \sum_{m_1=0}^{M_1-1} \sum_{m_2=0}^{M_2-1} \sum_{\tilde{m}_1=0}^{M_1-1} \sum_{\tilde{m}_2=0}^{M_2-1} D\left(\boldsymbol{b}_2^{(m_2)}, \tilde{\boldsymbol{b}}_2^{(\tilde{m}_2)}\right) P_{EP}\left(s_1^{(m_1)} | s_2^{(m_2)} \to \tilde{s}_1^{(\tilde{m}_1)} | \tilde{s}_2^{(\tilde{m}_2)}\right) \tag{2.32}$$

Again, considering that the PEPs shown in (2.26a) - (2.26c) for the three cases are not dependent on the fading channels, (2.31) and (2.32) can be simplified to the formulas of

$$\begin{aligned} \bar{P}_{bS}(M_1\text{SSK}) \leq & \frac{M_1}{2} \sum_{m_2=0}^{M_2-1} P_{EP}\left(s_1 | s_2^{(m_2)} \to \tilde{s}_1 | s_2^{(m_2)}\right) \\ & + \frac{M_1}{2} \sum_{m_2=0}^{M_2-1} \sum_{\tilde{m}_2 \neq m_2}^{M_2-1} P_{EP}\left(s_1 | s_2^{(m_2)} \to \tilde{s}_1 | \tilde{s}_2^{(\tilde{m}_2)}\right) \end{aligned} \tag{2.33}$$

$$\begin{aligned} \bar{P}_{bS}(M_2\text{APM}) \leq & \frac{M_1}{M_2 b_2} \sum_{m_2=0}^{M_2-1} \sum_{\tilde{m}_2 \neq m_2}^{M_2-1} D\left(\boldsymbol{b}_2^{(m_2)}, \tilde{\boldsymbol{b}}_2^{(\tilde{m}_2)}\right) P_{EP}\left(s_1 | s_2^{(m_2)} \to s_1 | \tilde{s}_2^{(\tilde{m}_2)}\right) \\ & + \frac{M_1(M_1-1)}{M_2 b_2} \sum_{m_2=0}^{M_2-1} \sum_{\tilde{m}_2 \neq m_2}^{M_2-1} D\left(\boldsymbol{b}_2^{(m_1)}, \tilde{\boldsymbol{b}}_2^{(\tilde{m}_1)}\right) P_{EP}\left(s_1 | s_2^{(m_2)} \to \tilde{s}_1 | \tilde{s}_2^{(\tilde{m}_2)}\right) \end{aligned} \tag{2.34}$$

In (2.33) and (2.34), the PEPs are respectively given in (2.26a) - (2.26c), which can be computed using (2.29) associated with (2.30).

2.4.2 Analysis of Approximate BER

In this section, we analyze the ABER of SM-SCDMA systems with MLD. In practice we are usually interested in the performance of an uncoded system at the specific ABER of about 10^{-3}, which can be readily corrected by FEC codes. For this ABER or a lower ABER, we can realize that the probability of two or more users being simultaneously in error at the same transmission instant should be negligible, provided that the number of (active) users is significantly smaller than 1/ABER. Hence, in order to make the analysis tractable, we assume that there is at most one user among the $(K-1)$ interfering users that may be in error.

Before we start analyzing the ABER of SM-SCDMA systems, we can readily obtain from (2.25) and (2.26a) - (2.26c) that the average symbol error rate (ASER) of the single-user

SM-SCDMA system is bounded as

$$\begin{aligned}\bar{P}_{sS} \leq & \frac{1}{M_1 M_2} \sum_{m_1=0}^{M_1-1} \sum_{m_2=0}^{M_2-1} \sum_{\tilde{m}_1=0}^{M_1-1} \sum_{\tilde{m}_2=0}^{M_2-1} P_{EP}\left(s_1^{(m_1)}|s_2^{(m_2)} \to \tilde{s}_1^{(\tilde{m}_1)}|\tilde{s}_2^{(\tilde{m}_2)}\right) \\ = & \frac{M_1-1}{M_2} \sum_{m_2=0}^{M_2-1} P_{EP}\left(s_1|s_2^{(m_2)} \to \tilde{s}_1|s_2^{(m_2)}\right) + \frac{M_1-1}{M_2} \sum_{m_2=0}^{M_2-1} \sum_{\tilde{m}_2 \neq m_2}^{M_2-1} P_{EP}\left(s_1|s_2^{(m_2)} \to s_1|\tilde{s}_2^{(\tilde{m}_2)}\right) \\ & + \frac{M_1-1}{M_2} \sum_{m_2=0}^{M_2-1} \sum_{\tilde{m}_2 \neq m_2}^{M_2-1} P_{EP}\left(s_1|s_2^{(m_2)} \to \tilde{s}_1|\tilde{s}_2^{(\tilde{m}_2)}\right) \end{aligned} \tag{2.35}$$

This probability will be used later for computing the ABER of the SM-SCDMA systems.

Let us now assume that there is a desired user indexed in the same way as in Section 2.4.1. Then, provided that all the $(K-1)$ interfering users are correctly detected, the ABER of the reference user is the same as (2.27).

By contrast, when an interfering user indexed as 'k', which can be any of the $(K-1)$ interfering users, is in error, we have the pairwise erroneous event of

$$\|\boldsymbol{y} - (\boldsymbol{I}_U \otimes \boldsymbol{c})\boldsymbol{h}_{\tilde{s}_1}\tilde{s}_2 - (\boldsymbol{I}_U \otimes \boldsymbol{c}_k)\boldsymbol{h}_{\tilde{s}_{k1}}\tilde{s}_{k2}\|^2 < \|\boldsymbol{y} - (\boldsymbol{I}_U \otimes \boldsymbol{c})\boldsymbol{h}_{s_1}s_2 - (\boldsymbol{I}_U \otimes \boldsymbol{c}_k)\boldsymbol{h}_{s_{k1}}s_{k2}\|^2 \tag{2.36}$$

from which we can derive the PEP, given as

$$P_{EP}^{(i)}(x, x_k \to \tilde{x}, \tilde{x}_k) = E_{\boldsymbol{H}}\left[Q\left(\sqrt{2\sum_{u=0}^{U-1}\gamma_u^{(i)}}\right)\right] \tag{2.37}$$

where x, $\tilde{x}$, x_k and $\tilde{x}_k$ represent respectively $s_1|s_2$, $\tilde{s}_1|\tilde{s}_2$, $s_{k1}|s_{k2}$ and $\tilde{s}_{k1}|\tilde{s}_{k2}$, while

$$\gamma_u^{(i)} = \gamma_0\|\boldsymbol{c}h_{\tilde{s}_1}^{(u)}\tilde{s}_2 + \boldsymbol{c}_k h_{\tilde{s}_{k1}}^{(u)}\tilde{s}_{k2} - \boldsymbol{c}h_{s_1}^{(u)}s_2 - \boldsymbol{c}_k h_{s_{k1}}^{(u)}s_{k2}\|^2/4 = \gamma_0\alpha/4 \tag{2.38}$$

where a superscript i is added to distinguish the different cases to be considered later.

When expressing the realizations of x, $\tilde{x}$, x_k, $\tilde{x}_k$ as $s_1^{(m_1)}|s_2^{(m_2)}$, $\tilde{s}_1^{(m_1)}|\tilde{s}_2^{(m_2)}$, $s_{k1}^{(m_{k1})}|s_{k2}^{(m_{k2})}$, $\tilde{s}_{k1}^{(m_{k1})}|\tilde{s}_{k2}^{(m_{k2})}$, similar to (2.25), we can represent the ABER of the SM-SCDMA system under the condition of a given interfering user k being incorrectly detected as

$$\begin{aligned}\bar{P}_{bM}(k) \approx & \frac{1}{M_1 M_2 b} \sum_{m_1=0}^{M_1-1} \sum_{m_2=0}^{M_2-1} \sum_{\tilde{m}_1=0}^{M_1-1} \sum_{\tilde{m}_2=0}^{M_2-1} \sum_{m_{k1}=0}^{M_1-1} \sum_{m_{k2}=0}^{M_2-1} \sum_{\tilde{m}_{k1}=0}^{M_1-1} \sum_{\tilde{m}_{k2}=0}^{M_2-1} D\left(\boldsymbol{b}_1^{(m_1)}|\boldsymbol{b}_2^{(m_2)}, \tilde{\boldsymbol{b}}_1^{(\tilde{m}_1)}|\tilde{\boldsymbol{b}}_2^{(\tilde{m}_2)}\right) \\ & \times P_{EP}\left(s_1^{(m_1)}|s_2^{(m_2)}, s_{k1}^{(m_{k1})}|s_{k2}^{(m_{k2})} \to \tilde{s}_1^{(\tilde{m}_1)}|\tilde{s}_2^{(\tilde{m}_2)}, \tilde{s}_{k1}^{(\tilde{m}_{k1})}|\tilde{s}_{k2}^{(\tilde{m}_{k2})}\right) \end{aligned} \tag{2.39}$$

where we simply use '$\approx$' to replace '$<$', since certain assumptions resulting in approximation are invoked, as noted at the beginning of this section. In order to evaluate (2.39),

we have to consider the following nine cases:

1. $P_{EP}^{(1)}(s_1|s_2,s_{k1}|s_{k2}\rightarrow\tilde{s}_1|s_2,\tilde{s}_{k1}|s_{k2})$: $\gamma_u^{(1)}=\gamma_0\|\boldsymbol{c}(h_{\tilde{s}_1}^{(u)}-h_{s_1}^{(u)})s_2+\boldsymbol{c}_k(h_{\tilde{s}_{k1}}^{(u)}-h_{s_{k1}}^{(u)})s_{k2}\|^2/4$
2. $P_{EP}^{(2)}(s_1|s_2,s_{k1}|s_{k2}\rightarrow s_1|\tilde{s}_2,\tilde{s}_{k1}|s_{k2})$: $\gamma_u^{(2)}=\gamma_0\|\boldsymbol{c}h_{s_1}^{(u)}(\tilde{s}_2-s_2)+\boldsymbol{c}_k(h_{\tilde{s}_{k1}}^{(u)}-h_{s_{k1}}^{(u)})s_{k2}\|^2/4$
3. $P_{EP}^{(3)}(s_1|s_2,s_{k1}|s_{k2}\rightarrow\tilde{s}_1|\tilde{s}_2,\tilde{s}_{k1}|s_{k2})$: $\gamma_u^{(3)}=\gamma_0\|\boldsymbol{c}(h_{\tilde{s}_1}^{(u)}\tilde{s}_2-h_{s_1}^{(u)}s_2)+\boldsymbol{c}_k(h_{\tilde{s}_{k1}}^{(u)}-h_{s_{k1}}^{(u)})s_{k2}\|^2/4$
4. $P_{EP}^{(4)}(s_1|s_2,s_{k1}|s_{k2}\rightarrow\tilde{s}_1|s_2,s_{k1}|\tilde{s}_{k2})$: $\gamma_u^{(4)}=\gamma_0\|\boldsymbol{c}(h_{\tilde{s}_1}^{(u)}-h_{s_1}^{(u)})s_2+\boldsymbol{c}_kh_{s_{k1}}^{(u)}(\tilde{s}_{k2}-s_{k2})\|^2/4$
5. $P_{EP}^{(5)}(s_1|s_2,s_{k1}|s_{k2}\rightarrow s_1|\tilde{s}_2,s_{k1}|\tilde{s}_{k2})$: $\gamma_u^{(5)}=\gamma_0\|\boldsymbol{c}h_{s_1}^{(u)}(\tilde{s}_2-s_2)+\boldsymbol{c}_kh_{s_{k1}}^{(u)}(\tilde{s}_{k2}-s_{k2})\|^2/4$
6. $P_{EP}^{(6)}(s_1|s_2,s_{k1}|s_{k2}\rightarrow\tilde{s}_1|\tilde{s}_2,s_{k1}|\tilde{s}_{k2})$: $\gamma_u^{(6)}=\gamma_0\|\boldsymbol{c}(h_{\tilde{s}_1}^{(u)}\tilde{s}_2-h_{s_1}^{(u)}s_2)+\boldsymbol{c}_kh_{s_{k1}}^{(u)}(\tilde{s}_{k2}-s_{k2})\|^2/4$
7. $P_{EP}^{(7)}(s_1|s_2,s_{k1}|s_{k2}\rightarrow\tilde{s}_1|s_2,\tilde{s}_{k1}|\tilde{s}_{k2})$: $\gamma_u^{(7)}=\gamma_0\|\boldsymbol{c}(h_{\tilde{s}_1}^{(u)}-h_{s_1}^{(u)})s_2+\boldsymbol{c}_k(h_{\tilde{s}_{k1}}^{(u)}\tilde{s}_{k2}-h_{s_{k1}}^{(u)}s_{k2})\|^2/4$
8. $P_{EP}^{(8)}(s_1|s_2,s_{k1}|s_{k2}\rightarrow s_1|\tilde{s}_2,\tilde{s}_{k1}|\tilde{s}_{k2})$: $\gamma_u^{(8)}=\gamma_0\|\boldsymbol{c}h_{s_1}^{(u)}(\tilde{s}_2-s_2)+\boldsymbol{c}_k(h_{\tilde{s}_{k1}}^{(u)}\tilde{s}_{k2}-h_{s_{k1}}^{(u)}s_{k2})\|^2/4$
9. $P_{EP}^{(9)}(s_1|s_2,s_{k1}|s_{k2}\rightarrow\tilde{s}_1|\tilde{s}_2,\tilde{s}_{k1}|\tilde{s}_{k2})$: $\gamma_u^{(9)}=\gamma_0\|\boldsymbol{c}(h_{\tilde{s}_1}^{(u)}\tilde{s}_2-h_{s_1}^{(u)}s_2)+\boldsymbol{c}_k(h_{\tilde{s}_{k1}}^{(u)}\tilde{s}_{k2}-h_{s_{k1}}^{(u)}s_{k2})\|^2/4$

In the above expression, the indices of m_i or $\tilde{m}_i$ are removed for notational simplicity. The same notational simplifications are used in our forthcoming discourse, whenever there is no confusion. Furthermore, in the case of, such as PEP, which is independent of the specific index, such as a specific TA, there is also no index for m_i or $\tilde{m}_i$.

As seen in (2.38) or the above formulas corresponding to the nine cases, the instantaneous SNR $\gamma_u^{(i)}$ is a function of the linear combination of 2-to-4 independent Gaussian random variables $h_{\tilde{s}_1}^{(u)}$, $h_{s_1}^{(u)}$, $h_{\tilde{s}_{k1}}^{(u)}$ and/or $h_{s_{k1}}^{(u)}$. Hence, for given $\boldsymbol{c}$, $\boldsymbol{c}_k$, s_2, $\tilde{s}_2$, s_{k2} and $\tilde{s}_{k2}$, the SNR $\gamma_u^{(i)}$ obeys the Gamma distribution with the PDF expressed in the form of [103, 118]

$$f_{\gamma_u^{(i)}}(x)=\frac{1}{\Gamma(\beta_i)}\left(\frac{\beta_i}{\bar{\gamma}_i}\right)^{\beta_i}x^{\beta_i-1}\exp\left(-\frac{\beta_i x}{\bar{\gamma}_i}\right),\ 0\leq x<\infty \tag{2.40}$$

where the average SNR $\bar{\gamma}_i$ and the shaping parameter β_i are determined by the first and second order moments of $\gamma_u^{(i)}$, given by

$$\bar{\gamma}_i=E[\gamma_u^{(i)}],\ \beta_i=\frac{\bar{\gamma}_i^2}{E\left[(\gamma_u^{(i)})^2\right]-\bar{\gamma}_i^2} \tag{2.41}$$

In order to compute $\bar{\gamma}_i$ and β_i with respect to the different cases, we need the second and fourth order moments of complex Gaussian random variables. Let us assume that $X=a+jb$, where both a and b are Gaussian distributed with zero mean and a variance

of σ^2. Then, we have $E[X^2] = 2\sigma^2$ and $E[X^4] = 8\sigma^2$. With these results in mind, we can readily derive $\bar{\gamma}_i$ and β_i for the nine cases, which are expressed respectively as

$$\begin{aligned}
\bar{\gamma}_1 =& \gamma_0(|s_2|^2 + |s_{k2}|^2)/2, \\
\beta_1 =& \frac{(|s_2|^2 + |s_{k2}|^2)^2}{|s_2|^4 + |s_{k2}|^4 + 2|\rho_k|^2|s_2|^2|s_{k2}|^2}; \qquad (2.42a) \\
\bar{\gamma}_2 =& \gamma_0(|\tilde{s}_2 - s_2|^2 + 2|s_{k2}|^2)/4, \\
\beta_2 =& \frac{(|\tilde{s}_2 - s_2|^2 + 2|s_{k2}|^2)^2}{|\tilde{s}_2 - s_2|^4 + 4|s_{k2}|^4 + 4|\rho_k|^2|\tilde{s}_2 - s_2|^2|s_{k2}|^2}; \qquad (2.42b) \\
\bar{\gamma}_3 =& \gamma_0(|\tilde{s}_2|^2 + |s_2|^2 + 2|s_{k2}|^2)/4, \\
\beta_3 =& \frac{(|\tilde{s}_2|^2 + |s_2|^2 + 2|s_{k2}|^2)^2}{(|\tilde{s}_2|^2 + s_2^2)^2 + 4|s_{k2}|^4 + 4|\rho_k|^2(|\tilde{s}_2|^2 + |s_2|^2)|s_{k2}|^2}; \qquad (2.42c) \\
\bar{\gamma}_4 =& \gamma_0(2|s_2|^2 + |\tilde{s}_{k2} - s_{k2}|^2)/4, \\
\beta_4 =& \frac{(2|s_2|^2 + |\tilde{s}_{k2} - s_{k2}|^2)^2}{4|s_2|^4 + |\tilde{s}_{k2} - s_{k2}|^4 + 4|\rho_k|^2|s_2|^2|\tilde{s}_{k2} - s_{k2}|^2} \qquad (2.42d) \\
\bar{\gamma}_5 =& \gamma_0(|\tilde{s}_2 - s_2|^2 + |\tilde{s}_{k2} - s_{k2}|^2)/4, \\
\beta_5 =& \frac{(|\tilde{s}_2 - s_2|^2 + |\tilde{s}_{k2} - s_{k2}|^2)^2}{|\tilde{s}_2 - s_2|^4 + |\tilde{s}_{k2} - s_{k2}|^4 + 2|\rho_k|^2|\tilde{s}_2 - s_2|^2|\tilde{s}_{k2} - s_{k2}|^2}; \qquad (2.42e)
\end{aligned}$$

$$\begin{aligned}
\bar{\gamma}_6 =& \gamma_0(|\tilde{s}_2|^2 + |s_2|^2 + |\tilde{s}_{k2} - s_{k2}|^2)/4, \\
\beta_6 =& \frac{(|\tilde{s}_2|^2 + |s_2|^2 + |\tilde{s}_{k2} - s_{k2}|^2)^2}{(|\tilde{s}_2|^2 + |s_2|^2)^2 + |\tilde{s}_{k2} - s_{k2}|^4 + 2|\rho_k|^2(|\tilde{s}_2|^2 + |s_2|^2)|\tilde{s}_{k2} - s_{k2}|^2}; \qquad (2.43a) \\
\bar{\gamma}_7 =& \gamma_0(2|s_2|^2 + |\tilde{s}_{k2}|^2 + |s_{k2}|^2)/4, \\
\beta_7 =& \frac{(2|s_2|^2 + |\tilde{s}_{k2}|^2 + |s_{k2}|^2)^2}{4|s_2|^4 + (|\tilde{s}_{k2}|^2 + |s_{k2}|^2)^2 + 4|\rho_k|^2|s_2|^2(|\tilde{s}_{k2}|^2 + |s_{k2}|^2)}; \qquad (2.43b) \\
\bar{\gamma}_8 =& \gamma_0(|\tilde{s}_2 - s_2|^2 + |\tilde{s}_{k2}|^2 + |s_{k2}|^2)/4, \\
\beta_8 =& \frac{(|\tilde{s}_2 - s_2|^2 + |\tilde{s}_{k2}|^2 + |s_{k2}|^2)^2}{|\tilde{s}_2 - s_2|^4 + (|\tilde{s}_{k2}|^2 + |s_{k2}|^2)^2 + 2|\rho_k|^2|\tilde{s}_2 - s_2|^2(|\tilde{s}_{k2}|^2 + |s_{k2}|^2)}; \qquad (2.43c) \\
\bar{\gamma}_9 =& \gamma_0(|\tilde{s}_2|^2 + |s_2|^2 + |\tilde{s}_{k2}|^2 + |s_{k2}|^2)/4, \\
\beta_9 =& \frac{(|\tilde{s}_2|^2 + |s_2|^2 + |\tilde{s}_{k2}|^2 + |s_{k2}|^2)^2}{(|\tilde{s}_2|^2 + |s_2|^2)^2 + (|\tilde{s}_{k2}|^2 + |s_{k2}|^2)^2 + 2|\rho_k|^2(|\tilde{s}_2|^2 + |s_2|^2)(|\tilde{s}_{k2}|^2 + |s_{k2}|^2)} \qquad (2.43d)
\end{aligned}$$

In the above equations, $\rho_k = \boldsymbol{c}^H \boldsymbol{c}_k$ is the cross-correlation between $\boldsymbol{c}$ and $\boldsymbol{c}_k$. From $\bar{\gamma}_i$ and β_i shown in (2.42a) - (2.43d), it is not hard for us to infer the following observations:

- In the formulas (2.42a) - (2.43d), when we set $|\tilde{s}_{k2}|^2 = 0$ and $|s_{k2}|^2 = 0$, we always obtain $\beta_i = 1$ for $i = 1, \ldots, 9$. Correspondingly, the nine cases are reduced to the three cases, which we considered earlier in Section 2.4.1 for the single-user scenario or that all the $(K-1)$ interfering users are correctly detected.

- $\bar{\gamma}_i$ is always increased due to the error event of a second user, meaning that having two users simultaneously in error is rare compared to having a single user in error in a SM-SCDMA system.

- As $0 \leq |\rho_k| < 1$, we can find $1 < \beta_i \leq 2$ for all the nine cases. Since a higher β_i value results in a lower error probability, as seen in [103,118] and below, again, this explains that the probability of two users being simultaneously in error is lower than that of only one user being in error.

- When the erroneous user k does not share any chips with the reference user, we then have $\rho_k = 0$. Consequently, the value of β_i becomes higher than that of the case, where the erroneous user k and the reference user share some chips for transmission. Therefore, an interfering user not sharing chips with the reference user imposes a lower impact on the error probability of the reference user than an interfering user sharing some chips with the reference user.

Having obtained $\bar{\gamma}_i$ and β_i for the different cases, the corresponding PEPs can be obtained via averaging (2.37) using (2.40), yielding [103,118]

$$P_{EP}^{(i)}(x, x_k \to \tilde{x}, \tilde{x}_k) = \frac{1}{\pi} \int_0^{\pi/2} \left(\frac{\beta_i \sin^2 \theta}{\beta_i \sin^2 \theta + \bar{\gamma}_i} \right)^{\beta_i U} d\theta, \ i = 1, \ldots, 9 \tag{2.44}$$

which, according to [103,118,120,121], can be represented in a closed-form as

$$\begin{aligned} P_{EP}^{(i)}(x, x_k \to \tilde{x}, \tilde{x}_k) = & \frac{\Gamma(\beta_i U + 1/2)}{2\sqrt{\pi}\Gamma(\beta_i U + 1)} \sqrt{\frac{\bar{\gamma}_i}{\beta_i + \bar{\gamma}_i}} \left(\frac{\beta_i}{\beta_i + \bar{\gamma}_i} \right)^{\beta_i U} \\ & \times {}_2F_1 \left(1, \beta_i U + \frac{1}{2}; \beta_i U + 1; \frac{\beta_i}{\beta_i + \bar{\gamma}_i} \right), \ i = 1, \ldots, 9 \end{aligned} \tag{2.45}$$

where ${}_2F_1(a, b; c; z)$ is the hypergeometric function defined as [122] ${}_2F_1(a, b; c; z) = \sum_{k=0}^{\infty} \frac{(a)_k (b)_k z^k}{(c)_k k!}$ and $(a)_k = a(a+1)\cdots(a+k-1)$, $(a)_0 = 1$.

Below we provide the expressions for computing the approximate error probabilities in some special cases of practical interest.

First, for the ABER of the SM-SCDMA systems supporting K users (one reference user plus $(K-1)$ interfering users), we assume that there is at most one interfering user in error. This assumption is reasonable due to the fact that when the SNR is sufficiently high, the probability of having two or more users simultaneously detected in error in addition to the reference user is negligible. For example, let us assume that the error rate of a user is about 10^{-3}, which is the error rate of interest in practice. Then, when an optimum detector is employed, the average number of users erroneously detected during a channel use is about $K \times 10^{-3}$, provided that K is comparable to the total number of chips used by the SM-SCDMA system. However, we should note that when there are two or more users simultaneously detected in error, the erroneous events of

these users generate some correlation, as implied by (2.42a) - (2.43d). Nevertheless, this correlation should not significantly affect the average number of erroneous users, because the probability of having two or more users simultaneously in error is insignificant, in comparison to that of having only one user in error. Based on the above assumption and (2.35), the ABER of the SM-SCDMA systems can be expressed as

$$\bar{P}_{bM} \approx (1-\bar{P}_{sS})^{K-1}\bar{P}_{bS} + [1-(1-\bar{P}_{sS})^{K-1}] \times \frac{1}{K-1}\sum_{k=1}^{K-1}\bar{P}_{bM}(k) \tag{2.46}$$

where $\bar{P}_{bM}(k)$ is the ABER of the reference user when the kth interfering user is in error, which is given by (2.39). When taking into account our nine cases, we have

$$\begin{aligned}
\bar{P}_{bM}(k) \approx & \frac{M_1^2(M_1-1)b_1}{2M_2 b}\sum_{m_2=0}^{M_2-1}\sum_{m_{k2}=0}^{M_2-1} P_{EP}\left(s_1|s_2^{(m_2)}, s_{k1}|s_{k2}^{(m_{k2})} \to \tilde{s}_1|s_2^{(m_2)}, \tilde{s}_{k1}|s_{k2}^{(m_{k2})}\right) \\
& + \frac{M_1(M_1-1)}{M_2 b}\sum_{m_2=0}^{M_2-1}\sum_{\tilde{m}_2\neq m_2}^{M_2-1}\sum_{m_{k2}=0}^{M_2-1} D\left(\boldsymbol{b}_2^{(m_2)}, \tilde{\boldsymbol{b}}_2^{(\tilde{m}_2)}\right) \\
& \times P_{EP}\left(s_1|s_2^{(m_2)}, s_{k1}|s_{k2}^{(m_{k2})} \to s_1|\tilde{s}_2^{(\tilde{m}_2)}, \tilde{s}_{k1}|s_{k2}^{(m_{k2})}\right) \\
& + \frac{M_1(M_1-1)}{M_2 b}\sum_{m_2=0}^{M_2-1}\sum_{\tilde{m}_2\neq m_2}^{M_2-1}\sum_{m_{k2}=0}^{M_2-1}\left[\frac{b_1 M_1}{2} + (M_1-1)D\left(\boldsymbol{b}_2^{(m_2)}, \tilde{\boldsymbol{b}}_2^{(\tilde{m}_2)}\right)\right] \\
& \times P_{EP}\left(s_1|s_2^{(m_2)}, s_{k1}|s_{k2}^{(m_{k2})} \to \tilde{s}_1|\tilde{s}_2^{(\tilde{m}_2)}, \tilde{s}_{k1}|s_{k2}^{(m_{k2})}\right) \\
& + \frac{M_1^2 b_1}{2M_2 b}\sum_{m_2=0}^{M_2-1}\sum_{m_{k2}=0}^{M_2-1}\sum_{\tilde{m}_{k2}\neq m_{k2}}^{M_2-1} P_{EP}\left(s_1|s_2^{(m_2)}, s_{k1}|s_{k2}^{(m_{k2})} \to \tilde{s}_1|s_2^{(m_2)}, s_{k1}|\tilde{s}_{k2}^{(\tilde{m}_{k2})}\right) \\
& + \frac{M_1}{M_2 b}\sum_{m_2=0}^{M_2-1}\sum_{\tilde{m}_2=\neq m_2}^{M_2-1}\sum_{m_{k2}=0}^{M_2-1}\sum_{\tilde{m}_{k2}\neq m_{k2}}^{M_2-1} D\left(\boldsymbol{b}_2^{(m_2)}, \tilde{\boldsymbol{b}}_2^{(\tilde{m}_2)}\right) \\
& \times P_{EP}\left(s_1|s_2^{(m_2)}, s_{k1}|s_{k2}^{(m_{k2})} \to s_1|\tilde{s}_2^{(\tilde{m}_2)}, s_{k1}|\tilde{s}_{k2}^{(\tilde{m}_{k2})}\right) \\
& + \frac{M_1}{M_2 b}\sum_{m_2=0}^{M_2-1}\sum_{\tilde{m}_2\neq m_2}^{M_2-1}\sum_{m_{k2}=0}^{M_2-1}\sum_{\tilde{m}_{k2}\neq m_{k2}}^{M_2-1}\left[\frac{b_1 M_1}{2} + (M_1-1)D\left(\boldsymbol{b}_2^{(m_2)}, \tilde{\boldsymbol{b}}_2^{(\tilde{m}_2)}\right)\right] \\
& \times P_{EP}\left(s_1|s_2^{(m_2)}, s_{k1}|s_{k2}^{(m_{k2})} \to \tilde{s}_1|\tilde{s}_2^{(\tilde{m}_2)}, \tilde{s}_{k1}|\tilde{s}_{k2}^{(\tilde{m}_{k2})}\right) \\
& + \frac{M_1^2(M_1-1)b_1}{2M_2 b}\sum_{m_2=0}^{M_2-1}\sum_{m_{k2}=0}^{M_2-1}\sum_{\tilde{m}_{k2}\neq m_{k2}}^{M_2-1} P_{EP}\left(s_1|s_2^{(m_2)}, s_{k1}|s_{k2}^{(m_{k2})} \to \tilde{s}_1|s_2^{(m_2)}, \tilde{s}_{k1}|\tilde{s}_{k2}^{(\tilde{m}_{k2})}\right) \\
& + \frac{M_1(M_1-1)}{M_2 b}\sum_{m_2=0}^{M_2-1}\sum_{\tilde{m}_2\neq m_2}^{M_2-1}\sum_{m_{k2}=0}^{M_2-1}\sum_{\tilde{m}_{k2}\neq m_{k2}}^{M_2-1} D\left(\boldsymbol{b}_2^{(m_2)}, \tilde{\boldsymbol{b}}_2^{(\tilde{m}_2)}\right) \\
& \times P_{EP}\left(s_1|s_2^{(m_2)}, s_{k1}|s_{k2}^{(m_{k2})} \to s_1|\tilde{s}_2^{(\tilde{m}_2)}, \tilde{s}_{k1}|\tilde{s}_{k2}^{(\tilde{m}_{k2})}\right) \\
& + \frac{M_1(M_1-1)}{M_2 b}\sum_{m_2=0}^{M_2-1}\sum_{\tilde{m}_2\neq m_2}^{M_2-1}\sum_{m_{k2}=0}^{M_2-1}\sum_{\tilde{m}_{k2}\neq m_{k2}}^{M_2-1}\left[\frac{b_1 M_1}{2} + (M_1-1)D\left(\boldsymbol{b}_2^{(m_2)}, \tilde{\boldsymbol{b}}_2^{(\tilde{m}_2)}\right)\right] \\
& \times P_{EP}\left(s_1|s_2^{(m_2)}, s_{k1}|s_{k2}^{(m_{k2})} \to \tilde{s}_1|\tilde{s}_2^{(\tilde{m}_2)}, \tilde{s}_{k1}|\tilde{s}_{k2}^{(\tilde{m}_{k2})}\right)
\end{aligned} \tag{2.47}$$

Note that, in (2.47), all the PEPs are in the form of (2.44) or (2.45), with the corresponding $\bar{\gamma}_i$ and β_i are respectively given in (2.42a) - (2.43d), which are determined by the specific symbols of $s_2^{(m_2)}$, $s_{k2}^{(m_{k2})}$, $\tilde{s}_2^{(\tilde{m}_2)}$, $\tilde{s}_{k2}^{(\tilde{m}_{k2})}$ as well as ρ_k of the cross-correlation between the sparse codes of the reference user and of the kth interfering user.

Secondly, in order to reduce the computations invoked, another ABER expression can be obtained by considering only the specific interfering users sharing at least one chip with the reference user. In this case, the ABER can be expressed as

$$\bar{P}'_{bM} \approx (1-\bar{P}_{sS})^{K-1}\bar{P}_{bS} + [1-(1-\bar{P}_{sS})^{K-1}] \times \frac{1}{K-1}\sum_{k\in\mathcal{K}} \bar{P}_{bM}(k) \tag{2.48}$$

where $\mathcal{K} = \{k|\mathcal{C}_k \cap \mathcal{C} \neq \varnothing \ \forall k = 1, 2, \ldots, K-1\}$, and $\varnothing$ is an empty set.

Thirdly, we are interested in the ABER of the reference user, when there is a single erroneous interfering user and this user does not share any chips with the reference user. This ABER can be formulated as

$$\bar{P}_{IM} \approx \bar{P}_{bM}(k) \tag{2.49}$$

where $k \notin \mathcal{K}$ can be any arbitrary user not in $\mathcal{K}$. Note that any $k \notin \mathcal{K}$ has the same impact on the reference user.

Finally, the ABER of the reference user on condition that there is only a single erroneous interfering user and this user shares some chips with the reference user can be expressed as

$$\bar{P}'_{IM} \approx \frac{1}{\sum 1_{k\in\mathcal{K}}}\sum_{k\in\mathcal{K}} \bar{P}_{bM}(k) \tag{2.50}$$

where $\sum 1_{k\in\mathcal{K}}$ denotes the total number of the interfering users sharing some chips with the reference user. Note that when regular sparse codes are employed, implying that the number of chips shared between any interfering user in $\mathcal{K}$ with the reference user is the same, then the averaging operation in (2.50) is not required. Instead, we can compute $\bar{P}'_{IM}$ by considering a single interfering user randomly chosen from $\mathcal{K}$.

2.5 Performance Results

In this section, both the theoretical error probability bounds and the simulation results of SM-SCDMA systems are presented. Firstly, we propose a new 8QAM constellation, which is then considered in some of the other figures. Then, the performance of SM-SCDMA systems associated with various parameters are characterized, based on which we also find the valid range of our formulas derived. Finally, we study the performance

of relatively large-scale SM-SCDMA systems, which are impervious to numerical simulations. Note that the parameters used for generating the results of a specific figure are detailed associated with the figure.

Again, let us propose a new 8QAM constellation for our forthcoming investigation. In the literature, typically the three 8QAM constellations of Fig. 2.4(b)-(d) are considered, all of which facilitate Gray coding [123]. Specifically, the constellation of Fig. 2.4(b) is designed based on the classic square-16QAM. It has a *peak-to-average ratio* (PAR) of 1.8, and the *minimum distance* of $0.63\sqrt{E_0}$, where E_0 is the average phasor energy [123]. Here, we propose a new 8QAM constellation also designed based on square-16QAM, as shown in Fig. 2.4(a). It can be shown that this new constellation has the same PAR as that shown in Fig. 2.4(b), but a *minimum distance* of $0.88\sqrt{E_0}$. However, the Gray coding cannot be fully applied, as each 8QAM symbol has only three bits, but there are two points, namely, '000' and '010', each having four neighbors.

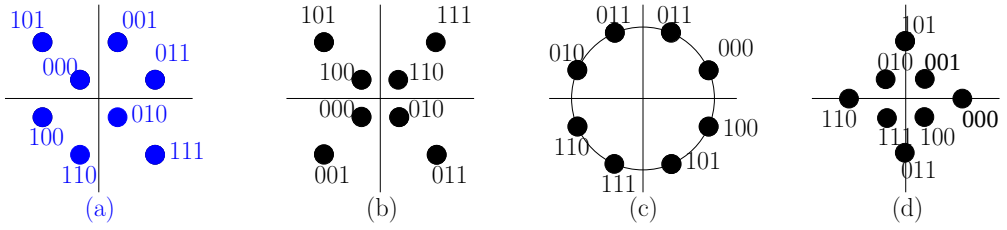

FIGURE 2.4: Different constellations for 8QAM.

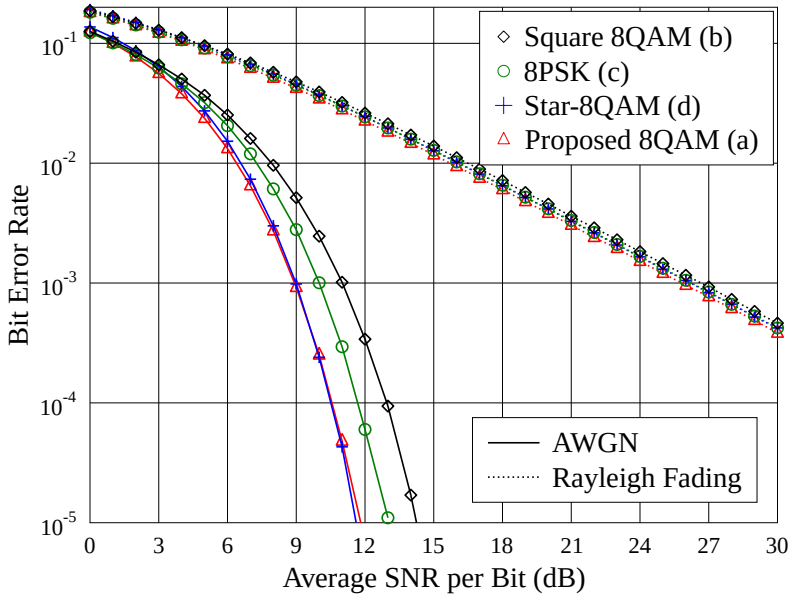

FIGURE 2.5: BER performance of different 8QAM constellations over Gaussian channels.

The BER performance of the above four 8QAM constellations when communicating over Gaussian or Rayleigh fading channels is depicted in Fig. 2.5. Explicitly, in Gaussian

channels, the proposed 8QAM scheme marginally outperforms all the others 8QAM schemes, when the SNR is lower than about 10 dB, i.e. in the SNR range of interest. By contrast, when considering Rayleigh fading channels, the proposed 8QAM scheme slightly outperforms the others 8QAM schemes across the whole SNR region considered. Note that, as the proposed 8QAM constellation is embedded in the 16QAM constellation, it is beneficial for the implementation of adaptive modulation [124] in practice. Therefore, in our following results, we assume the constellation of Fig. 2.4(a), when 8QAM is employed.

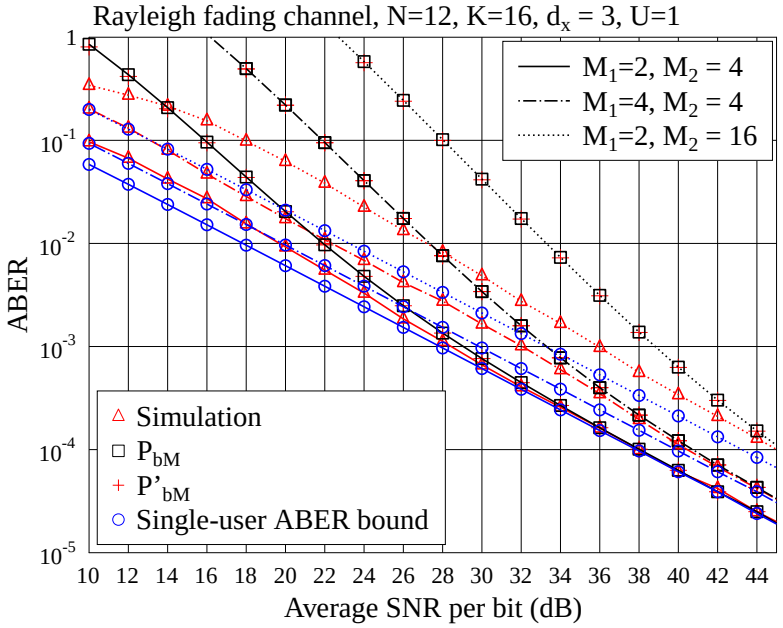

FIGURE 2.6: ABER performance of SM-SCDMA systems for different number of modulation levels over Rayleigh fading channels.

Fig. 2.6 shows the BER performance of SM-SCDMA systems, when different number of modulation levels are assumed for the M_1SSK and M_2QAM. In this figure, we also compare the results obtained by simulations and those evaluated from the ABER bounds of (2.46) and (2.48). Furthermore, the single-user ABER bound of (2.27) is provided. Based on the results, we have the following observations. Firstly, when the throughput is increased either by increasing M_1 or M_2, the BER performance degrades. Secondly, when the SNR increases, the BER performance of SM-SCDMA system using $N = 12$ chips to support $K = 16$ users, which corresponds to a normalized user-load factor of 4/3, converges to the single-user BER. Thirdly, the ABER bound evaluated by (2.46) and that evaluated by (2.48) are indistinguishable, which requires much less computation than (2.46). Furthermore, as expected, at the BER of about 10^{-3}, the ABER bounds evaluated from (2.46) or (2.48) are close to the corresponding results obtained via simulations, and they become closer, as the SNR increases. Therefore, when the SNR is sufficiently high, resulting in a BER of about 10^{-3} or lower, the single user ABER bound of (2.27) and the ABER bound of (2.46) or (2.48) can be used to predict the achievable performance of SM-SCDMA systems.

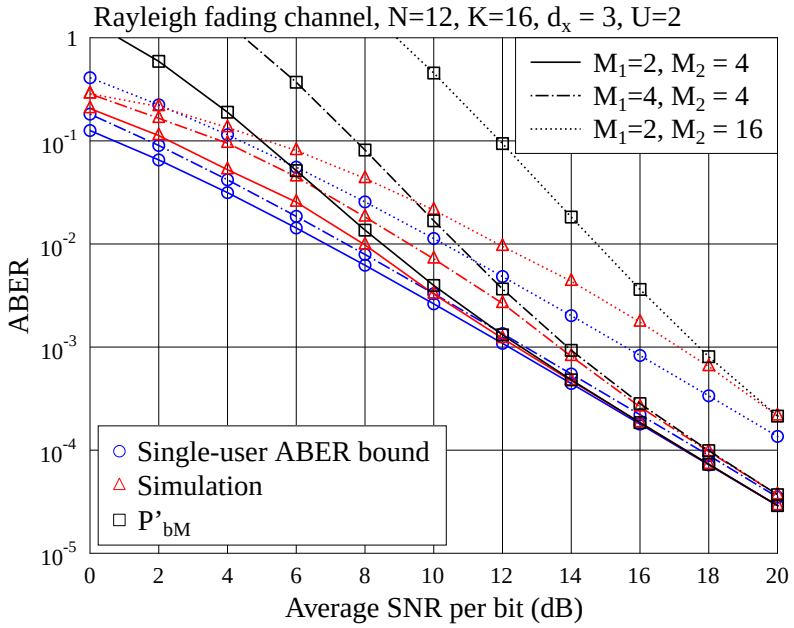

FIGURE 2.7: ABER performance of SM-SCDMA systems with different number of modulation levels over Rayleigh fading channels.

In Fig. 2.6, we assumed $U = 1$. By contrast, we assume $U = 2$ in Fig. 2.7. The other parameters are the same for both figures. By comparing the results of these two figures, we can see that a significant performance improvement is available, when the number of RAs is increased from $U = 1$ to $U = 2$, which is an explicit benefit of the diversity gain and the power gain. Furthermore, similar to Fig. 2.6, the BER obtained via simulations lies between the single-user ABER bound of (2.27) and the ABER bound of (2.48) (or (2.46)). Therefore, we may use (2.27) and (2.48) to predict the BER performance of SM-SCDMA systems, or simply use (2.48), when the SNR is sufficiently high, resulting in a BER of 10^{-3} or lower.

In Section 2.4, we have considered the ABER $\bar{P}_{IM}$ of a reference user, when there is a single erroneous interfering user without overlapping with the reference user, which is expressed in (2.49). We have also considered the ABER $\bar{P}'_{IM}$ of a reference user, when there is a single erroneous interfering user sharing some chips with the reference user, which is expressed in (2.50). In Fig. 2.8, we compare these two conditional ABERs as well as P_{bM} of (2.46). The results show that for a given SNR, $\bar{P}'_{IM}$ is much higher than $\bar{P}_{IM}$, implying that the ABER is dominated by those specific erroneous interfering users, which share some chips with the reference user. This also explain that in Figs. 2.6, P_{bM} and P'_{bM} are indistinguishable.

Fig. 2.9 depicts the performance of SM-SCDMA systems for the user-load factors of $K = 16$, 20 and 24, giving the normalized user-load factors of 4/3, 5/3 and 2. In addition to the observations from the previous figures, Fig. 2.9 shows that for the other parameters considered, the performance of the SCDMA systems only slightly degrades,

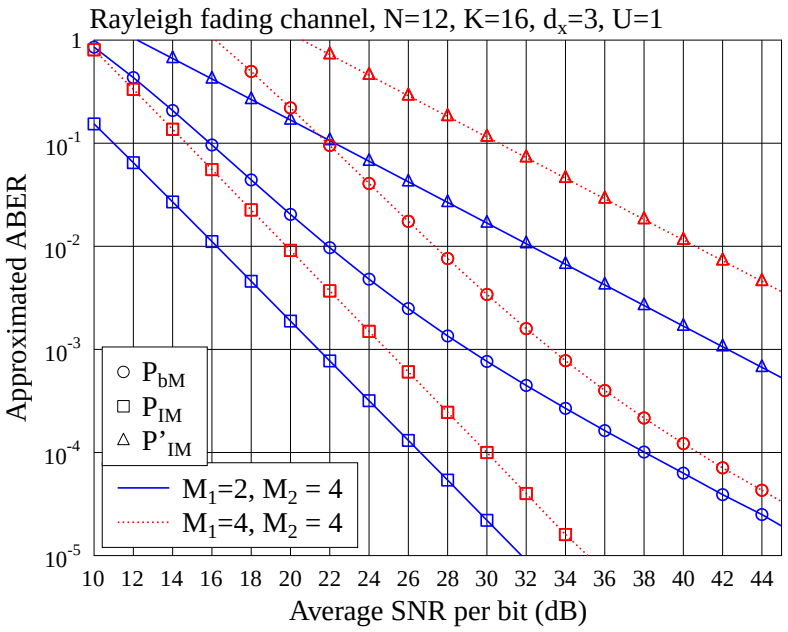

FIGURE 2.8: Comparison of the conditional ABER of $\bar{P}_{IM}$ and $\bar{P}'_{IM}$, and the ABER of $\bar{P}_{bM}$ of SM-SCDMA systems.

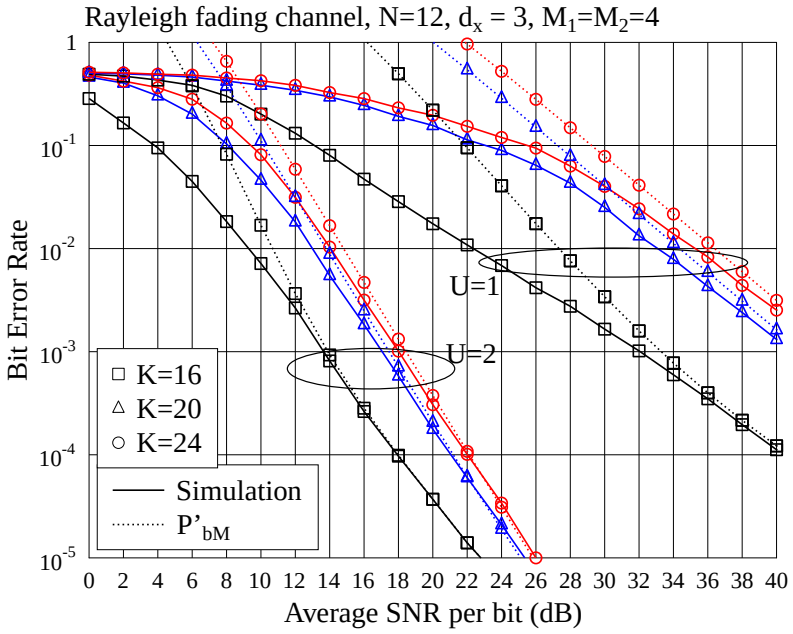

FIGURE 2.9: ABER performance of SM-SCDMA systems for different user-loads.

as the number of users increases. This is the case, in particular when a SM-SCDMA system employs $U = 2$ RAs. As shown in Fig. 2.9, a relatively substantial performance drop is observed, when the normalized user-load factor is changed from 4/3 to 5/3. By contrast, there is only a marginal performance loss, when the normalized user-load factor is increased from 5/3 to 2.

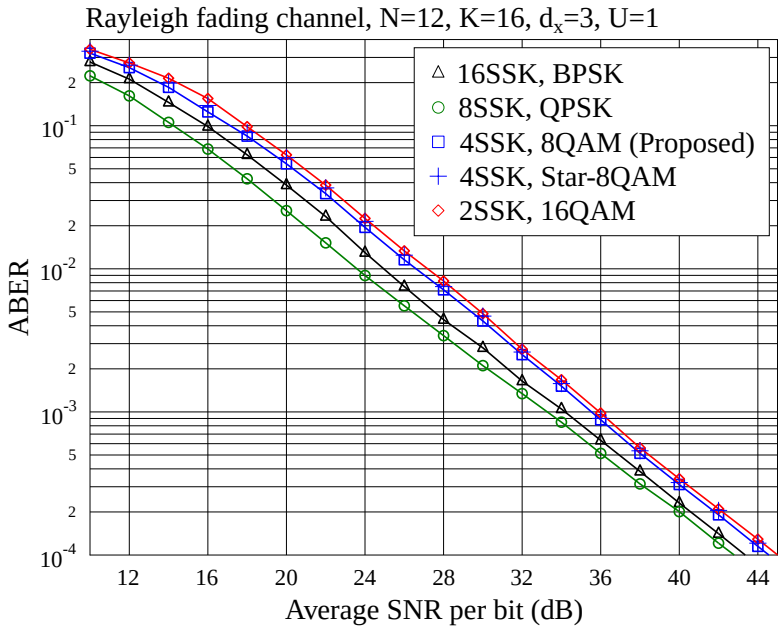

FIGURE 2.10: ABER performance of the SM-SCDMA system for different modulation schemes transmitting $b = 5$ bits per symbol.

Again, SM-SCDMA systems rely on two types of modulations schemes, i.e. the SSK and QAM. While SSK belongs to the family of energy-efficient modulation schemes, QAM is a bandwidth-efficient modulation scheme [119]. Hence, when fixing the bandwidth, there should be a trade-off between the numbers of bits allocated to these two modulation schemes. Therefore, in Fig. 2.10, we demonstrate this trade-off, when assuming that the total number of bits per symbol is fixed to 5. Explicitly, the combination of 8SSK and QPSK achieves the best error performance among the four possible combinations over the whole SNR region considered. Additionally, in Fig. 2.10 the proposed 8QAM shows slightly better ABER performance than the star 8QAM, when communicating over Rayleigh fading channels. This is also reflected in Fig. 2.10, where the proposed 8QAM scheme slightly outperforms the star 8QAM operating in Rayleigh fading channels over the whole SNR range considered.

So far, we have considered some relatively small SM-SCDMA systems with $N = 12$, so that we can use simulation results to validate our mathematical analysis and gain insights into the characteristics of the various expressions derived. Below we consider some relatively large-scale SM-SCDMA systems, whose performance is infeasible to study by Monte-Carlo simulations.

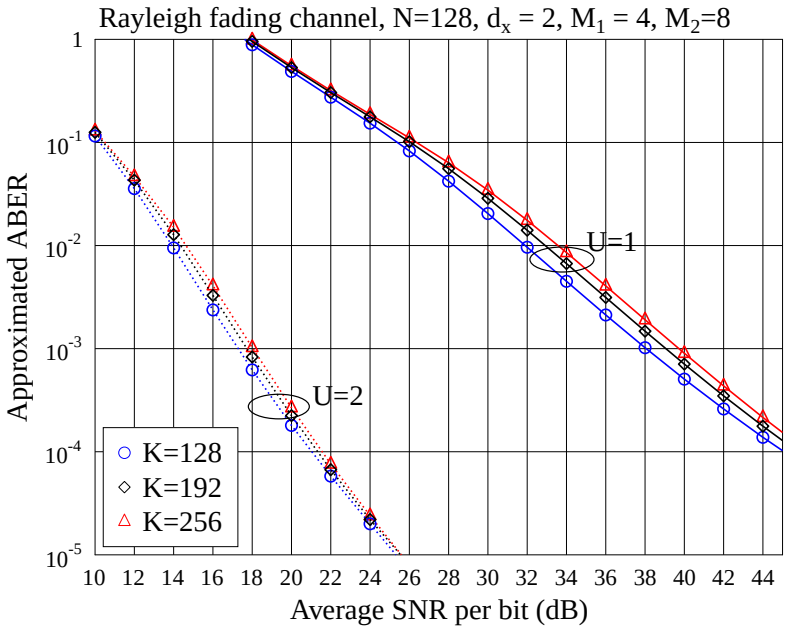

FIGURE 2.11: ABER performance of SM-SCDMA systems for different user-loads.

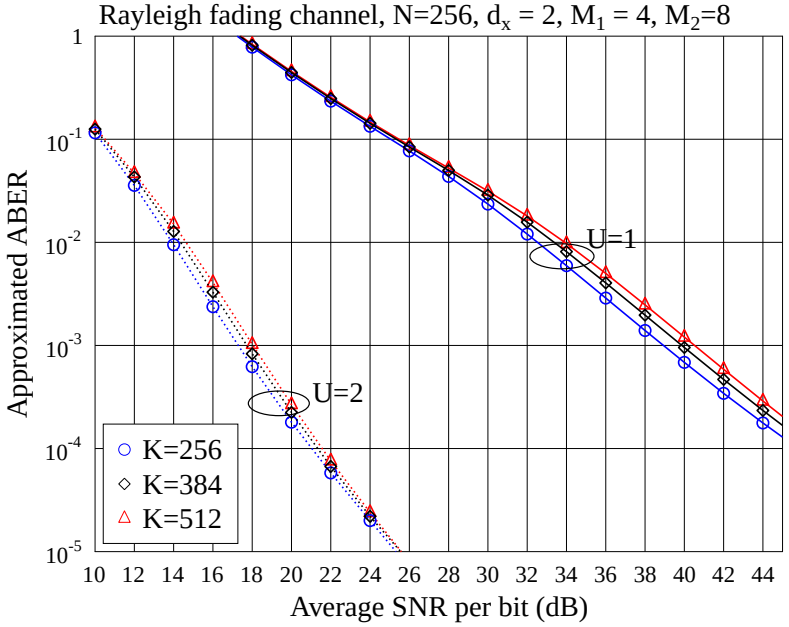

FIGURE 2.12: ABER performance of SM-SCDMA systems for different user-loads.

In Figs. 2.11 and 2.12, we plot the approximated ABER evaluated from $\bar{P}'_{bM}$ of (2.48) for $N = 128$ and 256, respectively. For both cases, we examine the performance, when the normalized user-load factors are respectively 1, 1.5 and 2. We can see from the results that the error performance curves of all the three loading factors are close to each other. From the results of Figs.2.9, 2.11 and 2.12 we infer that when a SM-SCDMA system becomes larger in terms of N, it is capable of supporting a heaver user-load at a given error rate.

2.6 Chapter Summary and Conclusions

In this chapter, we have proposed a SM-SCDMA system, which supports high-user-load MA transmission at a low complexity by integrating the SM and code-domain NOMA concepts. The main conclusions of this chapter are summarized in Table 2.1. In order to show the potential of SM-SCDMA and to allow it to achieve low-complexity near-optimum detection at a low complexity, we have compared the detection complexity of the MLD, MAPD and MPAD, as shown in Table 2.1. Furthermore, we have analyzed the ABER of SM-SCDMA systems employing MLD. A range of expressions have been derived for estimating the ABER of SM-SCDMA systems operating in different situations. Finally, the performance of SM-SCDMA systems has been investigated based on both simulations and numerical evaluation of the expressions derived. The SNRs required for achieving a BER of 10^{-3} under different normalized user loads are summarized in Table 2.1 as well.

TABLE 2.1: Main conclusions of Chapter 2.

System	SM-SCDMA system		
Example	$M_1 = M_2 = 4$, $U = 2$, $N = 12$		
SNR at a BER of 10^{-3}	$K = 16$	$K = 20$	$K = 24$
	13.8 dB	17.0 dB	18.0 dB
Complexity order	MLD	MAP	MPA
	$\mathcal{O}(M^K)$	$\mathcal{O}(M^{\lvert\mathcal{K}_l\rvert})$	$\mathcal{O}(M^{d_x(d_c-1)})$

Additionally, our studies and performance results also demonstrate that the SM-SCDMA is capable of supporting large-scale MA. The theoretical analysis of Section 2.4.2 can be directly applied to large-scale SM-SCDMA, so that attainable BER performance can be approximated without the requirement of actually implementing the system. Our SM-SCDMA system is also capable of exploiting the space-time domain resources for improving the energy efficiency. With the aid of the MAPD, our system is capable of supporting a normalized user-load of 2 without substantial performance degradation. Furthermore, we note that the error performance achieved by the MAPD is close to that attained by the MLD.

However, we only consider flat Rayleigh fading in this chapter, which fails to exploit the frequency diversity potential of frequency-selective fading channels. Therefore, we will eliminate this limitation in the next chapter.

Chapter 3

Spatial Modulation-Aided Multicarrier Sparse Code-Division Multiple Access

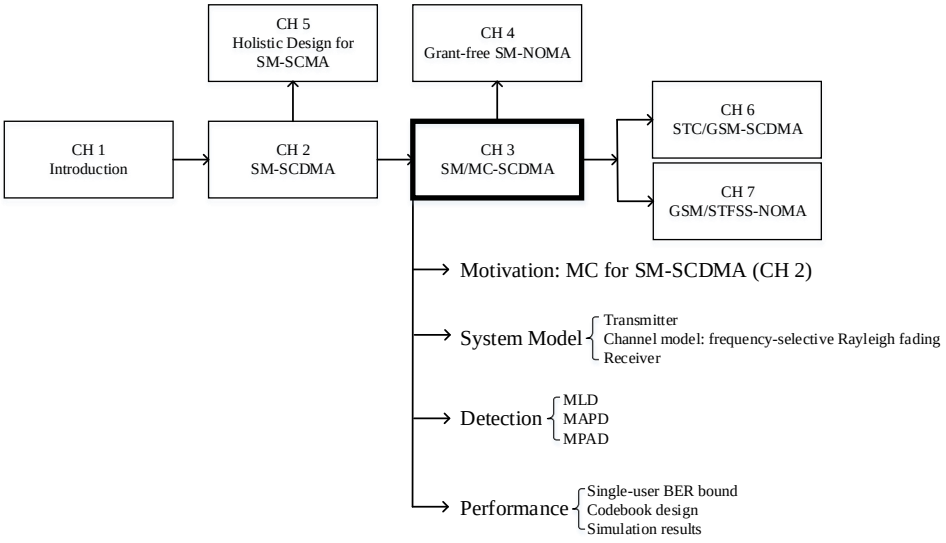

FIGURE 3.1: The relationship of Chapter 3 with the rest of the thesis.

3.1 Introduction

Spatial modulation (SM) has been widely investigated in the context of non-orthogonal multiple access NOMA [23–25,27,28], as summarized in Table 1.3. However, both Chapter 2 and the above-mentioned references on SM combined with code-domain NOMA

techniques assume frequency-flat fading channels. When practical frequency-selective fading channels are considered, the SM-aided sparse code division multiple access (SM-SCDMA) proposed in Chapter 2 will suffer from severe inter-symbol interference (ISI). Upon using the massage passing-aided detector (MPAD) for mitigating the ISI, its complexity is exponentially increased with the number of resolvable paths of the frequency-selective fading channels.

An effective solution technique of combatting frequency-selective fading is to employ multicarrier (MC) signalling [103], where numerous low-rate signals are transmitted by the parallel subcarriers. The resultant long symbols become immune to dispersion. When using frequency-domain (FD) spreading across the subcarriers, the system becomes capable of exploiting the energy scattered across the frequency-domain via combining the signals gleaned from different subcarriers. Furthermore, MC signalling benefits from the employment of efficient fast Fourier transform (FFT) based modulation techniques for low-complexity implementation. However, MC signalling has the disadvantage of high peak-to-average power ratio (PAPR), which requires the employment of high-linearity class-A amplification that are power-thirsty, which renders their employment in the uplink inefficient. This is a critical issue in device-centric communications. To be more specific, for a conventional MC system simultaneously activating all its N subcarriers, the peak power is proportional to N [103, 104]. By contrast, for a MC-SCMA system activating only d_x out of its N subcarriers, it is only d_x. Here, it is worth noting that d_x in SCMA-assisted systems is usually a small value, typically 2 or 3, regardless of the value of N [10, 26]. Hence, SCMA-assisted MC schemes are capable of mitigating the PAPR problem of conventional MC systems.

Bearing in mind the above-mentioned practical issues, we exploit the joint space-, time-, and frequency-domain (STFD) resources for transmission over frequency-selective fading channels. Explicitly, we propose a novel SM-aided MC SCDMA (SM/MC-SCDMA) system employing low density signature (LDS) spreading sequences, in order to support multiuser communications in ultra-dense deployments requiring massive connectivity. It is shown that our proposed SM/MC-SCDMA scheme is capable of circumventing the aforementioned problems, due to its following merits. Firstly, in contrast to [26], the SM/MC-SCDMA system incorporating MC signalling is capable of exploiting the frequency-selective fading to achieve frequency diversity. Secondly, as mentioned above, by introducing sparse code based spreading in the frequency-domain, which results in only a very small fraction (typically 2 or 3) of subcarriers being activated by each user, the PAPR problem can be efficiently mitigated. Furthermore, similar to [26], employing sparse spreading allows a SM/MC-SCDMA system to achieve near-optimum bit error rate (BER) performance, even when it is heavily loaded, operating at a normalized loading factor as high as two. Hence, the proposed SM/MC-SCDMA scheme relying on MPAD exhibits all the compelling characteristics required for supporting massive connectivity in device-centric communications.

Against this backdrop, the novel contributions of this chapter are summarized below.

- A SM/MC-SCDMA system is proposed for supporting massive uplink connectivity. In the proposed system, SM is employed for reducing the number of radio frequency (RF) chains. In contrast to the SM-SCDMA system proposed in [26], which assumes flat fading, the SM/MC-SCDMA employs MC signalling to combat frequency-selective fading. Sparse spreading is employed for the sake of facilitating low-complexity detection, whilst significantly alleviating the PAPR problem of MC systems. Furthermore, a MPAD is developed for the SM/MC-SCDMA system for low-complexity detection, even in the face of a high normalized user-load.
- Since our proposed SM/MC-SCDMA system is designed for operation in practical frequency-selective fading channels, which result in correlated fading in the frequency-domain, the single-user BER bounds derived in [105–108] cannot be directly exploited, since all of them assume independent flat Rayleigh fading. Therefore, we analyze the single-user BER bound of the SM/MC-SCDMA system, when assuming that the signals experience frequency-selective fading, whilst taking into account the correlation among the subcarriers.
- Based on the single-user BER bound, we propose the guidelines for sparse code design. Furthermore, we conceive a sparse code allocation technique for achieving a high diversity gain.
- The BER performance of the proposed SM/MC-SCDMA system using MPAD is studied both by Monte-Carlo simulations and by our analytical results. Additionally, the SM/MC-SCDMA scheme is generalized to the SM/MC-SCMA arrangement for the sake of obtaining extra shaping gain. Furthermore, the BER performance of both SM/MC-SCDMA and SM/MC-SCMA is compared to that of other related legacy MIMO schemes.

The rest of this chapter is structured as follows. Section 3.2 describes the transmitter and receiver schematics of the proposed SM/MC-SCDMA system. Different detection algorithms are detailed in Section 3.3, whereas the analysis of the single-user BER bound of SM/MC-SCDMA system is provided in Section 3.4. Section 3.5 characterizes the BER performance of the SM/MC-SCDMA systems in different scenarios. Finally, our main conclusions are summarized in Section 3.6.

3.2 System Model

In this section, we describe the SM/MC-SCDMA system model, which includes the transmitter model of Section 3.2.1 and the receiver of Section 3.2.2. In the SM/MC-SCDMA system considered, we assume that the number of subcarriers N is significantly

higher than the number of resolvable time-domain paths L, in line with the MC systems' typical design [104]. Hence, the individual subcarriers experience the flat fading, but the adjacent subcarriers may experience correlated attenuation. The other assumptions and notations will be detailed along with our discussions.

3.2.1 Transmitter Model

We investigate a single-cell uplink MC communication system, where K users simultaneously transmit their information to a base station (BS) over frequency-selective fading channels in the time-domain. We assume that each user employs M_1 transmit antennas (TAs), while the BS employs U receive antennas (RAs). For simplicity, during a symbol period, each user sends a symbol by activating one of the M_1 TAs to transmit an M_2-ary APM (M_2 amplitude-phase modulation) symbol using SM [18]. Our scheme can be readily extended to activating multiple TAs to convey multiple APM symbols [41, 125]. Therefore, as in [18,26], the symbol conveyed by the indices of the M_1 TAs is referred to as the space-shift keying (SSK) symbol, which assumes a value from $\mathcal{S}_1 = \{0, 1, ..., M_1 - 1\}$, and has $b_1 = \log_2 M_1$ bits per symbol (BPS). Meanwhile, the $b_2 = \log_2 M_2$ bits of an M_2-ary APM symbol takes a value from $\mathcal{S}_2 = \{s_{2,0}, s_{2,1}, ..., s_{2,M_2-1}\}$. Furthermore, we assume that the elements in $\mathcal{S}_2$ are normalized to satisfy $\sum_{i=0}^{M_2-1} |s_{2,i}|^2/M_2 = 1$.

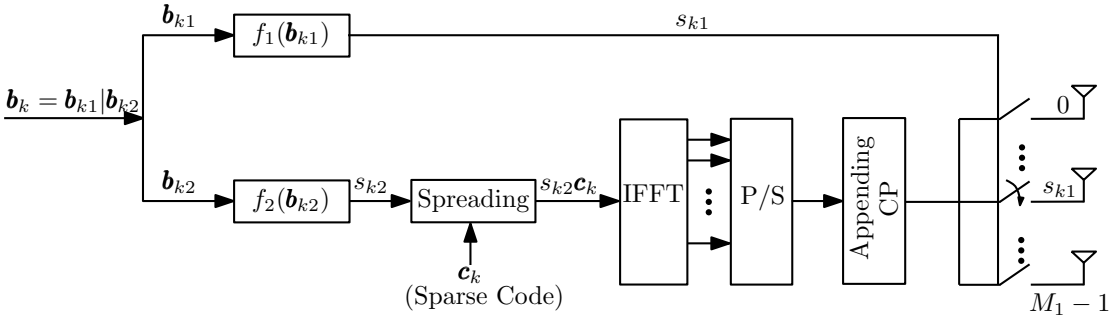

FIGURE 3.2: The transmitter schematic diagram of the kth user in the SM/MC-SCDMA system.

Fig. 3.2 represents the transmitter schematic of the kth user in a SM/MC-SCDMA system, where the b-bit symbol $\boldsymbol{b}_k$ of user k is first divided into two sub-symbols, $\boldsymbol{b}_{k1}$ and $\boldsymbol{b}_{k2}$. Explicitly, $\boldsymbol{b}_{k1}$ is mapped by $f_1(\boldsymbol{b}_{k1})$ to give a b_1-bit SSK symbol $s_{k1} \in \mathcal{S}_1$, which activates a TA. By contrast, $f_2(\boldsymbol{b}_{k2})$ maps $\boldsymbol{b}_{k2}$ to an M_2-ary APM symbol $s_{k2} \in \mathcal{S}_2$, which is first spread by a sparse code of length N assigned to user k. Let the spreading code assigned to user k be expressed as $\boldsymbol{c}_k = [c_{k0}, c_{k1}, ..., c_{k(N-1)}]^T$, which is normalized to satisfy $\|\boldsymbol{c}_k\|^2 = 1$ [10]. Then, the spread-spectrum signal $s_{k2}\boldsymbol{c_k}$ is inverse fast Fourier transform (IFFT) transformed to the time-domain, which is followed by the parallel-to-serial (P/S) conversion. Finally, after adding a cyclic prefix (CP) of sufficient length, the SM/MC-SCDMA signal is transmitted from the s_{k1}-th TA activated by the M_1-SSK symbol s_{k1}.

For the sparse spreading codes, we assume $d_x << N$ to be the maximum number of chips that a user's signal spreads over. Correspondingly, the number of users sharing one of the N chips is denoted by d_c, which has the property of $d_c << K$. For simplicity, we set both d_x and d_c to constants, implying that regular spreading codes are employed in our SM/MC-SCDMA system.

Additionally, for the convenience of our ensuing discussions, the symbols transmitted by K users is expressed as $\boldsymbol{x} = [x_0, x_1, \cdots, x_{K-1}]^T$, where x_k is $b = b_1 + b_2$ bits contributed by both the M_1-ary SSK symbol and the M_2-ary APM symbol. Hence, $x_k \in \mathcal{S} = \{\mathcal{S}_1 \otimes \mathcal{S}_2\} = \{s_0, s_1, \cdots, s_{M-1}\}$, which is a set consisting of all the $M = M_1 M_2$ different combinations of the elements in $\mathcal{S}_1$ and those in $\mathcal{S}_2$.

3.2.2 Receiver Model

Given the channel impulse response (CIR) between the s_{k1}th TA of user k and the uth RA of the BS as

$$\begin{aligned} \boldsymbol{h}_{s_{k1}}^{(u)} =& [h_{s_{k1},0}^{(u)}, h_{s_{k1},1}^{(u)}, \cdots, h_{s_{k1},L-1}^{(u)}]^T, \\ & s_{k1} = 0, \ldots, M_1 - 1; u = 1, 2, \cdots, U; k = 0, 1, \cdots, K-1, \end{aligned} \tag{3.1}$$

the corresponding frequency-domain channel transfer function (FDCHTF) experienced by the N subcarriers can be expressed as [103]

$$\hat{\boldsymbol{h}}_{s_{k1}}^{(u)} = \boldsymbol{\mathcal{F}} \boldsymbol{\Phi}_L \boldsymbol{h}_{s_{k1}}^{(u)}, \tag{3.2}$$

where $\boldsymbol{\Phi}_L$ is a $(N \times L)$ mapping matrix constituted by the first L columns of an identity matrix $\boldsymbol{I}_N$, and $\boldsymbol{\mathcal{F}}$ is the $(N \times N)$ FFT matrix having the property of $\boldsymbol{\mathcal{F}}\boldsymbol{\mathcal{F}}^H = \boldsymbol{\mathcal{F}}^H\boldsymbol{\mathcal{F}} = N\boldsymbol{I}_N$.

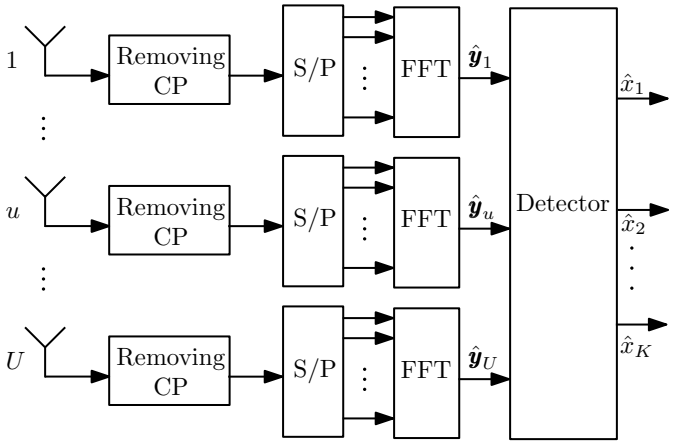

FIGURE 3.3: The receiver schematic diagram of uth antenna and kth user in the SM/MC-SCDMA system.

The receiver schematic of the SM/MC-SCDMA system is shown in Fig. 3.3, where the CP removal, S/P conversion and the FFT blocks are conventional, which follow [103]. Consequently, after the FFT-based detection operation to transform the time-domain signals to the frequency-domain, the observations obtained from the N subcarriers of the uth RA can be expressed as

$$\boldsymbol{y}_u = \sum_{k=1}^{K} \boldsymbol{C}_k \hat{\boldsymbol{h}}_{s_{k1}}^{(u)} s_{k2} + \boldsymbol{n}_u, \quad u = 0, 1, \cdots, U-1, \tag{3.3}$$

where we have $\boldsymbol{C}_k = \text{diag}\{\boldsymbol{c}_k\}$, the noise vector $\boldsymbol{n}_u$ obeys the zero-mean Gaussian distribution with a covariance matrix of $2\sigma^2\boldsymbol{I}_N$, expressed as $\mathcal{CN}(0, 2\sigma^2\boldsymbol{I}_N)$, where $\sigma^2 = 1/(2\gamma)$. Furthermore, $\gamma = b\gamma_0$ denotes the signal-to-noise ratio (SNR) per symbol, while γ_0 is the SNR per bit. Let $\boldsymbol{y} = [\boldsymbol{y}_0^T, \boldsymbol{y}_1^T, \cdots, \boldsymbol{y}_{U-1}^T]^T$, $\hat{\boldsymbol{h}}_{s_{k1}} = \left[\left(\hat{\boldsymbol{h}}_{s_{k1}}^{(0)}\right)^T, \left(\hat{\boldsymbol{h}}_{s_{k1}}^{(1)}\right)^T, \cdots, \left(\hat{\boldsymbol{h}}_{s_{k1}}^{(U-1)}\right)^T\right]^T$ and $\boldsymbol{n} = [\boldsymbol{n}_0^T, \boldsymbol{n}_1^T, \cdots, \boldsymbol{n}_{U-1}^T]^T$. Note that all these vectors are UN-dimensional. Then, it can be shown that we have

$$\begin{aligned}
\boldsymbol{y} &= \sum_{k=1}^{K} (\boldsymbol{I}_U \otimes \boldsymbol{C}_k) \hat{\boldsymbol{h}}_{s_{k1}} s_{k2} + \boldsymbol{n} \\
&= \sum_{k=1}^{K} (\boldsymbol{I}_U \otimes \boldsymbol{C}_k) \hat{\boldsymbol{H}}_k \boldsymbol{e}_{s_{k1}} s_{k2} + \boldsymbol{n} \\
&= \sum_{k=1}^{K} \boldsymbol{H}_k \boldsymbol{e}_{s_{k1}} s_{k2} + \boldsymbol{n} \\
&= \boldsymbol{H} \boldsymbol{e}_{s_1} \boldsymbol{s}_2 + \boldsymbol{n}.
\end{aligned} \tag{3.4}$$

In the above equations, $\otimes$ denotes the Kronecker product [112], and we have $\hat{\boldsymbol{H}}_k = [\hat{\boldsymbol{h}}_{0k}, \hat{\boldsymbol{h}}_{1k},$
$\cdots, \hat{\boldsymbol{h}}_{(M_1-1)k}]$, which is $(UN \times M_1)$-dimensional, where $\hat{\boldsymbol{h}}_{mk}$ is in the form of $\hat{\boldsymbol{h}}_{s_{k1}}$ defined above and with $s_{k1} = m$, while $\boldsymbol{e}_{s_{k1}}$ is a M_1-length vector with the s_{k1}th element being 1. The rest of the elements are zeros. Still referring to (3.4), we have $\boldsymbol{H}_k = (\boldsymbol{I}_U \otimes \boldsymbol{C}_k)\hat{\boldsymbol{H}}_k$, $\boldsymbol{H} = [\boldsymbol{H}_1, \boldsymbol{H}_2, \cdots, \boldsymbol{H}_K]$, which is a $(UN \times M_1K)$-dimensional matrix, and finally, we have $\boldsymbol{e}_{s_1} = \left[\boldsymbol{e}_{s_{11}}^T, \boldsymbol{e}_{s_{21}}^T, \cdots, \boldsymbol{e}_{s_{K1}}^T\right]^T$ and $\boldsymbol{s}_2 = [s_{12}, s_{22}, \cdots, s_{K2}]^T$. We consider the signal detection in the sequel.

3.3 Signal Detection

In this section, we first consider the optimal maximum-likelihood detection (MLD) in Section 3.3.1, followed by the optimal MAPD in Section 3.3.2. Then, a low-complexity near-optimal detector based on message passing algorithm (MPA) is introduced in Section 3.3.3.

3.3.1 Maximum-Likelihood Detection (MLD)

The MLD detects the symbols transmitted by K users based on the maximum likelihood principle. For consistence with Chapter 2, in this chapter, x, $\tilde{x}$ and $\hat{x}$ represent a transmitted symbol, a symbol hypothesized by the search algorithms and a detected symbol, respectively. Based on (3.4), the MLD finds the estimate of $\boldsymbol{x}$ by solving the optimization problem of

$$\begin{aligned}\hat{\boldsymbol{x}} &= \arg\min_{\tilde{\boldsymbol{x}}\in\mathcal{S}^K}\left\{\left\|\boldsymbol{y}-\sum_{k=1}^{K}(\boldsymbol{I}_U\otimes\boldsymbol{C}_k)\hat{\boldsymbol{h}}_{\tilde{s}_{k1}}\tilde{s}_{k2}\right\|^2\right\}\\ &= \arg\max_{\tilde{\boldsymbol{x}}\in\mathcal{S}^K}\left\{\sum_{k=1}^{K}\Re\{\tilde{s}_{k2}^*\hat{\boldsymbol{h}}_{\tilde{s}_{k1}}^H(\boldsymbol{I}_U\otimes\boldsymbol{C}_k)^H\boldsymbol{y}\}\right.\\ &\quad\left.-\frac{1}{2}\sum_{k=1}^{K}\sum_{i=1}^{K}\tilde{s}_{k2}^*\hat{\boldsymbol{h}}_{\tilde{s}_{k1}}^H(\boldsymbol{I}_U\otimes\boldsymbol{C}_k^H\boldsymbol{C}_i)\hat{\boldsymbol{h}}_{\tilde{s}_{i1}}\tilde{s}_{i2}\right\},\end{aligned}\tag{3.5}$$

where $\tilde{x}_k = \tilde{s}_{k1}|\tilde{s}_{k2}$ represents a composite SSK-APM symbol transmitted by user k, determining the corresponding CIR $\hat{\boldsymbol{h}}_{\tilde{s}_{k1}}$ and $\tilde{s}_{k2}$ used in (3.5), while $\Re\{a\}$ returns the real part of a. It can be readily shown that in (3.5), we have:

$$\begin{aligned}\hat{\boldsymbol{h}}_{\tilde{s}_{k1}}^H(\boldsymbol{I}_U\otimes\boldsymbol{C}_k)^H\boldsymbol{y} &= \sum_{u=0}^{U-1}\left(\hat{\boldsymbol{h}}_{\tilde{s}_{k1}}^{(u)}\right)^H\boldsymbol{C}_k^H\boldsymbol{y}_u\\ &= \sum_{u=0}^{U-1}\sum_{m\in\mathcal{C}_k}\left(\hat{h}_{\tilde{s}_{k1},m}^{(u)}\right)^* C_{km}^* y_{um},\end{aligned}\tag{3.6}$$

where $\mathcal{C}_k$ is a set defined to contain all the d_x indices having non-zero entries in $\boldsymbol{c}_k$. In (3.5), the second term can be simplified to

$$\tilde{s}_{k2}^*\hat{\boldsymbol{h}}_{\tilde{s}_{k1}}^H(\boldsymbol{I}_U\otimes\boldsymbol{C}_k^H\boldsymbol{C}_i)\hat{\boldsymbol{h}}_{\tilde{s}_{i1}}\tilde{s}_{i2} = \sum_{u=0}^{U-1}\sum_{m\in\mathcal{C}_k\cap\mathcal{C}_i}\tilde{s}_{k2}^*C_{km}^*C_{im}\hat{h}_{\tilde{s}_{k1},m}^{(u)\,*}\hat{h}_{\tilde{s}_{i1},m}^{(u)}\tilde{s}_{i2},\tag{3.7}$$

where the set $\mathcal{C}_k\cap\mathcal{C}_i$ represents the specific indices, where both $\boldsymbol{c}_k$ and $\boldsymbol{c}_i$ have non-zero entries. Upon applying the simplified results in (3.6) and (3.7) to (3.5), we obtain

$$\begin{aligned}\hat{\boldsymbol{x}} &= \arg\max_{\tilde{\boldsymbol{x}}\in\mathcal{S}^K}\left\{\sum_{k=1}^{K}\sum_{u=0}^{U-1}\sum_{m\in\mathcal{C}_k}\Re\{\tilde{s}_{k2}^*\hat{h}_{\tilde{s}_{k1},m}^{(u)\,*}C_{km}^*y_{um}\}\right.\\ &\quad\left.-\frac{1}{2}\sum_{k=1}^{K}\sum_{i=1}^{K}\sum_{u=0}^{U-1}\sum_{m\in\mathcal{C}_k\cap\mathcal{C}_i}C_{km}^*C_{im}\tilde{s}_{k2}^*\hat{h}_{\tilde{s}_{k1},m}^{(u)\,*}\hat{h}_{\tilde{s}_{i1},m}^{(u)}\tilde{s}_{i2}\right\}.\end{aligned}\tag{3.8}$$

Observe from (3.8) that for a given $\hat{\boldsymbol{x}}$ and assuming that two users share at most one subcarrier, the number of complex multiplications is about $(3d_xKU + 5K^2U)$, which is much lower than the value of $(3NKU + 5NK^2U)$ required, when full-weight spreading

sequences are employed. Nevertheless, the complexity order of the MLD is still $\mathcal{O}(M^K)$, given the M^K number of tests given by $\tilde{\boldsymbol{x}} \in \mathcal{S}^K$ in (3.8). Hence for the massive number of connections supported by a SM/MC-SCDMA system, this high complexity will prevent the MLD from practical implementation. Below we consider the symbol-based MAPD, which facilitates the implementation using belief propagation algorithms [74, 75, 126].

3.3.2 Maximum *A Posteriori* Detection (MAPD)

Given a user, the MAPD operated on a symbol-by-symbol basis maximizes the *a posteriori* probability of a symbol [127], for estimating the symbol transmitted by the user. In detail, given the observations of (3.4), the estimate of the kth user's symbol is obtained by solving the optimization problem of

$$\hat{x}_k = \arg\max_{\tilde{x}_k \in \mathcal{S}} \{P(\tilde{x}_k|\boldsymbol{y})\}, k = 1, 2, \cdots, K. \tag{3.9}$$

Upon applying Bayes' rule [128], we obtain

$$\begin{aligned} \hat{x}_k &= \arg\max_{\tilde{x}_k \in \mathcal{S}} p(\boldsymbol{y}|\tilde{x}_k) P(\tilde{x}_k) \\ &= \arg\max_{\tilde{x}_k \in \mathcal{S}} \left\{ \sum_{\boldsymbol{x}_k \in \mathcal{S}^{K-1}} P(\tilde{x}_k) P(\boldsymbol{x}_k) p(\boldsymbol{y}|\boldsymbol{x}_k, \tilde{x}_k) \right\}, \end{aligned} \tag{3.10}$$

where $p(\boldsymbol{y}|\tilde{x}_k)$ is the probability density function (PDF) of $\boldsymbol{y}$ for a given $\tilde{x}_k$, while $p(\boldsymbol{y}|\boldsymbol{x}_k, \tilde{x}_k)$ is the PDF of $\boldsymbol{y}$ for a given $(\boldsymbol{x}_k, \tilde{x}_k)$. Here $\boldsymbol{x}_i$ is a $(K-1)$-length vector obtained from $\boldsymbol{x}$ after removing the kth user's symbol, while $P(\tilde{x}_k)$ and $P(\boldsymbol{x}_k)$ are the *a priori* probabilities of $\tilde{x}_k$ and $\boldsymbol{x}_k$, respectively. It can be shown that for a given $(\boldsymbol{x}_k, \tilde{x}_k)$, the observations $\{y_{un}\}$ are independent. Hence, we can further express (3.10) as

$$\hat{x}_k = \arg\max_{\tilde{x}_k \in \mathcal{S}} \left\{ \sum_{\boldsymbol{x}_k \in \mathcal{S}^{|\mathcal{K}_k|}} P(\tilde{x}_k) P(\boldsymbol{x}_k) \prod_{u=0}^{U-1} \prod_{n=0}^{N-1} p(y_{un}|\boldsymbol{x}_k, \tilde{x}_k) \right\}, \tag{3.11}$$

where $\mathcal{K}_k$ is the set of users interfering with user k. To be more specific, the set $\mathcal{K}_k$ contains all the indices of the users sharing at least one subcarrier with user k. Correspondingly, $|\mathcal{K}_k|$ is the cardinality of $\mathcal{K}_k$.

Let $\boldsymbol{x}_{[n]}$ be a d_c-length vector containing the symbols sent by the d_c users sharing the nth subcarrier, which includes $\tilde{x}_k$, if user k occupies the nth subcarrier. Then (3.11) can be further simplified to

$$\hat{x}_k = \arg\max_{\tilde{x}_k \in \mathcal{S}} \left\{ \sum_{\boldsymbol{x}_k \in \mathcal{S}^{|\mathcal{K}_k|}} P(\tilde{x}_k) P(\boldsymbol{x}_k) \prod_{u=0}^{U-1} \prod_{n \in \mathcal{C}_k} p(y_{un}|\boldsymbol{x}_{[n]}) \right\}. \tag{3.12}$$

When $\boldsymbol{x}_{[n]}$ is given, the PDF of $p(y_{un}|\boldsymbol{x}_{[n]})$ can be expressed as

$$P(y_{un}|\boldsymbol{x}_{[n]}) = \frac{1}{2\pi\sigma^2} \exp\left(-\frac{\|y_{un} - \sum_{i\in\mathcal{D}_n} \hat{h}_{s_{i1}}^{(u)} s_{i2} c_{in}\|^2}{2\sigma^2}\right), \tag{3.13}$$

where we express $\mathcal{D}_n$ as the set containing the indices of the users sharing the nth subcarrier.

We can infer from (3.12) that the complexity of the MAPD is $\mathcal{O}(M^{|\mathcal{K}_k|})$. When sparse spreading codes are employed, $|\mathcal{K}_k|$ is determined by d_x and d_c. More specifically, when regular sparse codes are employed, resulting in d_x and d_c being constants, we can readily show that we have $|\mathcal{K}_k| = d_x(d_c - 1)$, provided that no two users share more than one subcarrier. Since we have $d_x \ll N$ and $d_c \ll K$, and typically $d_x = 2,\ 3$ and $d_c = 3,\ 4$ for SM/MC-SCDMA systems, the detection complexity of MAPD can be much lower than that of the MLD discussed in Section 3.3.1. Furthermore, as shown below, with the aid of the MPA, a MPAD having a further reduced detection complexity, yet attaining a near-MAPD performance can be implemented.

3.3.3 Message Passing Algorithm-Aided Detection (MPAD)

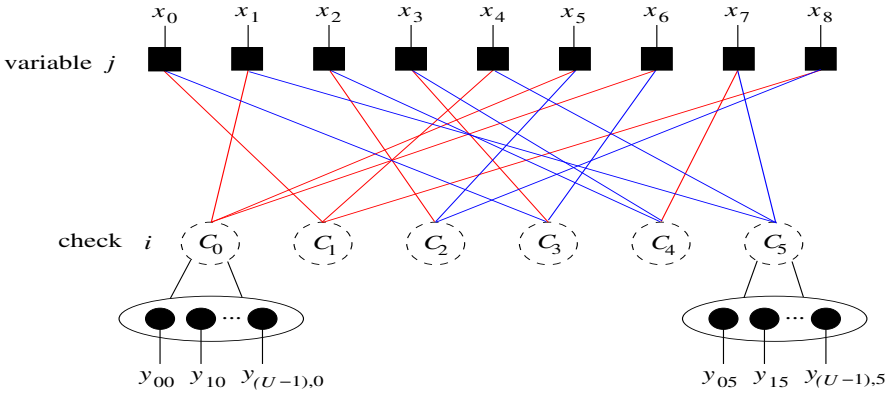

FIGURE 3.4: A example showing the factor graph representation of the the SM/MC-SCDMA system with regular sparse sequences and the parameters of $N = 6$, $K = 9$, $d_x = 2$, and $d_c = 3$.

The classic factor graph [10,74] that is convenient for characterizing the decoding of LDPC codes can be introduced to visualize the relationship between the K users' transmitted symbols and the observations obtained at the BS receiver in the proposed SM/MC-SCDMA system. As shown in Fig. 3.4 for the case of $K = 9$ and $N = 6$, the K symbols each taking a value from $\mathcal{S}$ are represented by the K variable nodes, whereas the UN observations obtained from N subcarriers and U RAs are represented by N check nodes. Each check node corresponds to a subcarrier and contains U observations obtained from the same subcarrier and U RAs. As shown in Fig. 3.4, each check node is connected to a small number of variable nodes, which is determined by the sparse spreading codes assigned to the K users. On the other hand, each variable node is connected to a small

fraction of check nodes, which is determined by the number of non-zero elements of the sparse spreading code assigned to the corresponding user. As shown in Fig. 3.4, each variable node is connected to two check nodes, representing that any sparse spreading code has two non-zero elements. By contrast, each check node is connected to three users, meaning that each subcarrier is shared by three users.

For describing the MPAD, let the d_c connections with the check node i, and the d_x connections with the variable node j be defined respectively by the sets

$$\begin{aligned}\mathcal{C}_i &= \{j : 1 \leq j \leq K, e_{j,i} \neq 0\}\,,\ i = 0, 1, \ldots, N-1 \\ \mathcal{X}_j &= \{i : 0 \leq i \leq N-1, e_{j,i} \neq 0\}\,,\ j = 0, 1, \ldots, K-1,\end{aligned} \tag{3.14}$$

where $e_{ji} \neq 0$ indicates that there exists an edge e_{ji} between the check node i and the variable node j. Based on the factor graph of Fig. 3.4, let us now detail the MPAD's operation in our proposed SM/MC-SCDMA system.

In Fig. 3.4, via the edge e_{ji}, information can be conveyed upward from the check node i to the variable node j. Information can also be conveyed downward from the variable node j to the check node i. Correspondingly, the probability $\delta_{i,j}^{a_m,t}$ defines the amount of information conveyed from the check node i to the variable node j during the tth iteration. Here, $\delta_{i,j}^{a_m,t}$ represents the probability of $x_j = a_m$, when given the probabilities received by the check node c_i from all the connected variable nodes, after excluding x_j. By contrast, the amount of information sent from the variable node x_j to the check node c_i in the tth iteration is expressed as $\eta_{j,i}^{a_m,t}$. Similarly, $\eta_{j,i}^{a_m,t}$ is the probability of $x_j = a_m$, when given the probabilities received by the variable node x_j from all the connected check nodes, after excluding c_i. With the aid of the above definitions, following [115], the MPAD relies on the following steps.

First, $\eta_{j,i}^{a_m,0}$ is initialised to $1/M$ for all $a_m \in \mathcal{S}$ and any $e_{j,i} \neq 0$. Then, at the t-th iteration, $\delta_{i,j}^{a_m,t}$ for $j \in \mathcal{X}_i$ and $i \in \mathcal{C}_j$ can be updated as

$$\begin{aligned}\delta_{i,j}^{a_m,t} = &\sum_{\boldsymbol{x}_{[i]} \in \mathcal{S}^{d_c-1}, x_j = a_m} \left(\prod_{x_v \in \boldsymbol{x}_{[i]} \setminus x_j} \eta_{j,i}^{x_v,t} \right) \prod_{u=0}^{U-1} p(y_{ui} | \boldsymbol{x}_{[i]}, x_j = a_m), \\ &m = 0, 1, \ldots, M-1,\end{aligned} \tag{3.15}$$

where $\prod_{x_v \in \boldsymbol{x}_{[i]} \setminus x_j} \eta_{j,i}^{x_v,t}$ is the *a priori* probability of a given $\boldsymbol{x}_{[i]}$ with $x_j = a_m$, while $p(y_{ui} | \boldsymbol{x}_{[i]}, x_j = a_m)$ is given by (3.13). Observe from (3.15) that the information conveyed by the check node i to the variable node j is the product of the information gleaned from all the other edges connected to the check node i. The total information conveyed to the variable node j is the sum of the information arriving from all the check nodes connected to the variable node j.

Next, at the $(t+1)$th iteration, the values $\delta_{i,j}^{a_m,t}$ obtained in the tth iteration are used to update $\eta_{j,i}^{a_m,t+1}$ for $i \in \mathcal{X}_j$ and $j \in \mathcal{C}_i$ as follows

$$\eta_{j,i}^{a_m,t+1} = \varepsilon_{j,i} \prod_{v \in \mathcal{X}_j \backslash i} \delta_{v,j}^{a_m,t}, \ m = 0, 1, \ldots, M-1, \tag{3.16}$$

where $\varepsilon_{j,i}$ is the normalisation factor to ensure that $\sum_{m=0}^{M-1} \eta_{j,i}^{a_m,t+1} = 1$.

Finally, after the pre-set number of iterations is reached, the detector detects the transmitted symbol of the kth user as

$$x_k = \arg \max_{a_m \in \mathcal{S}} \prod_{v \in \mathcal{X}_k} \delta_{v,j}^{a_m,t}, \ k = 0, 1, \ldots, K-1. \tag{3.17}$$

We can see from (3.15) that the computational complexity is primarily dominated by the upward information transition. The number of multiplications is determined by the size of $\boldsymbol{x}_{[i]}$, while the detection complexity is determined by the M^{d_c-1} possibilities in $\mathcal{S}^{d_c-1}$ of (3.15). Hence, the complexity of the MPAD is $\mathcal{O}(M^{d_c-1})$.

3.4 Analysis of the Single-User Performance and its Discussion

This section first analyses the error probability of the SM/MC-SCDMA system supporting a single user, which gives the performance upper-bound. Furthermore, as shown by the results of references [107, 129, 130] and those illustrated in Section 3.5, the single user BER performance bound can actually be viewed as the approximate BER performance of the SM/MC-SCDMA system with the optimum MUD or MPAD, when the system supports multiple users up to a loading factor of two, meaning that each subcarrier on average supports two users. Then, from the formulas derived in the single-user case, we gain insight into the performance impact of sparse sequences, and hence into their design.

3.4.1 Analysis of Single-User Average Bit Error Rate

According to the MLD of (3.8), when the SM/MC-SCDMA system supports a single user, we can represent the MLD as

$$\hat{x} = \arg \max_{\tilde{x} \in \mathcal{X}} \left\{ \sum_{u=0}^{U-1} \sum_{m \in \mathcal{C}} \Re\{\tilde{s}_2^* \hat{h}_{\tilde{s}_1,m}^{(u)\,*} C_m^* y_{um}\} - \frac{1}{2} \sum_{u=0}^{U-1} \sum_{m \in \mathcal{C}} \|\hat{h}_{\tilde{s}_1,m}^{(u)} \tilde{s}_2 C_m\|^2 \right\}, \tag{3.18}$$

where the index k is dropped for notational simplicity. Therefore, a detection error occurs, when we should have at least one scenario of $\tilde{x}(= \tilde{s}_1|\tilde{s}_2) \neq x(= s_1|s_2)$ resulting

in

$$\sum_{u=0}^{U-1}\sum_{m\in\mathcal{C}}\Re\{\tilde{s}_2^*\hat{h}_{\tilde{s}_1,m}^{(u)\,*}C_m^*y_{um}\}-\frac{1}{2}\sum_{u=0}^{U-1}\sum_{m\in\mathcal{C}}\|\hat{h}_{\tilde{s}_1,m}^{(u)}\tilde{s}_2C_m\|^2$$
$$>\sum_{u=0}^{U-1}\sum_{m\in\mathcal{C}}\Re\{s_2^*\hat{h}_{s_1,m}^{(u)\,*}C_m^*y_{um}\}-\frac{1}{2}\sum_{u=0}^{U-1}\sum_{m\in\mathcal{C}}\|\hat{h}_{s_1,m}^{(u)}s_2C_m\|^2. \tag{3.19}$$

After some simplifications, (3.19) can be expressed as

$$\sum_{u=0}^{U-1}\sum_{m\in\mathcal{C}}\Re\left\{(\tilde{s}_2^*\hat{h}_{\tilde{s}_1,m}^{(u)\,*}-s_2^*\hat{h}_{s_1,m}^{(u)\,*})C_m^*y_{um}\right\}>\frac{1}{2}\sum_{u=0}^{U-1}\sum_{m\in\mathcal{C}}(\|\hat{h}_{\tilde{s}_1,m}^{(u)}\tilde{s}_2C_m\|^2-\|\hat{h}_{s_1,m}^{(u)}s_2C_m\|^2). \tag{3.20}$$

Then, upon substituting $\boldsymbol{y}_n$ of (3.3) along with $K=1$ into (3.20), we can express the erroneous detection event in matrix (vector) form as

$$\Re\left\{(\boldsymbol{H}\boldsymbol{e}_{\tilde{s}_1}\tilde{s}_2-\boldsymbol{H}\boldsymbol{e}_{s_1}s_2)^H\boldsymbol{n}_U\right\}>\frac{1}{2}\|\boldsymbol{H}\boldsymbol{e}_{\tilde{s}_1}\tilde{s}_2-\boldsymbol{H}\boldsymbol{e}_{s_1}s_2\|^2, \tag{3.21}$$

where $\boldsymbol{n}_U=(\boldsymbol{I}_U\otimes\boldsymbol{C})^H\boldsymbol{n}$ is a complex Gaussian distributed vector having the PDF of $\mathcal{CN}(0,\gamma^{-1}\boldsymbol{I}_U)$. Consequently, the pairwise error probability (PEP), when the transmitted x is detected as $\tilde{x}\neq x$ is given by [131]

$$P_{EP}(x\to\tilde{x})=E_{\boldsymbol{H}}\left[Q\left(\sqrt{\frac{\gamma}{2}\|\boldsymbol{H}\boldsymbol{e}_{\tilde{s}_1}\tilde{s}_2-\boldsymbol{H}\boldsymbol{e}_{s_1}s_2\|^2}\right)\right], \tag{3.22}$$

where $Q(x)$ is defined as $Q(x)=(2\pi)^{-1/2}\int_x^\infty e^{-t^2/2}dt$, and $E_{\boldsymbol{H}}[\cdot]$ stands for the expectation with respect to the channels between the K users and the BS, which affect the terms $\boldsymbol{H}\boldsymbol{e}_{\tilde{s}_1}$ and $\boldsymbol{H}\boldsymbol{e}_{\tilde{s}_2}$ in (3.22). With the alternative representation of the Q-function [118] of $Q(x)=\pi^{-1}\int_0^{\pi/2}\exp\left(-\frac{x^2}{2\sin^2\theta}\right)d\theta$, the PEP of (3.22) can be expressed as

$$P_{EP}(x\to\tilde{x})=E_{\boldsymbol{H}}\left[\frac{1}{\pi}\int_0^{\frac{\pi}{2}}\exp\left(-\frac{\gamma}{4\sin^2\theta}\|\boldsymbol{H}\boldsymbol{e}_{\tilde{s}_1}\tilde{s}_2-\boldsymbol{H}\boldsymbol{e}_{s_1}s_2\|^2\right)d\theta\right] \tag{3.23a}$$
$$=\frac{1}{\pi}\int_0^{\frac{\pi}{2}}\Phi_{\|\boldsymbol{H}\boldsymbol{e}_{\tilde{s}_1}\tilde{s}_2-\boldsymbol{H}\boldsymbol{e}_{s_1}s_2\|^2}\left(-\frac{\gamma}{4\sin^2\theta}\right)d\theta, \tag{3.23b}$$

where $\Phi_{\|\boldsymbol{H}\boldsymbol{e}_{\tilde{s}_1}\tilde{s}_2-\boldsymbol{H}\boldsymbol{e}_{s_1}s_2\|^2}(x)$ is the moment generation function (MGF) of the random variable $\|\boldsymbol{H}\boldsymbol{e}_{\tilde{s}_1}\tilde{s}_2-\boldsymbol{H}\boldsymbol{e}_{s_1}s_2\|^2$.

Following the analysis in [116,117], the average bit error ratio (ABER) of the single-user SM/MC-SCDMA system can be approximately evaluated from the union-bound as

$$\bar{P}_{bS} \leq \frac{1}{M_1 M_2 b} \sum_{m_1=0}^{M_1-1} \sum_{m_2=0}^{M_2-1} \sum_{\tilde{m}_1=0}^{M_1-1} \sum_{\tilde{m}_2=0}^{M_2-1} D\left(\boldsymbol{b}_1^{(m_1)}|\boldsymbol{b}_2^{(m_2)}, \tilde{\boldsymbol{b}}_1^{(\tilde{m}_1)}|\tilde{\boldsymbol{b}}_2^{(\tilde{m}_2)}\right) \times P_{EP}\left(s_1^{(m_1)}|s_2^{(m_2)} \to \tilde{s}_1^{(\tilde{m}_1)}|\tilde{s}_2^{(\tilde{m}_2)}\right), \tag{3.24}$$

where $D(\cdot,\cdot)$ is the Hamming distance between two binary entries, and $\boldsymbol{b}_i^{(m)}$, $s_i^{(m)}$ give the binary representation and symbol of the m-th SSK symbol (when $i=1$) or of the m-th APM symbol (when $i=2$). Furthermore, in (3.24), $s_i^{(m_i)} \to \tilde{s}_i^{(\tilde{m}_i)}$ means that the erroneous event takes the transmitted $s_i^{(m_i)}$ into detected $\tilde{s}_i^{(\tilde{m}_i)}$. As shown in [116], errors may corrupt only the SSK symbol, only the APM symbol, or both of them. When considering those three cases separately, the corresponding $P_{EP}(x \to \tilde{x})$ of (3.23a) can be derived as follows.

Erroneous SSK Symbol Only: When only the SSK symbol is in error, we have $\tilde{s}_1 \neq s_1$ and $\tilde{s}_2 = s_2$. In this case, (3.23a) can be reduced to

$$\begin{aligned} P_{EP1}(s_1|s_2 \to \tilde{s}_1|s_2) =& E_{\boldsymbol{H}}\left[\frac{1}{\pi}\int_0^{\frac{\pi}{2}} \exp\left(-\frac{\gamma|s_2|^2}{4\sin^2\theta}\|\boldsymbol{H}\boldsymbol{e}_{\tilde{s}_1} - \boldsymbol{H}\boldsymbol{e}_{s_1}\|^2\right) d\theta\right] \\ =& E_{\boldsymbol{H}}\left[\frac{1}{\pi}\int_0^{\frac{\pi}{2}} \exp\left(-\frac{\gamma|s_2|^2}{4\sin^2\theta}\|\boldsymbol{H}\boldsymbol{v}_1\|^2\right) d\theta\right] \\ =& \frac{1}{\pi}\int_0^{\frac{\pi}{2}} \Phi_{\|\boldsymbol{H}\boldsymbol{v}_1\|^2}\left(-\frac{|s_2|^2\gamma}{4\sin^2\theta}\right) d\theta, \end{aligned} \tag{3.25}$$

where $\boldsymbol{v}_1 = \boldsymbol{e}_{\tilde{s}_1} - \boldsymbol{e}_{s_1}$.

Erroneous APM Symbol Only: When errors only corrupt the APM symbol, we have $\tilde{s}_2 \neq s_2$ and $\tilde{s}_1 = s_1$. In this case, (3.23a) can be reduced to

$$\begin{aligned} P_{EP2}(s_1|s_2 \to s_1|\tilde{s}_2) &= E_{\boldsymbol{H}}\left[\frac{1}{\pi}\int_0^{\frac{\pi}{2}} \exp\left(-\frac{\gamma}{4\sin^2\theta}\|\boldsymbol{H}\boldsymbol{e}_{s_1}\tilde{s}_2 - \boldsymbol{H}\boldsymbol{e}_{s_1}s_2\|^2\right) d\theta\right] \\ &= E_{\boldsymbol{H}}\left[\frac{1}{\pi}\int_0^{\frac{\pi}{2}} \exp\left(-\frac{|\tilde{s}_2 - s_2|^2\gamma}{4\sin^2\theta}\|\boldsymbol{H}\boldsymbol{e}_{s_1}\|^2\right) d\theta\right] \\ &= \frac{1}{\pi}\int_0^{\frac{\pi}{2}} \Phi_{\|\boldsymbol{H}\boldsymbol{v}_2\|^2}\left(-\frac{|\tilde{s}_2 - s_2|^2\gamma}{4\sin^2\theta}\right) d\theta, \end{aligned} \tag{3.26}$$

where $\boldsymbol{v}_2 = \boldsymbol{e}_{s_1}$.

Erroneous SSK and QAM Symbols: Finally, when errors occur simultaneously in both the SSK symbol and APM symbol, we have $\tilde{s}_1 \neq s_1$ and $\tilde{s}_2 \neq s_2$. Correspondingly,

(3.23a) can be modified to

$$\begin{aligned} P_{EP3}(s_1|s_2 \to \tilde{s}_1|\tilde{s}_2) =& E_{\boldsymbol{H}}\left[\frac{1}{\pi}\int_0^{\frac{\pi}{2}} \exp\left(-\frac{\gamma}{4\sin^2\theta}\|\boldsymbol{H}\boldsymbol{e}_{\tilde{s}_1}\tilde{s}_2 - \boldsymbol{H}\boldsymbol{e}_{s_1}s_2\|^2\right) d\theta\right] \\ =& E_{\boldsymbol{H}}\left[\frac{1}{\pi}\int_0^{\frac{\pi}{2}} \exp\left(-\frac{\gamma}{4\sin^2\theta}\|\boldsymbol{H}\boldsymbol{v}_3\|^2\right) d\theta\right] \\ =& \frac{1}{\pi}\int_0^{\frac{\pi}{2}} \Phi_{\|\boldsymbol{H}\boldsymbol{v}_3\|^2}\left(-\frac{\gamma}{4\sin^2\theta}\right) d\theta, \end{aligned} \tag{3.27}$$

where $\boldsymbol{v}_3 = \boldsymbol{e}_{\tilde{s}_1}\tilde{s}_2 - \boldsymbol{e}_{s_1}s_2$.

As shown in (3.25), (3.26) and (3.27), in order to evaluate the ABER of (3.24), we have to derive the MGFs of $\Phi_{\|\boldsymbol{H}\boldsymbol{v}_i\|^2}(t)$ for $i = 1, 2$ and 3. According to [132, 133], we know that

$$\begin{aligned} \|\boldsymbol{H}\boldsymbol{v}_i\|^2 =& \sum_{n=0}^{UN-1} \boldsymbol{H}(n)\boldsymbol{v}_i\boldsymbol{v}_i^H\boldsymbol{H}^H(n) \\ =& \boldsymbol{h}^T\left[\boldsymbol{I}_{UN} \otimes \left(\boldsymbol{v}_i\boldsymbol{v}_i^H\right)\right]\boldsymbol{h}^*, \end{aligned} \tag{3.28}$$

where $\boldsymbol{H}(n)$ represents the nth row of $\boldsymbol{H}$, and $\boldsymbol{h} = \text{vec}(\boldsymbol{H}^T)$ is a M_1UN-length vector obtained from the rows of $\boldsymbol{H}$. Since the channels experience correlated Rayleigh fading, the MGF of $\|\boldsymbol{H}\boldsymbol{v}_i\|^2$ can be derived in the same way as that in [132, 133], which can be expressed as

$$\Phi_{\|\boldsymbol{H}\boldsymbol{v}_i\|^2}(t) = \det\left[\boldsymbol{I}_{M_1UN} - t\boldsymbol{R}\left(\boldsymbol{I}_{UN} \otimes (\boldsymbol{v}_i\boldsymbol{v}_i^H)\right)\right]^{-1}, \tag{3.29}$$

where $\det(\boldsymbol{A})$ denotes the determinant of matrix $\boldsymbol{A}$, $\boldsymbol{R}$ is the covariance matrix of $\boldsymbol{h}$ that can be expressed as

$$\boldsymbol{R} = \begin{bmatrix} \sqrt{\rho_{00}} & \sqrt{\rho_{01}} & \cdots & \sqrt{\rho_{0(M_1UN-1)}} \\ \sqrt{\rho_{10}} & \sqrt{\rho_{11}} & \cdots & \sqrt{\rho_{1(M_1UN-1)}} \\ \vdots & \vdots & \ddots & \vdots \\ \sqrt{\rho_{(M_1UN-1)0}} & \sqrt{\rho_{(M_1UN-1)1}} & \cdots & \sqrt{\rho_{(M_1UN-1)(M_1UN-1)}} \end{bmatrix}. \tag{3.30}$$

In $\boldsymbol{R}$, ρ_{mn} $(m = 0, 1, \ldots, M_1UN-1;\ n = 0, 1, \ldots, M_1UN-1)$ can be obtained as follows. Let us express $m = M_1i + a$ and $n = M_1j + b$, where $i, j \in [0, NU-1]$ and $a, b \in [0, M_1-1]$. Furthermore, let $i = \lfloor \frac{i}{N} \rfloor N + c$ and $j = \lfloor \frac{j}{N} \rfloor N + d$, where $\lfloor x \rfloor$ gives the largest integer not exceeding x, while c and d are the two subcarrier indices derived from i and j, respectively. Then, we can see that the indices m and n correspond to the same TA and the same RA, only when $j = \lfloor \frac{i}{N} \rfloor N, \lfloor \frac{i}{N} \rfloor N + 1, \ldots, \lfloor \frac{i}{N} \rfloor N + N - 1$ and $a = b$. Furthermore, ρ_{mn} only becomes nonzero when the two subcarriers determined by i and j, i.e., subcarriers c and d, are activated by the spreading code. Based on the above analysis, we can show that the normalized correlation coefficient $\rho_{mn}(m, n)$ can

be expressed as [134]

$$\rho_{mn} = \begin{cases} \frac{1}{L} + \frac{1}{L^2} \sum_{u=0}^{L-1} \sum_{v=0, v\neq u}^{L-1} \cos\left(\frac{2\pi(c-d)(u-v)}{N}\right), & \text{if } m = M_1 i + a, n = M_1 j + b; \\ & i = \lfloor \frac{i}{N} \rfloor N + c,\ j = \lfloor \frac{j}{N} \rfloor N + d \text{ satisfy} \\ & a = b, c \in \mathcal{C}, d \in \mathcal{C}, \text{and} \\ & j = \lfloor \frac{i}{N} \rfloor N, \ldots, 2\lfloor \frac{i}{N} \rfloor N - 1, \\ 0, & \text{otherwise.} \end{cases} \tag{3.31}$$

From the above analysis and (3.31), we know that $\boldsymbol{R}$ is a sparse matrix having at most $UM_1d_x^2$ and at least UM_1d_x nonzero elements, corresponding to the pair of cases, when the d_x subcarrier channels between a TA and a RA are correlated and independent, respectively. Note that, ρ_{mm} on the diagonal of $\boldsymbol{R}$ is either zero, when the corresponding subcarrier is not used by the user, or one, if the user activates the corresponding subcarrier. Furthermore, if the d_x subcarriers activated by the user experience independent fading, the UM_1d_x number of 1's are all on the diagonal of $\boldsymbol{R}$.

Given the above preparation, we can now express (3.25), (3.26) and(3.27) respectively as

$$P_{EP1}(s_1|s_2 \to \tilde{s}_1|s_2) = \frac{1}{\pi} \int_0^{\frac{\pi}{2}} \det\left(\boldsymbol{I}_{M_1UN} + \frac{|s_2|^2 \gamma}{4\sin^2\theta} \boldsymbol{R}\left(\boldsymbol{I}_{UN} \otimes (\boldsymbol{v}_1 \boldsymbol{v}_1^H)\right)\right)^{-1} d\theta \tag{3.32a}$$

$$P_{EP2}(s_1|s_2 \to s_1|\tilde{s}_2) = \frac{1}{\pi} \int_0^{\frac{\pi}{2}} \det\left(\boldsymbol{I}_{M_1UN} + \frac{|\tilde{s}_2 - s_2|^2 \gamma}{4\sin^2\theta} \boldsymbol{R}\left(\boldsymbol{I}_{UN} \otimes (\boldsymbol{v}_2 \boldsymbol{v}_2^H)\right)\right)^{-1} d\theta \tag{3.32b}$$

$$P_{EP3}(s_1|s_2 \to \tilde{s}_1|\tilde{s}_2) = \frac{1}{\pi} \int_0^{\frac{\pi}{2}} \det\left(\boldsymbol{I}_{M_1UN} + \frac{\gamma}{4\sin^2\theta} \boldsymbol{R}\left(\boldsymbol{I}_{UN} \otimes (\boldsymbol{v}_3 \boldsymbol{v}_3^H)\right)\right)^{-1} d\theta. \tag{3.32c}$$

Let us express the nonzero eigenvalues of $\boldsymbol{R}\left[\boldsymbol{I}_{UN} \otimes (\boldsymbol{v}_1 \boldsymbol{v}_1^H)\right]$ as $\{\lambda_{11}, \lambda_{12}, \ldots, \lambda_{1G_1}\}$, that of $\boldsymbol{R}\left[\boldsymbol{I}_{UN} \otimes (\boldsymbol{v}_2 \boldsymbol{v}_2^H)\right]$ as $\{\lambda_{21}, \lambda_{22}, \ldots, \lambda_{2G_2}\}$, and that of $\boldsymbol{R}\left[\boldsymbol{I}_{UN} \otimes (\boldsymbol{v}_3 \boldsymbol{v}_3^H)\right]$ as $\{\lambda_{31}, \lambda_{32}, \ldots, \lambda_{3G_3}\}$. Then, we can express (3.32) as

$$P_{EP1}(s_1|s_2 \to \tilde{s}_1|s_2) = \frac{1}{\pi} \int_0^{\frac{\pi}{2}} \prod_{i=1}^{G_1} \left(1 + \frac{\lambda_{1i} |s_2|^2 \gamma}{4\sin^2\theta}\right)^{-1} d\theta \tag{3.33a}$$

$$P_{EP2}(s_1|s_2 \to s_1|\tilde{s}_2) = \frac{1}{\pi} \int_0^{\frac{\pi}{2}} \prod_{i=1}^{G_2} \left(1 + \frac{\lambda_{2i} |\tilde{s}_2 - s_2|^2 \gamma}{4\sin^2\theta}\right)^{-1} d\theta \tag{3.33b}$$

$$P_{EP3}(s_1|s_2 \to \tilde{s}_1|\tilde{s}_2) = \frac{1}{\pi} \int_0^{\frac{\pi}{2}} \prod_{i=1}^{G_3} \left(1 + \frac{\lambda_{3i}\gamma}{4\sin^2\theta}\right)^{-1} d\theta. \tag{3.33c}$$

Observe from the above derivation that the computation of $\bar{P}_{bS}$ is independent of the M_1SSK symbol s_1, as seen in (3.25), (3.26) and (3.27), where the impact of the M_1SSK symbol s_1 is imposed by the multiplication of $\boldsymbol{H}\boldsymbol{e}_{s_1}$ or $\boldsymbol{H}\boldsymbol{e}_{\tilde{s}_1}$. However, any of them represents the selection of a column from $\boldsymbol{H}$. Since all columns of $\boldsymbol{H}$ have the same statistical properties, the resultant MGFs of the different M_1SSK symbols are the same. Furthermore, according to [116], when a M_1SSK symbol is in error, the average number of erroneous bits is $b_1 M_1/[2(M_1-1)]$. By contrast, for the Gray encoded M_2APM symbols, a symbol error typically yields a single bit error. Consequently, after considering the three erroneous events, we can simplify the expression of (3.24) to

$$\begin{aligned}\bar{P}_{bS} \leq & \frac{M_1 b_1}{2M_2 b} \sum_{m_2=0}^{M_2-1} P_{EP1}(s_1|s_2^{(m_2)} \to \tilde{s}_1|s_2^{(m_2)}) \\ & + \frac{1}{M_2 b} \sum_{m_2=0}^{M_2-1} \sum_{\tilde{m}_2 \neq m_2}^{M_2-1} D\left(\boldsymbol{b}_2^{(m_2)}, \tilde{\boldsymbol{b}}_2^{(\tilde{m}_2)}\right) P_{EP2}(s_1|s_2^{(m_2)} \to s_1|\tilde{s}_2^{(\tilde{m}_2)}) \\ & + \frac{1}{M_2 b} \sum_{m_2=0}^{M_2-1} \sum_{\tilde{m}_2 \neq m_2}^{M_2-1} \left[\frac{b_1 M_1}{2} + (M_1-1) D\left(\boldsymbol{b}_2^{(m_2)}, \tilde{\boldsymbol{b}}_2^{(\tilde{m}_2)}\right)\right] \\ & \times P_{EP3}\left(s_1^{(m_1)}|s_2^{(m_2)} \to \tilde{s}_1^{(\tilde{m}_1)}|\tilde{s}_2^{(\tilde{m}_2)}\right), \end{aligned} \tag{3.34}$$

where $P_{EP1}(\cdot)$, $P_{EP2}(\cdot)$ and $P_{EP3}(\cdot)$ are given by (3.33a), (3.33b), and (3.33c), respectively. Note that in (3.34), the factor $M_1 b_1/2M_2 b$ in the first term at the right-hand side is obtained by letting, $\sum_{m_1=0}^{M_1-1} = M_1$, $\sum_{\tilde{m}_1=0}^{M_1-1} = M_1$, in (3.24), due to the above-mentioned fact that $\bar{P}_{bS}$ is independent of the M_1SSK symbol and owing to applying the average BER of $b_1 M_1/[2(M_1-1)]$ imposed by a M_1SSK symbol error after exploiting the approximation of $M_1 - 1 \approx M_1$. The factor of $1/M_2 b$ in the second term of (3.34) is obtained according to the condition of $s_1 = \tilde{s}_1$ and hence we have $\sum_{m_1=0}^{M_1-1} \sum_{\tilde{m}_1=0}^{M_1-1} = M_1$. Finally, as for the third term in (3.24), firstly, we have $\sum_{m_1=0}^{M_1-1} = M_1$ and $\sum_{\tilde{m}_1=0}^{M_1-1} = M_1$ because $s_1 \neq \tilde{s}_1$. Secondly, because both the M_1SSK and M_2QAM symbols are in error, the average number of erroneous bits per symbol is $\frac{b_1 M_1}{2(M_1-1)} + D\left(\boldsymbol{b}_2^{(m_2)}, \tilde{\boldsymbol{b}}_2^{(\tilde{m}_2)}\right)$. Upon substituting these results into the third term of (3.24), we arrive at the third term at the right-hand side of (3.34).

3.4.2 Discussions

From (3.32a) - (3.33c) we realize that given d_x and the fading environment, the eigenvalues in (3.33a) - (3.33c) are different when different sparse codes are used. Hence this results in different ABER performance. In order to minimize the ABER, it is required

to design sparse codes that maximize

$$J_1 = \prod_{i=1}^{G_1} \left(1 + \frac{\lambda_{1i} |s_2|^2 \gamma}{4 \sin^2 \theta}\right) \tag{3.35a}$$

$$J_2 = \prod_{i=1}^{G_2} \left(1 + \frac{\lambda_{2i} |\tilde{s}_2 - s_2|^2 \gamma}{4 \sin^2 \theta}\right) \tag{3.35b}$$

$$J_3 = \prod_{i=1}^{G_3} \left(1 + \frac{\lambda_{3i} \gamma}{4 \sin^2 \theta}\right). \tag{3.35c}$$

Therefore, the specific structure of sparse codes impacts the achievable performance of SM/MC-SCDMA systems.

When there is single user or when the number of users is small, which results in a factor graph that is not well connected, the d_x nonzero elements of a user should be distributed as evenly as possible. This allows the d_x subcarriers activated by a user to be evenly distributed, and hence the detector beneficially attains frequency diversity in frequency-selective fading channels. We infer from the above formulas that evenly distributed sparse codes results in higher values for J_1, J_2 or/and J_3 in (3.35).

When the system supports a relatively high number of users, the corresponding factor graph is usually well connected. In this case, the MPAD is capable of gleaning multiuser diversity from the information exchange between users. However, as our experiments in Section 3.5 show, when the fading channel's frequency-selectivity is relatively low, for example $L = 2, 3, 4$, the specific structure of sparse codes may still have a significant impact both on the values of J_1, J_2 or/and J_3, as well as on the achievable BER performance of SM/MC-SCDMA systems.

Below we provide our simulation results along with the single-user BER bound for characterizing the achievable BER performance of SM/MC-SCDMA systems.

3.5 Performance Results

In this section, the BER performance of SM/MC-SCDMA systems is characterized as a function of the number of TA/RAs and the number of resolvable paths, as well as that of the modulation levels and system scale. The SM/MC-SCDMA systems having different user loads of up to $K/N = 2$ are considered. Note that in our performance studies, the M_2APMs employed are M_2QAMs. For convenience, the parameters used for generating the results for the individual figures are detailed in the figures.

In Fig. 3.5, we consider a single-user SM/MC-SCDMA system having $N = 12$ subcarriers, 4SSK and QPSK modulation to investigate the impact of the channel's frequency-selectivity on the BER performance, where the user is randomly occupied $d_x = 2$ of the

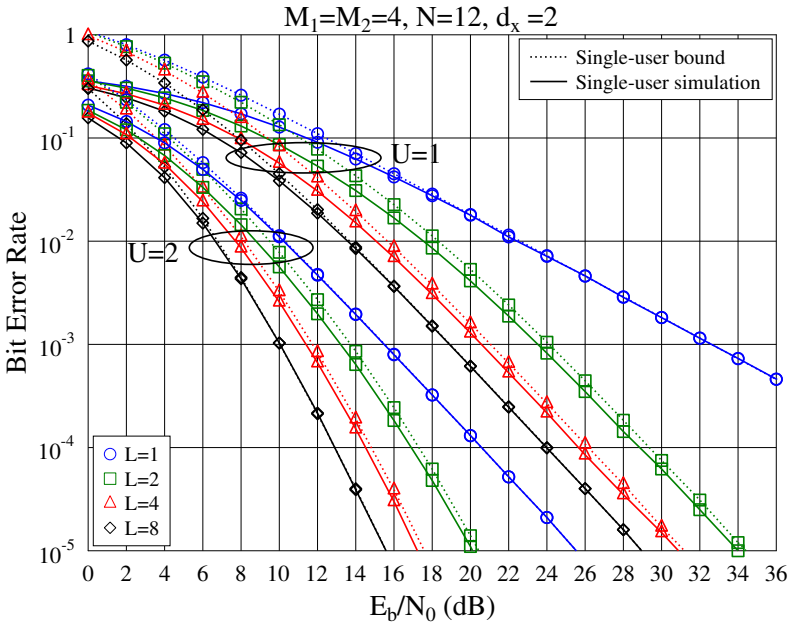

FIGURE 3.5: Single-user BER bound of (3.34) for SM/MC-SCDMA systems with $N = 12$ subcarriers communicating over frequency-selective Rayleigh fading channels having different number of paths.

12 subcarriers. Both simulation results and the single-user BER bounds are evaluated based on the expressions derived in Section 3.4. Explicitly, the analytical BER bounds converge to the simulated BER, as the SNR increases. More specifically, for $L = 1$, the BER bound is nearly the same as the simulated BER, provided that the SNR per bit obeys $\gamma_0 > 15$ dB, when $U = 1$, and $\gamma_0 > 8$ dB, when $U = 2$. For $L > 1$, we can observe that the BER bound approaches the simulated BER, as L increases from 2 to 3 and to 4. In general, the BER bound is tight, provided that the SNR is sufficiently high, resulting in a BER below 0.01. As shown in Fig. 3.5, the SM/MC-SCDMA system is capable of achieving both frequency diversity and space diversity, since the BER performance improves, as L or U increases.

Fig. 3.6 demonstrates the impact of the number of subcarriers occupied by a user on the frequency diversity gain achieved by the SM/MC-SCDMA systems communicating over frequency-selective Rayleigh fading channels. For this investigation, we assume random sparse spreading sequences and set $U = 1$, $K = 1$ as well as $d_x = 4$ and 16, respectively. Explicitly, in the case of $d_x = N = 16$, SM/MC-SCDMA achieves full frequency-diversity, and its performance is hence always better than that of the corresponding SM/MC-SCDMA associated with $d_x = 4$, provided that $L > 1$. We should note that for the case of $d_x = 4$, the achievable frequency-diversity gain is limited by both the values of L and d_x. Hence, as shown in Fig. 3.6, when L is relatively large, such as $L = 4$, 8, the loss of diversity gain due to the use of the sparse sequence of $d_x = 4$ is significant in comparison to the case of $d_x = 16$, which achieves full frequency diversity.

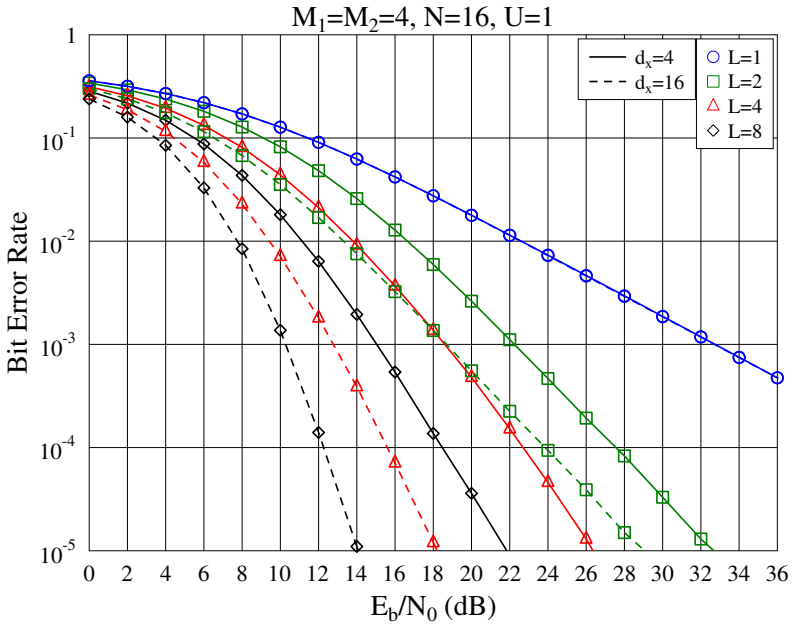

FIGURE 3.6: Single-user BER performance of SM/MC-SCDMA systems, when a user occupies $d_x = 4$ or all 16 subcarriers.

The above observation is augmented in Fig. 3.7, where we fix $L = 8$ and $U = 1$ or 2, but vary the value of d_x in a single-user SM/MC-SCDMA system communicating over frequency-selective Rayleigh fading channels. As expected, for a given value of U, the BER performance improves as d_x increases, and exhibits a converging trend for $d_x \geq 6$. Therefore, from the results shown in Figs. 3.6 and 3.7 we infer that in the SM/MC-SCDMA supporting single-user (or a low number of users), the employment of sparse sequences strikes a trade-off with the achievable frequency-diversity. Below we will illustrate that the structure of sparse sequences also has an impact on the BER performance of SM/MC-SCDMA systems.

In Fig. 3.8, we demonstrate the effect of the sparse codes having different structures on the achievable BER performance. Specifically, we compare two classes of sparse codes, namely the co-located and iteratively distributed sparse codes. Given the parameters of $N = K = 16$, $d_x = 2$, and that two adjacent users share a single nonzero element, the nonzero elements in these classes of sparse codes are designed to be allocated as follows. For the co-located sparse codes, the $d_x = 2$ nonzero elements of user k, $k = 0, 1, \ldots, 15$, are at the positions of $(k + l) \mod N$ for $l = 0, 1$. For the iteratively distributed sparse codes, the $d_x = 2$ nonzero elements of user $k = 0, 1, \ldots, 7$, are at the positions of $(k + 8l) \mod 16$ for $l = 0, 1$, while the $d_x = 2$ nonzero elements of user $k = 8, 9, \ldots, 15$, are at the positions of $(k + 9l) \mod 16$ for $l = 0, 1$. Observe from Fig. 3.8 that while the co-located sparse codes allow us to obtain multiuser diversity gain via information exchange between different users, the frequency diversity gain achieved by employing iteratively distributed sparse codes is significant for a relatively small value of L, such as $L = 2,\ 4$.

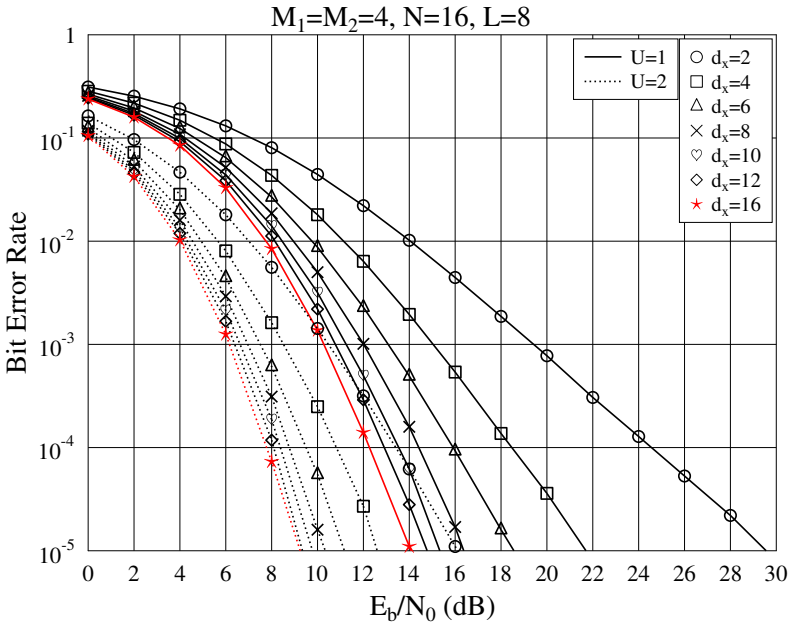

FIGURE 3.7: Single-user BER performance of SM/MC-SCDMA systems, when a user occupies different number of subcarriers (d_x) for information transmission.

Specifically for $L = 2$ and at the BER of 10^{-3}, instead of the co-located sparse codes, employing the iteratively distributed sparse codes is capable of attaining an extra of 5.5 dB diversity gain. However, when the channel is highly frequency-selective, resulting in say $L = 8$, the extra diversity gain provided by the iteratively distributed sparse codes is insignificant compared to that obtained by the co-located sparse codes.

In Fig. 3.9 the BER performance of the SM/MC-SCDMA systems supporting multiple users at a loading factor of $K/N = 1.5$ is investigated for several values of L. Note that in Fig. 3.9 and in the ensuing figures, the single-user bound evaluated from (3.34) is also plotted. First, we can explicitly observe the benefits of diversity gain, as demonstrated by the improved BER performance upon increasing L. Second, due to the multiuser interference (MUI), the BER performance observed in the low SNR region degrades against the single-user BER bound. However, when the SNR is sufficiently high to reduce the BER below 10^{-3} or 10^{-4}, the MPAD allows the highly loaded SM/MC-SCDMA systems to achieve a BER performance near the single-user BER bound.

By fixing $U = 1$, $d_x = 2$, $L = 4$ and $N = 16$, Fig. 3.10 depicts the BER of SM/MC-SCDMA systems supporting different number of users, with the loading factor up to $K/N = 2$. Here the co-located sparse codes are employed. In addition to the 16 codes used in Fig. 3.8, an extra 16 codes having non-zero positions at $(k + l) \mod N$ for $l = 0, 2$ are used, in order to support $K = 32$ users. From the results we infer the following observation. First, the existence of multiple users has twin-fold effect. On the one hand, it generates MUI as in any nonorthogonal multiuser systems. On the other hand, it attains a beneficial diversity gain, namely, multiuser diversity. In more

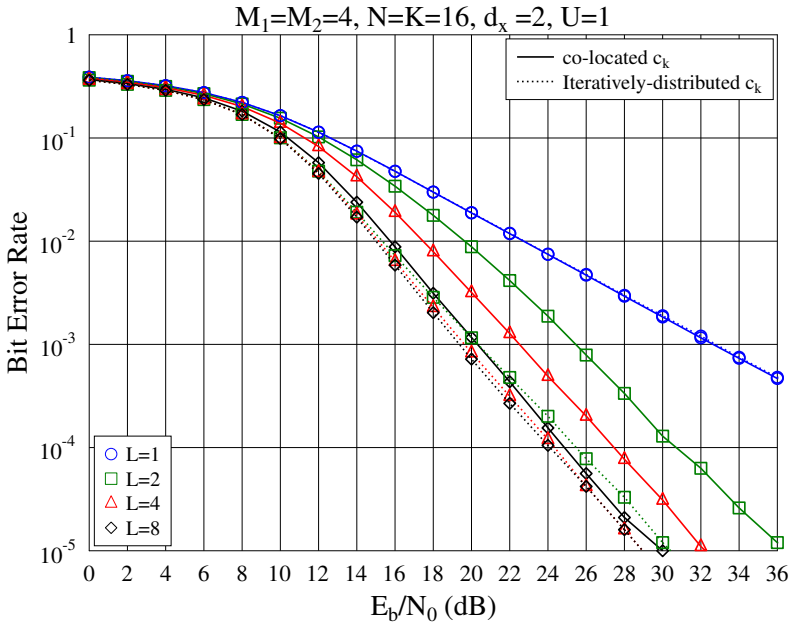

FIGURE 3.8: Performance comparison of SM/MC-SCDMA systems, when the non-zero elements of users are co-located or iteratively distributed.

detail, when the system only supports a single user, the maximum diversity order that can be achieved by the system is fixed to $d_x = 2$, since only $d_x = 2$ subcarriers are activated and hence the information used for detecting the user can only come from the two active subcarriers. By contrast, when there are multiple users, then more than two subcarriers are active. In this case, a higher diversity order can be exploited for detecting a user by the MPA algorithm via the resultant beneficial information exchange between the different subcarriers. Consequently, as seen in Fig. 3.10, the BER performance first improves, as the number of users increases from 1 to 4. However, as the number of users further increases, the MUI starts dominating the achievable performance, hence resulting in the degradation of the BER performance. Second, the results seen in Fig. 3.10 imply that the MPAD is near-optimum, and even with the loading factor of 2, there is no error-floor in the SNR range of interest. The performance of the SM/MC-SCDMA system is only about 5 dB worse than the best possible performance, which is achieved for $K = 4$ users.

Fig. 3.11 quantifies the effect of the number of modulation levels for M_1SSK and M_2QAM on the BER performance of SM/MC-SCDMA systems employing regular sparse sequences and $d_x = 2, d_c = 3$. First, as shown in Fig. 3.11 for M_2QAM modulation, while a higher QAM order achieves a higher bandwidth-efficiency, this is attained at the cost of a degraded BER performance [119]. However, the SM/MC-SCDMA system having the parameters of $M_1 = 16$, $M_2 = 2$ and $U = 1$ is outperformed by the system having the parameters of $M_1 = 4$, $M_2 = 2$ and $U = 1$.

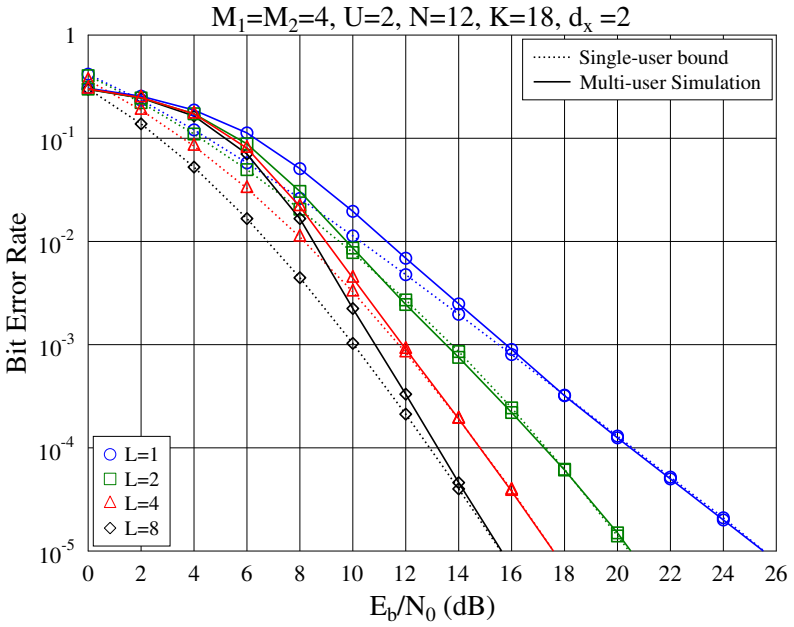

FIGURE 3.9: BER performance of SM/MC-SCDMA systems employing $N = 12$ subcarriers to support $K = 18$ users.

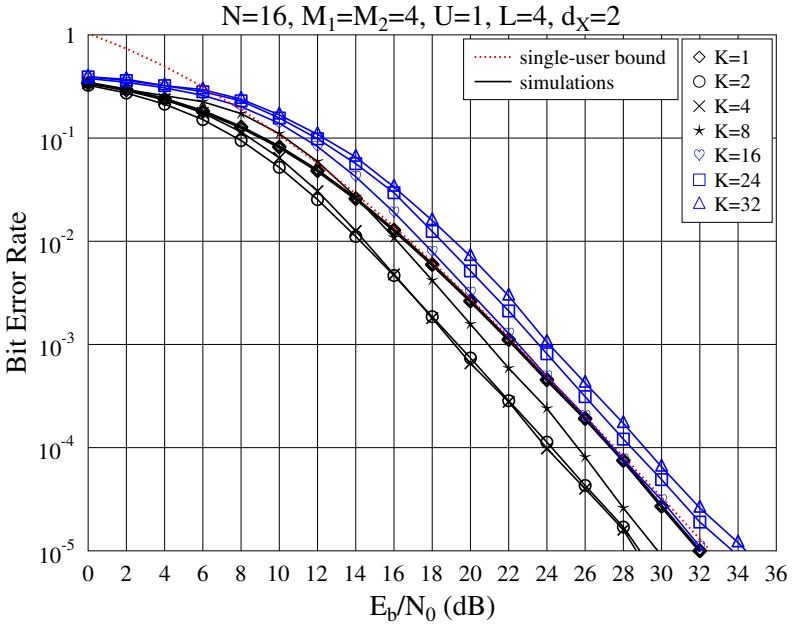

FIGURE 3.10: BER performance of SM/MC-SCDMA system employing $N = 16$ subcarriers to support different number of users.

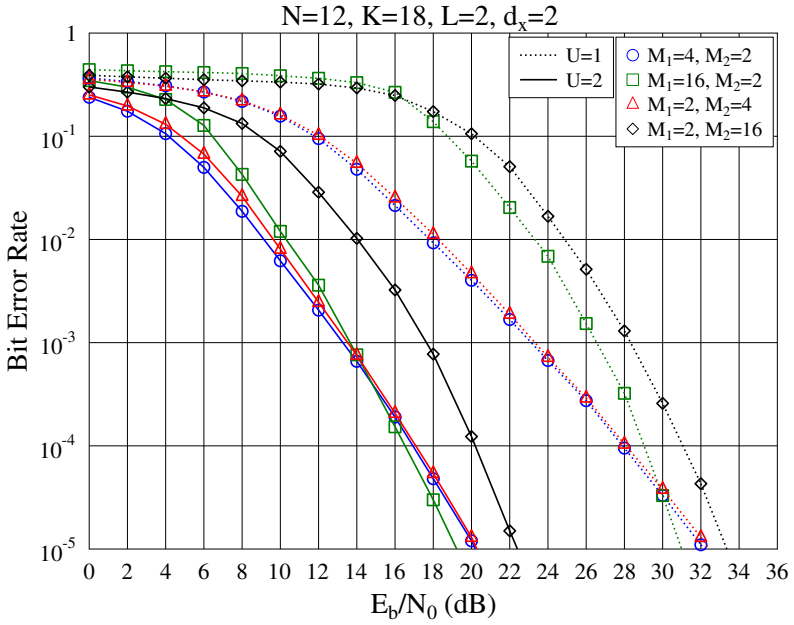

FIGURE 3.11: BER performance of SM/MC-SCDMA systems employing $N = 12$ subcarriers to support $K = 18$ users, i.e., with a loading factor of 1.5.

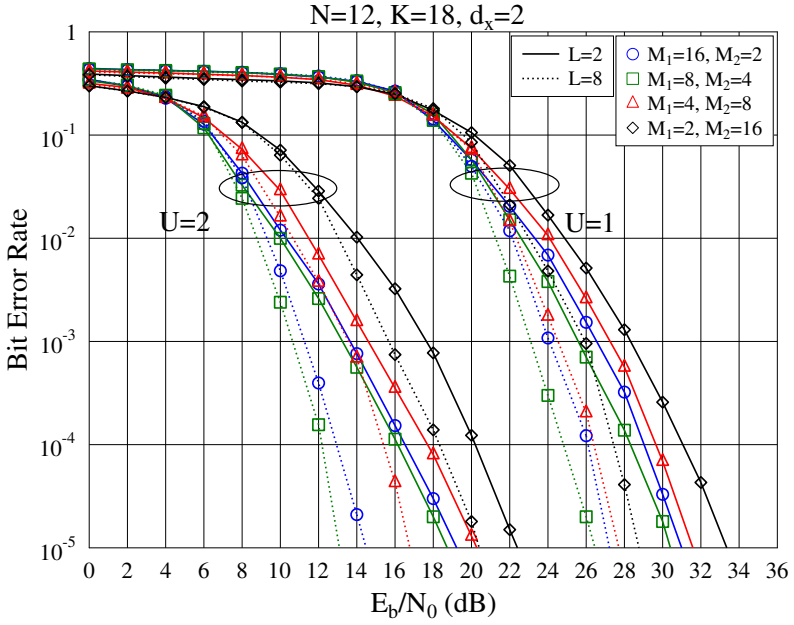

FIGURE 3.12: BER performance of the SM/MC-SCDMA systems with a loading factor of 1.5, when given $b = b_1 + b_2 = 5$ BPS but using different modulation levels.

In Fig. 3.11, we have demonstrated that the SSK and APM schemes exhibit different characteristics in terms of energy- and bandwidth-efficiency, as well as BER performance. Therefore, in Fig. 3.12 we further investigate the effect of bit allocation between the two modulation schemes on the system's error performance, under the constraint that the total number of BPS is given by $b = b_1 + b_2 = 5$. The other settings for Fig. 3.12 are the same as those for Fig. 3.11. The results in Fig. 3.12 show that for all the cases defined by $U = 1, 2$ and $L = 2, 8$, the combination of 8SSK with 4QAM achieves the best BER among the four combinations considered. This observation implies that given the total number of BPS, there exists an optimum bit sharing between SSK and APM that could result in the best BER.

Note that, the results of Figs. 3.5, 3.11, and 3.12 also demonstrate that employing more RAs improves the system's BER, owing to the increase of space diversity.

In Fig. 3.13, we now compare our SM/MC-SCDMA system to several other systems, including the SM/MC-SCMA system, which is the generalization of our SM/MC-SCDMA arrangement, the MC-SCDMA system operating without spatial modulation, and an extended version of the MC-SCMA system [135]. Note that, when SCMA [135] is considered, the modulation, constellation shaping and spreading are intrinsically amalgamated for generating a codebook. In this way, user data are no longer carried purely by the classic APM symbols but by the specifically designed multi-dimensional codewords. In Fig. 3.13 we assume that the system employs $N = 12$ subcarriers for supporting $K = 18$ users and transmits at a rate of $b = b_1 + b_2 = 4$ BPS per user. The SCMA codebook follows the design of [135], and the corresponding variable of $M_2 = 16$ represents the per user codebook size. As seen in Fig. 3.13, the spatial modulated schemes, namely the SM/MC-SCDMA and SM/MC-SCMA, achieve a better BER performance than the other two schemes operating without spatial modulation. Additionally, the SCMA-based scheme is capable of achieving about 1.5 dB gain over its corresponding SCDMA counterpart, which facilitates fair comparison with the SCMA and SCDMA schemes of [13]. Furthermore, for MPAD, the detection complexity of both SCDMA and of the corresponding SCMA is the same, since in both systems, factor graphs used by the MPA are the same. However, we should note that the transmitter of a SCMA system has higher complexity than that of the corresponding SCDMA system, where the extra complexity imposed by the codeword design, code allocation and storage. By contrast, in SCDMA systems, every user is only assigned a single code for spreading. Additionally, it it worth mentioning that the comparison of spatial modulated systems to conventional MIMO schemes was carried out in [19, 20, 28], demonstrating that a conventional MIMO scheme is capable of achieving a better BER performance than the corresponding spatial modulated scheme, but typically imposes a higher detection complexity, requires more RF chains, strict inter-antenna synchronization, etc.

Finally, in Fig. 3.14 we depict the BER of the SM/MC-SCDMA systems at different scales at a fixed loading factor of 2, when communicating over frequency-selective fading

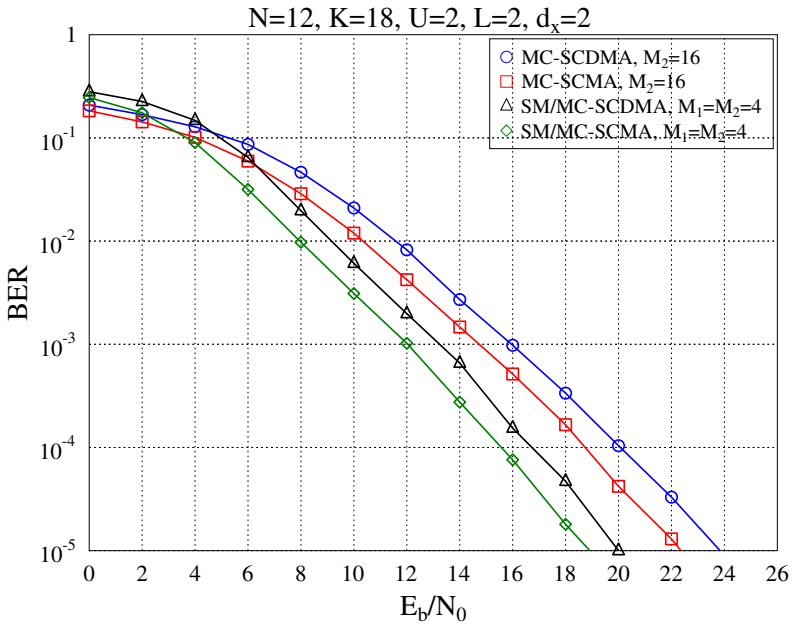

FIGURE 3.13: Comparison of BER performance of the SM/MC-SCDMA, MC-SCDMA, SM/MC-SCMA and MC-SCMA systems with a system load of 150%.

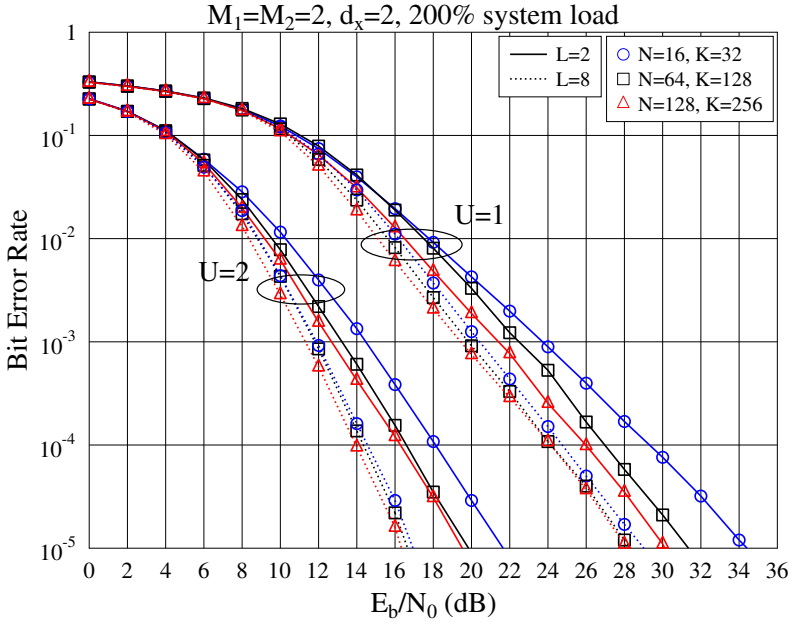

FIGURE 3.14: Comparison of BER performance of the SM/MC-SCDMA systems employing different number of subcarriers to support a fixed system load of 200%.

channels, and assuming 2SSK/BPSK modulation. Firstly, the results show that the BER improves for $U = 1$ and slightly also for $U = 2$, as the SM/MC-SCDMA system dimension becomes larger. This observation follows the MIMO principles [136]: the capacity of MIMO channels increases at least linearly upon increasing the minimum of the number of TA, and RAs. As shown in Fig. 3.14, when comparing the scenario of $L = 2,\ N = 128,\ K = 256$ to that of $L = 2,\ N = 16,\ K = 32$, where both cases attain the same bandwidth efficiency of 4 bits per subcarrier per symbol. However, the former scenario requires a 5 dB lower SNR at the BER of 10^{-4}. By contrast, when comparing the scenario of $L = 8,\ N = 128,\ K = 256$ to that of $L = 8,\ N = 16,\ K = 32$, the former scheme has a 1 dB SNR gain. Hence, although a more dispersive frequency-selective channel results in a lower SNR gain of 1dB, in general, the SM/MC-SCDMA system supported by the MPA detection becomes more efficient, as the system becomes larger. Secondly, benefiting from spreading and of MPA, a frequency diversity gain can be achieved, yielding a BER improvement, as the channel becomes more frequency-selective. Additionally, as also demonstrated in the previous figures, using more RAs improves the space diversity gain, hence resulting in significant performance improvement when increasing the number of RAs from $U = 1$ to $U = 2$.

3.6 Chapter Summary and Conclusions

In this chapter, a SM/MC-SCDMA scheme has been proposed with the motivation of exploiting the frequency diversity in the context of next-generation wireless systems supporting massive connectivity. In the proposed SM/MC-SCDMA, the spatially modulated bits activate a fraction of TAs to transmit the APM modulated bits, which are transmitted after sparse spreading in the frequency-domain over frequency-selective Rayleigh fading channels with the aid of MC signaling. A single-user BER bound has been derived based on the MGF, which is used for investigating the effect of the codes' sparsity on the BER performance. In terms of the detection, MPAD has been introduced for supporting low-complexity detection, while achieving near-MLD performance. Our results also demonstrate that in addition to frequency diversity, the proposed SM/MC-SCDMA system attains space diversity by employing RAs. We also observed that there exists an optimal bit-sharing between the SSK and APM modulations. We demonstrated that the BER performance only slightly degrades at a user load of 200%, and the system performs best, when its dimension is large. The main conclusions of this chapter are summarized in Table 3.1.

In summary, our SM/MC-SCDMA scheme has the following merits. With the aid of SM, MC signalling and low-complexity MPAD, our SM/MC-SCDMA scheme has a compellingly low complexity, as shown in Table 3.1. As a benefit of SM, the transmitter of SM/MC-SCDMA can relax the inter-antenna synchronization specifications. Employing

TABLE 3.1: Main conclusions of Chapter 3.

System	SM/MC-SCDMA system		
Example	$M_1 = M_2 = 4$, $U = 1$, $N = 16$, $L = 4$		
SNR at a BER of 10^{-3}	$K = 16$	$K = 24$	$K = 32$
	22.5 dB	23.5 dB	24.1 dB
Complexity order	MLD	MAP	MPA
	$\mathcal{O}(M^K)$	$\mathcal{O}(M^{\lvert\mathcal{K}_l\rvert})$	$\mathcal{O}(M^{d_x(d_c-1)})$

sparse spreading beneficially mitigates the PAPR problem of MC signalling at the transmitter, while enjoying the benefit of low-complexity MPAD at the receiver. With the advent of MC signalling and multiple RAs, the performance of SM/MC-SCDMA systems benefits from both space- and frequency-diversity. Lastly, the introduction of the low-complexity MPAD allows SM/MC-SCDMA systems to achieve near-MLD performance, even when the systems are heavily loaded, operating at loading factors as high as two or even higher. Owing to these merits, SM/MC-SCDMA constitutes a promising MA scheme for ultra-dense device-centric wireless systems requiring massive connectivity.

Furthermore, in this chapter we have compared the BER performance of our SM/MC-SCDMA and its generalized counterpart SM/MC-SCMA, showing that an extra shaping gain is attained by the latter.

However, both Chapters 2 and 3 are based on the assumption that all the users in the system are active simultaneously in each symbol duration, which is highly unlikely in the practical mMTC scenarios, where the users become active in a sporadic pattern. Hence, investigating the joint user activity and data detection will be our next research target, which will be discussed in more detail in the next chapter.

Chapter 4

Joint User-Activity and Data Detection for Grant-Free Spatial-Modulated Multi-Carrier Non-Orthogonal Multiple Access

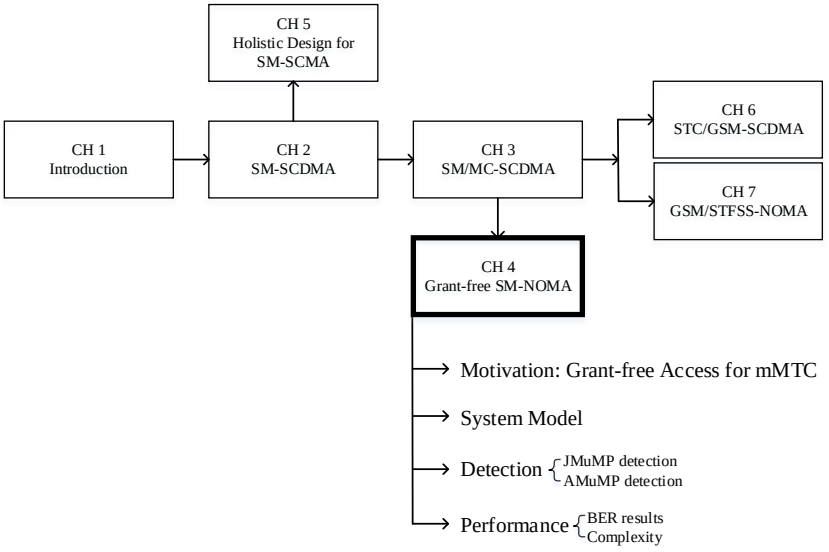

FIGURE 4.1: The relationship of Chapter 4 with the rest of the thesis.

4.1 Introduction

Both Chapters 2 and 3, as well as the contributions summarized in Table 1.3 have comprehensively investigated the family of SM-NOMA schemes. However, in practical massive Machine-Type Communication (mMTC) scenarios, the uplink tele-traffic is usually sporadic, where a 'massive' number of devices - potentially on the order of say a million or so - may connect to the base station (BS) [1,3,137], but each of them tends to transmit its signals to the BS at a low activity rate and at a low data rate [85].

Another challenge encountered in the mMTC scenario is the requirement of low latency, completed with their sporadic transmission pattern. The classic grant-based legacy access schemes require extra resources, such as time-slots for requesting access grant, which imposes extra latency. This is clearly undesirable for mMTC. Hence, grant-free access schemes are more promising in terms of satisfying the stringent low-latency requirements, whilst simultaneously supporting sporadic uplink transmissions without imposing any overhead. However, when incorporating grant-free transmissions, the receiver has to promptly detect both the user activity and the transmitted data.

In most mMTC scenarios, only a very small fraction of user devices is active at a time. This sparse activity of the grant-free NOMA systems inspired the application of compressive sensing (CS) algorithms [86], leading to the design of a range of low-complexity multi-user detectors [88–90, 92–94], which have been summarized in Table 1.4. In these CS-based detectors, the orthogonal matching pursuit (OMP) [95], subspace pursuit (SP) [96] and compressive sampling matching pursuit (CoSaMP) [97] have been adopted.

The benefit of SM-NOMA may be further enhanced in mMTC scenarios, where data are transmitted at a relatively low rate. However, the majority of SM-NOMA systems proposed in the literature are based on the simplifying assumption that all users are always active, which is highly unlikely in practical mMTC scenarios. Although the SM-NOMA schemes proposed in [91] astutely solved the user activity detection problem, they made the idealized simplifying assumption that the receiver has perfect knowledge of the number of active users, which prevents their application in the face of the realistic uncertainty encountered in grant-free mMTC scenarios. Additionally, in [91], flat-fading uplink transmission was assumed, whilst realistic mMTC systems experience correlated frequency-selective fading.

Against this background, our inspiration is to conceive powerful SM/MC-NOMA schemes for the realistic grant-free access scenarios of next generation systems by dispensing with the idealized simplifying assumptions routinely exploited at the current state-of-the-art. Crisply and explicitly, the main contributions of this chapter are contrasted to the literature in Table 4.1 and are summarized as follows.

TABLE 4.1: Overview of existing literature on the grant-free NOMA system.

Contributions	**This work**	[13]	[14]	[15]	[16]	[17]
Integrated with property of SM	✓					
Unknown number of active users	✓				✓	
Perfect channel state information (CSI)	✓	✓	✓	✓		✓
Imperfect CSI					✓	
Frequency-selective fading channels	✓					
Fixed number of users identified in each iteration	✓	✓	✓	✓	✓	✓
Adaptive number of users identified in each iteration	✓					
More accurate symbol mapping	✓					
Multiple TAs available at the transmitter	✓					
Multi-carrier (MC) transmission	✓			✓		✓

- We propose an uplink SM/MC-NOMA scheme for supporting large-scale grant-free multiple access for next-generation wireless communications. The proposed SM/MC-NOMA scheme gleans diversity gains from the often independently-fading frequency- and spatial-domains. SM is employed for reducing the number of R-F chains, while nonorthogonal FD spreading attains FD diversity gains for MC transmission over frequency-selective fading channels. In contrast to the existing research on SM-NOMA uplink transmissions, which assumes that all users are active all the time and transmit their data to the BS, we assume grant-free uplink transmission, where each user only becomes active at a small activation probability.

- In order to identify the active users and detect their transmitted data, an iterative Joint Multiuser Matching Pursuit (JMuMP) detector is proposed based on the SP algorithm of [96], which exploits the sparsity existing in both the user activity and in the SM antenna domain. In contrast to the original SP detector of [96], which recovers the user signals by exploiting the known activity at the receiver, the number of active users is estimated by our JMuMP detector before the detection of data conveyed by the space-shift keying (SSK) and the classic APM symbols, with the SSK data detection being intrinsically integrated into the active user identification process. Furthermore, a beneficial symbol mapping approach is proposed and integrated into our JMuMP detector.

- We also conceive an Adaptive MuMP (AMuMP) detector, which does not require the *a priori* knowledge of the user activity at the receiver, and yet further improves the bit error rate (BER) performance of the SM/MC-NOMA system employing the JMuMP detector. Naturally, this is achieved at the cost of a higher detection complexity and latency. In the proposed AMuMP detector, both the active users as well as their data are iteratively detected, until both the active users and their data are deemed to be reliably detected. This is more realistic, but also more challenging than the JMuMP philosophy of assuming that the number of users identified in each iteration remains unchanged. We demonstrate that the AMuMP scheme provides more reliable detection than the JMuMP detector, even when the user activation probability is as high as $p = 0.3$.

- The BER vs complexity trade-off of our SM/MC-NOMA system employing the JMuMP and AMuMP detectors is demonstrated by simulation results.

The rest of this chapter is structured as follows. Section 4.2 describes the system model of the proposed SM/MC-NOMA scheme, whereas Section 4.3 overviews the CS-based multiuser detectors. Following this, the proposed JMuMP and AMuMP detection algorithms are detailed in Sections 4.4 and 4.5, respectively. Then Section 4.6 characterizes the system performance in terms of its BER and computational complexity. Finally, Section VI provides our main conclusions and future research ideas.

Notations: In this chapter, the calligraphic letters $\mathcal{X}$ represent sets. The uppercase and lowercase boldface letters, $\boldsymbol{X}$ and $\boldsymbol{x}$, denote matrices and vectors, respectively. The calligraphic subscripts of the boldface letters $\boldsymbol{X}_{\mathcal{X}}$ and $\boldsymbol{x}_{\mathcal{X}}$ denote the column entries of $\boldsymbol{X}$ in the set $\mathcal{X}$, and the elements of $\boldsymbol{x}$ with indices in the set $\mathcal{X}$, respectively. Additionally, $(\cdot)^{-1}$, $(\cdot)^{T}$, and $(\cdot)^{H}$ represent matrix inversion, transpose, and Hermitian transpose operations, respectively. Furthermore, the ℓ_n-norm operation is expressed as $\|\cdot\|_n$.

4.2 System Model

In this section, we detail our uplink SM/MC-NOMA system supporting K potential users, each with an activation probability of p ($p \ll 1$). We assume that the channels of the active users experience frequency selective fading having L resolvable paths in the time domain (TD). Below we detail the transmitter and receiver models in Section 4.2.1, and 4.2.2, respectively, along with the assumptions used in our investigations.

4.2.1 Transmitter Model

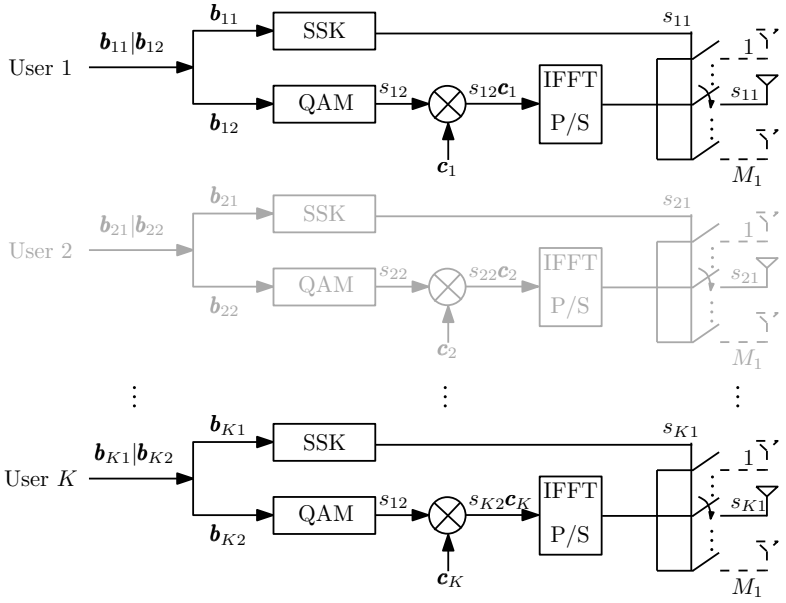

FIGURE 4.2: The transmitter schematic of our SM/MC-NOMA system, where the light-shaded diagrams represent the inactive users while the dark-shaded diagrams represent the active users.

We consider the single-cell uplink MC system of Fig. 4.2, under the following assumptions. Firstly, the system supports K potential users to communicate with a BS, and each user has a small and independent activation probability p ($p \ll 1$), yielding $K_a \ll K$ active users at a given time. Secondly, we assume that each of the K users employs M_1 TAs, which have the indices of $\{1, \cdots, M_1\}$. By contrast, the BS has U receive antennas (RAs). When the k-th user becomes active, it transmits b-bit information symbols,

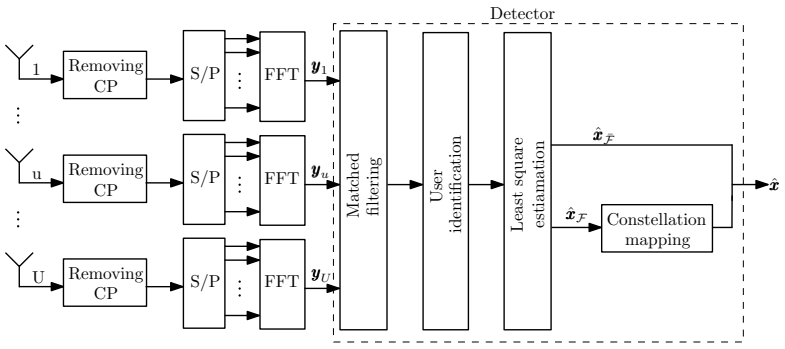

FIGURE 4.3: The receiver schematic of our grant-free SM/MC-NOMA system.

using M_1-ary SSK and M_2-ary quadrature amplitude modulation (QAM), which is the most well-known modulation scheme of the APM family. Specifically, the first b_1 bits are conveyed by M_1SSK relying on a 'spatial constellation' of $\mathcal{S}_1 = \{1, \cdots, M_1\}$, whereas the remaining $b_2 = (b - b_1)$ bits are conveyed by M_2QAM [20]. In other words, the M_1-ary symbol $s_{k1} \in \mathcal{S}_1$ activates the s_{k1}-th TA to transmit the M_2-ary QAM symbol $s_{k2} \in \mathcal{S}_2$, where $\mathcal{S}_2 = \{a_1, a_2, \cdots, a_{M_2}\}$ represents the M_2QAM constellation set, after sparse spreading, as shown in Fig. 4.2. We assume random spreading code pre-assigned to user k in the form of $\boldsymbol{c}_k = [c_{k1}, c_{k2}, ..., c_{kN}]^T$, where N is the number of subcarriers. Note that if we replace the random spreading code by the sparse spreading code, where most elements in $\boldsymbol{c}_k$ are zeros, we have a LDS-based code division multiple access (LDS-CDMA) [10].

Let us denote the transmitted symbol of user k by x_k, which is selected from the set of $\mathcal{S} = \mathcal{S}_1 \otimes \mathcal{S}_2 \cup 0$, where $\otimes$ denotes the Kronecker product [29] so that $\mathcal{S}$ is a set consisting of all the $M = M_1 M_2$ different combinations of the elements in $\mathcal{S}_1$ and those in $\mathcal{S}_2$, as well as a symbol 0, which is added to indicate inactive users. Following the transmit signal processing operations, which include the inverse fast Fourier transform (IFFT), parallel-to-serial (P/S) conversion, and cyclic prefix (CP) attachment, the signal of an active user k is transmitted from the s_{k1}-th TA, activated by the M_1SSK symbol s_{k1}.

4.2.2 Receiver Model

Let us express the channel impulse response (CIR) $\boldsymbol{h}_{s_{k1}}^{(u)}$ between the s_{k1}-th TA of the k-th active user and the u-th RA at the BS as

$$\begin{aligned} \boldsymbol{h}_{s_{k1}}^{(u)} =& [h_{s_{k1},0}^{(u)}, h_{s_{k1},1}^{(u)}, \cdots, h_{s_{k1},L-1}^{(u)}]^T, \\ & s_{k1} = 1, 2, \ldots, M_1; u = 1, 2, \cdots, U; k = 1, 2, \cdots, K, \end{aligned} \tag{4.1}$$

where $\boldsymbol{h}_{s_{k1}}^{(u)}$ are independent identically distributed (iid) complex Gaussian random variables with zero mean and a variance of $0.5/L$ per dimension. The schematic diagram of the receiver is shown in Fig. 4.3. According to the classic MC reception [103], including

sampling, CP-removal and FFT-based demodulation, the $(N \times 1)$ received observations $\boldsymbol{y}_u$ at the u-th RA can be expressed as

$$\boldsymbol{y}_u = \sum_{k=1}^{K} \boldsymbol{C}_k \hat{\boldsymbol{h}}_{s_{k1}}^{(u)} s_{k2} + \boldsymbol{n}_u, \quad u = 1, 2, \cdots, U, \tag{4.2}$$

where $\boldsymbol{C}_k = \text{diag}\{\boldsymbol{c}_k\}$ is a $(N \times N)$ diagonal matrix and the $(N \times 1)$-dimensional FD channel transfer function (FDCHTF) $\hat{\boldsymbol{h}}_{s_{k1}}^{(u)}$ experienced by the N subcarriers can be expressed as [103]

$$\hat{\boldsymbol{h}}_{s_{k1}}^{(u)} = \boldsymbol{\mathcal{F}} \boldsymbol{\Phi}_L \boldsymbol{h}_{s_{k1}}^{(u)}, \tag{4.3}$$

where $\boldsymbol{\Phi}_L$ is a $(N \times L)$-element mapping matrix constructed by the first L columns of the $(N \times N)$ identity matrix $\boldsymbol{I}_N$, and $\boldsymbol{\mathcal{F}}$ is the $(N \times N)$ FFT matrix having the property of $\boldsymbol{\mathcal{F}}\boldsymbol{\mathcal{F}}^H = \boldsymbol{\mathcal{F}}^H\boldsymbol{\mathcal{F}} = N\boldsymbol{I}_N$. Now the channel $\hat{\boldsymbol{h}}_{s_{k1}}^{(u)}$ experiences frequency-selective Rayleigh fading, having L CIR taps in the TD. In (4.2), the noise vector $\boldsymbol{n}_u$ obeys the zero-mean complex Gaussian distribution with a covariance matrix of $2\sigma^2\boldsymbol{I}_N$, expressed as $\mathcal{CN}(0, 2\sigma^2\boldsymbol{I}_N)$, where $\sigma^2 = 1/(2\gamma)$, $\gamma = b\gamma_0$ denotes the signal-to-noise ratio (SNR) per symbol, while γ_0 is the SNR per bit.

Let $\boldsymbol{y} = [\boldsymbol{y}_1^T, \boldsymbol{y}_2^T, \cdots, \boldsymbol{y}_U^T]^T$, $\hat{\boldsymbol{h}}_{s_{k1}} = \left[\left(\hat{\boldsymbol{h}}_{s_{k1}}^{(1)}\right)^T, \left(\hat{\boldsymbol{h}}_{s_{k1}}^{(2)}\right)^T, \cdots, \left(\hat{\boldsymbol{h}}_{s_{k1}}^{(U)}\right)^T\right]^T$ and $\boldsymbol{n} = [\boldsymbol{n}_1^T, \boldsymbol{n}_2^T, \cdots, \boldsymbol{n}_U^T]^T$, which are all UN-dimensional vectors. Then, it can be shown that we have

$$\begin{aligned}
\boldsymbol{y} &= \sum_{k=1}^{K} (\boldsymbol{I}_U \otimes \boldsymbol{C}_k) \hat{\boldsymbol{h}}_{s_{k1}} s_{k2} + \boldsymbol{n} \\
&= \sum_{k=1}^{K} (\boldsymbol{I}_U \otimes \boldsymbol{C}_k) \hat{\boldsymbol{H}}_k \boldsymbol{e}_{s_{k1}} s_{k2} + \boldsymbol{n} \\
&= \sum_{k=1}^{K} \boldsymbol{H}_k \boldsymbol{x}_k + \boldsymbol{n} \\
&= \boldsymbol{H}\boldsymbol{x} + \boldsymbol{n},
\end{aligned} \tag{4.4}$$

where $\hat{\boldsymbol{H}}_k = [\hat{\boldsymbol{h}}_{1k}, \hat{\boldsymbol{h}}_{2k}, \cdots, \hat{\boldsymbol{h}}_{M_1 k}]$ is $(UN \times M_1)$-dimensional, and $\hat{\boldsymbol{h}}_{mk}$ is in the form of (4.3) with $s_{k1} = m$, $\boldsymbol{e}_{s_{k1}}$ is the s_{k1}-th column of $\boldsymbol{I}_{M_1}$, $\boldsymbol{H}_k = (\boldsymbol{I}_U \otimes \boldsymbol{C}_k)\hat{\boldsymbol{H}}_k$, $\boldsymbol{H} = [\boldsymbol{H}_1, \boldsymbol{H}_2, \cdots, \boldsymbol{H}_K]$, which is a $(UN \times M_1 K)$-dimensional matrix, $\boldsymbol{x}_k = \boldsymbol{e}_{s_{k1}} s_{k2}$, and finally, we have M_1K-length $\boldsymbol{x} = \left[\boldsymbol{x}_1^T, \boldsymbol{x}_2^T, \cdots, \boldsymbol{x}_K^T\right]^T = \left[\boldsymbol{e}_{s_{11}}^T s_{12}, \boldsymbol{e}_{s_{21}}^T s_{22}, \cdots, \boldsymbol{e}_{s_{K1}}^T s_{K2}\right]^T$.

4.3 Overview of Compressive Sensing-Based Detectors

It may be observed from (4.4) that in the received signal, $\boldsymbol{x}$ is a M_1K-length sparse vector with the non-zero elements representing the active users and $\boldsymbol{H}$ can be viewed as

a measurement matrix. Furthermore, (4.4) is a typical MIMO equation. Hence, some of the popular signal detection methods can be applied at the receiver for information recovery. Let us use $\boldsymbol{x}$, $\tilde{\boldsymbol{x}}$ and $\hat{\boldsymbol{x}}$ to represent the transmitted symbol vector, the possible candidates and the final estimated symbol vector, respectively. Then, the optimal maximum-likelihood (ML) detector finds the estimates of the transmitted symbols by visiting each legitimate solution via solving the following optimization problem:

$$\hat{\boldsymbol{x}} = \arg \min_{\tilde{\boldsymbol{x}} \in \mathcal{S}^K} \left\{ \|\boldsymbol{y} - \boldsymbol{H}\tilde{\boldsymbol{x}}\|_2^2 \right\}, \tag{4.5}$$

where S^K represents all possible combinations of the constellation $\mathcal{S}$ of K users and where $\|\cdot\|_2$ represents the ℓ_2-norm.

It is widely recognized that the ML detector achieves the lower bound of the error probability at a full-search complexity. However, as mentioned above, $\boldsymbol{x}$ is a sparse vector due to a) a low activation probability p per user, and b) the employment of SM. Therefore, CS-based signal recovery may be performed for low-complexity detection. Before we detail the corresponding CS-based detection, let us first consider the restricted isometry property (RIP) defined in [138], which determines whether the signal can or cannot be recovered with good performance by the CS-based detection. According to [138], the measurement matrix $\boldsymbol{H}$ should satisfy the RIP condition expressed as

$$(1 - \delta_{K_a}) \|\boldsymbol{x}\|_2^2 \leqslant \|\boldsymbol{H}\boldsymbol{x}\|_2^2 \leqslant (1 + \delta_{K_a}) \|\boldsymbol{x}\|_2^2, \forall \|\boldsymbol{x}\|_0 \leqslant K_a, \tag{4.6}$$

where $\|\cdot\|_0$ represents the ℓ_0-norm and the constant obeys $\delta_{K_a} \in (0, 1)$. The best-known matrices that have been proven to satisfy the RIP condition are the random matrices obeying either the Gaussian distribution, or those that are obtained from the Fourier ensemble [138]. In our system, each column of $\boldsymbol{H}$ is independent and it is obtained after applying the FFT operation to the TD CIRs, hence the RIP requirement in general can be satisfied [139].

In the domain of CS-based detection, it may be inferred from (4.4) that the original CS recovery problem of estimating $\boldsymbol{x}$ may also be formulated as [86]

$$\min \|\tilde{\boldsymbol{x}}\|_0 \quad \text{s.t.} \quad \boldsymbol{y} = \boldsymbol{H}\tilde{\boldsymbol{x}} + \boldsymbol{n}, \tag{4.7}$$

However, the ℓ_0 minimization has been shown to be non-convex and NP-hard. Hence, usually relaxation techniques are applied to make the optimization problem convex and solvable by employing low-complexity algorithms. In the literature, typically two categories of CS-based detectors have been studied, namely convex optimisation employing the ℓ_1-norm [87], and greedy algorithms adopting ℓ_2-norm optimization [95–97]. However, the ℓ_1-norm optimization still leads to high computational complexity [87]. Therefore, we focus our attention on the greedy algorithm, which iteratively identifies the support set in a greedy manner using for example the classic least square (LS) algorithm, and performs

ℓ_2-norm based optimisation. Furthermore, the greedy algorithm-assisted detector has a linearly increasing complexity as a function of the search space size, but unfortunately it is prone to avalanche-like error propagation, owing to its serial detection process.

To be more specific, in this section, we first propose our JMuMP detector for the grant-free SM/MC-NOMA system in Section 4.4.1. Explicitly, we conceive an appropriately modified SP algorithm [96], which improves the signal detection accuracy, and tailor it for SM. Then, the corresponding termination criteria will be detailed in Section 4.4.2.

4.4 Joint Multiuser Matching Pursuit Detection

4.4.1 Description of our Joint Multiuser Matching Pursuit detection

The proposed JMuMP detector is developed by appropriately tailoring the iterative SP algorithm of [96], which is capable of recovering signals having known sparsity, whilst outperforming the conventional OMP algorithm of [95].

Again, the proposed JMuMP detector relies on similar operations to those of the SP algorithm, which are evolved further into a bespoke version tailor-made for SM. As a further benefit, it does not require the knowledge of the active user indices. In other words, it accomplishes joint active user and data detection. In our JMuMP detection, the sparsity of the received signal is first estimated according to the activation probability p. In detail, the JMuMP detector operates as follows.

- ***Step 1:***

Since the receiver does not have the knowledge of the number K_a of active users, the JMuMP detector commences its action by estimating the number of active users K_e, based on the activation probability p that is known to the receiver, in order to infer the grade of sparsity inherent in the received signal. In this case, the probability ε that the number of active users is higher than K_e is given by

$$\varepsilon = 1 - \sum_{k=0}^{K_e} \binom{K}{k} p^k (1-p)^{K-k}, \tag{4.8}$$

which may be interpreted as the outage probability (OP), when the receiver assumes that there are K_e active users. Hence, if we fix ε to a sufficiently low value, such as, 10^{-5}, then the OP is negligible. Hence, we may assume that the maximum number of active users at any time does not exceed K_e, which gives a relative sparsity of at most K_e/K for the operation of the SP algorithm, as detailed below, until any termination criterion to be detailed in Section 4.4.2 is met.

Algorithm 1 JMuMP detector

Input:

Received observations $\mathbf{y}$, user activation probability p and CIR $\boldsymbol{H}$

Output:

Detected symbols $\hat{\boldsymbol{x}}$.

Initialization: $i = 1, \boldsymbol{r}^{(0)} = \boldsymbol{y}, \mathcal{F}^{(0)} = \varnothing$, outage probability ε,

Calculate K_e using (4.8) for given ε;
while $i \leq I$ **do**
  $\boldsymbol{t}^{(i)} = \boldsymbol{H}^H \boldsymbol{r}^{(i-1)}$;
  for $k = 1, 2, \cdots, K$ **do**
    $\mathcal{T}_k^{(i)} = max(|\boldsymbol{t}_k^{(i)}|, 1)$;
  end for
  $\mathcal{T}^{(i)} = \mathcal{T}_1^{(i)} \cup \mathcal{T}_2^{(i)} \cup \cdots \cup \mathcal{T}_K^{(i)}$
  $\mathcal{M}^{(i)} = max(|\boldsymbol{t}_{\mathcal{T}^{(i)}}^{(i)}|, K_e)$;
  $\mathcal{V}^{(i)} = \mathcal{M}^{(i)} \cup \mathcal{F}^{(i-1)}$;
  $\boldsymbol{x}'^{(i)}_{\mathcal{V}^{(i)}} = (\boldsymbol{H}^H_{\mathcal{V}^{(i)}} \boldsymbol{H}_{\mathcal{V}^{(i)}})^{-1} \boldsymbol{H}^H_{\mathcal{V}^{(i)}} \boldsymbol{y}$;
  $\boldsymbol{x}'^{(i)}_{\bar{\mathcal{V}}^{(i)}} = \mathbf{0}$;
  for $k = 1, 2, \cdots, K$ **do**
    $\hat{\boldsymbol{x}}_k^{(i)} = \arg\min_{\tilde{\boldsymbol{x}} \in \mathcal{S} \cup \mathbf{0}} \|\boldsymbol{x}'^{(i)}_k - \tilde{\boldsymbol{x}}\|_2^2$;
    if $\hat{\boldsymbol{x}}_k^{(i)} \neq \mathbf{0}$ **then**
      $\mathcal{B}_k^{(i)} = max(|\hat{\boldsymbol{x}}_k^{(i)}|, 1)$;
      $d^{(i)}_{\mathcal{B}_k^{(i)}} = |x'^{(i)}_{\mathcal{B}_k^{(i)}} - \hat{x}^{(i)}_{\mathcal{B}_k^{(i)}}|$;
    else
      $\mathcal{B}_k^{(i)} = \varnothing$;
    end if
  end for
  $\mathcal{B}^{(i)} = \mathcal{B}_1^{(i)} \cup \mathcal{B}_2^{(i)} \cup \cdots \cup \mathcal{B}_K^{(i)}$;
  $\mathcal{F}^{(i)} = min(\boldsymbol{d}^{(i)}_{\mathcal{B}^{(i)}}, K_e)$;
  $\boldsymbol{r}^{(i)} = \boldsymbol{y} - \boldsymbol{H}_{\mathcal{F}^{(i)}} \hat{\boldsymbol{x}}^{(i)}_{\mathcal{F}^{(i)}}$;
  if $\|\boldsymbol{r}^{(i)}\|_2^2 < \beta U N \sigma^2$ **then**
    break;
  end if
  if $\|\boldsymbol{r}^{(i)}\|_2^2 \geq \|\boldsymbol{r}^{(i-1)}\|_2^2$ **then**
    break;
  end if
  $i = i + 1$;
end while
return Detected symbol $\hat{\boldsymbol{x}}$.

- ***Step 2:***

We then proceed by determining the indices of the most-likely active users. Hence, we subject the received signal $\boldsymbol{y}$ to matched filtering (MF), at the first iteration to obtain a vector $\boldsymbol{t}^{(1)}$

$$\boldsymbol{t}^{(1)} = \boldsymbol{H}^H \boldsymbol{y} = \left(\boldsymbol{H}^H \boldsymbol{H}\right) \boldsymbol{x} + \boldsymbol{H}^H \boldsymbol{n}. \tag{4.9}$$

Notably, the signals received from the active users have a significantly higher power than all other hypothetical signals received from the inactive users, who have zero transmit power. Therefore, we can distinguish the signals received from the active users and that from the inactive users based on the power difference of the elements in $\boldsymbol{t}^{(1)}$. More specifically, if we define the absolute value of the n-th element of the vector $\boldsymbol{t}^{(1)}$ as $|t_n^{(1)}|$, then $|\boldsymbol{t}^{(1)}|$ represents the absolute values of each element in $\boldsymbol{t}^{(1)}$. A higher $|t_n^{(1)}|$ indicates a higher signal power and the corresponding user is more likely to be active.

It is now time for us to exploit that the SSK modulation restricts the distribution of the potential active signals, where among the $[(k-1)M_1+1]$-st to kM_1-th elements in $\boldsymbol{t}^{(1)}$ transmitted by user k ($k = 1, 2, \cdots, K$), at most one element contains non-zero value. Therefore, in contrast to the SP algorithm, which identifies the active users by tentatively considering all the KM_1 elements in $\boldsymbol{t}^{(1)}$, we instead identify the highest receive signal value in $|\boldsymbol{t}_k^{(1)}| = [|t_{(k-1)M_1+1}^{(1)}|, \cdots, |t_{kM_1}^{(1)}|]^T$ for each possible user k, and store the corresponding index in the set $\mathcal{T}_k^{(1)}$, which is expressed as

$$\mathcal{T}_k^{(1)} = max(|\boldsymbol{t}_k^{(1)}|, 1), \tag{4.10}$$

where $max(\boldsymbol{a}, b)$ represents the operation of selecting b largest elements from $\boldsymbol{a}$. Then the indices of the highest received signal for all the K users are stored in $\mathcal{T}^{(1)}$ as follows:

$$\mathcal{T}^{(1)} = \mathcal{T}_1^{(1)} \cup \mathcal{T}_2^{(1)} \cup \cdots \cup \mathcal{T}_K^{(1)}. \tag{4.11}$$

Then, during the first iteration of the JMuMP algorithm, the K_e largest elements in $|\boldsymbol{t}_{\mathcal{T}^{(1)}}^{(1)}|$ are identified in order to form the candidate set $\mathcal{M}^{(1)}$, formulated as

$$\mathcal{M}^{(1)} = max(|\boldsymbol{t}_{\mathcal{T}^{(1)}}^{(1)}|, K_e). \tag{4.12}$$

We should note that due to the non-negligible cross-correlation between user signals, both false-alarms and misidentifications may occur. In this case, the identified users in the set $\mathcal{M}^{(1)}$ may not actually be the active users. However, this inaccuracy will be mitigated later by the symbol detection stage of ***Step 4***.

- ***Step 3:***

Once the potential active users have been identified, classic LS estimation can be performed in order to detect the symbols sent by these potential active users, whose indices are in the set of $\mathcal{M}^{(1)}$, by minimizing $\|\boldsymbol{H}_{\mathcal{M}^{(1)}}\tilde{\boldsymbol{x}}_{\mathcal{M}^{(1)}} - \boldsymbol{y}\|^2$, where $\boldsymbol{H}_{\mathcal{M}^{(1)}}$ is structured by the column entries of $\boldsymbol{H}$ corresponding to the set $\mathcal{M}^{(1)}$, and $\tilde{\boldsymbol{x}}_{\mathcal{M}^{(1)}}$ represents the elements of $\tilde{\boldsymbol{x}}$ having the indices provided by the set $\mathcal{M}^{(1)}$. Therefore, the LS estimate of $\boldsymbol{x}_{\mathcal{M}^{(1)}}$ given by the first iteration is formulated as:

$$\boldsymbol{x}'^{(1)}_{\mathcal{M}^{(1)}} = (\boldsymbol{H}^H_{\mathcal{M}^{(1)}}\boldsymbol{H}_{\mathcal{M}^{(1)}})^{-1}\boldsymbol{H}^H_{\mathcal{M}^{(1)}}\boldsymbol{y}. \tag{4.13}$$

For all remaining $(KM_1 - K_e)$ elements not in the candidate set $\mathcal{M}^{(1)}$, their values can be set to $\boldsymbol{x}'^{(1)}_{\bar{\mathcal{M}}^{(1)}} = \boldsymbol{0}$. Furthermore, by combining $\boldsymbol{x}'^{(1)}_{\mathcal{M}^{(1)}}$ and $\boldsymbol{x}'^{(1)}_{\bar{\mathcal{M}}^{(1)}}$, we can obtain an estimate $\boldsymbol{x}'^{(1)}$ for the transmitted SM signals of all the users.

- ***Step 4:***

Following the classic LS estimation, the elements in $\boldsymbol{x}'^{(1)}_{\mathcal{M}^{(1)}}$ are then mapped to the constellation $\mathcal{S} \cup \boldsymbol{0}$. More specifically, based on $\boldsymbol{x}'^{(1)}$, we can obtain $\boldsymbol{x}'^{(1)}_k$ for user k, which is given by M_1 elements of $\boldsymbol{x}'^{(1)}$ spanning from $[(k-1)M_1 + 1]$ to kM_1. At this stage, if $\boldsymbol{x}'^{(1)}_k = \boldsymbol{0}$, user k is deemed to be inactive. However, if $\boldsymbol{x}'^{(1)}_k \neq \boldsymbol{0}$, user k may potentially be active or inactive. Hence, a further detection stage is required for recovering the M_1SSK and M_2QAM symbol. Specifically, given $\boldsymbol{x}'^{(1)}_k$, this detection process can be formulated as:

$$\hat{\boldsymbol{x}}^{(1)}_k = \arg\min_{\tilde{\boldsymbol{x}} \in \mathcal{S} \cup \boldsymbol{0}} \|\boldsymbol{x}'^{(1)}_k - \tilde{\boldsymbol{x}}\|_2^2, \tag{4.14}$$

where if $\hat{\boldsymbol{x}}_k = 0$ is detected, the k-th user is deemed to be inactive.In this way, the misidentification problem encountered at ***Step 2*** will be circumvented.

- ***Step 5:***

Then, the residual signal $\boldsymbol{r}^{(1)}$ of the current iteration is obtained as

$$\boldsymbol{r}^{(1)} = \boldsymbol{y} - \boldsymbol{H}_{\mathcal{M}^{(1)}}\hat{\boldsymbol{x}}^{(1)}_{\mathcal{M}^{(1)}}. \tag{4.15}$$

Finally, after the first iteration, the indices of the tentatively identified users are stored in a set $\mathcal{F}^{(1)}$, i.e. $\mathcal{F}^{(1)} = \mathcal{M}^{(1)}$. The corresponding estimated SSK/QAM symbols are then expressed as $\hat{\boldsymbol{x}}^{(1)}_{\mathcal{F}^{(1)}}$. Note that $\mathcal{F}^{(i)}, i = 1, 2, \cdots, I$, where I denotes the maximum number of iterations, is a set containing the indices of the K_e active users estimated during the algorithm. After the termination of the algorithm, the indices of the finally identified K_e users are given by the set $\mathcal{F}$.

Following the first iteration, during the i-th iteration ($i \in [2, I]$), similar operations to these of the first iteration are performed. To be more specific, at ***Step 2***, a MF processing is performed on the residual $\boldsymbol{r}^{(i-1)}$ obtained from the $(i-1)$-st iteration in the form of (4.15), yielding

$$\boldsymbol{t}^{(i)} = \boldsymbol{H}^H \boldsymbol{r}^{(i-1)} = \boldsymbol{H}^H \left(\boldsymbol{y} - \boldsymbol{H}_{\mathcal{F}^{(i-1)}} \hat{\boldsymbol{x}}^{(i-1)}_{\mathcal{F}^{(i-1)}} \right). \tag{4.16}$$

Then, after identifying the largest element in $|\boldsymbol{t}^{(i)}_k|$ to form a candidate index set $\mathcal{T}^{(i)}$ following (4.10) and (4.11), a set $\mathcal{M}^{(i)}$ is obtained from the K_e largest elements in $|\boldsymbol{t}^{(i)}_{\mathcal{T}^{(i)}}|$, expressed as

$$\mathcal{M}^{(i)} = max(|\boldsymbol{t}^{(i)}_{\mathcal{T}^{(i)}}|, K_e). \tag{4.17}$$

These indices identified in $\mathcal{M}^{(i)}$ are merged with the indices in $\mathcal{F}^{(i-1)}$ for forming a set as $\mathcal{V}^{(i)} = \mathcal{M}^{(i)} \cup \mathcal{F}^{(i-1)}$, which has at most $2K_e$ indices. Then, based on $\mathcal{V}^{(i)}$, the algorithm performs the classic LS estimation at ***Step 3***, yielding the estimate of $\boldsymbol{x}_{\mathcal{V}^{(i)}}$ expressed as

$$\boldsymbol{x}'^{(i)}_{\mathcal{V}^{(i)}} = (\boldsymbol{H}^H_{\mathcal{V}^{(i)}} \boldsymbol{H}_{\mathcal{V}^{(i)}})^{-1} \boldsymbol{H}^H_{\mathcal{V}^{(i)}} \boldsymbol{y}. \tag{4.18}$$

For the elements that are not in $\mathcal{V}^{(i)}$, the values are set to $\boldsymbol{x}'^{(i)}_{\bar{\mathcal{V}}^{(i)}} = \boldsymbol{0}$.

At ***Step 4***, the classic constellation mapping is performed on the non-zero elements in $\boldsymbol{x}'^{(i)}$, i.e. $\boldsymbol{x}'^{(i)}_{\mathcal{V}^{(i)}}$, in order to recover the M_1SSK and M_2QAM symbols, expressed as

$$\hat{\boldsymbol{x}}^{(i)}_k = \arg \min_{\tilde{\boldsymbol{x}} \in \mathcal{S} \cup \boldsymbol{0}} \|\boldsymbol{x}'^{(i)}_k - \tilde{\boldsymbol{x}}\|_2^2, \tag{4.19}$$

Now, we have to update $\mathcal{F}^{(i-1)}$ to $\mathcal{F}^{(i)}$ by the reliability of identification and detection, measured according to the distance between the LS estimated signal and the mapped signal. In detail, if $\hat{\boldsymbol{x}}^{(i)}_k \neq \boldsymbol{0}$, then user k may be an active user. According to the principles of SM, at most one element in $\hat{\boldsymbol{x}}^{(i)}_k$ is a non-zero value. Hence, we only consider the distance between the non-zero LS estimated element in $\boldsymbol{x}'^{(i)}_k$ and the detected non-zero element in $\hat{\boldsymbol{x}}^{(i)}_k$. This is obtained by first finding the largest element value in $|\hat{\boldsymbol{x}}^{(i)}_k|$ for all $\hat{\boldsymbol{x}}^{(i)}_k \neq \boldsymbol{0}$ and storing its index in the set $\mathcal{B}^{(i)}_k$ expressed as

$$\mathcal{B}^{(i)}_k = \begin{cases} max(|\hat{\boldsymbol{x}}^{(i)}_k|, 1), & \text{if } \hat{\boldsymbol{x}}^{(i)}_k \neq \boldsymbol{0}; \\ \varnothing, & \text{else.} \end{cases} \tag{4.20}$$

Furthermore, let $\mathcal{B}^{(i)} = \mathcal{B}^{(i)}_1 \cup \mathcal{B}^{(i)}_2 \cup \cdots \cup \mathcal{B}^{(i)}_K$. Then the distance between the non-zero LS estimated element and the detected element in the constellation for the specific users in the set $\mathcal{B}^{(i)}$ is calculated as

$$d^{(i)}_{\mathcal{B}^{(i)}_k} = |x'^{(i)}_{\mathcal{B}^{(i)}_k} - \hat{x}^{(i)}_{\mathcal{B}^{(i)}_k}|. \tag{4.21}$$

A smaller distance $d^{(i)}_{\mathcal{B}_k^{(i)}}$ indicates a more reliable symbol recovery. Hence, $\mathcal{F}^{(i)}$ can be updated as

$$\mathcal{F}^{(i)} = min(\boldsymbol{d}_{\mathcal{B}^{(i)}}, K_e), \tag{4.22}$$

where $min(\boldsymbol{a}, b)$ represents a function that returns the indices of the b smallest elements in $\boldsymbol{a}$.

Note that if the size of $\mathcal{B}^{(i)}$ is smaller than K_e, then the final set is updated with a size determined by $\mathcal{B}^{(i)}$. Finally, at the ***Step 5*** of the i-th iteration, the residual signal is updated to $\boldsymbol{r}^{(i)} = \boldsymbol{y} - \boldsymbol{H}_{\mathcal{F}^{(i)}}\hat{\boldsymbol{x}}^{(i)}_{\mathcal{F}^{(i)}}$ for ensuring $(i+1)$-st iteration.

Finally, after I iterations, the JMuMP algorithm is terminated. A range of other termination criteria will be discussed in Section 4.4.2. In summary, the JMuMP algorithm is formally stated as Algorithm 1.

4.4.2 Termination Criteria for Joint Multiuser Matching Pursuit Detection

There are three plausible conditions for terminating the JMuMP algorithm, which may be jointly incorporated for striking an attractive performance vs complexity trade-off.

1. When the residual signal stops improving, i.e. when $\|\boldsymbol{r}^{(i)}\|_2^2 \geq \|\boldsymbol{r}^{(i-1)}\|_2^2$, implying that no columns in the residual $\boldsymbol{r}^{(i)}$ have a significant amount of energy, the iteration stops.

2. When the residual power $\|\boldsymbol{r}^{(i)}\|_2^2$ sinks below a certain a threshold $\beta UN\sigma^2$, where β can be set to a small value, the iteration stops. Note that the threshold is set in harmony with the noise level σ^2 for the following reason. Let us assume that perfect recovery is achieved. Then the estimated signal can be expressed as

$$\hat{\boldsymbol{x}}_{\mathcal{F}} = \boldsymbol{x}'_{\mathcal{F}} = (\boldsymbol{H}_{\mathcal{F}}^H \boldsymbol{H}_{\mathcal{F}})^{-1} \boldsymbol{H}_{\mathcal{F}}^H \boldsymbol{y}, \tag{4.23}$$

   where the superscript (i) is omitted for the sake of simplicity. Then, the signal's residual power can be expressed as

$$\begin{aligned} \|\boldsymbol{r}\|_2^2 =& \boldsymbol{r}^H \boldsymbol{r} \\ =& (\boldsymbol{y} - \boldsymbol{H}_{\mathcal{F}} \boldsymbol{x}'_{\mathcal{F}})^H (\boldsymbol{y} - \boldsymbol{H}_{\mathcal{F}} \boldsymbol{x}'_{\mathcal{F}}) \\ =& \boldsymbol{y}^H \boldsymbol{y} - \boldsymbol{y}^H \boldsymbol{H}_{\mathcal{F}} (\boldsymbol{H}_{\mathcal{F}}^H \boldsymbol{H}_{\mathcal{F}})^{-1} \boldsymbol{H}_{\mathcal{F}}^H \boldsymbol{y}. \end{aligned} \tag{4.24}$$

Substituting (4.15) into (4.24), we obtain

$$\begin{aligned}\|\boldsymbol{r}\|_2^2 =& \boldsymbol{x}^H\boldsymbol{H}^H\boldsymbol{H}\boldsymbol{x} + \boldsymbol{x}^H\boldsymbol{H}^H\boldsymbol{n} + \boldsymbol{n}^H\boldsymbol{H}\boldsymbol{x} + \boldsymbol{n}^H\boldsymbol{n} \\ & - \boldsymbol{x}^H\boldsymbol{H}^H\boldsymbol{H}_{\mathcal{F}}(\boldsymbol{H}_{\mathcal{F}}^H\boldsymbol{H}_{\mathcal{F}})^{-1}\boldsymbol{H}_{\mathcal{F}}^H\boldsymbol{H}\boldsymbol{x} \\ & - \boldsymbol{x}^H\boldsymbol{H}^H\boldsymbol{H}_{\mathcal{F}}(\boldsymbol{H}_{\mathcal{F}}^H\boldsymbol{H}_{\mathcal{F}})^{-1}\boldsymbol{H}_{\mathcal{F}}^H\boldsymbol{n} \\ & - \boldsymbol{n}^H\boldsymbol{H}_{\mathcal{F}}(\boldsymbol{H}_{\mathcal{F}}^H\boldsymbol{H}_{\mathcal{F}})^{-1}\boldsymbol{H}_{\mathcal{F}}^H\boldsymbol{H}\boldsymbol{x} \\ & - \boldsymbol{n}^H\boldsymbol{H}_{\mathcal{F}}(\boldsymbol{H}_{\mathcal{F}}^H\boldsymbol{H}_{\mathcal{F}})^{-1}\boldsymbol{H}_{\mathcal{F}}^H\boldsymbol{n}. \end{aligned} \tag{4.25}$$

The expectation of $\|\boldsymbol{r}\|_2^2$ can be shown to be

$$\begin{aligned}E\left[\|\boldsymbol{r}\|_2^2\right] =& (UN - K_a)\sigma^2 + E\left[\boldsymbol{x}^H\boldsymbol{H}^H\boldsymbol{H}\boldsymbol{x}\right] \\ & - E\left[\boldsymbol{x}^H\boldsymbol{H}^H\boldsymbol{H}_{\mathcal{F}}(\boldsymbol{H}_{\mathcal{F}}^H\boldsymbol{H}_{\mathcal{F}})^{-1}\boldsymbol{H}_{\mathcal{F}}^H\boldsymbol{H}\boldsymbol{x}\right]. \end{aligned} \tag{4.26}$$

Since ideal recovery is assumed, we have $\boldsymbol{H}\boldsymbol{x} = \boldsymbol{H}_{\mathcal{F}}\boldsymbol{x}_{\mathcal{F}}$. Hence, (4.26) can be simplified to

$$E\left[\|\boldsymbol{r}\|_2^2\right] = (UN - K_a)\sigma^2. \tag{4.27}$$

Based on (4.27), we can surmise that the iterations can be terminated if the residual $\|\boldsymbol{r}\|_2^2$ reaches a sufficiently small value, say approximately $\beta UN\sigma^2$ $(0 < \beta < 1)$. Furthermore, a smaller β may result in a better BER performance at the cost of imposing a higher complexity and a longer detection delay.

3. Finally, the detection process is terminated when the number of iterations reaches the limit I. Our investigations have shown that I can be set to a value of $I = 5$, since the performance usually converges after about $I = 3$ iterations.

4.5 Adaptive Multiuser Matching Pursuit Detection

In this section, we propose another novel detector, referred to as the AMuMP detector, which does not require the knowledge of user activation probability p at the receiver. Instead of identifying K_e active users at each iteration, the AMuMP detector adopts the concept of the sparsity-adaptive matching pursuit (SAMP) algorithm proposed in [140], for identifying and detecting an arbitrary number of 'likely-to-be-active' users. The description and termination criteria of the AMuMP detector will be detailed in Sections 4.5.1 and 4.5.2, respectively.

4.5.1 Description of the Adaptive Multiuser Matching Pursuit Detector

The AMuMP algorithm is formally stated as Algorithm 2.

- ***Step 1:***

Identically to the JMuMP detector, the AMuMP detector first carries out the MF operation formulated in (4.9) applied to the received signal $\boldsymbol{y}$ in (4.4) at the beginning, obtaining a vector $\boldsymbol{t}^{(1)}$. As discussed in Section 4.4.1, a larger element value $|t_n^{(1)}|$ in $|\boldsymbol{t}^{(1)}|$ indicates that the corresponding user is more likely to be active. Hence, by exploiting the nature of SM, a set $\mathcal{T}^{(1)}$ is formed for storing the highest value in $\boldsymbol{t}_k^{(1)}$ $(k = 1, 2, \ldots, K)$ following (4.10) and (4.11). However, in contrast to our JMuMP detector of Section 4.4.1 that identifies and detects K_e candidates from $|\boldsymbol{t}_{\mathcal{T}^{(1)}}^{(1)}|$, the AMuMP detector starts by identifying a much smaller number of potentially active users $l = z$ $(z < K_a)$. Then the set of identified candidates is linearly expanded within one and over different iterations, until a certain termination criterion is met. In this way, a more accurate active user set may be constructed at the cost of an increased detection complexity and latency.

In more detail, the AMuMP detector relies on a small integer value z as its step size. Following the MF processing of the 1-st iteration, the z largest elements in $|\boldsymbol{t}_{\mathcal{T}^{(1)}}^{(1)}|$ are identified, with the corresponding indices stored in the candidate set $\mathcal{M}^{(1)}$ and also in the set $\mathcal{F}^{(1)}$.

- ***Step 2 & 3:***

After the LS estimation of $\boldsymbol{x}_{\mathcal{M}^{(1)}}^{(1)}$ following (4.13), a further detection is performed for recovering the M_1SSK and M_2QAM symbols, as shown in (4.14).

- ***Step 4:***

Then, the residual signal $\boldsymbol{r}^{(1)} = \boldsymbol{y} - \boldsymbol{H}_{\mathcal{M}^{(1)}}\hat{\boldsymbol{x}}_{\mathcal{M}^{(1)}}^{(1)}$ is obtained and the AMuMP algorithm continues its iterations, as shown in Algorithm 2.

Specifically, during the ***Step 1*** of the 2-nd iteration, MF processing of $\boldsymbol{r}^{(1)}$ is carried out to obtain $\boldsymbol{t}^{(2)}$ and $\mathcal{T}^{(2)}$ is formed for storing the largest element in $\boldsymbol{t}_k^{(2)}$ $(k = 1, 2, \cdots, K)$. Then $l = z$ candidates are selected as the users corresponding to the l largest elements in $|\boldsymbol{t}_{\mathcal{T}^{(2)}}^{(2)}|$. Then, as shown in Algorithm 2, these z candidates are merged with the set of z candidates obtained during the 1-st iteration, forming the set $\mathcal{V}^{(2)}$, which has at most $2z$ candidates.

Now, the AMuMP algorithm carries out the classic LS estimation following (4.18) at ***Step 2*** and a further mapping process following (4.19) is applied to the candidates in $\mathcal{V}^{(2)}$ at ***Step 3***, yielding $\boldsymbol{x}_{\mathcal{V}^{(2)}}^{\prime(2)}$ and $\hat{\boldsymbol{x}}_{\mathcal{V}^{(2)}}^{(2)}$. Then, from the detected symbols in $\hat{\boldsymbol{x}}_{\mathcal{V}^{(2)}}^{(2)}$, z candidates are selected according to the distance between the estimated and detected symbols, as shown in (4.20) and (4.21), in order to form the final candidate set of

$$\mathcal{F}^{(2)} = min(\boldsymbol{d}_{\mathcal{B}^{(2)}}^{(2)}, z). \tag{4.28}$$

Then, at ***Step 4***, the residual signal is updated to $\boldsymbol{r}^{(2)}$ according to $\boldsymbol{r}^{(2)} = \boldsymbol{y} - \boldsymbol{H}_{\mathcal{F}^{(i)}}\hat{\boldsymbol{x}}_{\mathcal{F}^{(i)}}$. To proceed from this point, depending on the specific values of $\|\boldsymbol{r}^{(2)}\|_2^2$, there are different ways for the algorithm to continue.

Firstly, if we have $\|\boldsymbol{r}^{(2)}\|^2 < \beta UN\sigma^2$ for a preset β value, implying that all active users have been identified, or if $\|\boldsymbol{r}^{(1)}\|_2^2 - \varphi < \|\boldsymbol{r}^{(2)}\|_2^2 < \|\boldsymbol{r}^{(1)}\|_2^2$, indicating no improvement of the most recent residual signal, the identification and detection process is deemed to be completed.

Secondly, if $\|\boldsymbol{r}^{(2)}\|_2^2 \geq \|\boldsymbol{r}^{(1)}\|_2^2$, there are likely to be more than $l = z$ active users. Hence, the algorithm prepares to expand the set of active users by returning to line 6 of the algorithm, in order to obtain a new active user set $\mathcal{F}^{(2)}$ having $l = l + z$ candidates, expressed as $\mathcal{F}^{(2)} = min(\boldsymbol{d}^{(2)}_{\mathcal{B}^{(2)}}, l)$. Then an updated residual $\boldsymbol{r}^{(2)}$ is prepared for the next stage of identification and detection.

Finally, if none of the above-mentioned conditions is met, implying that $\beta UN\sigma^2 < \|\boldsymbol{r}^{(2)}\|_2^2 < \|\boldsymbol{r}^{(1)}\|_2^2 - \varphi$, the algorithm proceeds to the third iteration and repeats the operations of the 2-nd iteration.

This process continues either until the above mentioned termination conditions are met, or until the maximum affordable number of iterations is reached.

It is plausible that the specific choice of the initial candidate set size is determined by the step size z, which has to strike a trade-off between the detection latency, complexity and accuracy. When a smaller step size z is employed, the search for potential active users becomes slower, since a higher number of step size expansions are required to reach the size of the final candidate set, hence resulting in a higher detection complexity. As a benefit, a more accurate estimate will be obtained. These extra step size expansions have to be carried out serially, which also leads to an increased detection latency. By contrast, a higher step size z reduces the detection latency and complexity at the cost of less accurate estimation. This may also result in an error-floor problem, which will be demonstrated and analysed in Section 4.6.1.

4.5.2 Termination Criteria of the Adaptive Multiuser Matching Pursuit Algorithm

In general, there are three natural conditions of terminating the AMuMP algorithm, which may be jointly considered for striking an attractive performance vs complexity trade-off .

1. The first termination criterion is the same as that employed by the JMuMP, i.e. when $\|\boldsymbol{r}^{(i)}\|_2^2 < \beta UN\sigma^2$, the detection is deemed to be completed.

Algorithm 2 AMuMP detector

Input:

Received observations $\mathbf{y}$, CIR $\boldsymbol{H}$ and step size z,

Output:

Detected symbol $\hat{\boldsymbol{x}}$.

Initialization: $i = 1, l = z, \boldsymbol{r}^{(0)} = \boldsymbol{y}, \mathcal{F}^{(0)} = \varnothing, \mathcal{V}^{(0)} = \varnothing,$

1: **while** $i \leq I$ **do**
2: $\quad \boldsymbol{t}^{(i)} = \boldsymbol{H}^H \boldsymbol{r}^{(i-1)};$
3: $\quad$ **for** $k = 1, 2, \cdots, K$ **do**
4: $\quad\quad \mathcal{T}_k^{(i)} = max(|\boldsymbol{t}_k^{(i)}|, 1);$
5: $\quad$ **end for**
6: $\quad \mathcal{T}^{(i)} = \mathcal{T}_1^{(i)} \cup \mathcal{T}_2^{(i)} \cup \cdots \cup \mathcal{T}_K^{(i)}$
7: $\quad \mathcal{M}^{(i)} = max(|\boldsymbol{t}_{\mathcal{T}^{(i)}}^{(i)}|, l);$
8: $\quad \mathcal{V}^{(i)} = \mathcal{M}^{(i)} \cup \mathcal{F}^{(i-1)};$
9: $\quad \boldsymbol{x}'^{(i)}_{\mathcal{V}^{(i)}} = (\boldsymbol{H}^H_{\mathcal{V}^{(i)}} \boldsymbol{H}_{\mathcal{V}^{(i)}})^{-1} \boldsymbol{H}^H_{\mathcal{V}^{(i)}} \boldsymbol{y};$
10: $\quad \boldsymbol{x}'^{(i)}_{\bar{\mathcal{V}}^{(i)}} = \mathbf{0};$
11: $\quad$ **for** $k = 1, 2, \cdots, K$ **do**
12: $\quad\quad \hat{\boldsymbol{x}}_k^{(i)} = \arg\min_{\tilde{\boldsymbol{x}} \in \mathcal{S} \cup \mathbf{0}} \|\boldsymbol{x}'^{(i)}_k - \tilde{\boldsymbol{x}}\|_2^2;$
13: $\quad\quad$ **if** $\hat{\boldsymbol{x}}_k^{(i)} \neq \mathbf{0}$ **then**
14: $\quad\quad\quad \mathcal{B}_k^{(i)} = max(|\hat{\boldsymbol{x}}_k^{(i)}|, 1);$
15: $\quad\quad\quad d^{(i)}_{\mathcal{B}_k^{(i)}} = |x'^{(i)}_{\mathcal{B}_k^{(i)}} - \hat{x}^{(i)}_{\mathcal{B}_k^{(i)}}|;$
16: $\quad\quad$ **else**
17: $\quad\quad\quad \mathcal{B}_k^{(i)} = \varnothing;$
18: $\quad\quad$ **end if**
19: $\quad$ **end for**
20: $\quad \mathcal{B}^{(i)} = \mathcal{B}_1^{(i)} \cup \mathcal{B}_2^{(i)} \cup \cdots \cup \mathcal{B}_K^{(i)};$
21: $\quad \mathcal{F}^{(i)} = min(\boldsymbol{d}^{(i)}_{\mathcal{B}^{(i)}}, l);$
22: $\quad \boldsymbol{r}^{(i)} = \boldsymbol{y} - \boldsymbol{H}_{\mathcal{F}^{(i)}} \hat{\boldsymbol{x}}^{(i)}_{\mathcal{F}^{(i)}};$
23: $\quad$ **if** $\|\boldsymbol{r}^{(i)}\|_2^2 < \beta U N \sigma^2$ **then**
24: $\quad\quad$ break;
25: $\quad$ **end if**
26: $\quad$ **if** $\|\boldsymbol{r}^{(i-1)}\|_2^2 - \|\boldsymbol{r}^{(i)}\|_2^2 < \varphi$ **then**
27: $\quad\quad$ break;
28: $\quad$ **end if**
29: $\quad$ **if** $\|\boldsymbol{r}^{(i)}\|_2^2 \geq \|\boldsymbol{r}^{(i-1)}\|_2^2$ **then**
30: $\quad\quad l = l + z;$
31: $\quad\quad$ go to line 6;
32: $\quad$ **end if**
33: $\quad i = i + 1;$
34: **end while**
35: **return** Detected symbol $\hat{\boldsymbol{x}}$.

2. If the residual signal reduction becomes limited, i.e., if $\|\boldsymbol{r}^{(i-1)}\|_2^2 - \|\boldsymbol{r}^{(i)}\|_2^2 < \varphi$, where φ is a small threshold, it is assumed to be due to the noise imposed on the inactive users. Hence, the AMuMP algorithm is terminated for avoiding excessive expansion of the active user set. In the following simulations in Section 4.6.1, φ is fixed at 0.1.

3. Finally, the AMuMP detection terminates, when the number of iterations reaches the maximum limit I. Again, in our simulations, we set $I = 5$.

4.6 Performance Results and Discussion

In this section, the BER vs complexity of the JMuMP and the AMuMP detectors is analyzed for the grant-free SM/MC-NOMA system in Sections 4.6.1 and 4.6.2.

4.6.1 Bit Error Rate Performance

Let us commence by investigating the impact of K_e on the system performance. Figs. 4.4 and 4.5 compare the BER performance of our JMuMP detector for different K_e values for transmission over an $L = 16$-path frequency selective channel to that of the SP algorithm [96], where the latter has perfect knowledge of the number K_a of active users at the receiver. The 128×128 SM/MC-NOMA system of Figs. 4.4 and 4.5 adopts $N = 128$ subcarriers to support $K = 128$ users equipped with 4 TAs, where 4QAM and 16QAM are employed in Figs. 4.4 and 4.5, respectively. Each user of the SM/MC-NOMA system is randomly activated with an activation probability of $p = 0.1$. Here, in the case of $p = 0.1$, $K_e = 22$ indicates that the probability of having more than $K_e = 22$ active users is below 10^{-4}, which corresponds to the ε of (4.8) discussed in Section 4.4.1. Similarly, $K_e = 25$ ensures having $\varepsilon \leq 10^{-5}$. If the receiver has perfect knowledge of K_a, then instead of K_e users, K_a users are identified and detected in each iteration by the SP algorithm, as shown in Figs. 4.4 and 4.5. We can see that although JMuMP using $K_e = 25$ achieves better BER performance than that with $K_e = 22$, it also includes a higher detection complexity, since K_e determines the column size of $\boldsymbol{H}_{\mathcal{F}}$. Additionally, as shown in Fig. 4.4, in the case of $U = 1$ RA, there is an approximately 1 dB degradation at a BER of 10^{-3} for our JMuMP detector, compared to the SP detector that has perfect *a priori* knowledge of the user activity. Furthermore, a maximum of 1 dB SNR difference is seen between the SP detector and the JMuMP detector using $K_e = 25$ at a BER of 10^{-4} when $U = 2$ RAs are employed. However, the JMuMP detector using $K_e = 22$ still suffers from an error floor formation around BER$= 10^{-4}$.

The BER performance of AMuMP detection with $z = 4$ is also shown in Fig. 4.4. We can see that the error floor can be mitigated when the AMuMP detector is employed. The influence of the initial candidate set size z on AMuMP detection is demonstrated in

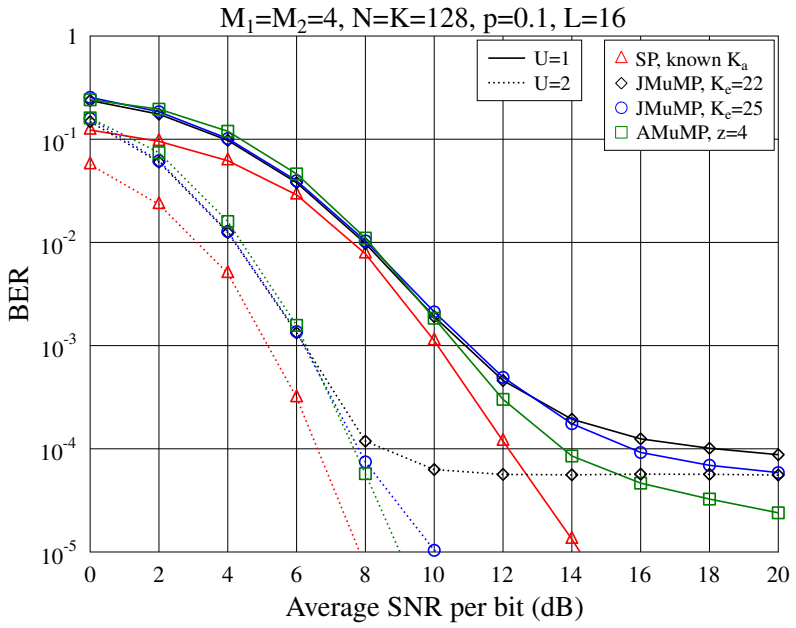

FIGURE 4.4: BER performance of the JMuMP and AMuMP detectors for a 128 × 128 SM/MC-NOMA system for transmission over an $L = 16$-path frequency-selective Rayleigh fading channel, where $p = 0.1$, 4SSK and 4QAM are employed.

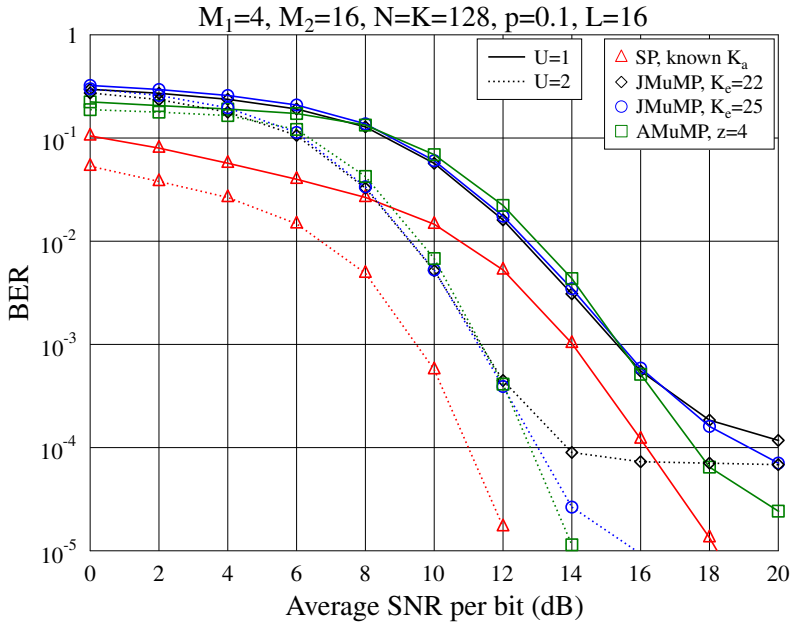

FIGURE 4.5: BER performance of the JMuMP and AMuMP detectors for a 128 × 128 SM/MC-NOMA system for transmission over an $L = 16$-path frequency-selective Rayleigh fading channel, where $p = 0.1$, 4SSK and 16QAM are employed.

Fig. 4.6, where a higher activation probability of $p = 0.2$ is considered and $U = 2$ RAs are employed. While a better BER performance is obtained with a smaller z in the lower SNR regions, an error floor occurs when the step size is too small, e.g., $z = 2$, since the success of signal detection in the later iterations critically depends on the accuracy of user cancellation in the previous iterations.

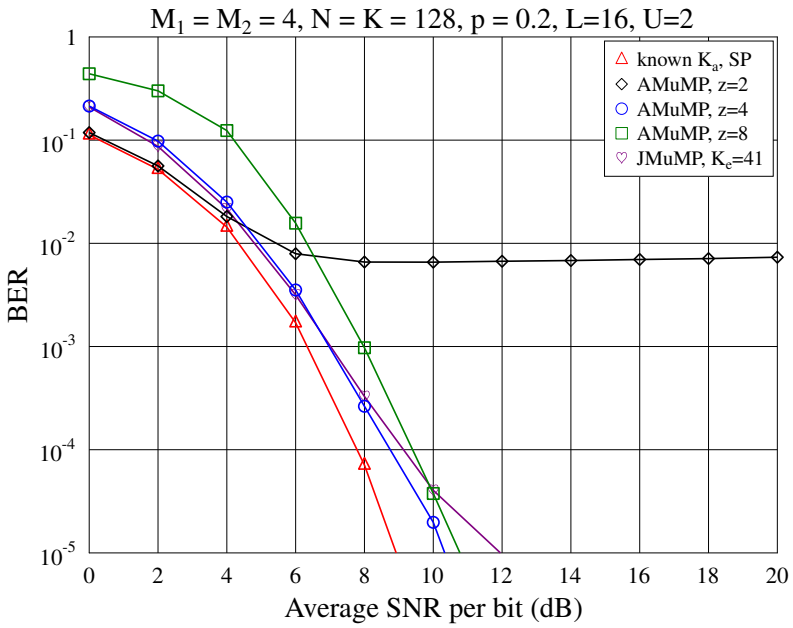

FIGURE 4.6: BER performance of a 128×128 SM/MC-NOMA system with $U = 2$ RAs employing the AMuMP detector with $z = 2, 4$ and 8 for transmission over an $L = 16$-path frequency-selective Rayleigh fading channel, where $p = 0.2$, 4SSK and 4QAM are employed.

Fig. 4.7 investigates the influence of $\beta = 0.01, 0.1, 0.2$ and 0.5 on the proposed JMuMP detector, where the other parameters employed in Fig. 4.7 are the same as those in Fig. 3. It can be observed from Fig. 4.7 that while a higher β results in better BER performance in the low SNR region, it suffers from a higher error floor. By contrast, the JMuMP detector associated with $\beta = 0.1$ and that with 0.01 achieve similar BER performance, which is superior to that associated with $\beta = 0.2$ or 0.5 after SNR = 6 dB. Hence, $\beta = 0.1$ is sufficient for the JMuMP detector in practical implementations. Similarly, the proposed AMuMP detector using $\beta = 0.1$ also achieves the best performance among the different β values, but we omit the simulation results, since they exhibit very similar trends to those of Fig. 4.7.

Figs. 4.8 and 4.9 compare the BER performance of a 128×192 SM/MC-NOMA system using $N = 128$ subcarriers to support $K = 192$ users, which employs the JMuMP and AMuMP detectors, respectively, in conjunction with different user activation probabilities for transmission over an $L = 16$-path frequency-selective Rayleigh fading channel, where K_e is carefully selected for ensuring $\varepsilon \leq 10^{-5}$ for JMuMP and $z = 4$ is chosen for

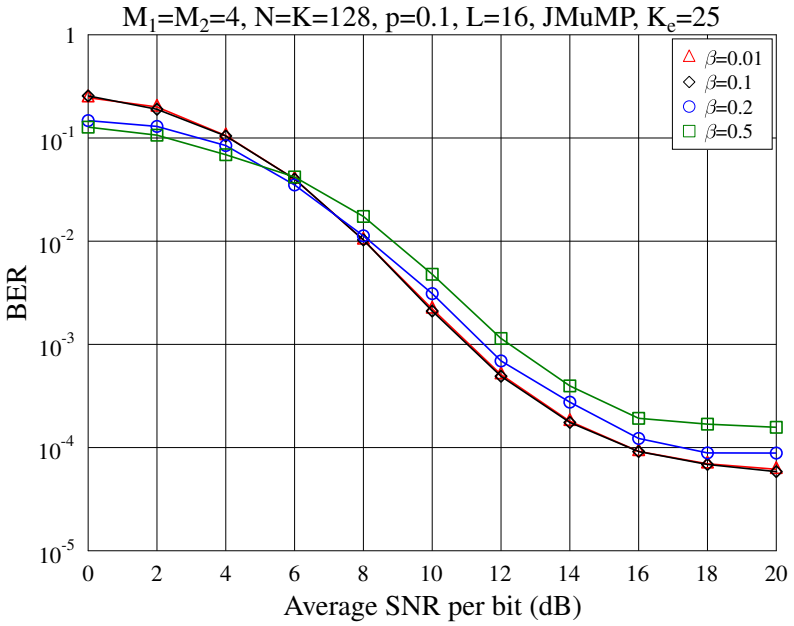

FIGURE 4.7: BER performance of a 128×128 SM/MC-NOMA system using $U = 1$ RA employing the JMuMP detector associated with $\beta = 0.01, 0.1, 0.2$ and 0.5 for transmission over an $L = 16$-path frequency-selective Rayleigh fading channel, where $p = 0.1$, 4SSK and 4QAM are employed.

AMuMP detection. We can see from Fig. 4.8 that in the case of $U = 1$ RA, as p increases, the average number of active users K_a increases, which prevents the system from maintaining a good sparsity. Therefore, JMuMP detection suffers from a pronounced error floor formulation. The increase of RAs to $U = 2$ does mitigate the error floor, hence allowing the system to maintain good performance up to $p = 0.3$.

By contrast, as shown in Fig. 4.9, when AMuMP detection is employed, the error floor formation is clearly mitigated, with all the system parameters remaining the same as those in Fig. 4.8. The 128×192 SM/MC-NOMA system using $U = 2$ RAs employing $z = 4$ and the AMuMP detector is capable of supporting up to $p = 0.30$ user activation probability, which indicates that on average 58 users are active at a time. This is in contrast to the 128×192 SM/MC-NOMA system using $U = 2$ RAs employing the JMuMP detector, where an error floor appears after a $p = 0.3$ user activation probability. Furthermore, while JMuMP requires the knowledge of the activation probability p at the receiver, the AMuMP detector does not require the knowledge of p.

4.6.2 Complexity

Let us now discuss the detection complexity of the proposed JMuMP and AMuMP detectors by quantifying the number of floating point operations (FLOPs) required for completing the iterative detection process. Let us first define the number of FLOPs required for matrix or vector multiplication, addition and norm calculations [141]. Given

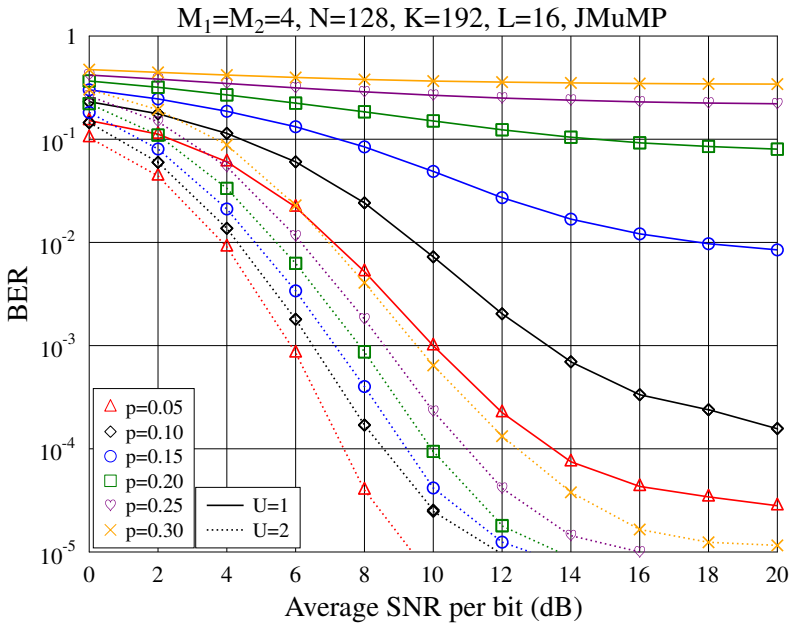

FIGURE 4.8: BER performance of the JMuMP detector for a 128×192 SM/MC-NOMA system with different user activation probabilities for transmission over an $L = 16$-path frequency-selective Rayleigh fading channel, where 4SSK and 4QAM are employed.

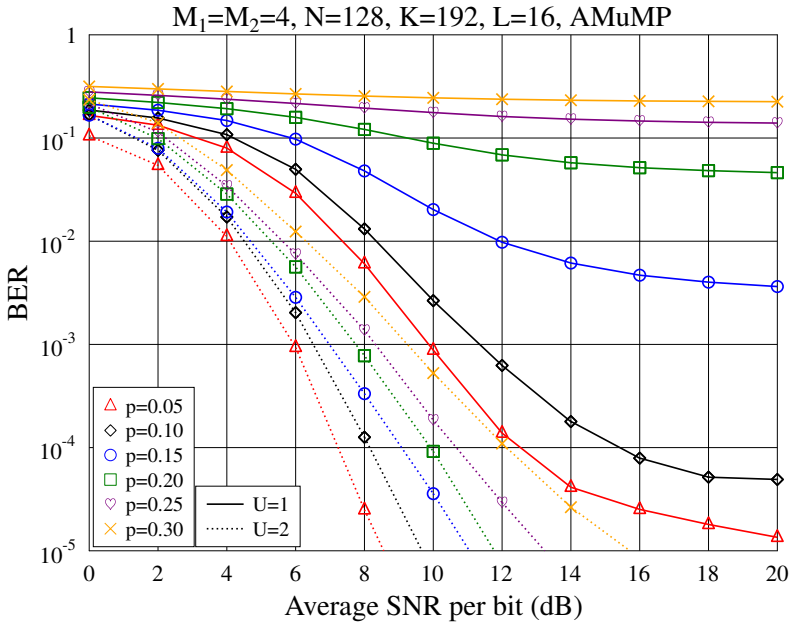

FIGURE 4.9: BER performance of the AMuMP detector for a 128×192 SM/MC-NOMA system with different user activation probabilities for transmission over an $L = 16$-path frequency-selective Rayleigh fading channel, where 4SSK and 4QAM are employed.

$\boldsymbol{c}, \boldsymbol{d} \in \mathbb{C}^{n\times 1}, \boldsymbol{A} \in \mathbb{C}^{m\times n}$ and $\boldsymbol{B} \in \mathbb{C}^{n\times p}$, the operation of $\boldsymbol{c} \pm \boldsymbol{d}$ requires $2n$ FLOPs, $\boldsymbol{A} \times \boldsymbol{B}$ requires $8mnp - 2mp$ FLOPs and $\|\boldsymbol{c}\|_2^2$ requires $(4n-1)$ FLOPs.

The computations in each iteration of JMuMP detection are comprised of four steps: the MF processing, the LS estimation, the constellation mapping and the residual computation. Firstly, during the MF processing of (4.9), only matrix multiplications are performed, giving a complexity of $C_{MF} = 8UNKM_1 - 2KM_1$. Secondly, there are two commonly employed direct methods of the $m \times n$ LS operations, namely the QR decomposition and the Cholesky decomposition. As discussed in [141], the QR decomposition requires $C_{LS,QR} \approx 8n^2m - (8/3)n^3 + 8mn + 4n^2$ FLOPs for carrying out the LS operation, whereas $C_{LS,Cho} \approx 4n^2m + (4/3)n^3 + 8mn + 11n^2$ FLOPs are required for Cholesky decomposition. It has been demonstrated in [142] that the QR decomposition attains a higher accuracy at the cost of higher complexity. Therefore, in our complexity analysis, we opted for the Cholesky decomposition in the following discussions, in order to achieve a lower overall complexity. Thirdly, the mapping process requires at most $2K_e(4M_1 - 1)(M_1M_2 + 1)$ FLOP operations. Finally, the residual update requires another $C_{residual} = 8UNK_e$ FLOPs.

The maximum total computational complexity $C_{\text{JMuMP,max}}$ is the sum of C_{MF}, $C_{LS,Cho}$, $C_{mapping}$ and $C_{residual}$, which can be expressed as

$$\begin{aligned} C_{\text{JMuMP,max}} =& I \times (C_{MF} + C_{LS,Cho} + C_{mapping} + C_{residual}) \\ =& I[\underbrace{8UNKM_1 - 2KM_1}_{C_{MF}} + \underbrace{4UNK_e^2 + (4/3)K_e^3 + 8UNK_e + 11K_e^2}_{C_{LS,Cho}} \\ &+ \underbrace{2K_e(4M_1 - 1)(M_1M_2 + 1)}_{C_{mapping}} + \underbrace{8UNK_e}_{C_{residual}}]. \end{aligned} \tag{4.29}$$

By comparison, the MLD requires $M_2^K \cdot 8UNKM_1$ FLOPs to complete the detection, which is much higher than that of our proposed JMuMP detector.

Similar to (4.29), we may also calculate the maximum computational complexity of A-MuMP detection. Since up to $2l$ elements are identified during each candidate expansion

step and a maximum of I iterations are required for the detection, the maximum complexity of AMuMP detection $C_{\text{AMuMP, max}}$ may be expressed as

$$\begin{aligned} C_{\text{AMuMP, max}} &= \sum_{i=1}^{I}(C_{MF} + C_{LS,Cho} + C_{mapping} + C_{residual}) \\ &= \sum_{i=1}^{I}[\underbrace{8UNKM_1 - 2KM_1}_{C_{MF}} \\ &\quad \underbrace{+ 4UN(\sum_{j=1}^{j^{(i)}} l_{i,j})^2 + (4/3)K_e^3 + 8UN(\sum_{j=1}^{j^{(i)}} l_{i,j}) + 11(\sum_{j=1}^{j^{(i)}} l_{i,j})^2}_{C_{LS,Cho}} \\ &\quad \underbrace{+ 2(\sum_{j=1}^{j^{(i)}} l_{i,j})(4M_1 - 1)(M_1M_2 + 1)}_{C_{mapping}} + \underbrace{8UN(\sum_{j=1}^{j^{(i)}} l_{i,j})}_{C_{residual}}], \end{aligned} \tag{4.30}$$

where $j^{(i)}$ is the number of candidate set expansions in the i-th iteration and $l_{i,j}$ is the step size at the j-th candidate set expansion in the i-th iteration.

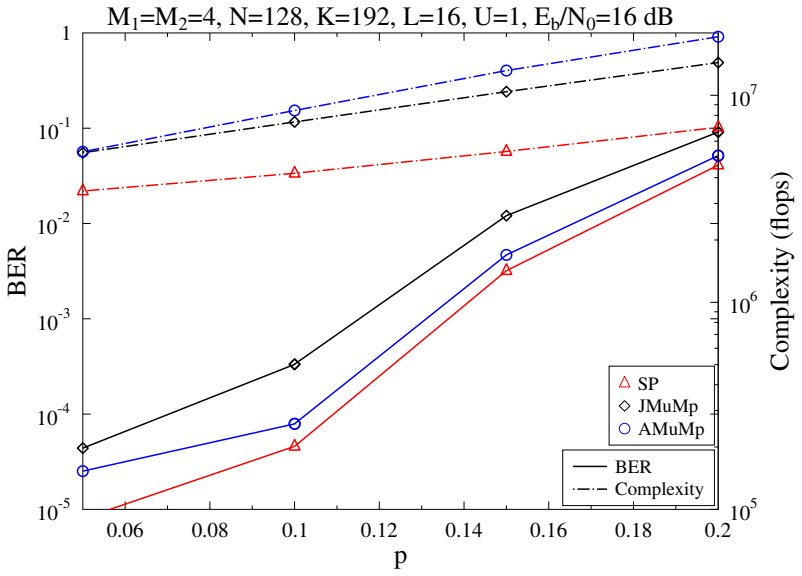

FIGURE 4.10: BER and complexity of the SP, JMuMP and AMuMP detectors for a 128×192 SM/MC-NOMA system at $E_b/N_0 = 16$ dB vs the user activation probability for transmission over an $L = 16$-path frequency-selective Rayleigh fading channel, where 4SSK and 4QAM are employed.

Fig. 4.10 demonstrates the BER vs complexity of the two detectors for the grant-free SM/MC-NOMA system having $N = 128$ subcarriers supporting $K = 192$ users at $E_b/N_0 = 16$ dB, where different user activation probabilities up to $p = 0.2$ are considered. Furthermore, the complexity of the SP detector, which has perfect knwoledge of the number of active users is included in Fig. 4.10 as the benchmark. Since in reality K_a is unknown at the receiver, the proposed JMuMP and AMuMP detectors imposed an

increased detection complexity, compared to that of the SP detector, where K_a is known at the receiver. We can also see a BER vs complexity trade-off, where the AMuMP detector achieves an improved BER at the cost of a higher complexity than that of the JMuMP detector.

4.7 Chapter Summary and Conclusions

TABLE 4.2: Main conclusions of Chapter 4.

System	Grant-free SM/MC-NOMA			
Example	$M_1 = M_2 = 4$, $U = 2$, $N = 128$, $K = 192$, $L = 16$			
Eb/N_0 at a BER of 10^{-3}	p	$p = 0.05$	$p = 0.1$	$p = 0.2$
	JMuMP	6 dB	6.6 dB	8.0 dB
	AMuMP	6 dB	6.5 dB	7.7 dB
Complexity	JMuMP (4.29)		AMuMP (4.30)	

In this chapter, we have relaxed one of the simplifying assumptions of Chapters 2 and 3, which assume all users to be active in each symbol duration in the system. Explicitly, we have proposed an grant-free SM/MC-NOMA uplink scheme for supporting massive connectivity in the mMTC scenarios of next-generation communications, where the users transmit in a sporadic pattern at a low rate. The main conclusions of this chapter are summarized in Table 4.2.

More specifically, a pair of CS-based low-complexity detectors were proposed for jointly detecting both the user activity and the transmitted data, which were referred to as the JMuMP and the AMuMP detector. In contrast to the family of state-of-the-art CS-based detectors designed for grant-free NOMA systems, where the user sparsity is expected to be known at the receiver, the proposed JMuMP detector estimates the user sparsity based on the user activation probability known at the receiver. By contrast, the more sophisticated AMuMP detector does not require any prior knowledge about the user activity of our SM/MC-NOMA system at all. The BER performance of both detectors demonstrates convergence to the ideal condition, where the receiver has perfect knowledge of the user activity. Additionally, the complexity of the two detectors was quantified in terms of the number of floating point operations, and the associated BER vs. complexity trade-off was quantified.

Chapter 5

Hybrid Iterative Detection and Decoding of Near-Instantaneously Adaptive Turbo-Coded Sparse Code Multiple Access

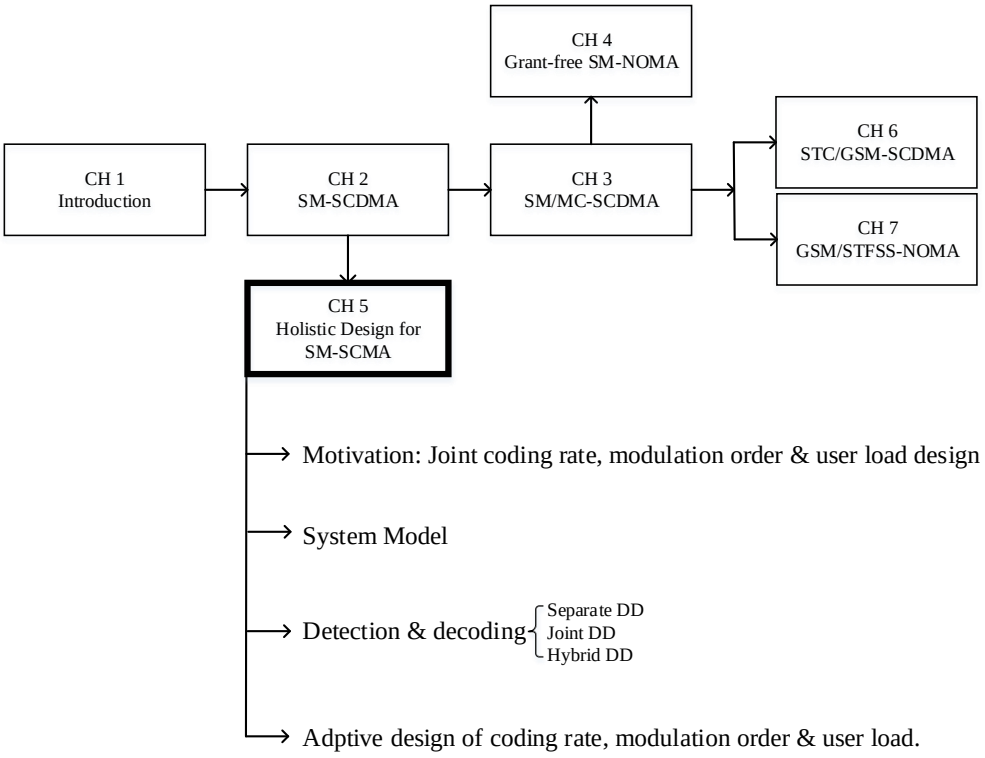

FIGURE 5.1: The relationship of Chapter 5 with the rest of the thesis.

5.1 Introduction

A suite of uncoded SM aided nonorthogonal multiple access (NOMA) systems has been investigated in Chapters 2-4, demonstrating the power of SM and NOMA in the context of non-iterative receivers. In order to exploit the benefits of the powerful 'turbo' principle, in this chapter we extend our interest into the holistic design of channel coded systems. Additionally, for the sake of explicitly focusing our attention on the powerful principles of iterative detection and decoding the family of channel-coded SCMA systems is considered without ameliorating effects of SM.

The SCMA arrangement amalgamated with different channel coding schemes has been investigated in [143–149], as summarised in Table 5.1. To be more specific, an iterative multiuser receiver inspired by the 'turbo' principle was employed by the turbo-coded SCMA system is proposed in [143, 149] for increasing the coding gain. This extra performance gain is particularly crucial in the case of heavy user loads. The joint detection and decoding (JDD) of a low-density parity-check (LDPC)-coded SCMA system was first proposed by Xiao *et al.* [144], which achieved a beneficial performance gain over the separate SCMA detector and LDPC decoder. As a further development, a joint factor graph was designed by Han *et al.* [145] for improving the extrinsic information exchange between the SCMA detector and the LDPC decoder. A similar joint factor graph design has also been proposed for a polar-coded SCMA system in [146, 147], which improved the BER performance and reduced the detection complexity by relying on a sophisticated polar code construction.

However, most prior research has been focusing on improving the BER, whilst there is a paucity of literature on the complexity and latency improvement of coded SCMA systems. For instance, the end-to-end latency of the 5G new radio (NR) ultra-reliable low latency communication (URLLC) mode [150] must remain within 1 ms at a frame error rate (FER) of 10^{-5} [151], which imposes an extremely stringent constraint on the signal processing time at the receiver. Therefore, improvements are required for these JDD algorithms in terms of latency reduction and throughput increase. Naturally, the channel-coding parameters and the resultant BER, throughput, delay as well as complexity trade-offs play a pivotal role in this context. It was shown by comparing LDPC, polar and turbo codes that turbo codes exhibit the best BER performance at low to moderate coding rates [151, 152], which is promising for providing ultra-high reliability in future URLLC applications, such as augmented reality and automated driving [153, 154].

In addition to optimizing the JDD algorithm, another potent technique of improving the system performance for transmission over multipath fading channels is constructed by adaptive modulation and coding [155, 156], which improves the system's overall throughput at favorable channel conditions. To be more specific, in a turbo-coded SCMA system the different factors influencing the system performance may be jointly optimised

TABLE 5.1: Contrasting the novelty of this contribution to the literature.

Contributions	**HDD**	[143]	[144]	[145]	[146]	[147]	[148]	[149]
JDD design	✓	✓	✓	✓	✓	✓	✓	✓
EXIT chart Analysis	✓					✓		✓
User overload investigation	✓							
Fading channel performance	✓	✓	✓			✓	✓	✓
Joint factor graph design			✓	✓	✓	✓		
Complexity reduction	✓				✓			✓
Early termination	✓							
BER improvement	✓	✓	✓	✓		✓		✓
Adaptive system design	✓							

to combat the deleterious effects of fading. In this way, the throughput improvement in terms of bits per symbol (BPS) will directly result in the reduction of the latency.

Motivated by satisfying the URLLC requirement, we first improve the activation order of the SCMA detection and turbo decoding iterations based on EXtrinsic Information Transfer (EXIT) chart analysis [157] and propose a hybrid detection and decoding (HDD) scheme for our turbo-coded SCMA system, which is capable of reducing the latency, while maintaining a high reliability. Additionally, a near-instantaneously adaptive system is designed for mitigating the multipath effects and for further improving the system's throughput. The main contributions of our chapter are summarised as follows.

- Firstly, we investigate the impact of the iterative extrinsic logarithmic likelihood ratio (LLR) exchange between the massage passing algorithm (MPA) detector and the Logarithmic Bahl-Cocke-Jelinek-Raviv (Log-BCJR) turbo decoder by comparing the BER of separate detection and decoding (SDD) to that of the JDD scheme in each iteration. The significant BER improvement of JDD shows the advantage of iterative extrinsic information exchange.

- Secondly, by analysing the convergence behaviour by EXIT charts, we propose an HDD algorithm, which maintains the BER performance compared to the conventional JDD, but achieves a beneficial complexity reduction. To be more specific, we optimize the activation order of detection and decoding scheduling for achieving early termination with the aid of EXIT chart analysis. In this way, the detection and decoding latency can be significantly reduced at a similar BER to that of HDD. Additionally, by exploiting the resultant early-termination property, the proposed HDD achieves a complexity reduction of up to 25%.

- Finally, we propose a near-instantaneously adaptive turbo-coded SCMA system, where the transmitter selects the most appropriate transmission mode according to the prevalent near-instantaneous channel conditions. Our adaptive turbo-coded SCMA system configures itself in the most appropriate mode of operation by jointly selecting the user load, coding rate as well as modulation order by maintaining the data rate at the target BER. Our adaptive system design principle can be readily extended to SCMA systems in combination with other channel coding schemes, such as LDPC codes and polar codes, just to name a few.

The rest of this chapter is structured as follows. Section 5.2 describes the transmitter and receiver schematics of the turbo-coded SCMA system, followed by the state-of-the-art review of the detection and decoding processes in Section 5.3. Section 5.4 provides the system performance analysis and proposes the HDD for our turbo-coded SCMA system based on the EXIT chart analysis. Then, Section 5.5 proposes an adaptive turbo-coded system design example along with characterizing the adaptive system performance

employing HDD. Finally, our main conclusions and future research are summarized in Section 5.6.

5.2 System Model

In this section, the transmitter and receiver structures of our turbo-coded SCMA system are detailed in Sections 5.2.1 and 5.2.2, respectively, along with our main assumptions and notations.

5.2.1 Transmitter Model

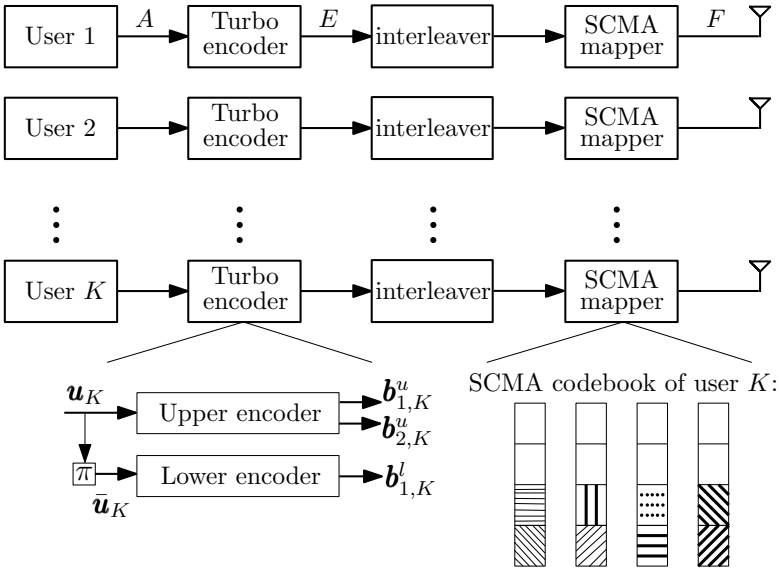

FIGURE 5.2: Transmitter schematic of the turbo-coded SCMA system.

Let us consider the uplink (UL) of a multiuser system supporting K users simultaneously transmitting their information to a base station (BS) over wireless communication channels with the aid of N orthogonal resources in the time domain ($K \geq N$), as shown in Fig. 5.2. To be more specific, in a turbo-coded SCMA system, the A information bits $\boldsymbol{u}_k$ transmitted by user k ($1 \leq k \leq K$) are first interleaved and turbo encoded into E encoded bits $\boldsymbol{b}_k$, resulting in a coding rate of $R = A/E$. Here, we assume that each user transmits the same number of information bits. Note that for the long term evolution (LTE) turbo codes, the length of 188 legitimate information bits varies from $A = 40$ to $A = 6144$ and the coding rate R lies in the range of $(0, 1)$. The turbo encoding process can be illustrated in Fig. 5.2, where two identical convolutional decoders, referred to as the upper and lower decoder, respectively, operate in an identical manner and are connected through the interleaver [157]. To be more specific, the information bits of user k, $\boldsymbol{u}_k$, are first convolutional encoded by the upper encoder, which generates A *parity bits* $\boldsymbol{b}^{(u)}_{1,k}$ and A *systematic bits* $\boldsymbol{b}^{(u)}_{2,k}$. In the mean time, the information bit sequence $\boldsymbol{u}_k$

is interleaved by the LTE interleaver and input to the lower decoder of Fig. 5.2. The interleaved information bits can be denoted as $\bar{\boldsymbol{u}}_k = \pi(\boldsymbol{u}_k)$. The lower decoder of Fig. 5.2 generates only A *parity bits* $\boldsymbol{b}_{1,k}^{(l)}$. Concatenating the three bit frames, $\boldsymbol{b}_{2,k}^{(u)}, \boldsymbol{b}_{1,k}^{(u)}$, and $\boldsymbol{b}_{1,k}^{(l)}$, we have a $\bar{E} = 3A$-length turbo coded sequence $\bar{\boldsymbol{b}}_k$, resulting in a coding rate of 1/3. By puncturing or repeating some of the coded bits, a variable coding rate of $R \in (0, 1)$ can be achieved, resulting in E-bit turbo encoded coded sequences $\boldsymbol{b}_k$.

After the turbo encoder of Fig. 5.2, the encoded bits $\boldsymbol{b}_k$ are interleaved and then mapped by the SCMA codebook $\mathcal{S}_k$ of user k to $F = E/\log_2(M)$ codewords, each of which contain only d_c ($d_c \ll N$) non-zero bits, where M is the modulation order and the cardinality of $\mathcal{S}_k$ is $|\mathcal{S}_k| = M$. The positions of the non-zero elements of the f-th SCMA symbol of all K users $\boldsymbol{X}^{(f)} = [\boldsymbol{x}_1^{(f)}, \boldsymbol{x}_2^{(f)} \cdots \boldsymbol{x}_K^{(f)}]^T$ can be denoted by the indicator matrix $\boldsymbol{V}$ [26]. For example, the most common indicator matrix $\boldsymbol{V}$ of a 4×6 SCMA system is expressed as

$$\boldsymbol{V} = \begin{bmatrix} 1 & 1 & 1 & 0 & 0 & 0 \\ 1 & 0 & 0 & 1 & 1 & 0 \\ 0 & 1 & 0 & 1 & 0 & 1 \\ 0 & 0 & 1 & 0 & 1 & 1 \end{bmatrix}. \tag{5.1}$$

Let us also define the normalised user load for a regular $N \times K$ SCMA system as

$$\lambda = \frac{K}{N} = \frac{d_c}{d_x}. \tag{5.2}$$

After the SCMA mapper of Fig. 5.2, the transmitted symbol frame of the k-th user becomes:

$$\boldsymbol{x}_k = [\boldsymbol{x}_k^{(1)T}, \boldsymbol{x}_k^{(2)T}, \cdots, \boldsymbol{x}_k^{(F)T}]^T. \tag{5.3}$$

5.2.2 Receiver Model

The receiver schematic of the turbo-coded SCMA system is shown in Fig. 5.3. We assume that the channel experiences uncorrelated Rayleigh fading, and the channel gains between the N subcarriers of user k and the BS for the f-th symbol can be expressed as a N-length vector $\boldsymbol{h}_k^{(f)}$. Furthermore, we assume that the receiver has the perfect knowledge of the CIR. Then, the N received signal observations of the f-th symbol in the frame ($f \in [1, F]$) can be expressed as

$$\boldsymbol{y}^{(f)} = \sum_{k=1}^{K} \text{diag}\left(\boldsymbol{h}_k^{(f)}\right) \boldsymbol{x}_k^{(f)} + \boldsymbol{n}_u, \tag{5.4}$$

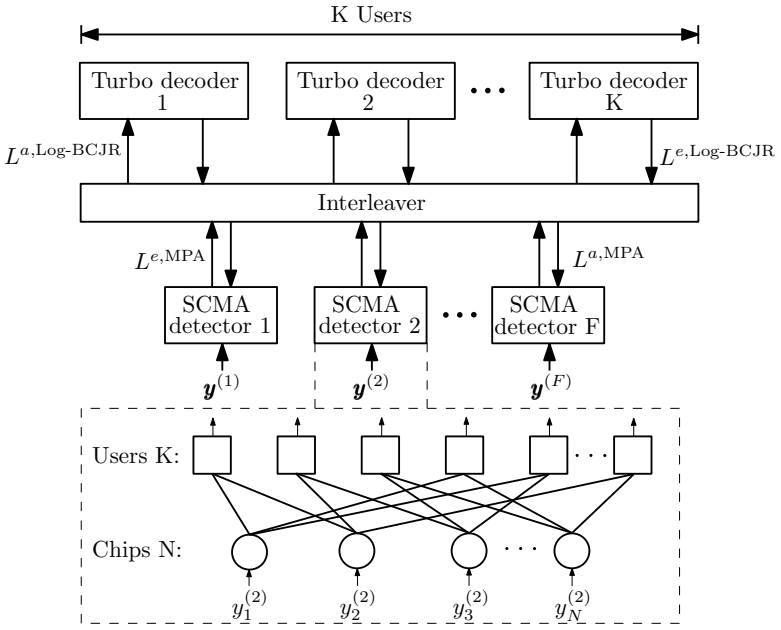

FIGURE 5.3: Receiver schematic of the turbo-coded SCMA system.

where $\boldsymbol{y}^{(f)}$ is a $(N \times 1)$-element vector and $\boldsymbol{n}_u$ obeys the zero-mean complex Gaussian distribution having a covariance matrix of $2\sigma^2\boldsymbol{I}_N$, expressed as $\mathcal{CN}(0, 2\sigma^2\boldsymbol{I}_N)$, where $\sigma^2 = 1/(2\gamma)$, $\gamma = b\gamma_0$ denotes the signal-to-noise ratio (SNR) per symbol, while γ_0 is the SNR per bit.

Then the received signal observations of all the F symbols can be expressed as

$$\boldsymbol{Y} = \left[\boldsymbol{y}^{(1)}, \boldsymbol{y}^{(2)}, \cdots, \boldsymbol{y}^{(F)}\right]. \tag{5.5}$$

5.3 Signal Detection and Decoding

In this section, we first detail the separate detection and decoding (SDD) algorithm of the turbo-coded SCMA system employing the MPA for SCMA detection and the Log-BCJR algorithm for turbo decoding. Then JDD is introduced, which exploits the gradually improved LLRs gleaned from the iterative extrinsic information exchange between the MPA detector and Log-BCJR decoder.

5.3.1 Separate Signal Detection and Decoding

In the SDD, first, MPA detection is applied to the received signal $\boldsymbol{Y}$, followed by the Log-BCJR turbo decoder, where the output LLRs of the MPA detector are used as the *a priori* systematic LLRs of the turbo decoder. For fair comparison with the benchmark schemes to be detailed in the following sections, we define each inner iteration of either the

MPA detector or the Log-BCJR turbo decoder as one half iteration, so that a complete iteration is comprised of 2 half iterations.

The input-output relationship of the MPA detector can be explicitly described by the factor graph [10] of Fig. 5.3, where the f-th symbol $\boldsymbol{x}_k^{(f)}$ sent by user k, is represented by a variable node (VN) j, while the N corresponding observations of the f-th symbol of all K users in $\boldsymbol{y}^{(f)}$ are considered as N check nodes (CNs). In the following description, (f) is omitted for simplicity, since we will detail the MPA detection of the f-th symbol and the MPA detection operations for all the F symbols are identical. As exemplified in Fig. 5.3, users 1 and 2 share the $i = 1$-st CN. Although these two users do interfere with each other on the 1-st chip, information carried by the different chips conveyed by the two users can also be transferred from one chip to another via the connections of the factor graph. Before we detail the operations of the MPA detector, we first define a pair of sets for characterizing the connections of the factor graph as

$$\begin{aligned} \mathcal{X}_j &= \{i : 1 \leq i \leq N, e_{j,i} \neq 0\}, \ j = 1, 2, \ldots, K \\ \mathcal{C}_i &= \{j : 1 \leq j \leq K, e_{j,i} \neq 0\}, \ i = 1, 2, \ldots, N, \end{aligned} \tag{5.6}$$

where we have $|\mathcal{X}_j| = d_x$, representing the d_x connections with the VN j, and $|\mathcal{C}_i| = d_c$, giving the d_c connections with the CN i.

Additionally, the symbol set of user k is expressed as $\mathcal{S}_k = \{s_1^k, s_2^k, \ldots, s_M^k\}$, whereas the probability $\eta_{j,i}^{a_m^j,(t)}$ is defined as the message sent from the VN j to the CN i during the t-th iteration. More specifically, $\eta_{j,i}^{a_m^j,t}$ is the probability that we have $x_j = a_m^j$, given all the messages received by the j-th VN from all of its neighboring CNs, excluding the CN i. By contrast, the message sent from the CN i to the VN j during the t-th inner iteration iteration, $\delta_{i,j}^{a_m^j,t}$, is defined as the probability that $x_j = a_m^j$, given the specific messages received by the CN i from all its neighboring VNs, excluding x_j. Then, following [114] and with the aid of the factor graph of Fig. 5.3, the MPA detector can be described as follows.

Firstly, for all $a_m^k \in \mathcal{S}_k$, and for any specific (j, i) pairs, where $j \in \mathcal{X}_j$ and $i \in \mathcal{C}_i$ the probability $\eta_{j,i}^{a_m^j}$ is initialised as $\eta_{j,i}^{a_m^j,0} = 1/M$. Then, during the t-th ($t \geq 1$) MPA inner iteration, the probability $\delta_{i,j}^{a_m^j,t}$ can be expressed as

$$\begin{aligned} \delta_{i,j}^{a_m^j,t} = & \sum_{\boldsymbol{x}_{[i]} \in \mathcal{X}_{[i]\backslash j}, x_j = a_m^j} \left(\prod_{x_v \in \boldsymbol{x}_{[i]} \backslash x_j} \eta_{j,i}^{x_v,t} \right) \\ & \times p(y_i | \boldsymbol{x}_{[i]}, x_j = a_m^j), \ m = 1, 2, \ldots, M, \end{aligned} \tag{5.7}$$

for $i \in \mathcal{C}_i$ and $j \in \mathcal{X}_j$, where $\boldsymbol{x}_{[i]}$ is a d_c-length vector containing the symbols sent by the d_c users sharing the i-th subcarrier, $\mathcal{X}_{[i]\backslash j}$ represents the combination of symbols in the user codebooks for those specific $(d_c - 1)$ users who share the i-th subcarrier, except for

user j. Still referring to 5.7, $\prod_{x_v \in \boldsymbol{x}_{[i]} \setminus x_j} \eta_{j,i}^{x_v,t}$ is the *a priori* probability of a given $\boldsymbol{x}_{[i]}$ associated with $x_j = a_m^j$, while $p(y_i|\boldsymbol{x}_{[i]})$ can be expressed as

$$p(y_i|\boldsymbol{x}_{[i]}) = \frac{1}{2\pi\sigma^2} \exp\left(-\frac{\|y_i - \sum_{k\in\mathcal{D}_i} h_{ki}x_{ki}\|^2}{2\sigma^2}\right), \tag{5.8}$$

where we define $\mathcal{D}_i$ as the set containing the indices of the specific users sending their information on the i-th subcarrier.

Then, during the $(t+1)$-st MPA inner iteration, the values $\delta_{i,j}^{a_m^j,t}$ for $i \in \mathcal{C}_i$ and $j \in \mathcal{X}_j$ are used for computing $\eta_{j,i}^{a_m^j,t+1}$ for $j \in \mathcal{X}_j$ and $i \in \mathcal{C}_i$, using the expression of

$$\eta_{j,i}^{a_m^j,t+1} = \xi_{j,i} \prod_{v\in\mathcal{X}_j\setminus i} \delta_{v,j}^{a_m^j,t}, \ m = 1, 2, \ldots, M, \tag{5.9}$$

where $\xi_{j,i}$ is applied for ensuring $\sum_{m=1}^{M} \eta_{j,i}^{a_m^j,t+1} = 1$.

Finally, when the maximum affordable number T_{MPA} of inner iterations has been exhausted, the likelihood of the f-th codeword symbol $x_j = a_m^j$ can be formulated as

$$\eta_j^{a_m^j,f} = \prod_{v\in\mathcal{X}_j} \delta_{v,j}^{a_m^j,t}, \ j = 1, 2, \ldots, K. \tag{5.10}$$

Then the extrinsic LLR of the v-th bit $\hat{b}_{v,j}$ in the codeword symbol x_j can be expressed as

$$L^{e,\text{MPA}}(\hat{b}_{v,j}) = \ln \frac{\sum_{s_m^j\in\mathcal{S}_j, \hat{b}_{v,j}=0} \eta_j^{a_m^j,f}}{\sum_{s_m^j\in\mathcal{S}_j, \hat{b}_{v,j}=1} \eta_j^{a_m^j,f}} - L^{a,\text{MPA}}(\hat{b}_{v,j}), \tag{5.11}$$

where $L^{a,\text{MPA}}(\hat{b}_{v,j})$ is the *a priori* LLR of the $\hat{b}_{v,j}$. When the bit LLRs of all F symbols transmitted by user k have been generated, de-interleaving is performed, and these interleaved extrinsic LLRs are then input to the Log-BCJR turbo decoder [158], which can be expressed as

$$L^{a,\text{Log-BCJR}}(\hat{\boldsymbol{b}}_k) = \Pi^{-1}\left(L^{e,\text{MPA}}(\hat{\boldsymbol{b}}_k)\right). \tag{5.12}$$

The LLRs $L^{a,\text{Log-BCJR}}(\hat{\boldsymbol{b}}_k)$ are 'de-punctured' or 'de-repeated' according to the approaches adopted at the encoder to provide the upper decoder with both the parity and systematic *a priori* LLRs $L^{a,\text{Log-BCJR}}(\hat{\boldsymbol{b}}_{1,k}^{(u)})$ and $L^{a,\text{Log-BCJR}}(\hat{\boldsymbol{b}}_{2,k}^{(u)})$, while the lower decoder is furnished with the parity *a priori* LLRs $L^{a,\text{Log-BCJR}}(\hat{\boldsymbol{b}}_{1,k}^{(l)})$ of user k, respectively.

The iterative Log-BCJR decoding process is illustrated in Fig. 5.4. To be more specific, in the q-th inner iteration, the upper and lower decoders operate alternately, where

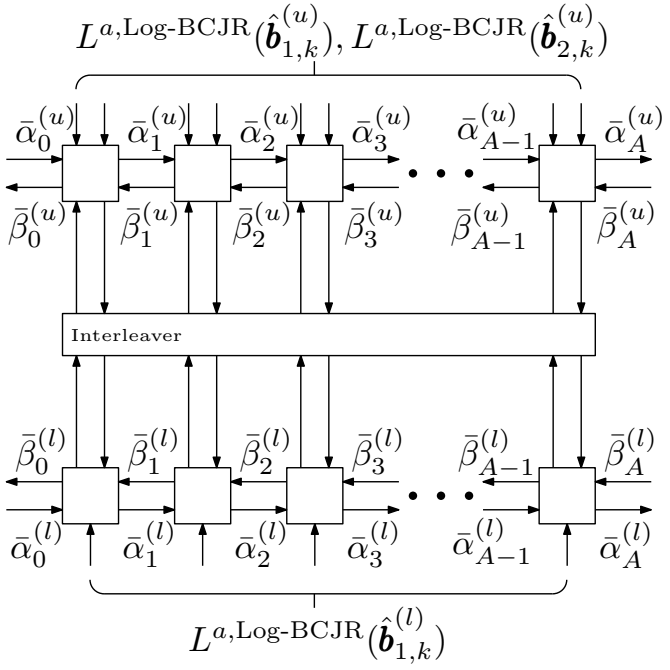

FIGURE 5.4: The operations of the Log-BCJR turbo decoder.

each decoder element of Fig. 5.4 generates the corresponding one of the *extrinsic* LLRs $L^{e,\text{Log-BCJR}}(\hat{\boldsymbol{b}}_{1,k}^{(u)})$ or $L^{e,\text{Log-BCJR}}(\hat{\boldsymbol{b}}_{1,k}^{(l)})$, which are interleaved to provide the *a priori* LLRs $L^{a,\text{Log-BCJR}}(\hat{\boldsymbol{b}}_{1,k}^{(u)})$ or $L^{a,\text{Log-BCJR}}(\hat{\boldsymbol{b}}_{1,k}^{(l)})$ for the next decoding operation of the other decoder.

In addition to the LLRs described above, each decoder element of the v-th bit in Fig. 5.4 is provided with a vector of forward state metrics $\bar{\boldsymbol{\alpha}}_{v-1}^{(u)}$ or $\bar{\boldsymbol{\alpha}}_{v-1}^{(l)}$ as well as with a vector of backward state metrics $\bar{\boldsymbol{\beta}}_v^{(u)}$ or $\bar{\boldsymbol{\beta}}_v^{(l)}$, which are used for initiating the forward and backward processing recursions, respectively [157]. During the forward recursion, each successive decoder element in a left-to-right order is processed in each successive clock cycle. Simultaneously, the backward recursion activates the successive decoder element in a right-to-left order during the successive clock cycles. Each successive decoder element passes a vector of state metric values $\bar{\boldsymbol{\alpha}}_v^{(u)}$, $\bar{\boldsymbol{\alpha}}_v^{(l)}$, $\bar{\boldsymbol{\beta}}_{v-1}^{(ul)}$ or $\bar{\boldsymbol{\beta}}_{v-1}^{(l)}$ to the next decoder element in the forward or backward recursion, respectively.

Furthermore, once the two recursions have crossed over, extrinsic LLRs are generated, as mentioned above, based on both the forward and the backward state metrics. Here, we omit the calculation of the forward and backward state metrics for the sake of simplicity, but the details of these calculations can be found in [157]. After several iterations[1], the transmitted bits $\hat{\boldsymbol{b}}_k$ of user k, are decoded according to the extrinsic LLRs. The SDD algorithm is summarised in Algorithm 1.

[1] $T_{\text{Log-BCJR}} = 8$ iterations may be required in order to achieve iterative decoding convergence to the best possible BER [158].

Algorithm 3 SDD of the turbo-coded SCMA system.

Initialization:

$\eta_{j,i}^{a_m^j,0} = 1/M$ for all $a_m^j \in \mathcal{S}_j$, $i \in \mathcal{X}_j$ and $j \in \mathcal{C}_i$;

for $t = 1, ..., T_{\text{MPA}}$ **do**

  MPA detection following (7), (8), (9), (10);

end for

Calculate the corresponding extrinsic LLRs (11);

Deinterleave the LLRs using (12);

for $q = 1, ..., T_{\text{Log-BCJR}}$ **do**

  Log-BCJR Turbo decoding [157];

end for

5.3.2 Joint Signal Detection and Decoding

In contrast to the SDD, the JDD scheme facilitates LLR exchange between the MPA detector and Log-BCJR decoder in each iteration, which improves the BER performance, as it will be demonstrated in Section 5.4.

Similar to the SDD, after the same initialisation as that of the MPA detector of SDD, the JDD starts out by updating $\eta_{j,i}^{a_m^j,t}$ based on (5.7) in the t-th iteration. Then the updated codeword probability $\eta_{j,i}^{a_m^j,t}$ is converted to bit LLRs according to (5.11) and input to the upper turbo decoder of Fig. 5.4 as the *a priori* LLR. In the meantime, these LLRs are interleaved and forwarded to the lower decoder as the parity LLRs. After the t-th inner iteration of the turbo decoder, the output extrinsic bit LLRs are remapped to the probability of the codeword symbol.

The new $\eta_{j,i}^{a_m^j,f}$ is then fed back to the MPA detector of Fig. 5.3 for updating $\delta_{i,j}^{a_m^j,f}$ according to (5.9) for the next iteration. Note that in the JDD scheme, a complete iteration includes the update of $\delta_{i,j}^{a_m^j,t}$, one inner iteration of the Log-BCJR decoder and the update of $\eta_{j,i}^{a_m^j,t+1}$. The JDD algorithm is summarised at a glance in Algorithm 2.

Algorithm 4 JDD of the turbo-coded SCMA system.

Initialization:

$\eta_{j,i}^{a_m^j,0} = 1/M$ for all $a_m^j \in \mathcal{S}_j$, $i \in \mathcal{X}_j$ and $j \in \mathcal{C}_i$;

for $t = 1, ..., T_{max}$ **do**

  MPA detection following (7), (8), (9), (10);

  Generate extrinsic LLRs using (11);

  Deinterleave extrinsic LLRs following (12);

  Log-BCJR decoding [157];

  Interleave using (12);

  Covert the LLRs to codeword probability;

end for

5.4 System Performance and Hybrid Detection and Decoding

In this section, we analyse the performance of the turbo-coded SCMA system employing either SDD or JDD in terms of their capacity upper bound, BER performance as well as convergence rate in Sections 5.4.1 to 5.4.3. In the simulations, $M = 4$ and the LTE turbo code having a coding rate of $R \in [1/3, 1/2]$ are employed. Furthermore, based on our EXIT chart analysis, we will advocate the HDD algorithm as a benefit of its BER vs. complexity advantage demonstrated in Section 5.4.4, based on its complexity comparison to that of the SDD and JDD discussed in Section 5.4.5.

5.4.1 Capacity

We first analyse the capacity of the SCMA UL, where K users simultaneously transmit their f-th symbol to the BS in the f-th time slot. In the following derivations, we only employ the superscript (f) when necessary. Since the signals are transmitted by N orthogonal subcarriers of the SCMA system and received by U receive antennas (RAs), the achievable rate is upper bounded by the discrete-input continuous-output memoryless channel (DCMC) capacity [159, 160]. Therefore, we may view the N subcarriers as N transmit antennas (TAs) of a conventional MIMO system and derive the DCMC capacity for the SCMA system following [160].

First, let us define the symbol set $\mathcal{X}_{[i]}$ as the combinational symbol set for the d_c users who share the i-th subcarrier as

$$\mathcal{X}_{[i]} = \{a_1, a_2, \cdots, a_{M^{d_c}}\}. \tag{5.13}$$

Hence, we have $\boldsymbol{x}_{[i]} = a_m \in \mathcal{X}_{[i]}$. Then, according to [160], the DCMC capacity can be expressed as

$$\begin{aligned} C = & \frac{1}{d_x} \sum_{i=1}^{N} \max_{p(\boldsymbol{x}_{[i]}=a_m), a_m \in \mathcal{X}_{[i]}} \sum_{m=1}^{M^{d_c}} \int_{-\infty}^{+\infty} p(y_i, \boldsymbol{x}_{[i]} = a_m) \\ & \times \log_2 \left(\frac{p(y_i | \boldsymbol{x}_{[i]} = a_m)}{\sum_{v=1}^{M^{d_c}} p(y_i, \boldsymbol{x}'_{[i]} = a_v)} \right) \mathrm{d}y_i, \end{aligned} \tag{5.14}$$

where $p(y_i|\boldsymbol{x}_{[i]} = a_m)$ is given by (5.8). Note that (5.14) is maximised in the case of equiprobable transmitted symbols, where we have $p(\boldsymbol{x}_{[i]} = a_m) = 1/(M^{d_c})$, $\forall m$. Hence,

we arrive at

$$\begin{aligned}
&\log_2\left(\frac{p(y_i|\boldsymbol{x}_{[i]}=a_m)}{\sum_{v=1}^{M^{d_c}} p(y_i,\boldsymbol{x}'_{[i]}=a_v)}\right)\\
&\quad=\log_2\left(\frac{p(y_i|\boldsymbol{x}_{[i]}=a_m)}{\sum_{v=1}^{M^{d_c}} p(y_i|\boldsymbol{x}'_{[i]}=a_v)p(\boldsymbol{x}'_{[i]}=a_v)}\right)\\
&\quad=-\log_2\left(\frac{1}{M^{d_c}}\sum_{v=1}^{M^{d_c}}\frac{p\left(p(y_i|\boldsymbol{x}_{[i]}=a_m)\right)}{p(y_i|\boldsymbol{x}'_{[i]}=a_v)}\right)\\
&\quad=\log_2(M^{d_c})-\log_2\sum_{v=1}^{M^{d_c}}\exp\left(\Psi_i\right),
\end{aligned}\tag{5.15}$$

where by substituting (5.8) into (5.15), Ψ_i is expressed as

$$\Psi_i=-\frac{\left(\left(\boldsymbol{x}_{[i]}-\boldsymbol{x}'_{[i]}\right)\boldsymbol{h}_{[i]}+n_i\right)^2+(n_i)^2}{\sigma^2},\tag{5.16}$$

with $\boldsymbol{h}_{[i]}^T$ representing a d_c-length vector of the channel gains between the i-th subcarrier of the d_c users sharing this subcarrier and the BS, while n_i is the i-th element in $\boldsymbol{n}$.

Hence, if the symbols are transmitted at equal probabilities, we arrive at the upper bound of the DCMC capacity expressed as

$$\begin{aligned}
C_{\max}&=\frac{1}{d_x}\\
&\times\left(\log_2(M^{d_c})-\frac{1}{M^{d_c}}\sum_{m=1}^{M^{d_c}}\mathbb{E}_{\boldsymbol{h},\boldsymbol{n}}\left[\log_2\sum_{i=1}^{N}\sum_{v=1}^{M^{d_c}}\exp(\Psi_i)\right]\right).
\end{aligned}\tag{5.17}$$

Fig. 5.5 shows the upper bound of the DCMC capacity for the turbo-coded SCMA system obtained from (5.17), where we can see that a higher normalised user load λ results in a higher DCMC capacity bound, at the cost of the degraded BER performance, as will be demonstrated in Section 5.4.2. Another factor that influences the DCMC capacity bound is the SCMA modulation order M, as a higher order enables more non-zero information bits transmitted by a single SCMA codeword. Furthermore, a turbo-coded system supporting $K=32$ users with $M=4$ achieves the same DCMC capacity bound compared to that supporting $K=16$ users with $M=8$, since the number of bits transmitted by per subcarrier remains the same.

5.4.2 Error Correction Performance

The BER performance of the turbo-coded SDD and JDD-aided SCMA system having different λ values for transmission over the AWGN channel is shown in Figs. 5.6 and

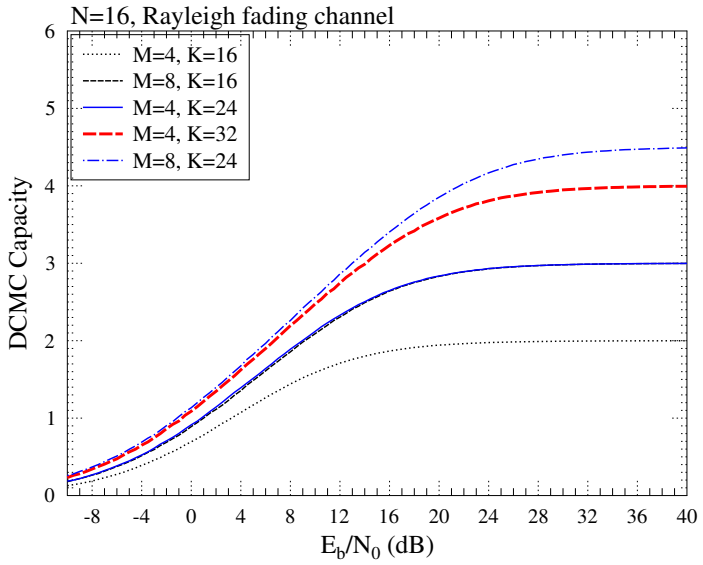

FIGURE 5.5: Upper bound of the DCMC capacity of (5.17) for the turbo-coded SCMA system.

5.7, where we have $N = 16, K = 16, 24$ or $32, F = 512$. Furthermore, continuous-input continuous-output memoryless channels (CCMC) Shannon capacity [161] is shown in Fig. 5.6 as the benchmarker of the coded system. We can see that compared to the SDD, up to 1 dB gain can be attained at a BER level of 10^{-5} by the JDD as a benefit of exchanging extrinsic LLRs between the MPA detector and Log-BCJR decoder during each iteration. The highest gain is attained at a normalised user-load of $\lambda = 1$, where the multi-user interference is the least severe.

Naturally, the coding rate R also influences the system performance, as seen by comparing Figs. 5.6 and 5.7. Explicitly, the turbo-coded SCMA system using $R = 1/3$ in Fig. 5.7 requires about 1 dB lower E_b/N_0 than that of $R = 1/2$ shown in Fig. 5.6. To be more specific, $R = 1/2$ is arrived by puncturing some of the information bits. While this redundancy reduction gives a higher useful data rate, it results in the slight performance degradation.

Fig. 5.8 compares the influence of the *normalised user load* λ and of the coding rate R on the turbo-coded system. Let us first define the *normalised system load* as $\omega = \lambda R = KR/N$, before investigating the relationship of λ and R. As shown in Fig. 5.8, a $R = 2/3$ turbo-coded system supporting $K = 24$ users has the same normalised system load of $\omega = 4$ as a $R = 1/2$ turbo-coded system supporting $K = 32$ users, but achieves better BER performance. Similar conclusions may be drawn for the case of a $K = 16, R = 3/4$ and a $K = 24, R = 1/2$ turbo-coded SCMA system. Note that $R > 1/3$ is achieved by puncturing some of the parity bits.

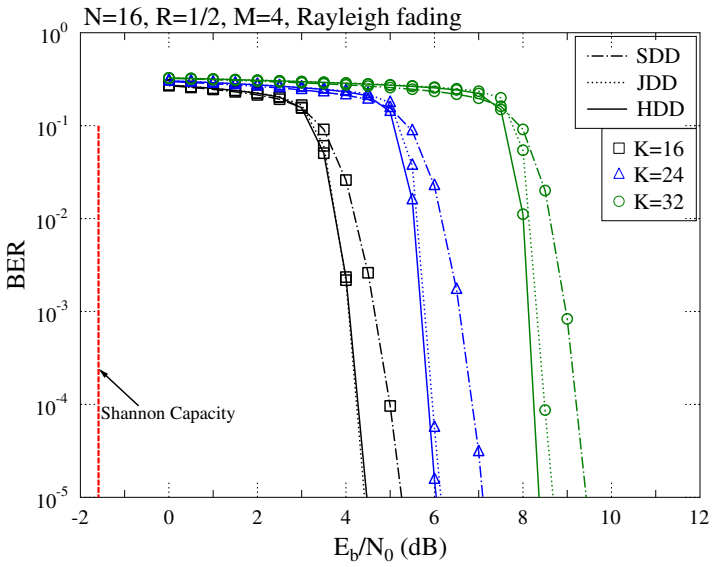

FIGURE 5.6: BER performance of the turbo-coded SCMA system relying on $N = 16$ chips for supporting different number of users over an uncorrelated Rayleigh fading channel, where the coding rate R is fixed at 1/2.

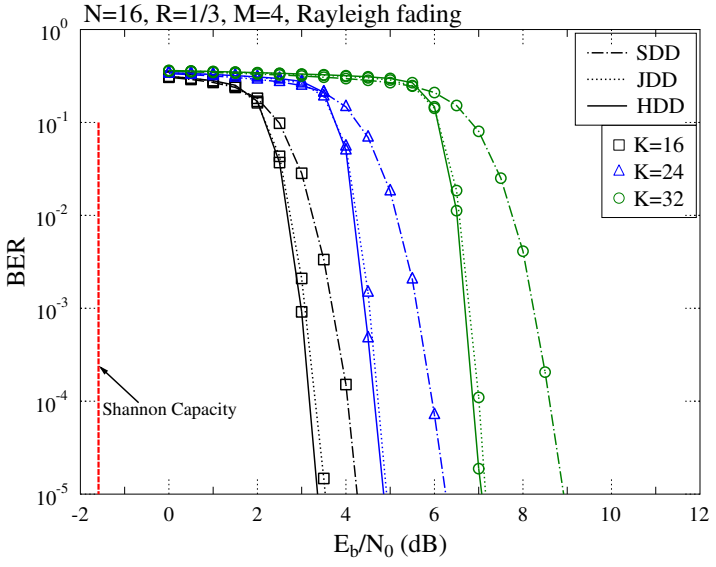

FIGURE 5.7: BER performance of the turbo-coded SCMA system with $N = 16$ chips supporting different number of users over an uncorrelated Rayleigh fading channel, where the coding rate R is fixed at 1/3.

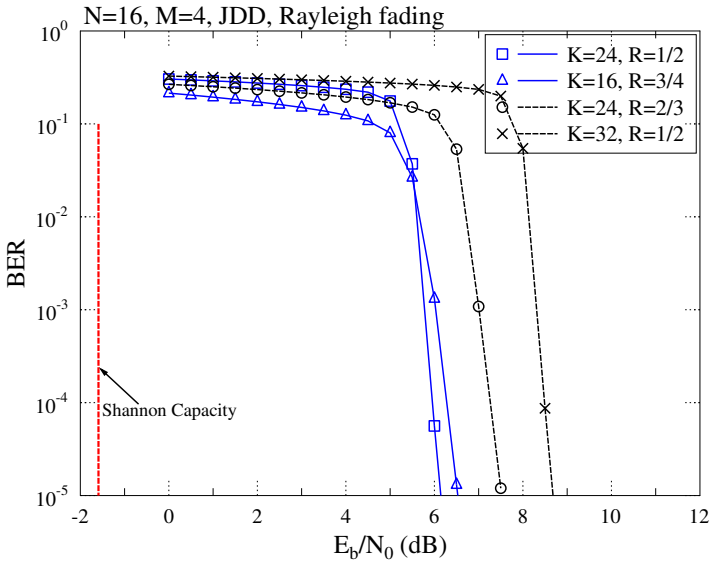

FIGURE 5.8: BER performance of the turbo-coded SCMA system of different coding rates with $N = 16$ chips for the normalized user loads of $\lambda = 1, 1.5$ or 2 and system load of $\omega = 3/4$ or 1 over an uncorrelated Rayleigh fading channel.

5.4.3 EXtrinsic Information Transfer Chart Analysis

Let us now employ EXIT charts for visualising the convergence behavior of our MPA and Log-BCJR schemes. Originally, EXIT charts were proposed for characterising the mutual information (MI) of a pair of concatenated components in a communication system. In this section, we employ EXIT charts for characterising the relationship between the *a priori* and extrinsic information of the MPA detector and the Log-BCJR decoder. First, following [162] and assuming that the *a priori* LLRs $L^{a,\text{MPA}}$ of the MPA detector obeys Gaussian random distribution with a mean of μ_A and a variance of σ_A^2 satisfying $\mu_A = \sigma_A^2/2$, the conditional probability density function (PDF) associated with $L^{a,\text{MPA}}(\hat{\boldsymbol{b}}_k)$ can be expressed as

$$p_a(\zeta|X=x) = \frac{1}{\sqrt{2\pi}\sigma_A} \exp\left(-\frac{(\zeta - \frac{\sigma_A^2}{2})^2}{2\sigma_A^2}\right). \tag{5.18}$$

Then, the MI between the *a priori* LLRs $L^{a,\text{MPA}}(\hat{\boldsymbol{b}}_k)$ of the MPA detector and the turbo encoded bits $\hat{\boldsymbol{b}}_k$ can be expressed as

$$\begin{aligned} I_{a,\text{MPA}} =& 1 - \frac{1}{\sqrt{2\pi}\sigma_A} \int_{-\infty}^{+\infty} \exp\left(-\frac{(\zeta - \frac{\sigma_A^2}{2})^2}{2\sigma_A^2}\right) \\ & \times \log_2\left[1 + e^{-\zeta}\right] \mathrm{d}\zeta. \end{aligned} \tag{5.19}$$

By contrast, the MI between the *extrinsic* LLRs $L^{e,\mathrm{MPA}}(\hat{\boldsymbol{b}}_k)$ of the MPA detector and turbo encoded bits can be expressed as

$$I_{e,\mathrm{MPA}} = \frac{1}{2} \cdot \sum_{u=-1,+1} \int_{-\infty}^{+\infty} p_e\left(\zeta|U=u\right) \times \log_2 \frac{2p_e\left(\zeta|U=u\right)}{p_e\left(\zeta|U=-1\right)+p_e\left(\zeta|U=1\right)} \mathrm{d}\zeta, \tag{5.20}$$

where $p_e\left(\zeta|U=u\right)$ is obtained by the classic Monte-Carlo method. From (5.20), we can express $I_{e,\mathrm{MPA}}$ as a function of $I_{a,\mathrm{MPA}}$ and E_b/N_0 defined as

$$I_{e,\mathrm{MPA}} = \mathcal{T}_{\mathrm{MPA}}(I_{a,\mathrm{MPA}}, E_b/N_0). \tag{5.21}$$

In contrast to $I_{e,\mathrm{MPA}}$, the extrinsic information transfer function of the turbo decoder is independent of E_b/N_0, since the only input of the decoder is the soft-interleaved extrinsic LLR sequence $L^{e,\mathrm{MPA}}(\hat{\boldsymbol{b}}_k)$ of the MPA detector, as shown in Fig. 5.3. Therefore, the extrinsic information transfer characteristic is defined as

$$I_{e,\text{Log-BCJR}} = \mathcal{T}_{\text{Log-BCJR}}(I_{a,\text{Log-BCJR}}), \tag{5.22}$$

where $I_{a,\text{Log-BCJR}}$ is the MI between the turbo-coded bits $\boldsymbol{b}_k$ and *a priori* LLRs $L^{a,\text{Log-BCJR}}(\hat{\boldsymbol{b}}_k)$ of the Log-BCJR decoder.

Fig. 5.9 shows the EXIT chart of an $N = 16$ turbo-coded SCMA system supporting $K = 24$ users for transmission over AWGN channels. This will be used for determining the most beneficial activation order of both the SCMA MPA detector and of the LTE turbo decoder, so that we can achieve receiver-processing latency reduction at a given BER performance, as it will be detailed in Section 5.4.4.

5.4.4 Improved Scheduling of Detection and Decoding

According to the EXIT chart of Fig. 5.9, we now propose a HDD, which improves the activation order of the SCMA MPA detector and Log-BCJR turbo decoder, for reducing the complexity and latency of the detection and decoding without degrading the BER performance. To be more specific, the HDD aims for a relatively high initial MI at $I_{e,\text{Log-BCJR}} = 0$ and a wider open tunnel, which would lead to expedited convergence overall. Therefore, the HDD commences with several inner SCMA MPA iterations first for attaining a higher initial MI. Then the extrinsic LLRs at its output are entered into the Log-BCJR decoder as *a priori* LLRs. Furthermore, we can see from Fig. 5.9 that the MI obtained from $T_{\mathrm{MPA}} = 1, 2$ and 4 SCMA MPA iterations eventually converges to $I_{e,\mathrm{MPA}} = 0.77$ at $I_{e,\text{Log-BCJR}} = 1$, therefore the marginal improvement attained by further MI exchanges remains rather limited, despite increasing the detection complexity of the receiver. Therefore, the JDD philosophy may be adopted after the first several

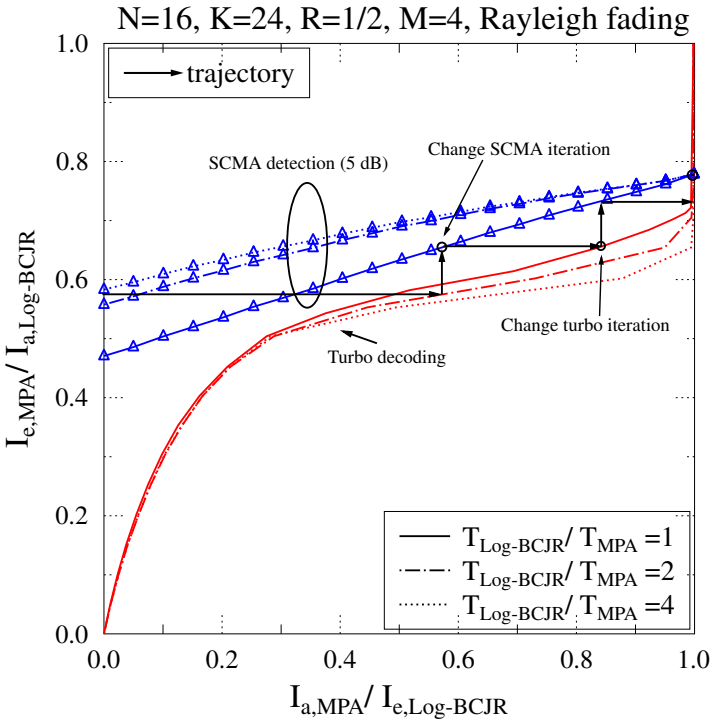

FIGURE 5.9: The EXIT chart for the Log-BCJR turbo decoder and for SCMA MPA detector using $N = 16$ chips for supporting $K = 24$ users for transmission over an uncorrelated Rayleigh fading channel. The triangles indicate the SCMA MPA curves, while the lines without symbols are the turbo decoder's curves. The curves are not shown for more than $T_{\text{MPA}} = 4$, because $T_{\text{MPA}} = 8$ becomes indistinguishable from $T_{\text{MPA}} = 4$.

iterations. To be more specific, let us use a design example to detail our proposed low-complexity HDD. Let us still assume that $T_{max} = 8$ complete iterations will be employed at the receiver, as in the previous sections. Therefore, in the case of a turbo-coded SCMA system using $N = 16, F = 512$, we first employ the first 4 half iterations, i.e. 2 iterations, for SCMA MPA detection, which gives a higher MI at $I_{e,\text{Log-BCJR}} = 0$, as shown in Table 5.2. Note that even though 8 half iterations gives a slightly better MI compared to 4 half iterations, this improvement remains rather marginal, despite its doubled complexity. Then, the following 2 half iterations are employed for turbo decoding, relying on iterative LLR exchange. Then, two half iterations are employed for MPA detection. Following this two iterations are employed to perform the JDD activation, as shown in Table 5.2. Note that the HDD scheduling is also visualized by the stair-case shaped decoding trajectory seen in Fig. 5.9. In this way, only 10 half iterations, i.e. a total of 5 iterations are required for completing the iterative detection and decoding, hence achieving early termination of the iterations.

Fig. 5.10 compares the E_b/N_0 distance from the CCMC Shannon capacity of the 3 different activation schemes at each iteration and shows the influence of frame length

TABLE 5.2: Scheduling of different iterative detection and decoding schemes for the turbo-coded SCMA system.

	Iterations (T)	1	2	3	4	5	6	7	8
SDD	SCMA	✓	✓	✓	✓	-	-	-	-
	Turbo	-	-	-	-	✓	✓	✓	✓
JDD	SCMA	✓	-	✓	-	✓	-	✓	-
	Turbo	-	✓	-	✓	-	✓	-	✓
HDD	SCMA	✓	✓	-	-	✓	-	-	-
	Turbo	-	-	✓	✓	-	-	-	-

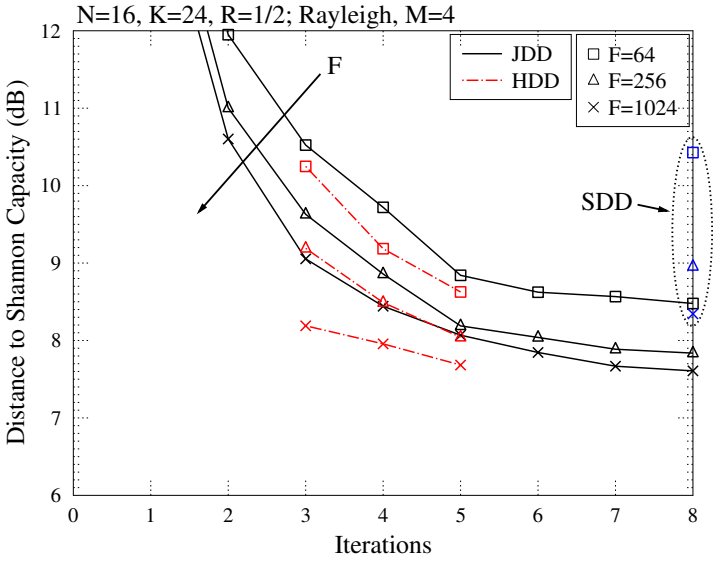

FIGURE 5.10: The distance to the Shannon capacity of SDD, JDD and HDD for a $N = 16, K = 24$ turbo-coded SCMA system in each iteration at a BER level of 10^{-3} over the uncorrelated Rayleigh fading channel, where $M = 4$ and $R = 1/2$.

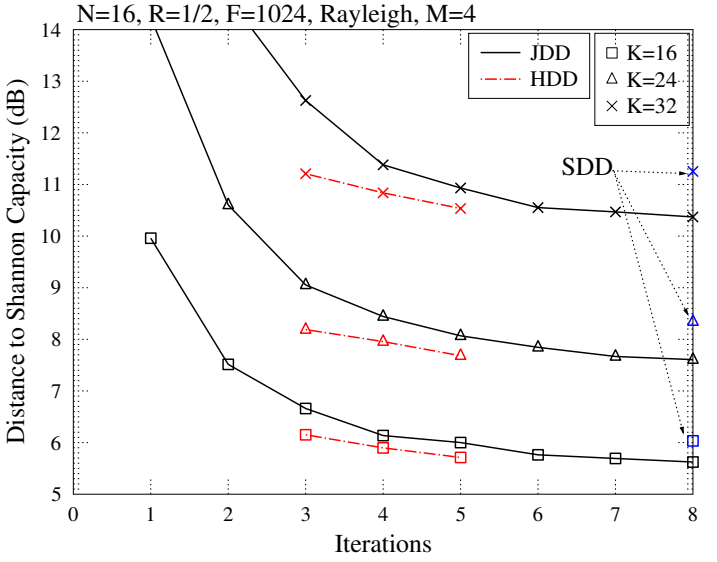

FIGURE 5.11: The distance to the Shannon capacity of SDD, JDD and HDD for the turbo-coded SCMA system supporting different number of users in each iteration at a BER level of 10^{-3} over the uncorrelated Rayleigh fading channel, where $N = 16, R = 1/2$ and $M = 4$.

TABLE 5.3: Complexity of the different detection and decoding schemes, where $N = 16$, $M = 4$.

Scheme	Iterations	Complexity ($\times 10^7$) when $F = 512$			Complexity ($\times 10^7$) when $F = 1024$		
		$K = 16$	$K = 24$	$K = 32$	$K = 16$	$K = 24$	$K = 32$
SDD / JDD	8	3.00	15.51	89.46	6.00	31.01	178.93
HDD	5	1.97	11.22	66.54	3.94	22.42	133.08

F at a BER level of 10^{-3}, whereas Fig. 5.11 shows influence of the normalized user-load λ. We can see that the HDD is capable of achieving slightly better BER than the JDD, despite its reduced number of iterations. This reduces the complexity as well as power consumption at the receiver and improves the detection latency. The BER performance of HDD in Figs. 5.10 and 5.11 provide us with design guidelines for the practical implementation of the receiver, where low-latency detection is attained at a given SNR based on our EXIT chart.

5.4.5 Complexity Analysis

The receiver complexity is quantified by the number of additions, multiplications, and max* calculations. The complexity of the Log-BCJR turbo decoder decoding A bits is defined in [158] as

$$\mathcal{C}_{\text{Log-BCJR}} = 171 AKT_{\text{Log-BCJR}}, \tag{5.23}$$

while the complexity of the MPA detector can be expressed as [78]

$$\mathcal{C}_{\text{MPA}} = \left[(2d_c + 4)M^{d_c} d_x + (d_x - 2 + M^{d_c - 1})M d_x - d_x\right] \times FKT_{\text{MPA}} + M(d_x - 1)KF. \tag{5.24}$$

Therefore, the total complexity of the different decoding and detection schemes is the sum of $\mathcal{C}_{\text{Log-BCJR}}$ in (5.23) and $\mathcal{C}_{\text{MPA}}$ in (5.24). Table 5.3 compares the complexity of SDD, JDD and HDD for turbo-coded SCMA systems at different λ values. We can see that by employing our HDD, a complexity reduction of up to 25% is achieved in the case of $\lambda = 2$, since only $T_{\text{Log-BCJR}} = 4$ and $T_{\text{MPA}} = 6$ inner iterations are required for Log-BCJR decoding and MPA detection, respectively.

5.5 Adaptive Turbo-Coded Sparse Code Multiple Access System

In this section, we propose an adaptive turbo-coded SCMA system design for transmission over correlated fading channels by harmonizing the user load λ, modulation order M and coding rate R based on different instantaneous SNR (iSNR). In this way, an

increased BPS throughput can be achieved at a given BER. The system design of the adaptive turbo-coded SCMA system will be detailed in Section 5.5.1, followed by the corresponding adaptive system performance in Section 5.5.2.

5.5.1 Adaptive System Design

In an adaptive modulation system, S transmission modes achieving different BPS throughputs are available at the transmitter, where the receiver estimates the iSNR and then determines the most appropriate transmission mode to be employed by the transmitter. According to [163], given the channel gains of the f-th transmitted symbol as $\bar{\boldsymbol{h}}_f$, the iSNR γ_i associated with transmitting a frame comprising F symbols can be expressed as

$$\gamma_i = \frac{\|\bar{\boldsymbol{h}}\|^2}{F}\gamma = \frac{\|\bar{\boldsymbol{h}}\|^2}{2F\sigma^2}, \tag{5.25}$$

where $\bar{\boldsymbol{h}} = [\bar{\boldsymbol{h}}_1^T, \bar{\boldsymbol{h}}_2^T, \cdots, \bar{\boldsymbol{h}}_F^T]^T$.

Then the iSNR γ_i is compared to the SNR thresholds at the receiver, which are required by the D fixed transmission modes to attain the target BER level. The mode selection requirements may be expressed as

$$\text{Mode Selection} = \begin{cases} \text{Mode 1}, & \text{if} \quad \gamma_i \leq \rho_1; \\ \text{Mode 2}, & \text{if} \quad \rho_1 < \gamma_i < \rho_2; \\ \vdots & \vdots \\ \text{Mode D}, & \text{if} \quad \gamma_i \geq \rho_{D-1}. \end{cases} \tag{5.26}$$

In this way, when the channel conditions are more favorable, a higher throughput may be achieved by selecting a higher-BPS mode, whereas a more robust but lower-BPS transmission mode will be employed in poorer channels.

In this section, we conceive $D = 3$ transmission mode candidates, as listed in Table 5.4, for our adaptive turbo-coded SCMA system, which jointly assign different normalised user loads, coding rates as well as modulation orders. As demonstrated in Section 5.4.2, the turbo-coded SCMA system is capable of supporting normalized user loads up to $\lambda = 2$. Therefore, two loads are selected, i.e. $\lambda = 1.5$ or 2. Meanwhile, the coding rates selected for the proposed adaptive system are $R = 1/4, 1/3$ and $1/2$, whereas the modulation order of different modes is either $M = 2$ or $M = 4$. To be more specific, in low-quality channels associated with low iSNRs, $\gamma_i < \rho_1$, a more robust mode associated with a lower throughput is selected, where the normalised user load λ is restricted to 1.5 and $R = 1/4$, $M = 2$ are employed. When iSNR γ_i exceeds the threshold ρ_1, we switch to Mode 2 for achieving a higher-throughput, associated with $\lambda = 1.5, R = 1/3$ $M = 4$. Finally, for the most favorable channels Mode 3 is activated, achieving the highest BPS by adopting $\lambda = 1.5$, $R = 1/3$ and $M = 4$.

TABLE 5.4: Transmission modes for the adaptive turbo-coded SCMA system.

Mode	Normalised user load λ	Code rate R	Modulation order M	BPS $\lambda R \log_2 M$
1	1.5	$\frac{1}{4}$	2	$\frac{3}{8}$
2	1.5	$\frac{1}{3}$	4	1
3	2	$\frac{1}{2}$	4	2

5.5.2 Performance of the Adaptive Turbo-Coded Sparse Code Multiple Access System

In this section, the performance of the proposed adaptive turbo-coded SCMA system employing HDD is evaluated for transmission over the Extended Typical Urban (ETU) channel model with a Doppler frequency of $f = 70$ Hz [164]. In this case, the mobile velocity v can be calculated as [165]

$$v = \frac{f \cdot c}{f_c} = 8.75 \text{ m/s}, \tag{5.27}$$

where $f_c = 2.4$ GHz is the carrier frequency employed in the IEEE 802.11 standard [166] and $c = 3 \times 10^8$ m/s is the speed of light.

Fig. 5.12 shows the BER performance of the three different modes of Table 5.4 and of the adaptive design switching amongst the three modes. Here, the switching thresholds of the different modes are determined by the average SNR required for achieving a BER of 10^{-3}, as shown in Fig. 5.12. For the three candidate modes conceived in Table 5.4, we have a pair of mode-switching thresholds, namely $\rho_1 = 8.4$ dB and $\rho_2 = 15.9$ dB. When $\gamma_i \leq \rho_1 = 8.4$ dB, Mode 1 is selected for transmission, giving a BPS throughput of 3/8. As and when the channel conditions become more favorable, i.e. for $\rho_1 = 8.4 < \gamma_i < \rho_2 = 15.9$ dB, the transmission mode is switched to Mode 2. Finally, when $\gamma_i \geq \rho_2 = 15.9$ dB, Mode 3 is selected for transmitting the users' signal. We can see that by adopting our adaptive transmission scheme, the BPS throughput varies from 3/8 to 2, depending on the choice of transmission modes. The corresponding PDF of the three modes in the adaptive system at different SNRs is shown in Fig. 5.13, which shows the dominant transmission mode at a specific SNR. It is also notable that at the threshold SNRs of 8.4 dB and 15.9 dB, the adjacent modes share equal probability of 0.5.

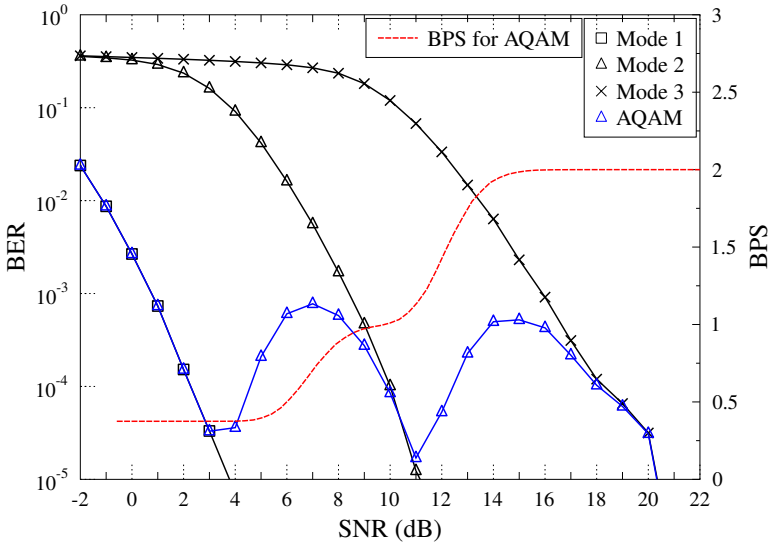

FIGURE 5.12: BER performance of the turbo-coded SCMA system over the ETU channel with a Doppler frequency of 70 Hz employing fixed or adaptive modulation design, where $N = 16$ is fixed for all scenarios, where the parameters of Table 5.4 are used.

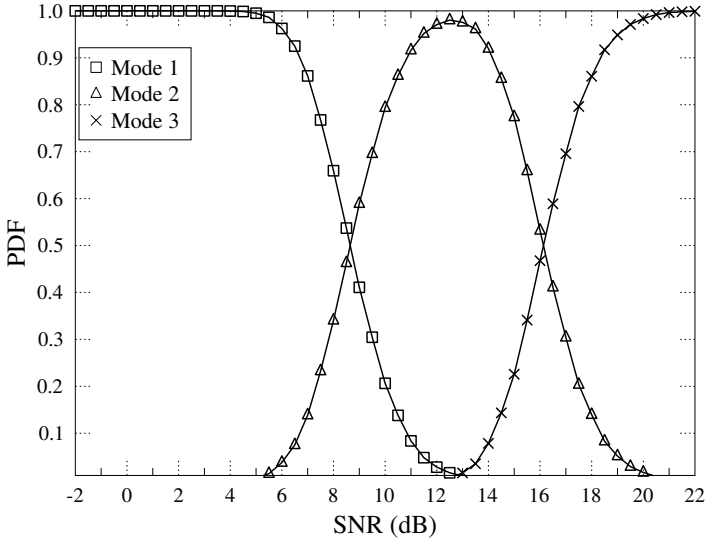

FIGURE 5.13: The PDF of the different modes in Table 5.4 in the adaptive turbo-coded SCMA system.

5.6 Chapter Summary and Conclusions

TABLE 5.5: Main conclusions of Chapter 5.

System	Adaptive Turbo-coded SCMA system		
Example	$M = 4$, $N = 16$, $F = 1024$		
Distance to Shannon Capacity of HDD at a BER of 10^{-3}	$K = 16$	$K = 24$	$K = 32$
	5.6 dB	6.6 dB	10.4 dB
Complexity when supporting $K = 24$ users ($\times 10^7$)	SDD	JDD	HDD
	31.01	31.01	22.42
Dominant mode at different SNRs (dB)	Mode 1	Mode 2	Mode 3
	$\gamma_i \leq 8.4 < \gamma_i$	$8.4 < \gamma_i < 15.9$	$\gamma_i \geq 15.9$

In this chapter, we focused our attention on the holistic design of SCMA systems, and have conceived an EXIT-chart-aided HDD algorithm for turbo-coded SCMA, which reduced the complexity of the conventional JDD by 25%, without degrading its BER performance. The main conclusions of this chapter are summarized in Table 5.5.

Furthermore, we proposed an adaptive turbo-coded SCMA system, where the transmitter selects its specific transmission mode according to the near-instantaneous channel conditions. The adaptive turbo-coded SCMA system harmonizes the user load, coding rate as well as modulation order so that a higher data rate is achieved in more favorable channel conditions by employing the high-BPS transmission modes, whereas the BER target performance is still maintained in the face of poorer channels by employing the more robust low-BPS transmission mode. Finally, our adaptive system design principle can be readily extended to SCMA systems in combination relying other channel coding schemes, such as LDPC codes and polar codes.

Chapter 6

Space-Time-Coded Generalized Spatial Modulation for Sparse Code Division Multiple Access

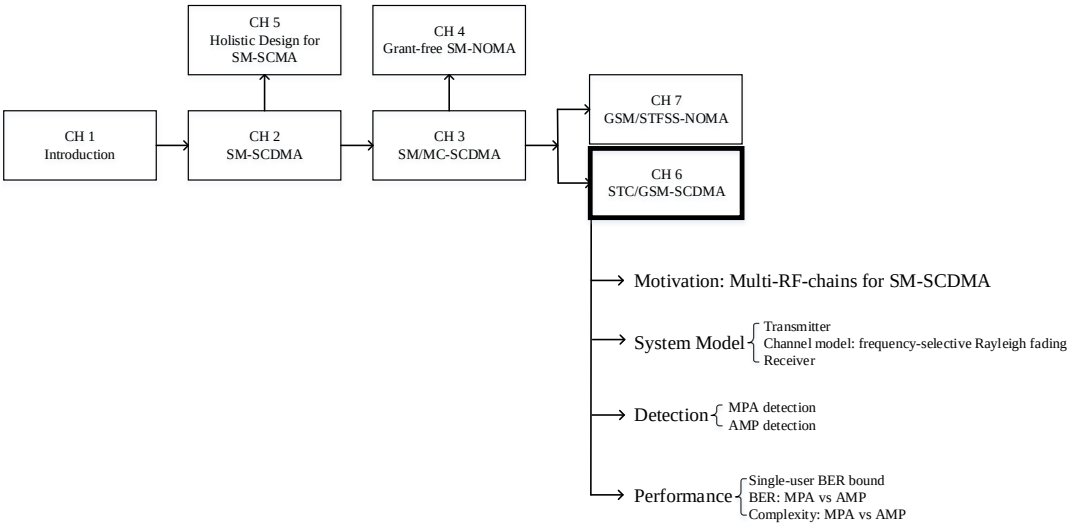

FIGURE 6.1: The relationship of Chapter 6 with the rest of the thesis.

6.1 Introduction

In this chapter, we extend our spatial-modulated nonorthogonal multiple access (SM-NOMA) systems investigated in Chapters 2 to 4, which activate a single transmit antenna (TA), to NOMA system assisted by multiple active TAs.

Currently, most studies of multiple-input multiple-output (MIMO)-NOMA rely on power-domain NOMA for downlink (DL) transmission. Since a pair of transmit antennas (TAs) has been standardized for the user's uplink (UL) transmission in the 3rd generation partnership project (3GPP) Release 16 [167,168], substantial transmit diversity gain may be attained in UL multiuser MIMO transmission. A higher number of TAs may be employed in the context of massive MIMO techniques for next-generation communications [169].

Motivated to exploit the uplink (UL) transmit diversity of the SM-SCMA system, we propose a space-time coded generalized spatial modulation (GSM) for SCMA (STC/GSM-SCMA) system along with a pair of detection algorithms. The properties of typical SM- or MIMO-NOMA systems [26,29,91,110,149,170] existing in literature is summarized in Table 6.1. The main contributions of this chapter are summarized as follows.

- Firstly, we propose a STC/GSM-SCDMA system for supporting the heavily-loaded multiuser (MU) multicarrier (MC) uplink, while achieving a beneficial transmit diversity gain both in the spatial- and in the FD. In our STC/GSM-SCDMA system, GSM is employed both for reducing the number of RF chains and for transmitting extra information bits via the activated TA indices, while STC is employed for exploiting spatial domain diversity. Meanwhile, by adopting the LDS concept in the FD, MC signalling can also be activated for mitigating the deleterious effects of frequency-selective fading. Furthermore, in contrast to the conventional orthogonal MU systems, where 'only' up to 100% normalized user-load can be attained, each orthogonal FD resource unit in the proposed STC/GSM-SCDMA system is capable of supporting more than 'just' a single user. Hence, our solution supports a high normalized user-load.

- Secondly, we design a joint factor graph for representing the connections of the proposed STC/GSM-SCDMA system, which combines the GSM symbols with the quadrature amplitude modulation (QAM) symbols and aggregates all observations at all RAs of each subcarrier. Then bespoke MPA detection is conceived based on the proposed joint factor graph.

- Thirdly, a 3-dimensional (3D) factor graph is designed, where the connections between users and TAs as well as those between subcarriers and RAs are separately illustrated, based on which a low-complexity AMP detector is proposed. The AMP detector conceived in this chapter imposes 1000 times lower computational complexity than the MPA detector, at the cost of a modest 2 dB BER SNR increase.

- Finally, the theoretical single-user performance bound is derived for the proposed STC/GSM-SCDMA system for transmission over frequency-selective Rayleigh fading channels, which is employed as the benchmark of the multiuser STC/GSM-SCDMA systems. Our simulation results also demonstrate that our STC/GSM-SCDMA system outperforms the MIMO-NOMA systems of [29,110].

TABLE 6.1: Overview of existing literature related to MIMO-NOMA systems.

Contributions	**STC/GSM-SCMA**	[91]	[26]	[170]	[110]	[149]	[29]
Generalized spatial modulation (GSM)	✓	✓					
Multiple-input multiple-output (MIMO)	✓	✓		✓	✓	✓	
Space-time coding (STC)	✓			✓	✓		
Sparse code multiple access (SCMA)	✓		✓		✓	✓	✓
3-dimensional (3D) diversity	✓				✓		
Multicarrier communications	✓						✓
Factor graph design	✓					✓	✓
Message passing-aided (MPA) detection	✓		✓	✓	✓		✓
Low-complexity detection	✓	✓				✓	
BER over frequency-selective channels	✓		✓				✓
Union bound	✓		✓		✓		✓

The rest of this chapter is structured as follows. Section 6.2 describes the transmitter and receiver of the proposed STC/GSM-SCDMA system. A pair of detection algorithms are proposed in Section 6.3, whereas the analysis of the single-user performance in a STC/GSM-SCDMA system is discussed in Section 6.4. Following this, Section 6.5 demonstrates the numerical results of the STC/GSM-SCDMA system performance in different cases. Finally, main conclusions of our work will be provided in Section 6.6.

6.2 System Model

In this section, we introduce the transmitter and receiver models of the proposed uplink STC/GSM-SCDMA system in Sections 6.2.1 and 6.2.2, respectively, along with the main assumptions used in the study.

6.2.1 Transmitter Model

Explicitly, we consider the uplink of a multiuser MC communication system, where K users simultaneously transmit their signals mapped to N subcarriers and N_T activated transmit antennas (TAs) per user to a single base station (BS) equipped with N_R receiver antennas (RAs). Frequency-selective Rayleigh fading channels having L CIR taps are considered. The STC/GSM-SCDMA transmitter of user k ($k \in [1, K]$) is shown in Fig. 6.2, where N_A TAs out of the total N_T TAs are activated to transmit user k's signal.

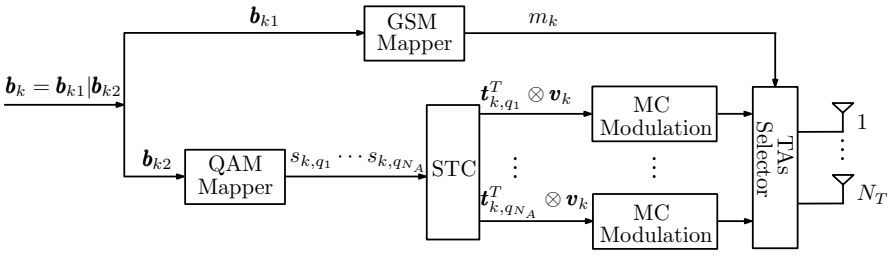

FIGURE 6.2: The transmitter schematic diagram of the kth user in the STC/GSM-SCDMA system.

More specifically, within a single symbol duration (SD), user k transmits the bit sequence $\boldsymbol{b}_k = \boldsymbol{b}_{k1}|\boldsymbol{b}_{k2}$ of $b = b_1 + b_2$ bits by N_A activated TAs chosen from the N_T TAs. Here, $\boldsymbol{b}_{k1}$ comprising $b_1 = \lfloor \log_2 \binom{N_T}{N_A} \rfloor$[1] bits is employed to activate N_A TA indices, forming a GSM symbol m_k in the GSM symbol set $\mathcal{M}_1 = \{\bar{m}_1, \cdots, \bar{m}_{M_1}\}$, where $M_1 = 2^{b_1}$. Table 6.2 exemplifies the bit-GSM symbol-TA mapping for a $N_T = 6$, $N_A = 2$ GSM/STC-SCDMA system. Hence, there exist $\binom{N_T}{N_A} = \binom{6}{2} = 15$ activated TA combinations, which indicates that $b_1 = \lfloor \log_2 15 \rfloor = 3$ bits can be conveyed by the TA activation patterns [41]. For

[1] $\lfloor x \rfloor$ represents the largest integer that is smaller than x.

TABLE 6.2: The bit-GSM symbol-TA mapping for a $N_T = 6$, $N_A = 2$ STC/GSM-SCDMA system.

$\boldsymbol{b}_{k1}$	$\mathcal{M}_1$	TA indices
000	$\bar{m}_1$	(1,4)
001	$\bar{m}_2$	(1,5)
010	$\bar{m}_3$	(1,6)
011	$\bar{m}_4$	(2,4)
100	$\bar{m}_5$	(2,5)
101	$\bar{m}_6$	(2,6)
110	$\bar{m}_7$	(3,5)
111	$\bar{m}_8$	(3,6)

instance, as shown in Table 6.2, $\boldsymbol{b}_{k1} = [000]$ maps to the GSM symbol $\bar{m}_1$, which activates the $q_1 = 1$-st and $q_2 = 4$-th TAs to transmit user k's signal. Meanwhile, a ($b_2 = N_A \log_2 M_2$)-bit sequence $\boldsymbol{b}_{k2}$ is mapped to N_A M_2QAM symbols, $\underbrace{s_{k,q_1}, s_{k,q_2}, \cdots, s_{k,q_{N_A}}}_{N_A}$, where $s_{k,q_a} \in \mathcal{S}$, $\mathcal{S}$ is the QAM symbol set and q_a, $a = 1, \cdots, N_A$, is the antenna index of the a-th activated TA.

Later, STC is performed on the N_A symbols $\underbrace{s_{k,q_1}, s_{k,q_2}, \cdots, s_{k,q_{N_A}}}_{N_A}$ of user k to achieve transmit diversity in the spatial domain. The well-known Alamouti STC code is formulated as [171]

$$\mathcal{G}_{k,2} = \frac{1}{\sqrt{2}} \begin{bmatrix} s_{k,q_1} & -s^*_{k,q_2} \\ s_{k,q_2} & s^*_{k,q_1} \end{bmatrix}, \tag{6.1}$$

where s_{k,q_1} and s_{k,q_2} represent the QAM symbols transmitted by the q_1-th and q_2-th TAs, respectively, in the $z = 1$-st SD, $-s^*_{k,q_2}$ and s^*_{k,q_1} denote the QAM symbols transmitted by the q_1-th and q_2-th TA, respectively, in the $z = 2$-nd SD.

In a more general form, the STC-coded QAM symbol of a general GSM/STC-SCDMA system employing N_A TA over the Z SDs can be expressed as

$$\boldsymbol{T}_k = \mathcal{G}^{(Z)}_{N_A,k} = \frac{1}{\sqrt{Z}} \begin{bmatrix} t^{(1)}_{k,q_1} & t^{(2)}_{k,q_1} & \cdots & t^{(Z)}_{k,q_1} \\ t^{(1)}_{k,q_2} & t^{(2)}_{k,q_2} & \cdots & t^{(Z)}_{k,q_2} \\ \vdots & \vdots & \ddots & \vdots \\ t^{(1)}_{k,q_{N_A}} & t^{(2)}_{k,q_{N_A}} & \cdots & t^{(Z)}_{k,q_{N_A}} \end{bmatrix}, \tag{6.2}$$

where $\mathcal{G}^{(Z)}_{N_A,k}$ represents the $(N_A \times Z)$-dimensional STC structure and $t^{(z)}_{k,q_a}$, $a = 1, \cdots, N_A$, and $z = 1, \cdots, Z$, is the STC-coded QAM symbol transmitted by q_a-th TA in the z-th SD. Since the QAM symbol s_{k,q_a} will be transmitted after STC in its original form s_{k,q_a}, or as s^*_{k,q_a}, or as $-s_{k,q_a}$, or as $-s^*_{k,q_a}$ in the z-th SD, we define $\tilde{\mathcal{S}}^{(z)}$ as the 'STC-transformed' QAM symbol set in the z-th SD. Again, considering the Alamouti-coded QAM symbols

of (6.1) transmitted by the q_1-th TA as an example, we have $t^{(1)}_{k,q_1} = s^{(1)}_{k,q_1} \in \tilde{\mathcal{S}}^{(1)} = \mathcal{S}$, which indicates that in the 1-st SD, $s^{(1)}_{k,q_1}$ is selected from the original set $\mathcal{S}$ without any transformation. By contrast, we have $t^{(2)}_{k,q_1} = -s^{*(2)}_{k,q_1} \in \tilde{\mathcal{S}}^{(2)} = -\mathcal{S}^*$, which means that in the 2-nd SD, the QAM symbol conveyed by the q_1-th TA will be transmitted in the form of $t^{(2)}_{k,q_1} = -s^{*(2)}_{k,q_1}$, where each symbol in the QAM symbol set $\mathcal{S}$ should be in this specific form, giving $\tilde{\mathcal{S}}^{(2)} = -\mathcal{S}^*$.

Following the STC, each STC-coded QAM symbol $t^{(z)}_{k,q_a}$ is sparsely spread over d_c subcarriers by adopting the $(N \times 1)$ LDS $\boldsymbol{v}_k$ preassigned to user k. The d_c non-zero elements in the sparse sequence $\boldsymbol{v}_k$ select the subcarriers employed for transmitting the QAM symbols of user k and are normalized to satisfy $\|\boldsymbol{v}_k\|^2 = 1$. The positions of the non-zero elements in $\boldsymbol{v}_k$ can be represented by an indicator matrix $\boldsymbol{V} = [\bar{\boldsymbol{v}}_1, \bar{\boldsymbol{v}}_2, \cdots, \bar{\boldsymbol{v}}_K]$, where $\bar{\boldsymbol{v}}_k$ is comprised of '1's and '0's representing the positions of non-zero elements and those of zero elements, respectively, in $\boldsymbol{v}_k$. For instance, for a $N = 4$, $K = 6$ GSM/STC-SCDMA system, we may have an indicator matrix $\boldsymbol{V}$ expressed as

$$\boldsymbol{V} = \begin{bmatrix} 1 & 1 & 1 & 0 & 0 & 0 \\ 1 & 0 & 0 & 1 & 1 & 0 \\ 0 & 1 & 0 & 1 & 0 & 1 \\ 0 & 0 & 1 & 0 & 1 & 1 \end{bmatrix}. \tag{6.3}$$

Correspondingly, the number of users sharing one of the N subcarriers is expressed as d_x, which has to obey $d_x << K$. Then, in the example of the Alamouti's code, the $(2N \times 2)$-dimensional transmit signal matrix can be formulated as

$$\boldsymbol{T}_k \otimes \boldsymbol{v}_k = \begin{bmatrix} s_{k,q_1} & -s^*_{k,q_2} \\ s_{k,q_2} & s^*_{k,q_1} \end{bmatrix} \otimes \boldsymbol{v}_k = \begin{bmatrix} t^{(1)}_{k,q_1} & t^{(2)}_{k,q_1} \\ t^{(1)}_{k,q_2} & t^{(2)}_{k,q_2} \end{bmatrix} \otimes \boldsymbol{v}_k, \tag{6.4}$$

where $\otimes$ is the Kronecker product.

6.2.2 Receiver Model

Let us express the L-path channel impulse response (CIR) $\boldsymbol{h}^{(r)}_{k,p}$ between the p-th TA $(p = 1, 2, \cdots, N_T)$ of user k and the r-th RA $(r = 1, 2, \cdots, N_R)$ at the BS in the TD as

$$\boldsymbol{h}^{(r)}_{k,p} = [h^{(r)}_{k,p,1}, h^{(r)}_{k,p,2}, \cdots, h^{(r)}_{k,p,L}]^T, \tag{6.5}$$

where $\boldsymbol{h}^{(r)}_{k,p}$ are independent identically distributed (iid) complex Gaussian random vectors with a zero mean and a variance of $0.5/L$ per dimension. Then, the corresponding FD channel transfer function (FD-CHTF) $\bar{\boldsymbol{h}}^{(r)}_{k,p}$ experienced by the N subcarriers can be

expressed as [103]

$$\bar{\boldsymbol{h}}_{k,p}^{(r)} = \boldsymbol{\mathcal{F}}\boldsymbol{\Phi}_L \boldsymbol{h}_{k,p}^{(r)}, \tag{6.6}$$

where $\boldsymbol{\Phi}_L$ is a $(N \times L)$ mapping matrix constituted by the first L columns of an identity matrix $\boldsymbol{I}_N$, and $\boldsymbol{\mathcal{F}}$ is the $(N \times N)$ FFT matrix having the property of $\boldsymbol{\mathcal{F}}\boldsymbol{\mathcal{F}}^H = \boldsymbol{\mathcal{F}}^H\boldsymbol{\mathcal{F}} = N\boldsymbol{I}_N$. When considering all the $(N_T \times N_R)$ antennas, the $(NN_R \times N_T)$-dimensional FD channel matrix $\bar{\boldsymbol{H}}_k$ of user k can be collectively expressed as

$$\bar{\boldsymbol{H}}_k = \begin{bmatrix} \bar{\boldsymbol{h}}_{k,1}^{(1)} & \cdots & \bar{\boldsymbol{h}}_{k,N_T}^{(1)} \\ \vdots & \ddots & \vdots \\ \bar{\boldsymbol{h}}_{k,1}^{(N_R)} & \cdots & \bar{\boldsymbol{h}}_{k,N_T}^{(N_R)} \end{bmatrix}. \tag{6.7}$$

Similar to the assumption employed in STC, we assume that the CIR $\bar{\boldsymbol{h}}_{k,p}^{(r)}$ of the proposed STC/GSM-SCDMA system remains constant across the Z SDs of one STC frame. Therefore, the $(N \times Z)$-dimensional received observations $\boldsymbol{Y}^{(r)}$ at the r-th RA over the Z SDs of a STC/GSM-SCDMA system having N_A activated TAs can be expressed as

$$\begin{aligned} \boldsymbol{Y}^{(r)} =& \frac{1}{\sqrt{Z}} \sum_{k=1}^{K} \left[\mathrm{diag}(\bar{\boldsymbol{h}}_{k,q_1}^{(r)}), \mathrm{diag}(\bar{\boldsymbol{h}}_{k,q_2}^{(r)}), \cdots, \mathrm{diag}(\bar{\boldsymbol{h}}_{k,q_a}^{(r)}) \right] (\boldsymbol{T}_k \otimes \boldsymbol{v}_k) + \boldsymbol{N}^{(r)} \\ =& \frac{1}{\sqrt{Z}} \sum_{k=1}^{K} \mathrm{diag}(\boldsymbol{v}_k) \left[\bar{\boldsymbol{h}}_{k,q_1}^{(r)} \cdots, \bar{\boldsymbol{h}}_{k,q_{N_A}}^{(r)} \right] \boldsymbol{T}_k + \boldsymbol{N}^{(r)} \\ =& \frac{1}{\sqrt{Z}} \sum_{k=1}^{K} \mathrm{diag}(\boldsymbol{v}_k) \bar{\boldsymbol{H}}_{m_k}^{(r)} \boldsymbol{T}_k + \boldsymbol{N}^{(r)}, \end{aligned} \tag{6.8}$$

where $\mathrm{diag}(\cdot)$ represents the diagonal matrix constructed by a vector, $\bar{\boldsymbol{H}}_{m_k}^{(r)} = \left[\bar{\boldsymbol{h}}_{k,q_1}^{(r)} \cdots, \bar{\boldsymbol{h}}_{k,q_{N_A}}^{(r)} \right]$ is a $(N \times N_A)$-dimensional channel matrix representing the FD CIRs between the N_A activated TAs selected by $m_k \in \mathcal{M}_1$ and the r-th RA at the BS. Additionally, $\boldsymbol{N}^{(r)}$ is the additive white Gaussian noise (AWGN) with each column obeying the Gaussian distribution with zero-mean and a covariance matrix of $2\sigma^2\boldsymbol{I}_N$, which may be expressed as $\mathcal{CN}(0, 2\sigma^2\boldsymbol{I}_N)$, where $\sigma^2 = 1/(2\gamma)$, γ denotes the signal-to-noise ratio (SNR) per symbol.

If we define the received observations $\boldsymbol{Y}$ of N_r RAs over the Z SDs of a STC/GSM-SCDMA system having N_A activated TAs as $\boldsymbol{Y} = \left[\left(\boldsymbol{Y}^{(1)}\right)^T, \left(\boldsymbol{Y}^{(2)}\right)^T, \cdots, \left(\boldsymbol{Y}^{(N_R)}\right)^T \right]^T$

and let $\bar{\boldsymbol{H}}_{m_k} = \left[\left(\bar{\boldsymbol{H}}_{m_k}^{(1)}\right)^T, \left(\bar{\boldsymbol{H}}_{m_k}^{(2)}\right)^T, \cdots, \left(\bar{\boldsymbol{H}}_{m_k}^{(N_R)}\right)^T\right]^T$, then we have

$$\begin{aligned}\boldsymbol{Y} =& \frac{1}{\sqrt{Z}} \sum_{k=1}^{K} \left(\boldsymbol{I}_{N_R} \otimes \mathrm{diag}(\boldsymbol{v}_k)\right) \bar{\boldsymbol{H}}_{m_k} \boldsymbol{T}_k + \boldsymbol{n} \\ =& \frac{1}{\sqrt{Z}} \sum_{k=1}^{K} \left(\boldsymbol{I}_{N_R} \otimes \mathrm{diag}(\boldsymbol{v}_k)\right) \bar{\boldsymbol{H}}_k \boldsymbol{E}_{m_k} \boldsymbol{T}_k + \boldsymbol{n} \\ =& \frac{1}{\sqrt{Z}} \sum_{k=1}^{K} \boldsymbol{H}_k \boldsymbol{E}_{m_k} \boldsymbol{T}_k + \boldsymbol{n}, \end{aligned} \tag{6.9}$$

where by definition, we have $\boldsymbol{H}_k = \left(\boldsymbol{I}_{N_R} \otimes \mathrm{diag}(\boldsymbol{v}_k)\right) \bar{\boldsymbol{H}}_k$, with $\bar{\boldsymbol{H}}_k$ given by (6.7) and $\boldsymbol{E}_{m_k}$ is a $(N_T \times N_A)$ dimensional TA selection matrix, whose a-th column has only the q_a-th $(a = 1, \cdots, N_A)$ element set to '1', while all the remaining elements are '0'.

Having obtained the MIMO observation equation of (6.9), let us now consider both our new message passing algorithm (MPA) and approximate message passing (AMP) based detector in the next section.

6.3 Detection Algorithms

In Sections 6.3.1 and 6.3.2, we propose the above pair of detectors for our STC/GSM-SCDMA system, respectively, following the introduction of two different factor graph representations of the received signals.

6.3.1 Message Passing-Aided Detection

Similar to other code-domain NOMA systems, the user-subcarrier relationship of the STC/GSM-SCDMA system can be visualized by a joint factor graph, comprising K variable nodes (VNs), representing the K symbols transmitted by K users, and N check nodes (CNs), related to the observations on N subcarriers. In contrast to the conventional factor graph, where a single VN is only associated with a single QAM symbol, the k-th $(k \in [1, K])$ VN in our proposed joint factor graph combines not only the GSM symbol determined by the activated TAs, but also the N_A QAM symbols transmitted by N_A activated TAs of user k, whereas, the n-th $(n \in [1, N])$ CN is comprised of the N_R observations from N_R RAs of the n-th subcarrier. For convenience, let us define the GSM-QAM symbol transmitted by the N_A activated TAs of user k as $u_k = \left(m_k | s_{k,q_1}, s_{k,q_2}, \cdots, s_{k,q_{N_A}}\right)$, with $u_k \in \mathcal{M} = \mathcal{M}_1 \otimes \mathcal{S}^{N_A}$.

The joint factor graph of our the STC/GSM-SCDMA system having $N = 4$ subcarriers, $d_c = 2$ and $d_x = 3$, supporting $K = 6$ users is exemplified in Fig. 6.3.

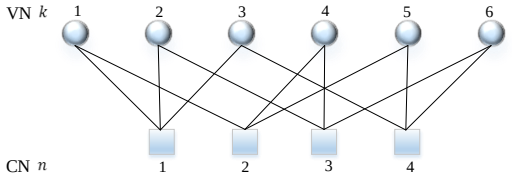

FIGURE 6.3: An example of the proposed joint factor graph design of the STC/GSM-SCDMA system with the parameters of $N = 4$, $d_c = 2$, $d_x = 3$ and $K = 6$.

Before we detail our MPA detector, let us first define the connections to the VN k and those to the CN n in the factor graph into two sets, which can be respectively expressed as

$$\mathcal{U}_k = \{n : 1 \leqslant n \leqslant N, e_{k,n} \neq 0\}, k = 1, \cdots, K \tag{6.10}$$

$$\mathcal{C}_n = \{k : 1 \leqslant k \leqslant K, e_{k,n} \neq 0, \}, n = 1, \cdots, N. \tag{6.11}$$

As shown in Fig. 6.3, information can be conveyed both upwards from the CN n to VN k and downward from VN k to CN n. Let us define $\delta_{n\to k}^{(g,i)}$ ($g \in \mathcal{M}$) as the information conveyed from CN n to VN k during the i-th iteration of the MPA detection, which represents the probability of $g = u_k$, when given the probabilities received by CN n from all the connected VNs $[n]$, excluding VN k, which can be expressed as $[n]\backslash k \in \{\mathcal{C}_n \backslash k\}$, where '\' represents the operation of exclusion. By contrast, the information transmitted from VN k to CN n in the i-th iteration is expressed as $\eta_{k\to n}^{(g,i)}$, which represents the probability of $g = u_k$, given the probabilities received by VN k from all the connected CNs $[k]$ excluding CN n, which can be expressed as $[k]\backslash n \in \{\mathcal{U}_k \backslash n\}$. Then the MPA based detector [29] operates as follows:

6.3.1.1 Initialisation

Since we assume equiprobable transmission of all symbols, $\eta_{k\to n}^{(g,0)}$ is initialised to $1/M$ for all $g = u_k \in \mathcal{M}$ and any $e_{k\to n} \neq 0$, where $M = M_1 \times M_2^{N_A}$.

6.3.1.2 Variable Node Update

Then, at the i-th iteration, the information conveyed by CN n to VN k, i.e. $\delta_{n\to k}^{(g,i)}$ for $k \in \mathcal{C}_n$ and $n \in \mathcal{U}_k$ is the product of the information gleaned from all the other edges connected to CN n, whereas the information received at VN k is the sum of the information arriving from all the CNs that are connected to VN k, which can be expressed

as

$$\delta_{n\to k}^{g,i} = \sum_{\boldsymbol{u}_{[n]}\in\mathcal{M}^{d_x-1}} \left(\prod_{u_{k'}\in\boldsymbol{u}_{[n]}\backslash u_k} \eta_{k'\to n}^{(g,i)} \right) \prod_{r=1}^{N_R} \prod_{z=1}^{Z} p(y_{nr}^{(z)}|\boldsymbol{u}_{[n]}, u_k = g), \tag{6.12}$$

where $\mathcal{M}^{d_x-1}$ represents the GSM-QAM symbol sets of the users connected to CN n excluding user k and $\prod_{u_{k'}\in\boldsymbol{u}_{[n]}\backslash u_k} \eta_{k'\to n}^{(g,i)}$ is the *a priori* probability of a given $\boldsymbol{u}_{[n]}\backslash u_k$ with $u_{k'} = g$. When $\boldsymbol{u}_{[n]}$ is given, the PDF of $p(y_{nr}^{(z)}|\boldsymbol{u}_{[n]})$ can be expressed as

$$p(y_{nr}^{(z)}|\boldsymbol{u}_{[n]}) = \frac{1}{2\pi\sigma^2} \exp\left(-\frac{|y_{nr}^{(z)} - \frac{1}{\sqrt{Z}} \sum_{k\in\mathcal{C}_n} \sum_{q_a\in m_k} h_{k,q_a,n}^{(r)} t_{k,q_a}^{(z)}|^2}{2\sigma^2} \right), \tag{6.13}$$

where $q_a \in m_k$ represents the activated TA selected by m_k and $\mathcal{C}_n$ is given in (6.11).

In particular, when Alamouti's code is employed, we have $N_A = 2, Z = 2$, and

$$p(y_{nr}^{(1)}|\boldsymbol{u}_{[n]}) = \frac{1}{2\pi\sigma^2} \exp\left(-\frac{\left| y_{nr}^{(1)} - \frac{1}{\sqrt{2}} \sum_{k\in\mathcal{C}_n} \left(h_{k,q_1,n}^{(r)} s_{k,q_1} + h_{k,q_2,n}^{(r)} s_{k,q_2} \right) \right|^2}{2\sigma^2} \right), \tag{6.14}$$

$$p(y_{nr}^{(2)}|\boldsymbol{u}_{[n]}) = \frac{1}{2\pi\sigma^2} \exp\left(-\frac{\left| y_{nr}^{(2)} - \frac{1}{\sqrt{2}} \sum_{k\in\mathcal{C}_n} \left(-h_{k,q_1,n}^{(r)} s_{k,q_2}^{*} + h_{k,q_2,n}^{(r)} s_{k,q_1}^{*} \right) \right|^2}{2\sigma^2} \right). \tag{6.15}$$

6.3.1.3 Check Node Update

Next, at the $(i+1)$-st iteration, the values $\delta_{n\to k}^{(g,i)}$ obtained in the i-th iteration are used to update $\eta_{k\to n}^{(g,i+1)}$, which can be expressed as

$$\eta_{k\to n}^{(g,i+1)} = \varepsilon_{k,n} \prod_{n'\in\mathcal{U}_k\backslash n} \delta_{n'\to k}^{(g,i)}, \tag{6.16}$$

where $\varepsilon_{k,n}$ is the normalisation factor enabling $\sum_{g\in\mathcal{M}} \eta_{k\to n}^{(g,i+1)} = 1$.

6.3.1.4 Symbol Mapping

Finally, after the pre-set number of iterations I is reached, the detector detects the transmitted symbol of the kth user as

$$\hat{u}_k = (\hat{m}_k|\hat{s}_{k,q_1}, \cdots, \hat{s}_{k,q_a}) = \arg\max_{g\in\mathcal{M}} \prod_{n\in\mathcal{U}_k} \delta_{n\to k}^{(g,I)},\ k = 1, 2, \ldots, K. \tag{6.17}$$

We can see from (6.12) that the computational complexity is primarily dominated by the upward information transition, giving a complexity order of $\mathcal{O}(M^{d_x-1}) = \mathcal{O}((M_1 M_2^{N_A})^{d_x-1})$.

6.3.2 Approximated Message Passing Detection

From the above discussion we know that the MPA complexity order is $\mathcal{O}\left[(M_1 M_2^{N_A})^{d_x-1}\right]$, which increases exponentially with the number of users d_x sharing a single subcarrier, and the number of TAs activated per symbol. In order to reduce the detection complexity, we now propose a novel detection algorithm for our STC/GSM-SCDMA system by appropriately adapting the AMP algorithm [172,173], which approximates the downward propagation of STC-coded QAM symbol $t_{k,q_a}^{(z)}$ transmitted by q_a-th TA of user k at z-th SD to obey a complex Gaussian distribution $\mathcal{N}_{\mathbb{C}}(t_{k,q_a}^{(z)}; \mu_{km_k\to nr}^{(q_a,z,i)}, \omega_{km_k\to nr}^{(q_a,z,i)})$ [173, 174], where $\mu_{km_k\to nr}^{(q_a,z,i)}$ and $\omega_{km_k\to nr}^{(q_a,z,i)}$ represent the mean and variance of the complex random variable $t_{k,q_a}^{(z)}$, respectively.

Now that the STC-coded QAM symbols and the GSM symbol are detected separately, we design a 3D factor graph representation of the STC/GSM-SCDMA systems, as exemplified in Fig. 6.4, before we introduce the AMP detection. More specifically, VN k in the joint factor graph of Fig. 6.3 is now expanded to M_1 sub-nodes, which represent the M_1 GSM symbols that are possibly employed to select user k's activated TAs. Hence, VN km_k represents the N_A activated TAs of user k determined by the GSM symbol $m_k \in \mathcal{M}_1$, as exemplified in Table 6.2. By contrast, each CN in the 3D factor graph now combines all the N_R observations obtained from the N_R RAs, such that CN nr $(n = 1, 2, \cdots, N,\ r = 1, 2, \cdots, N_R,)$ represents the observation of the n-th subcarrier at the r-th RA at the receiver.

Therefore, the connections to VN km_k and to CN nr in the proposed 3D factor graph can then be defined in two sets, expressed as

$$\mathcal{U}_{km_k} = \{n : 1 \leqslant n \leqslant N, r : 1 \leqslant r \leqslant N_R, e_{km_k,nr} \neq 0\}, k = 1, \cdots, K, m_k \in \mathcal{M}_1 \tag{6.18}$$

$$\mathcal{C}_{nr} = \{m_k \in \mathcal{M}_1, k : 1 \leqslant k \leqslant K, e_{km_k,nr} \neq 0\}, n = 1, \cdots, N, r = 1, \cdots, N_R \tag{6.19}$$

Similar to the MPA detection, the AMP detection also passes information both upwards and downwards via the 3D factor graph of Fig. 6.4. Now let us define the information

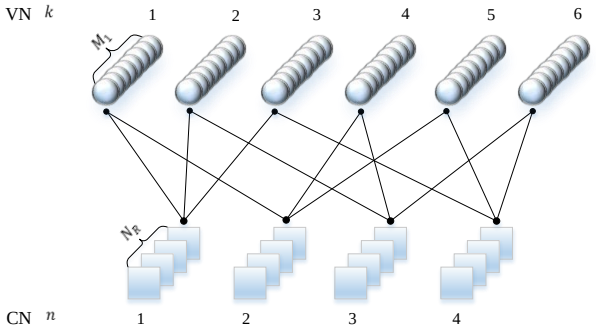

FIGURE 6.4: An example of the proposed 3D factor graph design of the STC/GSM-SCDMA system with the parameters of $N = 4$, $d_c = 2$, $d_x = 3$ and $K = 6$.

associated with $t_{k,q_a}^{(z)}$ passed from VN km_k to CN nr in the i-th iteration as $\eta_{km_k \to nr}^{(i)}(t_{k,q_a}^{(z)})$, whereas the reverse information transmission from CN nr to VN km_k in the i-th iteration as $\delta_{nr \to km_k}^{(i)}(t_{k,q_a}^{(z)})$. Then, the proposed AMP detector for the STC/GSM-SCDMA system operates the following steps:

6.3.2.1 Initialisation

The initialisation of the information $\eta_{km_k \to nr}^{(0)}(t_{k,q_a}^{(z)})$ from VN km_k to CN nr is under the assumption of equiprobable transmission, which can be expressed as $\eta_{km_k \to nr}^{(0)}(t_{k,q_a}^{(z)}) = 1/M$. Hence, in the 1-st iteration we have the mean $\mu_{km_k \to nr}^{(q_a,z,1)}$ and variance $\omega_{km_k \to nr}^{(q_a,z,1)}$ for the Gaussian distributed variable $t_{k,q_a}^{(z)}$, which are expressed as

$$\mu_{km_k \to nr}^{(q_a,z,1)} = \sum_{t_{k,q_a}^{(z)} \in \tilde{\mathcal{S}}^{(z)}} t_{k,q_a}^{(z)} \cdot \eta_{km_k \to nr}^{(0)}(t_{k,q_a}^{(z)}) = \frac{1}{M} \sum_{t_{k,q_a}^{(z)} \in \tilde{\mathcal{S}}^{(z)}} t_{k,q_a}^{(z)} \tag{6.20}$$

$$\omega_{km_k \to nr}^{(q_a,z,1)} = \sum_{t_{k,q_a}^{(z)} \in \tilde{\mathcal{S}}^{(z)}} \left| t_{k,q_a}^{(z)} \right|^2 \cdot \eta_{km_k \to nr}^{(0)}(t_{k,q_a}^{(z)}) - \left| \mu_{km_k \to nr}^{(q_a,z,1)} \right|^2, \tag{6.21}$$

respectively, where $\tilde{\mathcal{S}}^{(z)}$ represents the 'STC-transformed' QAM symbol set of user k in the z-th SD, as defined in Section II-A.

6.3.2.2 Variable Node Update

Rather than updating $\eta_{km_k \to nr}^{(i)}(t_{k,q_a}^{(z)})$ using (6.12), as that in MPA detector, the AMP detector approximates $\eta_{km_k \to nr}^{(i)}(t_{k,q_a}^{(z)})$ as a complex Gaussian variable with the distribution $\mathcal{N}_{\mathbb{C}}(t_{k,q_a}^{(z)}; \mu_{km_k \to nr}^{(q_a,z,i)}, \omega_{km_k \to nr}^{(q_a,z,i)})$, which will be derived after the description of the CN update in the next step, as given in (6.29) and (6.30).

Then, in the i-th iteration of the AMP detection, the update of $\delta^{(i)}_{nr\to km_k}(t^{(z)}_{k,q_a})$ is similar to that of the MPA detector, which is also the product of the information obtained from all the other edges connected to CN nr, and can be expressed as

$$\delta^{(i)}_{nr\to km_k}(t^{(z)}_{k,q_a}) = \sum_{\boldsymbol{u}_{[n]}\setminus(m_k|t^{(z)}_{k,q_a})} \left(\prod_{k'm'_k\in\mathcal{C}_{nr}\setminus km_k} \prod_{q'_a\in m'_k} \mathcal{N}_{\mathbb{C}}(t^{(z)}_{k',q'_a}; \mu^{(q'_a,z,i)}_{k'm'_k\to nr}, \omega^{(q'_a,z,i)}_{k'm'_k\to nr}) \right) p(y^{(z)}_{nr}|\boldsymbol{u}_{[n]}), \tag{6.22a}$$

$$= \mathcal{N}_{\mathbb{C}}(h^{(r)}_{k,q_a,n} t^{(z)}_{k,q_a}; \alpha^{(q_a,z,i)}_{nr\to km_k}, \beta^{(q_a,z,i)}_{nr\to km_k}), \tag{6.22b}$$

where $p(y^{(z)}_{nr}|\boldsymbol{u}_{[n]})$ is given by (6.13) and is also Gaussian distributed. Hence, $\delta^{(i)}_{nr\to km_k}(t^{(z)}_{k,q_a})$ can also be approximated by a Gaussian distribution $\mathcal{N}_{\mathbb{C}}(h^{(r)}_{k,q_a,n} t^{(z)}_{k,q_a}; \alpha^{(q_a,z,i)}_{nr\to km_k}, \beta^{(q_a,z,i)}_{nr\to km_k})$, as shown in (6.22b), where $\alpha^{(q_a,z,i)}_{nr\to km_k}$ and $\beta^{(q_a,z,i)}_{nr\to km_k}$ are the mean and variance of the variable $h^{(r)}_{k,q_a,n} t^{(z)}_{k,q_a}$ and can be expressed as

$$\alpha^{(q_a,z,i)}_{nr\to km_k} = y^{(z)}_{nr} - \sum_{k'm'_k\in\mathcal{C}_{nr}} \sum_{q'_a\in m'_k} \left(h^{(r)}_{k',q'_a,n} \mu^{(q'_a,z,i)}_{k'm'_k\to nr} \right) + h^{(r)}_{k,q_a,n} \mu^{(q_a,z,i)}_{km_k\to nr}, \tag{6.23}$$

$$\beta^{(q_a,z,i)}_{nr\to km_k} = \sigma^2 + \sum_{k'm'_k\in\mathcal{C}_{nr}} \sum_{q'_a\in m'_k} \left(|h^{(r)}_{k',q'_a,n}|^2 \omega^{(q'_a,z,i)}_{k'm'_k\to nr} \right) - |h^{(r)}_{k,q_a,n}|^2 \omega^{(q_a,z,i)}_{km_k\to nr}, \tag{6.24}$$

respectively.

6.3.2.3 Check Node Update

The updated $\delta^{(i)}_{nr\to km_k}(t^{(z)}_{k,q_a})$ will be conveyed to CN nr via the edge $\bar{e}_{km_k,nr}$ of the 3D factor graph, for updating $\eta^{(q,i)}_{k,n}$. Following the message passing rules, we have

$$\eta^{(i)}_{km_k\to nr}(t^{(z)}_{k,q_a}) = \varepsilon_{km_k,nr} \prod_{n'r'\in\mathcal{U}_{km_k}\setminus nr} \delta^{(i)}_{n'r'\to km_k}(t^{(z)}_{k,q_a}), \tag{6.25}$$

where $\varepsilon_{km_k,nr}$ is the normalisation factor enabling $\sum_{m_k\in\mathcal{M}_1} \sum_{t^{(z)}_{k,q_a}\in\tilde{\mathcal{S}}} \eta^{(i)}_{km_k\to nr}(t^{(z)}_{k,q_a}) = 1$. By applying (6.22b) to (6.25), we obtain

$$\eta^{(i)}_{km_k\to nr}(t^{(z)}_{k,q_a}) = \frac{\mathcal{N}_{\mathbb{C}}\left(t^{(z)}_{k,q_a}; \lambda^{(q_a,z,i)}_{km_k\to nr}, \varphi^{(q_a,z,i)}_{km_k\to nr}\right)}{\sum_{m'_k\in\mathcal{M}_1} \sum_{t'^{(z)}_{k,q_a}\in\tilde{\mathcal{S}}} \mathcal{N}_{\mathbb{C}}\left(t'^{(z)}_{k,q_a}; \lambda^{(q_a,z,i)}_{km'_k\to nr}, \varphi^{(q_a,z,i)}_{km'_k\to nr}\right)} \tag{6.26}$$

where $\varphi^{(q_a,z,i)}_{km_k\to nr}$ and $\lambda^{(q_a,z,i)}_{km_k\to nr}$ can be expressed respectively as

$$\varphi^{(q_a,z,i)}_{km_k\to nr} = \lambda^{(q_a,z,i)}_{km_k\to nr} \left(\sum_{n'r'\in\mathcal{U}_{km_k}} \frac{h^{*(r')}_{k,q_a,n'} \alpha^{(q_a,z,i)}_{n'r'\to km_k}}{\beta^{(q_a,z,i)}_{n'r'\to km_k}} - \frac{h^{*(r)}_{k,q_a,n} \alpha^{(q_a,z,i)}_{nr\to km_k}}{\beta^{(q_a,z,i)}_{nr\to km_k}} \right) \tag{6.27}$$

$$\lambda_{km_k\to nr}^{(q_a,z,i)} = \left(\sum_{n'r'\in\mathcal{U}_{km_k}} \frac{|h_{k,q_a,n'}^{(r')}|^2}{\beta_{n'r'\to km_k}^{(q_a,z,i)}} - \frac{|h_{k,q_a,n}^{(r)}|^2}{\beta_{nr\to km_k}^{(q_a,z,i)}} \right)^{-1}. \tag{6.28}$$

A classic technique of finding the Gaussian approximation of $\eta_{km_k\to nr}^{(i)}(t_{k,q_a}^{(z)})$ in the i-th iteration is by minimizing the inclusive Kullback-Leibler (KL) divergence [173, 175], expressed as $\mathrm{KL}\Big(\eta_{km_k\to nr}^{(i)}(t_{k,q_a}^{(z)}) \parallel \tilde{\eta}_{km_k\to nr}^{(i)}(t_{k,q_a}^{(z)})\Big)$, giving the mean and variance of

$$\mu_{km_k\to nr}^{(q_a,z,i)} = \sum_{t_{k,q_a}^{(z)}\in\tilde{\mathcal{S}}^{(z)}} t_{k,q_a}^{(z)} \cdot \eta_{km_k\to nr}^{(i-1)}(t_{k,q_a}^{(z)}) \tag{6.29}$$

$$\omega_{km_k\to nr}^{(q_a,z,i)} = \sum_{t_{k,q_a}^{(z)}\in\tilde{\mathcal{S}}} \left|t_{k,q_a}^{(z)}\right|^2 \cdot \eta_{km_k\to nr}^{(i-1)}(t_{k,q_a}^{(z)}) - \left|\mu_{km_k\to nr}^{(q_a,z,i)}\right|^2. \tag{6.30}$$

Furthermore, since STC is employed in the proposed STC/GSM-SCDMA system, the QAM symbol $s_{k,q_a}^{(1)}$ of user k, which is initially transmitted by the q_a-th TA, is also re-transmitted by the other activated TAs in the following $(Z-1)$ SDs, after some form of 'STC-transformation', for example, in its additive inverse or conjugate form, as discussed in Section 6.2.1. Hence, the information associated with $s_{k,q_a}^{(1)}$ can be obtained over all the Z SDs and can be exploited for improving the reliability of the information passing in the next iteration. For example, when Alamouti's code of (6.1) is employed, the mean $\varphi_{km_k\to nr}^{(q_a,z,i)}$ and variance $\lambda_{km_k\to nr}^{(q_a,z,i)}$ for $z=1$, 2, and $q_a=q_1$, $q_a=q_2$ can be expressed in (6.31) and (6.32), respectively as

$$\varphi_{km_k\to nr}^{(q_1,1,i)} = \lambda_{km_k\to nr}^{(q_1,1,i)} \left(\sum_{n'r'\in\mathcal{U}_{km_k}} \frac{h_{k,q_1,n'}^{*(r')}\alpha_{n'r'\to km_k}^{(q_1,1,i)}}{\beta_{n'r'\to km_k}^{(q_1,1,i)}} + \sum_{n'r'\in\mathcal{U}_{km_k}} \frac{h_{k,q_2,n'}^{*(r')}\alpha_{n'r'\to km_k}^{*(q_2,2,i)}}{\beta_{n'r'\to km_k}^{(q_2,2,i)}} - \frac{h_{k,q_1,n}^{*(r)}\alpha_{nr\to km_k}^{(q_1,1,i)}}{\beta_{nr\to km_k}^{(q_1,1,i)}} \right) \tag{6.31a}$$

$$\varphi_{km_k\to nr}^{(q_2,1,i)} = \lambda_{km_k\to nr}^{(q_2,1,i)} \left(\sum_{n'r'\in\mathcal{U}_{km_k}} \frac{h_{k,q_2,n'}^{*(r')}\alpha_{n'r'\to km_k}^{(q_2,1,i)}}{\beta_{n'r'\to km_k}^{(q_2,1,i)}} - \sum_{n'r'\in\mathcal{U}_{km_k}} \frac{h_{k,q_1,n'}^{*(r')}\alpha_{n'r'\to km_k}^{*(q_1,2,i)}}{\beta_{n'r'\to km_k}^{(q_1,2,i)}} - \frac{h_{k,q_2,n}^{*(r)}\alpha_{nr\to km_k}^{(q_2,1,i)}}{\beta_{nr\to km_k}^{(q_2,1,i)}} \right) \tag{6.31b}$$

$$\varphi_{km_k\to nr}^{(q_1,2,i)} = \lambda_{km_k\to nr}^{(q_1,2,i)} \left(\sum_{n'r'\in\mathcal{U}_{km_k}} \frac{h_{k,q_1,n'}^{*(r')}\alpha_{n'r'\to km_k}^{(q_1,2,i)}}{\beta_{n'r'\to km_k}^{(q_1,2,i)}} + \sum_{n'r'\in\mathcal{U}_{km_k}} \frac{h_{k,q_2,n'}^{*(r')}\alpha_{n'r'\to km_k}^{*(q_2,1,i)}}{\beta_{n'r'\to km_k}^{(q_2,1,i)}} - \frac{h_{k,q_1,n}^{*(r)}\alpha_{nr\to km_k}^{(q_1,2,i)}}{\beta_{nr\to km_k}^{(q_2,1,i)}} \right) \tag{6.31c}$$

$$\varphi_{km_k\to nr}^{(q_2,2,i)} = \lambda_{km_k\to nr}^{(q_2,2,i)} \left(\sum_{n'r'\in\mathcal{U}_{km_k}} \frac{h_{k,q_2,n'}^{*(r')}\alpha_{n'r'\to km_k}^{(q_2,2,i)}}{\beta_{n'r'\to km_k}^{(q_2,2,i)}} + \sum_{n'r'\in\mathcal{U}_{km_k}} \frac{h_{k,q_1,n'}^{*(r')}\alpha_{n'r'\to km_k}^{*(q_1,1,i)}}{\beta_{n'r'\to km_k}^{(q_1,1,i)}} - \frac{h_{k,q_2,n}^{*(r)}\alpha_{nr\to km_k}^{(q_2,2,i)}}{\beta_{nr\to km_k}^{(q_2,1,i)}} \right) \tag{6.31d}$$

$$\lambda_{km_k\to nr}^{(q_1,1,i)} = \left(\sum_{n'r'\in\mathcal{U}_{km_k}} \frac{|h_{k,q_1,n'}^{(r')}|^2}{\beta_{n'r'\to km_k}^{(q_1,1,i)}} + \sum_{n'r'\in\mathcal{U}_{km_k}} \frac{|h_{k,q_2,n'}^{(r')}|^2}{\beta_{n'r'\to km_k}^{(q_2,2,i)}} - \frac{|h_{k,q_1,n}^{(r)}|^2}{\beta_{nr\to km_k}^{(q_1,1,i)}} \right)^{-1} \tag{6.32a}$$

$$\lambda_{km_k\to nr}^{(q_2,1,i)} = \left(\sum_{n'r'\in\mathcal{U}_{km_k}} \frac{|h_{k,q_2,n'}^{(r')}|^2}{\beta_{n'r'\to km_k}^{(q_2,1,i)}} + \sum_{n'r'\in\mathcal{U}_{km_k}} \frac{|h_{k,q_1,n'}^{(r')}|^2}{\beta_{n'r'\to km_k}^{(q_1,2,i)}} - \frac{|h_{k,q_2,n}^{(r)}|^2}{\beta_{nr\to km_k}^{(q_2,1,i)}} \right)^{-1} \tag{6.32b}$$

$$\lambda_{km_k\to nr}^{(q_1,2,i)} = \left(\sum_{n'r'\in\mathcal{U}_{km_k}} \frac{|h_{k,q_1,n'}^{(r')}|^2}{\beta_{n'r'\to km_k}^{(q_1,2,i)}} + \sum_{n'r'\in\mathcal{U}_{km_k}} \frac{|h_{k,q_2,n'}^{(r')}|^2}{\beta_{n'r'\to km_k}^{(q_2,1,i)}} - \frac{|h_{k,q_1,n}^{(r)}|^2}{\beta_{nr\to km_k}^{(q_1,2,i)}} \right)^{-1} \tag{6.32c}$$

$$\lambda_{km_k\to nr}^{(q_2,2,i)} = \left(\sum_{n'r'\in\mathcal{U}_{km_k}} \frac{|h_{k,q_2,n'}^{(r')}|^2}{\beta_{n'r'\to km_k}^{(q_2,2,i)}} + \sum_{n'r'\in\mathcal{U}_{km_k}} \frac{|h_{k,q_1,n'}^{(r')}|^2}{\beta_{n'r'\to km_k}^{(q_1,1,i)}} - \frac{|h_{k,q_2,n}^{(r)}|^2}{\beta_{nr\to km_k}^{(q_2,2,i)}} \right)^{-1}. \tag{6.32d}$$

Considering (6.31) as an example, we combine the statistics of the QAM symbol s_{k,q_1} over the $Z = 2$ SDs. Since s_k^2 is transmitted by the q_1-th TA in the 1-st SD and its conjugate form s_{k,q_1}^* is transmitted by q_2-th TA in the 2-nd SD, the mean $\alpha_{nr\to km_k}^{(q_2,2,i)}$ of the Gaussian distribution $\mathcal{N}_{\mathbb{C}}(h_{k,q_2,n}^{(r)}t_{k,q_2}^{(2)}; \alpha_{nr\to km_k}^{(q_2,2,i)}, \beta_{nr\to km_k}^{(q_2,2,i)})$ has to be conjugated before combining, giving the expression of the second term of (6.31).

6.3.2.4 Final Iteration

After a pre-determined number $\bar{I}$ of iterations is reached, we calculate the information of the km_k-th VN gleaned from all CNs that are connected to the km_k-th VN, which can be expressed as

$$\eta_{km_k}^{(\bar{I})}(t_{k,q_a}^{(z)}) = \frac{\mathcal{N}_{\mathbb{C}}\left(t_{k,q_a}^{(z)}; \lambda_{km_k}^{(q_a,z,\bar{I})}, \varphi_{km_k}^{(q_a,z,\bar{I})}\right)}{\sum_{m_k'\in\mathcal{M}_1}\sum_{t_{k,q_a}^{\prime(z)}\in\tilde{\mathcal{S}}}\mathcal{N}_{\mathbb{C}}\left(t_{k,q_a}^{\prime(z)}; \lambda_{km_k'}^{(q_a,z,\bar{I})}, \varphi_{km_k'}^{(q_a,z,\bar{I})}\right)}, \tag{6.33}$$

where $\lambda_{km_k}^{(q_a,z,\bar{I})}$ and $\varphi_{km_k}^{(q_a,z,\bar{I})}$ are the mean and variance of the variable $t_{k,q_a}^{(z)}$ in the $\bar{I}$-th iteration and can be respectively expressed as

$$\varphi_{km_k}^{(q_a,z,\bar{I})} = \lambda_{km_k}^{(q_a,z,I)} \left(\sum_{n'r' \in \mathcal{U}_{km_k}} \frac{h_{k,q_a,n'}^{*(r')} \alpha_{n'r'}^{(q_a,z,\bar{I})}}{\beta_{n'r'\to km_k}^{(q_a,z,I)}} \right) \tag{6.34}$$

$$\lambda_{km_k}^{(q_a,z,\bar{I})} = \left(\sum_{n'r' \in \mathcal{U}_{km_k}} \frac{|h_{k,q_a,n'}^{(r')}|^2}{\beta_{n'r'}^{(q_a,z,I)}} \right)^{-1}. \tag{6.35}$$

6.3.2.5 Symbol Mapping

The symbol mapping process can be expressed as

$$\hat{m}_k | \hat{t}_{k,q_1}^{(z)}, \cdots, \hat{t}_{k,q_a}^{(z)} = \arg \max_{\substack{m_k \in \mathcal{M}_1, q_a \in m_k \\ t_{k,q_a}^{(z)} \in \tilde{\mathcal{S}}^{(z)}}} \eta_{km_k}^{(\bar{I})}(t_{k,q_a}^{(z)}), \ k = 1, 2, \ldots, K. \tag{6.36}$$

In summary, the proposed AMP detection algorithm of our STC/GSM-SCDMA system is summarized in Algorithm 5 and the complexity of the proposed AMP detector as well as its comparison to the MPA detector will be discussed in Section 6.5.2.

Algorithm 5 AMP detection for STC/GSM-SCDMA

Input:

Received observations $\boldsymbol{y}^{(r)}$, CSI $\bar{\boldsymbol{h}}_{m_k}^{(r)}$ for $m_k \in \mathcal{M}_1$, $r = 1, 2, \cdots, N_R$ and indicator matrix $\boldsymbol{V}$;

Output:

Detected symbols $\left(\hat{m}_k | \hat{t}_{k,q_1}^{(z)}, \cdots, \hat{t}_{k,q_a}^{(z)} \right)$.

Initialization:

$\eta_{km_k \to nr}^{(0)}(t_{k,q_a}^{(z)}) = 1/M$, $t_{k,q_a}^{(z)} \in \tilde{\mathcal{S}}^{(z)}$, $nr \in \mathcal{U}_{km_k}$, $k = 1, 2, \cdots, K$.

1: **for** $i = 1, \cdots, \bar{I}$ **do**
2: Calculate $\mu_{km_k \to nr}^{(q_a,z,i)}$ and $\omega_{km_k \to nr}^{(q_a,z,i)}$ using (6.29) and (6.30), respectively;
3: Calculate $\alpha_{nr \to km_k}^{(q_a,z,i)}$ and $\beta_{nr \to km_k}^{(q_a,z,i)}$ using (6.23) and (6.24), respectively;
4: Calculate $\lambda_{km_k \to nr}^{(q_a,z,i)}$ and $\varphi_{km_k \to nr}^{(q_a,z,i)}$ using (6.27) and (6.28), respectively;
5: Update $\eta_{km_k \to nr}^{(i)}(t_{k,q_a}^{(z)})$ using (6.26);
6: **end for**
7: Calculate the parameter $\lambda_{km_k}^{(q_a,z,\bar{I})}$ and $\varphi_{km_k}^{(q_a,z,\bar{I})}$ using (6.34) and (6.35), respectively;
8: Update $\eta_{km_k}^{(\bar{I})}(t_{k,q_a}^{(z)})$ using (6.33);
9: Obtain $\left(\hat{m}_k | \hat{t}_{k,q_1}^{(z)}, \cdots, \hat{t}_{k,q_a}^{(z)} \right)$ using (6.36).

6.4 Single-User Performance Analysis

In this section, we analyse the single-user performance bound as the benchmark of our proposed STC/GSM-SCDMA system for transmission over frequency selective channels. When the proposed STC/GSM-SCDMA system supports only a single user, the received observations of (6.9) become

$$\boldsymbol{Y} = \frac{1}{\sqrt{Z}} \boldsymbol{H} \boldsymbol{E}_m \boldsymbol{T} + \boldsymbol{n}. \tag{6.37}$$

Then, following [51], the pairwise error probability (PEP) when the transmitted $\boldsymbol{E}_m \boldsymbol{T}$ is detected as $\boldsymbol{E}_{\tilde{m}} \tilde{\boldsymbol{T}} \neq \boldsymbol{E}_m \boldsymbol{T}$ can be expressed as

$$P(\boldsymbol{E}_m \boldsymbol{T} \to \boldsymbol{E}_{\tilde{m}} \tilde{\boldsymbol{T}}) = E_{\boldsymbol{H}} \left[Q\left(\sqrt{\frac{\gamma}{2} \| \boldsymbol{H} \boldsymbol{E}_{\tilde{m}} \tilde{\boldsymbol{T}} - \boldsymbol{H} \boldsymbol{E}_m \boldsymbol{T} \|} \right) \right], \tag{6.38}$$

where the Q-function $Q(x)$ is defined as $Q(x) = (2\pi)^{-1/2} \int_x^\infty e^{-t^2/2} dt$, and $E_{\boldsymbol{H}}[\cdot]$ denotes the average with respect to the channels between the user and the BS. Upon invoking the alternative representation of $Q(x)$ of $Q(x) = \pi^{-1} \int_0^{\pi/2} \exp\left(-\frac{x^2}{2\sin^2\theta} \right) d\theta$ [118], the PEP of (6.38) can be expressed as

$$P(\boldsymbol{E}_m \boldsymbol{T} \to \boldsymbol{E}_{\tilde{m}} \tilde{\boldsymbol{T}}) = E_{\boldsymbol{H}} \left[\frac{1}{\pi} \int_0^{\frac{\pi}{2}} \exp\left(-\frac{\gamma}{4\sin^2\theta} \| \boldsymbol{H} \boldsymbol{E}_{\tilde{m}} \tilde{\boldsymbol{T}} - \boldsymbol{H} \boldsymbol{E}_m \boldsymbol{T} \|^2 \right) d\theta \right] \tag{6.39a}$$

$$= \frac{1}{\pi} \int_0^{\frac{\pi}{2}} \Phi_{\| \boldsymbol{H} \boldsymbol{E}_{\tilde{m}} \tilde{\boldsymbol{T}} - \boldsymbol{H} \boldsymbol{E}_m \boldsymbol{T} \|^2} \left(-\frac{\gamma}{4\sin^2\theta} \right) d\theta, \tag{6.39b}$$

where $\Phi_{\| \boldsymbol{H} \boldsymbol{E}_{\tilde{m}} \tilde{\boldsymbol{T}} - \boldsymbol{H} \boldsymbol{E}_m \boldsymbol{T} \|^2}(\cdot)$ is the moment generation function (MGF) of the variable $\| \boldsymbol{H} \boldsymbol{E}_{\tilde{m}} \tilde{\boldsymbol{T}} - \boldsymbol{H} \boldsymbol{E}_m \boldsymbol{T} \|^2$.

In the STC/GSM-SCDMA system, errors may optionally corrupt only the GSM symbol, only the QAM symbols, or both of them. When considering these three cases separately, the corresponding PEP $P(\boldsymbol{E}_m \boldsymbol{T} \to \boldsymbol{E}_{\tilde{m}} \tilde{\boldsymbol{T}})$ of (6.39b) can be derived as follows.

1. **Errors in GSM Symbol Only**

   When only the GSM symbol is erroneous, i.e. $\boldsymbol{E}_{\tilde{m}} \neq \boldsymbol{E}_m$ and $\tilde{\boldsymbol{T}} = \boldsymbol{T}$, the PEP $P_1(\boldsymbol{E}_m \boldsymbol{T} \to \boldsymbol{E}_{\tilde{m}} \boldsymbol{T})$ can be expressed as

$$\begin{aligned} P_1(\boldsymbol{E}_m \boldsymbol{T} \to \boldsymbol{E}_{\tilde{m}} \boldsymbol{T}) &= E_{\boldsymbol{H}} \left[\frac{1}{\pi} \int_0^{\frac{\pi}{2}} \exp\left(-\frac{\gamma \| \boldsymbol{T} \|^2}{4\sin^2\theta} \| \boldsymbol{H} \boldsymbol{E}_{\tilde{m}} - \boldsymbol{H} \boldsymbol{E}_m \|^2 \right) d\theta \right] \\ &= E_{\boldsymbol{H}} \left[\frac{1}{\pi} \int_0^{\frac{\pi}{2}} \exp\left(-\frac{\gamma \| \boldsymbol{T} \|^2}{4\sin^2\theta} \| \boldsymbol{H} \boldsymbol{\Omega}_1 \|^2 \right) d\theta \right] \\ &= \frac{1}{\pi} \int_0^{\frac{\pi}{2}} \Phi_{\| \boldsymbol{H} \boldsymbol{\Omega}_1 \|^2} \left(-\frac{\| \boldsymbol{T} \|^2 \gamma}{4\sin^2\theta} \right) d\theta, \end{aligned} \tag{6.40}$$

where $\boldsymbol{\Omega}_1 = \boldsymbol{E}_{\tilde{m}} - \boldsymbol{E}_m$.

2. **Errors in QAM Symbols Only**

   By contrast, when the errors corrupt only the QAM symbol(s), we have $\tilde{\boldsymbol{T}} \neq \boldsymbol{T}$ and $\boldsymbol{E}_{\tilde{m}} = \boldsymbol{E}_m$. Then the PEP of (6.39b) can re-written as

$$\begin{aligned} P_2(\boldsymbol{E}_m\boldsymbol{T} \to \boldsymbol{E}_m\tilde{\boldsymbol{T}}) =& E_{\boldsymbol{H}}\left[\frac{1}{\pi}\int_0^{\frac{\pi}{2}} \exp\left(-\frac{\gamma}{4\sin^2\theta}\|\boldsymbol{H}\boldsymbol{E}_m\tilde{\boldsymbol{T}} - \boldsymbol{H}\boldsymbol{E}_m\boldsymbol{T}\|^2\right) d\theta\right] \\ =& E_{\boldsymbol{H}}\left[\frac{1}{\pi}\int_0^{\frac{\pi}{2}} \exp\left(-\frac{\|\tilde{\boldsymbol{T}} - \boldsymbol{T}\|^2\gamma}{4\sin^2\theta}\|\boldsymbol{H}\boldsymbol{E}_{s_1}\|^2\right) d\theta\right] \\ =& \frac{1}{\pi}\int_0^{\frac{\pi}{2}} \Phi_{\|\boldsymbol{H}\boldsymbol{\Omega}_2\|^2}\left(-\frac{\|\tilde{\boldsymbol{T}} - \boldsymbol{T}\|^2\gamma}{4\sin^2\theta}\right) d\theta, \end{aligned} \tag{6.41}$$

   where $\boldsymbol{\Omega}_2 = \boldsymbol{E}_m$.

3. **Errors in both GSM and QAM Symbols**

   Finally, when the errors occur in both the GSM and QAM symbol(s), we have $\boldsymbol{E}_{\tilde{m}} \neq \boldsymbol{E}_m$ and $\tilde{\boldsymbol{T}} \neq \boldsymbol{T}$. Correspondingly, (6.39b) can be modified to

$$\begin{aligned} P_3(\boldsymbol{E}_m\boldsymbol{T} \to \boldsymbol{E}_{\tilde{m}}\tilde{\boldsymbol{T}}) &= E_{\boldsymbol{H}}\left[\frac{1}{\pi}\int_0^{\frac{\pi}{2}} \exp\left(-\frac{\gamma}{4\sin^2\theta}\|\boldsymbol{H}\boldsymbol{E}_{\tilde{m}}\tilde{\boldsymbol{T}} - \boldsymbol{H}\boldsymbol{E}_m\boldsymbol{T}\|^2\right) d\theta\right] \\ &= E_{\boldsymbol{H}}\left[\frac{1}{\pi}\int_0^{\frac{\pi}{2}} \exp\left(-\frac{\gamma}{4\sin^2\theta}\|\boldsymbol{H}\boldsymbol{\Omega}_3\|^2\right) d\theta\right] \\ &= \frac{1}{\pi}\int_0^{\frac{\pi}{2}} \Phi_{\|\boldsymbol{H}\boldsymbol{\Omega}_3\|^2}\left(-\frac{\gamma}{4\sin^2\theta}\right) d\theta, \end{aligned} \tag{6.42}$$

   where $\boldsymbol{\Omega}_3 = \boldsymbol{E}_{\tilde{m}}\tilde{\boldsymbol{T}} - \boldsymbol{E}_m\boldsymbol{T}$.

Since the channels experience correlated Rayleigh fading, the MGF of $\|\boldsymbol{H}\boldsymbol{\Omega}_i\|^2$ can be derived in the same way as that in [29, 133], which can be expressed as

$$\Phi_{\|\boldsymbol{H}\boldsymbol{\Omega}_i\|^2}(t) = \det\left[\boldsymbol{I}_{N_RNZ} - t\boldsymbol{R}\left(\boldsymbol{I}_{N_RN} \otimes (\boldsymbol{\Omega}_i\boldsymbol{\Omega}_i^H)\right)\right]^{-1}, \tag{6.43}$$

where $\det(\cdot)$ denotes the determinant of a matrix and $\boldsymbol{R}$ is the $(N_RNZ \times N_RNZ)$ covariance matrix of $\text{vec}(\boldsymbol{H}^T)$, where $\text{vec}(\cdot)$ represents the vectorization operation of a matrix, converting the columns of a matrix into a single column vector. Note that we omit the calculations of $\boldsymbol{R}$, since it has been demonstrated in [29, 103].

If we substitute $\Phi_{\|\boldsymbol{H}\boldsymbol{\Omega}_i\|^2}(t)$ of (6.40)-(6.42) with (6.43) into (6.40), (6.41) and (6.42), respectively, the PEPs of (6.40), (6.41) and (6.42) representing the three erroneous scenarios can be re-written respectively as

$$P_1(\boldsymbol{E}_m\boldsymbol{T} \to \boldsymbol{E}_{\tilde{m}}\boldsymbol{T}) = \frac{1}{\pi}\int_0^{\frac{\pi}{2}} \det\left(\boldsymbol{I}_{M_1UN} + \frac{\|\boldsymbol{T}\|^2\gamma}{4\sin^2\theta}\boldsymbol{R}\left(\boldsymbol{I}_{UN}\otimes(\boldsymbol{\Omega}_1\boldsymbol{\Omega}_1^H)\right)\right)^{-1} d\theta \quad (6.44a)$$

$$P_2(\boldsymbol{E}_m\boldsymbol{T} \to \boldsymbol{E}_m\tilde{\boldsymbol{T}}) = \frac{1}{\pi}\int_0^{\frac{\pi}{2}} \det\left(\boldsymbol{I}_{M_1UN} + \frac{\|\tilde{\boldsymbol{T}}-\boldsymbol{T}\|^2\gamma}{4\sin^2\theta}\boldsymbol{R}\left(\boldsymbol{I}_{UN}\otimes(\boldsymbol{\Omega}_2\boldsymbol{\Omega}_2^H)\right)\right)^{-1} d\theta \quad (6.44b)$$

$$P_3(\boldsymbol{E}_m\boldsymbol{T} \to \boldsymbol{E}_{\tilde{m}}\tilde{\boldsymbol{T}}) = \frac{1}{\pi}\int_0^{\frac{\pi}{2}} \det\left(\boldsymbol{I}_{M_1UN} + \frac{\gamma}{4\sin^2\theta}\boldsymbol{R}\left(\boldsymbol{I}_{UN}\otimes(\boldsymbol{\Omega}_3\boldsymbol{\Omega}_3^H)\right)\right)^{-1} d\theta. \quad (6.44c)$$

Consequently, following the analysis in [29] and considering the three PEPs, the upper bound of the average BER (ABER) P_e of the single-user STC/GSM-SCDMA system can be expressed as

$$P_e \leq \frac{1}{bM_1M_2^{N_A}} \sum_{m\in\mathcal{M}_1}\sum_{\boldsymbol{s}\in\mathcal{X}}\sum_{\tilde{m}\in\mathcal{M}_1}\sum_{\tilde{\boldsymbol{s}}\in\mathcal{S}} D\left(\boldsymbol{b}_1|\boldsymbol{b}_2, \tilde{\boldsymbol{b}}_1|\tilde{\boldsymbol{b}}_2\right) P(\boldsymbol{E}_m\boldsymbol{T} \to \boldsymbol{E}_{\tilde{m}}\tilde{\boldsymbol{T}}), \quad (6.45)$$

where $D(\cdot,\cdot)$ is defined as the Hamming distance between two binary entries, and $\tilde{\boldsymbol{b}}_i$, $i = 1, 2$, represents the mistaken detection of the bit sequence $\boldsymbol{b}_i$.

6.5 Performance Results

In this section, the proposed STC/GSM-SCDMA system is characterized in terms of its BER vs. complexity in Sections 6.5.1 and 6.5.2, respectively.

6.5.1 Bit Error Rate Performance

First, we quantify the single-user bound of (6.45) for the proposed STC/GSM-SCDMA system, when communicating over the $L = 1, 2$ and 4 frequency-selective Rayleigh fading channels, as shown in Fig. 6.5, where the user spreads its signal over $d_c = 2$ out of $N = 16$ subcarriers, and $N_T = 6, N_A = 2, N_R = 8$ or 16 is employed. The simulation results of the proposed STC/GSM-SCDMA system supporting a single user are also included in Fig. 6.5, where we can see that the theoretical bound and the simulation BER tend to converge upon increasing the SNR. Hence, we can conclude that when the SNR is

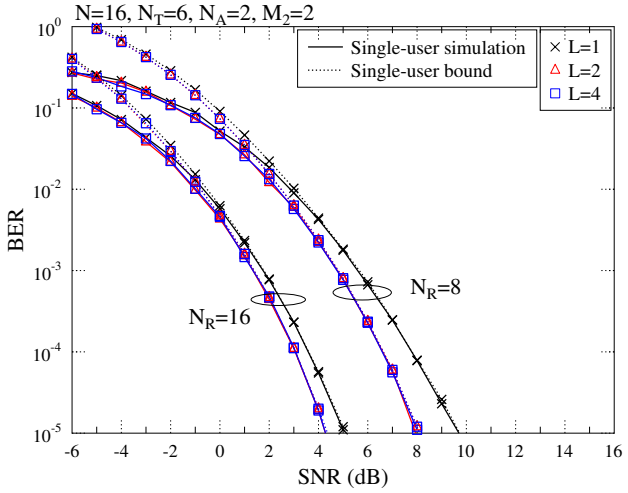

FIGURE 6.5: Theoretical union bound of the proposed STC/GSM-SCDMA system and the simulated BER performance of the $N_T = 6$, $N_A = 2$, $N_R = 4$ STC/GSM-SCDMA system supporting $K = 1$ user over $L = 1, 2$ and 4 frequency-selective Rayleigh fading channels.

sufficiently high so that a BER below 10^{-2} can be attained, the theoretical bound of (6.45) derived in Section 6.4 can be employed as the single-user performance bound of our STC/GSM-SCDMA system, which provides design guidelines concerning the system parameters without the need for practical implementations.

Furthermore, we compare the BER performance of the proposed STC/GSM-SCDMA system to that of the popular MIMO-NOMA systems of [29, 110]. More specifically, Fig. 6.6 shows the BER performance of the SM-SCDMA [29], STC-SCDMA [110] and the proposed STC/GSM-SCDMA systems supporting $K = 24$ users employing $N = 16$ subcarriers when communicating over the frequency-selective Rayleigh fading channels having $L = 4$. For fair comparison, all the systems considered transmit their signal at the same 6 BPS where all of them employ the MPA detector, associated with (a) $N_R = 8$ and (b) $N_R = 16$. We can see from both figures that our proposed STC/GSM-SCDMA system achieves superior BER performance, over the MIMO-NOMA benchmarkers considered in Fig. 6.6, since our STC/GSM-SCDMA system exploits the diversity in the SFD and conveys the information bits both by the TA indices and by the QAM symbols.

Fig. 6.7 further investigates the BER performance of the proposed STC/GSM-SCDMA systems in demanding large-scale access scenarios at a normalized user load of 150%, where employing the MPA detector for communicating over frequency-selective Rayleigh fading channel having $L = 4$. We can see that the performance is rather similar, when the proposed STC/GSM-SCDMA system supports a higher number of users, as long as the normalized user load remain unchanged at 150%. This is promising for demanding mMTC scenarios, where a BS may have to support thousands or even millions of devices.

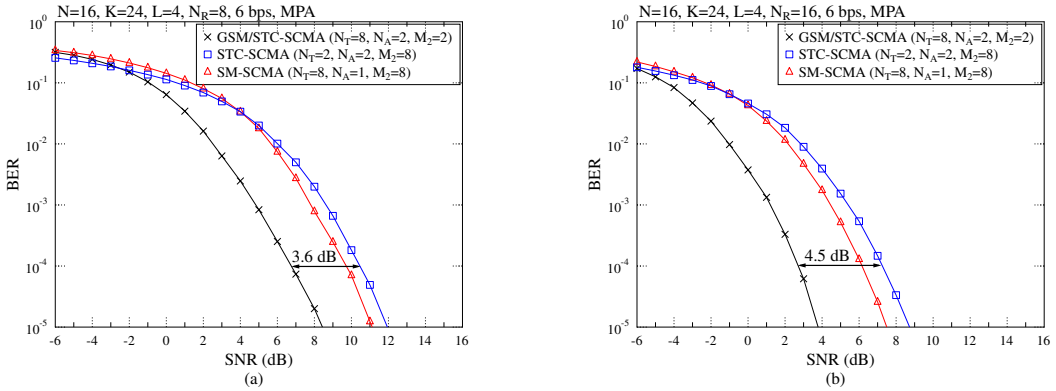

FIGURE 6.6: BER performance of the SM-SCDMA, STC-SCMA and the proposed STC/GSM-SCDMA systems supporting $K = 24$ users using $N = 16$ subcarriers when communicating over the $L = 4$ frequency-selective Rayleigh fading channel at the same rate of 6 BPS, where all the considered systems employ the MPA detection, with (a) $N_R = 8$ and (b) $N_R = 16$.

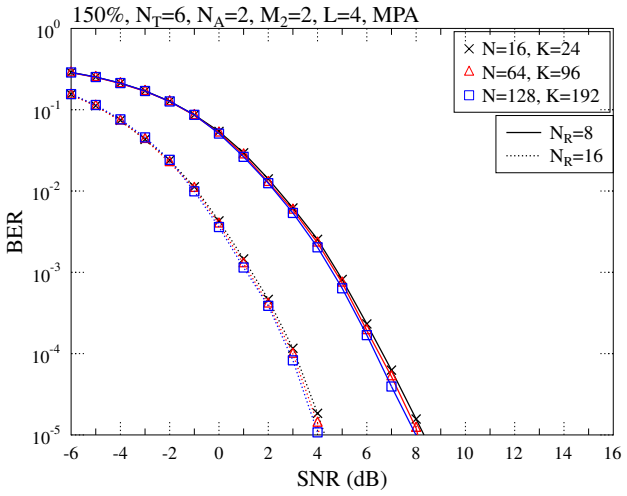

FIGURE 6.7: BER performance of the proposed STC/GSM-SCDMA systems with $N_T = 6$, $N_A = 2$, $N_R = 8$ or 16 employing the MPA detection with a normalized user load of 150% when communicating over the $L = 4$ frequency-selective Rayleigh fading channel.

Let us now demonstrate the influence of the normalized user load on the BER performance of the proposed STC/GSM-SCDMA systems, as shown in Fig. 6.8. More specifically, in Fig. 6.8, we have $N_T = 6$ TAs at each user's transmitter with $N_A = 2$ TAs activated within a single SD, supporting $K = 16, 24$ and 32 users by $N = 16$ subcarriers, where $N_R = 8$ or 16 RAs are employed. The single-user bound is included as the benchmarker. A slight performance loss can be observed at the demanding normalized user load of 200% in the low-SNR region. But when the BER is below 10^{-2}, the BER of our STC/GSM-SCDMA system supporting $K = 32$ users converges to that supporting $K = 16$ users and even to the single-user bound. Therefore, our STC/GSM-SCDMA system has the potential of supporting heavily-loaded NOMA systems in next-generation

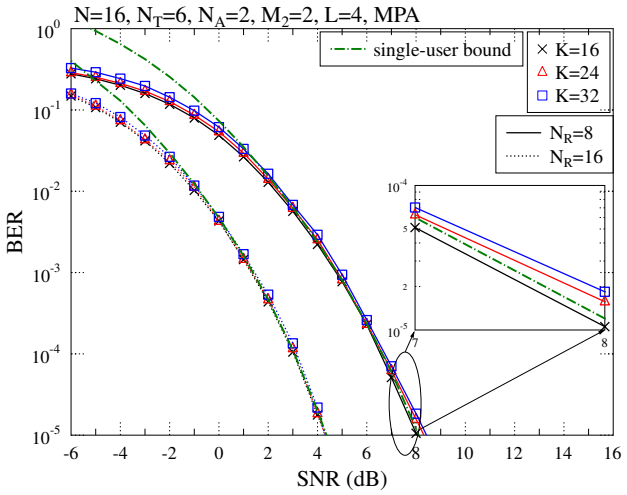

FIGURE 6.8: BER performance of the proposed STC/GSM-SCDMA systems with $N = 16$, $N_T = 6$, $N_A = 2$, $N_R = 8$ or 16 employing the MPA detection with a normalized user load of 100%, 150% and 200% when communicating over the $L = 4$ frequency-selective Rayleigh fading channel.

communications. It is also noticeable that in the case of 100% normalized user load, the MU BER performance is still upper bounded by the single-user bound.

The BER performance of the proposed low-complexity AMP detector of our STC/GSM-SCDMA system is shown in Fig. 6.9 and compared to the MPA detector, where $N_T = 6$ TAs, and $N_A = 2$ activated TAs are employed by each of the $K = 16$ users and $N_R = 16$ RAs are used by the BS. Again, $N = 16$ subcarriers are employed to support $K = 24$ users, when communicating over frequency-selective Rayleigh fading channels having $L = 1, 2$ and 4. In the case of $L = 4$, a 1.5 dB SNR loss can be observed from Fig. 6.9 at the BER of 10^{-3}, when the AMP detection is employed, compared to that of the MPA detector. However, this is achieved at a potentially 1000 times lower detection complexity, which will be detailed in Section 6.5.2.

The influence of M_1 and M_2 on the BER performance of our STC/GSM-SCDMA system is demonstrated in Fig. 6.10, where the $N_R = 16$ STC/GSM-SCDMA system supports $K = 24$ users by $N = 16$ subcarriers and the AMP detector is employed. Firstly, it can be concluded that when the number of activated TAs is fixed, increasing N_T tends to result in a BER degradation, but extra bits may be conveyed. In Fig. 6.10, when N_A is fixed to 2, $N_T = 4, 6$ and 7 give $b_1 = 2, 3$ and 4 bits to be conveyed by the activated TA indices per SD. By contrast, the increase of M_2 from 2 to 4 results in less than 0.5 dB SNR loss at a BER of 10^{-3}, regardless of N_Ts, while doubling the spectral efficiency.

Finally, Fig. 6.11 characterizes the convergence of the proposed low-complexity AMP detector for the $N_R = 16$ STC/GSM-SCDMA systems at the SNR of $\gamma = 2$ and 4 dB. The system parameters employed in Fig. 6.11 are the same as those adopted in Fig.

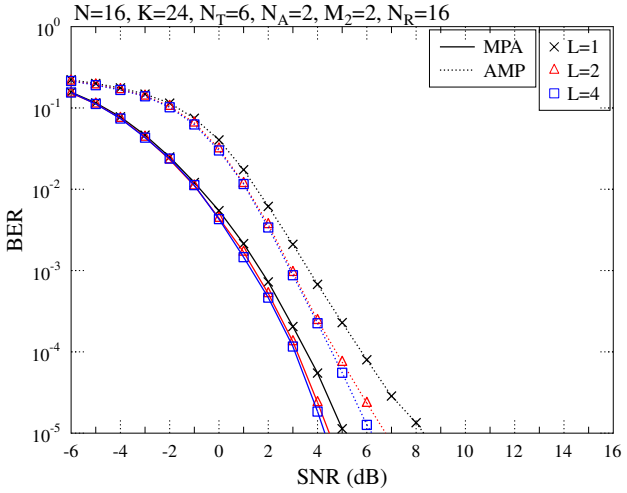

FIGURE 6.9: BER comparison of the $N_T = 6$, $N_A = 2$, $N_R = 16$ STC/GSM-SCDMA system employing the MPA detection and that employing AMP detection for supporting $K = 24$ users by $N = 16$ subcarriers, when communicating over the $L = 1, 2$ and 4 frequency-selective Rayleigh fading channels.

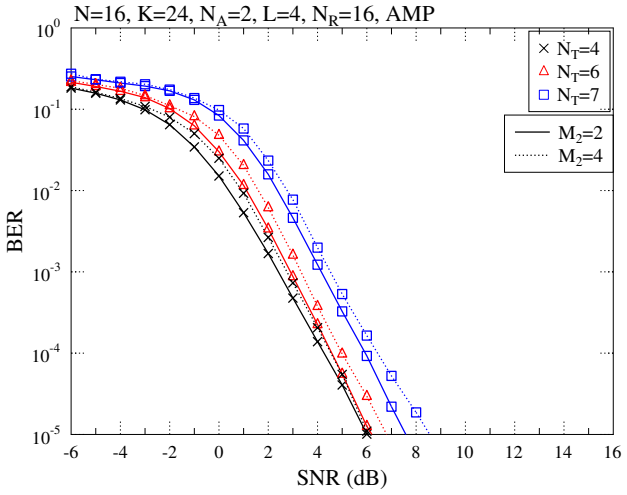

FIGURE 6.10: BER comparison of the $N_A = 2$, $N_R = 16$ STC/GSM-SCDMA systems employing AMP detection for supporting $K = 24$ users by $N = 16$ subcarriers, where each user is equipped with $N_T = 4, 6$ or 7 TAs, when communicating over the $L = 4$ frequency-selective Rayleigh fading channel.

6.10. Since the BER always converges after the first 4 iterations, we fix the number of iterations to $I = \bar{I} = 8$ in all simulations of the MPA or AMP detectors.

6.5.2 Complexity

In this section, the computational complexity per iteration of the proposed MPA and AMP detectors is quantified and compared in terms of the number of floating point operations (FLOPs). More specifically, we assume that

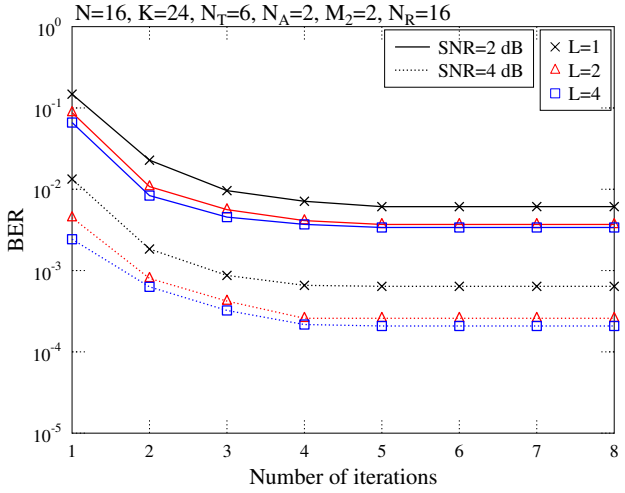

FIGURE 6.11: BER vs. the number of iterations the $N_R = 16$ STC/GSM-SCDMA systems employing AMP detection for supporting $K = 24$ users by $N = 16$ subcarriers at the SNR $\gamma = 2$ and 4 dB, where each user is equipped with $N_T = 4, 6$ or 7 TAs, when communicating over the $L = 4$ frequency-selective Rayleigh fading channel.

1. the multiplication of two real numbers requires a single FLOP;
2. the multiplication of a single complex number and a single real number requires 2 FLOPs;
3. the multiplication of a pair of complex numbers (excluding the conjugate multiplication) requires 6 FLOPs;
4. the multiplication of a complex number and its conjugate requires 3 FLOPs.

We also assume that the calculation of $\exp(\cdot)$ is carried by a look-up table [173].

First, as discussed in Section 6.3.1, the complexity $\mathcal{C}_{\text{MPA}}$ of the MPA detector per iteration is comprised of the VN update of (6.12) and CN update of (6.16). The complexity of the MPA detection is already given in [176], which can be expressed as

$$\mathcal{C}_{\text{MPA}} = N_R N Z d_x [(7d_x - 1)(M_1 M_2^{N_A})^{d_x} + (d_c - 1) M_1 M_2^{N_A}]. \tag{6.46}$$

By contrast, during each AMP operation, the number of FLOPs required to perform the operations of Lines 2-5 in Algorithm 1 is summarized in Table 6.3. Hence, the complexity per iteration of the AMP detector in terms of FLOPs can be expressed as the sum of the expressions in Table 6.3, which can be formulated as

$$\mathcal{C}_{\text{AMP}} = \sum_{j=1}^{7} C_j. \tag{6.47}$$

TABLE 6.3: The number of FLOPs required for the equations employed in the AMP detection.

Equation	FLOPs
(6.29)	$C_1 = 4N_R NZN_A M_1 M_2 d_x$
(6.30)	$C_2 = N_R NZN_A M_1 d_x (6M_2 - 1)$
(6.23)	$C_3 = N_R NZ[6N_A M_1 (d_x - 1) + 2]$
(6.24)	$C_4 = N_R NZ[N_A M_1 (d_x - 1) + 1]$
(6.27)	$C_5 = KM_1 N_A Z[N_R (d_c - 1) + 1]$
(6.28)	$C_6 = KM_1 N_A Z[8N_R (d_c - 1) + 1]$
(6.26)	$C_7 = KN_R d_c Z(11N_A M_1 M_2 + 1)$

Fig. 6.12 characterizes the computational complexity per iteration vs. the number of TAs at each user of the proposed $N_A = 2$ STC/GSM-SCDMA systems employing MPA or AMP detection for supporting $K = 16, 24$ and 32 users by $N = 16$ subcarriers, where $N_R = 16$, when communicating over the frequency-selective Rayleigh fading channel having $L = 4$, where (a) $M_2 = 2$ and (b) $M_2 = 4$. We can see from both Fig. 6.12(a) and Fig. 6.12(b) that the AMP detector requires a much lower number of FLOPs to complete a single iteration. For instance, when detecting a $N = 16$ and $K = 24$ STC/GSM-SCDMA system employing $N_T = 6$ TAs, $N_A = 2$ activated TAs and $N_R = 16$ RAs, the AMP detection requires only 1.2×10^6 FLOPs to complete a single iteration, which is 1000 times lower than that of the MPA detector. Furthermore, we can see from Fig. 6.12(b) that in the case of $M_2 = 4$, when detecting the same $N = 16$ and $K = 24$ STC/GSM-SCDMA system employing $N_T = 6$ TAs, $N_A = 2$ activated TAs and $N_R = 16$ RAs, the complexity per iteration of the MPA detector is in excess of 10^{10}, which is excessive for its practical implementation. By contrast, the complexity per iteration of detecting the same STC/GSM-SCDMA system using the AMP detector only linearly increases to 2.3×10^6 FLOPs, which readily facilitates the implementation of more complex STC/GSM-SCDMA systems.

6.6 Chapter Summary and Conclusions

A STC/GSM-SCMA scheme has been proposed in this chapter, which exploited transmit diversity in the STF domain and provides a promising solution to the pervasive connectivity of the devices in next-generation communications. The main conclusions of this chapter are summarized in Table 6.4.

More specifically, a single-user BER bound was derived as the benchmark of our STC/GSM-SCMA system. Furthermore, a pair of novel detectors have been conceived for our proposed STC/GSM-SCMA system with the performance in terms of BER and complexity demonstrated and compared. In particular, the AMP detector requires only 0.1% complexity, compared to that of the MPA detector, at the cost of less than 2 dB gains, when

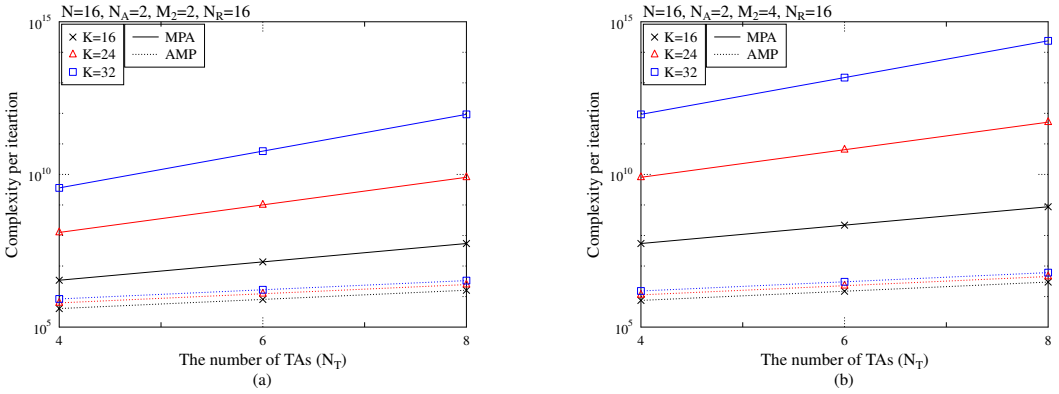

FIGURE 6.12: Computational complexity per iteration vs. the number N_T of TAs equipped at each user of the proposed $N_A = 2$, $N_R = 16$ STC/GSM-SCDMA systems employing MPA or AMP detection for supporting $K = 16, 24$ and 32 users by $N = 16$ subcarriers, where (a) $M_2 = 2$ and (b) $M_2 = 4$.

TABLE 6.4: Main conclusions of Chapter 6.

System	STC/GSM-SCMA system		
Example	$M_1 = M_2 = 4$, $U = 1$, $N = 16$, $L = 4$		
SNR at a BER of 10^{-3}	$K = 16$	$K = 24$	$K = 32$
	22.5 dB	23.5 dB	24.1 dB
Complexity order	MLD	MAP	MPA
	$\mathcal{O}(M^K)$	$\mathcal{O}(M^{\lvert\mathcal{K}_l\rvert})$	$\mathcal{O}(M^{d_x(d_f-1)})$

detecting the STC/GSM-SCMA system with a normalized user load of 150%. Our BER results also demonstrated that the proposed STC/GSM-SCMA system achieves superior performance compared to existing MIMO-NOMA schemes in literature.

Chapter 7

Sparse Space-Time-Frequency-Domain Spreading for Large-Scale Non-Orthogonal Multiple Access

7.1 Introduction

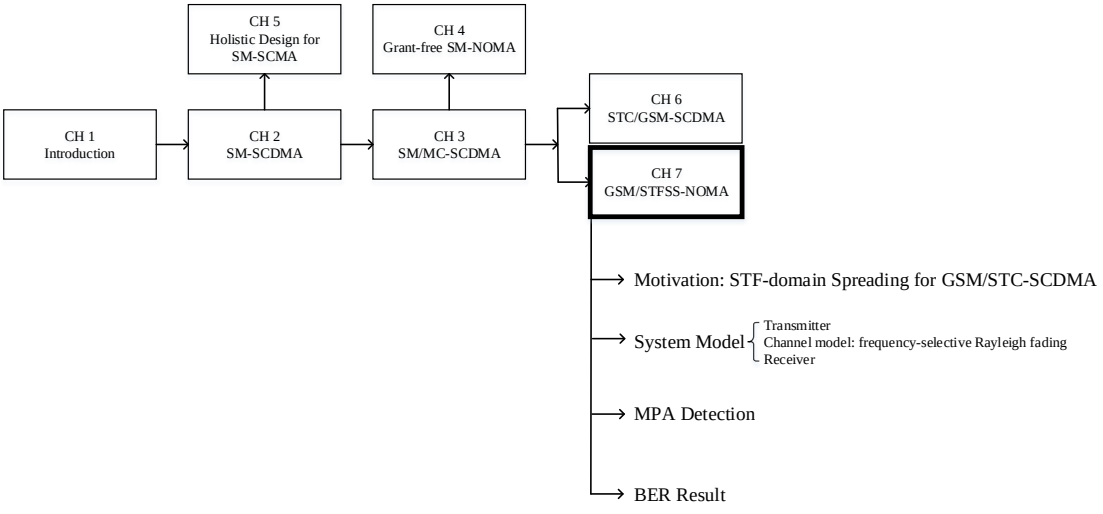

FIGURE 7.1: The relationship of Chapter 7 with the rest of the thesis.

While Chapter 6 employs space-time coding (STC) for achieving transmit diversity, this chapter proposes an alternative transmit diversity technique by developing sparse space-time-frequency spreading (SSTFS) for sparse code division multiple access (SCDMA) system.

As discussed in Chapter 6, a pair of transmit antennas (TAs) has been standardized for the user's uplink (UL) transmission by the 3rd generation partnership project (3GPP) Release 16 [167,168], for attaining a substantial transmit diversity gain. A higher number of TAs may be employed in the context of massive MIMO techniques for next-generation communications [169]. However, there is a paucity of literature on simultaneously exploiting multi-dimensional spreading for enhancing the performance of nonorthogonal multiple access (NOMA) systems. Motivated by achieving transmit diversity at the user side and inspired by the benefits of space-time spreading (STS) technique that was originally designed for code-division multiple-access (CDMA) systems [177], we propose a generalized spatial modulation-aided sparse space-time-frequency spreading (GSM/SSTFS) scheme for NOMA systems, in order to support large-scale access in next-generation systems. The contributions of this chapter are summarised as follows:

- First, we propose a GSM/SSTFS scheme for supporting large-scale access at a high normalized user-load by involving space-, time-, and frequency-domain (STFD) spreading. More specifically, in the GSM/SSTFS system relying on two active TAs, each user spreads its signal over two symbol durations, two active TAs, and multiple subcarriers by a unique, user-specific sparse code, before transmitting the signal over the channel. Furthermore, with the aid of GSM, extra information bits are embedded in the TA indices, for increasing the attainable throughput.
- Secondly, a joint factor graph is designed for signal detection, which is eminently suitable for visualizing the message-propagation by the STFD spreading. Based on the connections of the proposed joint factor graph, a joint message passing-aided (JMPA) detector is conceived for attaining a near-single-user bit error rate (BER) at a low complexity.
- Finally, our BER performance results have demonstrated that the proposed GSM/SSTF-S scheme achieves superior BER, compared to the conventional MIMO-NOMA schemes at the same number of bits per symbol (BPS).

The rest of this chapter is structured as follows. Section 7.2 describes the transmitter and receiver of the proposed GSM/SSTFS system. Following this, Section 7.3 introduces our JMPA detection and the BER performance of the proposed GSM/SSTFS system is characterized in Section 7.4. Finally, our main conclusions and future research ideas will be discussed in Section 7.5.

7.2 System Model

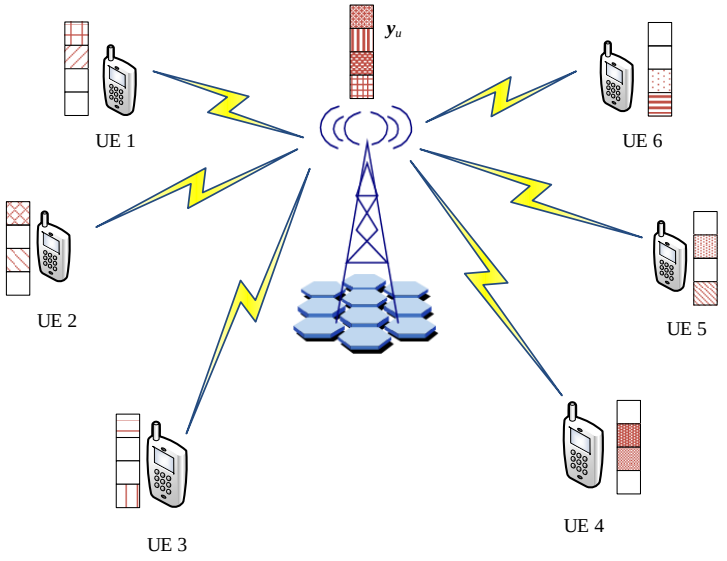

FIGURE 7.2: An example of the uplink GSM/SSTFS network employing $N = 4$ to support $K = 6$ users.

In this section, the transmitter and receiver models of the proposed GSM/SSTFS UL are introduced in Sections 7.2.1 and 7.2.2, respectively. In this chapter, a single-cell UL MIMO multi-carrier (MC) communication system is assumed, as shown in Fig. 7.2, where K users simultaneously transmit their UL signals to a single BS by N subcarriers ($K \geq N$) over frequency-selective Rayleigh fading channels having L resolvable paths.

7.2.1 Transmitter Model

At the transmitter, each of the K users is equipped with N_T TAs, whereas the BS at the receiver employs U receive antennas (RAs). Furthermore, we assume that N subcarriers ($N > L$) are employed for transmitting the UL signal to the BS, in line with the MC systems' typical design [103], so that the individual subcarriers experience flat fading,

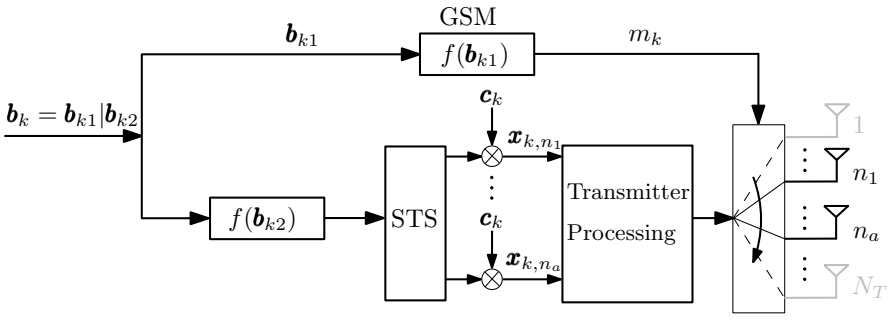

FIGURE 7.3: The transmitter structure of the kth user in the GSM/SSTFS system.

but the adjacent subcarriers may experience correlated fading. Following the principles of GSM, within each symbol duration, only t TAs ($t < N_T$) of a user are activated. The GSM/SSTFS transmitter of user k is shown in Fig. 7.3.

More specifically, for user k, a total of $b = b_1 + b_2$ bits are transmitted in each symbol duration, where $b_1 = \lfloor \log_2 \binom{N_T}{t} \rfloor$[1] bits are mapped to the TA indices [41], where the GSM symbol set is expressed as $\mathcal{M}_1 = \{p_1, \cdots, p_{M_1}\}$ and $M_1 = 2^{b_1}$. By contrast, the remaining $b_2 = t \log_2 M_2$ bits are conveyed by the M_2-QAM symbols of the set $\mathcal{M}_2 = \{s_1, \cdots, s_{M_2}\}$. For instance, for a ($N_T = 4$, $t = 2$) GSM system, we have $\binom{N_T}{t} = \binom{4}{2} = 6$ TA combinations, which can be exploited for transmitting $b_1 = 2$ bits per GSM symbol, using the bit-symbol-TA mapping of Table 7.1, where $t_i \in \mathcal{M}_1$ is the GSM symbol and (n_1, n_2) are the indices of the active TAs. Furthermore, b_2 bits are mapped to t M_2-QAM symbols expressed as $\boldsymbol{s}_k = [\underbrace{s_{k,n_1}, s_{k,n_2}, \cdots, s_{k,n_t}}_{t}]^T$, where $s_{k,n_i} \in \mathcal{M}_2$, which are transmitted by the n_1-, $\cdots$, n_t-th TAs, respectively.

TABLE 7.1: Bit-symbol-TA mapping table for the GSM with $N_T = 4$, $t = 2$.

$\boldsymbol{b}_{k1}$	$\mathcal{M}_1$	(n_1, n_2)
00	p_1	(1,3)
01	p_2	(2,4)
10	p_3	(1,4)
11	p_4	(2,3)

As shown in Fig. 7.3, following the M_2-QAM mapping, SSTFS is applied to the t M_2-QAM symbols, in order to simultaneously achieve diversity in both the spatial-domain (SD), time-domain (TD) and frequency-domain (FD). In the following discussions, we only consider the case of $t = 2$ active TAs, since employing a pair of radio frequency (RF) chains has been adopted for MIMO UL transmission in the 3GPP Release 16 for 5G new radio (NR) [167].

Firstly, sparse FD spreading is carried out by adopting the code-domain NOMA principles relying on low-density signatures (LDS) [10]. More specifically, a sparse spreading sequence $\boldsymbol{c}_k = [c_{k1}, c_{k2}, ..., c_{kN}]^T$ is preassigned to user k and it is normalized to satisfy $\|\boldsymbol{c}_k\|^2 = 1$. We assume that in $\boldsymbol{c}_k$, only d_x ($d_x << N$) of the N elements are non-zero, which represent the number of subcarriers that user k spreads its signal over in the FD. For example, for a $N = 4$, $K = 6$ GSM/SSTFS system, the spreading matrix $\boldsymbol{V}$, which indicates the non-zero element-positions for all $K = 6$ users can be expressed as

$$\boldsymbol{V} = \begin{bmatrix} 1 & 1 & 1 & 0 & 0 & 0 \\ 1 & 0 & 0 & 1 & 1 & 0 \\ 0 & 1 & 0 & 1 & 0 & 1 \\ 0 & 0 & 1 & 0 & 1 & 1 \end{bmatrix}. \tag{7.1}$$

[1] $\lfloor x \rfloor$ represents the largest integer that is smaller than x.

Correspondingly, the number of users sharing one of the N subcarriers, i.e. the number of non-zero elements in each row of $\boldsymbol{V}$, is expressed as d_c, which has the property of $d_c << K$.

In contrast to the conventional STS scheme [177], where two QAM symbols are spread across two TAs over two symbol durations by a dense spreading sequence, again, we adopt the sparse FD spreading sequence $\boldsymbol{c}_k$ for SD spreading. Specifically, for user k, a pair of sparse spreading sequences are formed as

$$\begin{aligned} \boldsymbol{c}_{k1} =& \frac{1}{\sqrt{2}} \left[\boldsymbol{c}_k^T \quad \boldsymbol{c}_k^T \right]^T, \\ \boldsymbol{c}_{k2} =& \frac{1}{\sqrt{2}} \left[\boldsymbol{c}_k^T \quad -\boldsymbol{c}_k^T \right]^T, \end{aligned} \tag{7.2}$$

Furthermore, the pair of symbols, s_{k,n_1} and s_{k,n_2}, to be transmitted by the n_1-th and n_2-th activated TAs, respectively, are space-time coded (STC) by Alamouti's code $\mathcal{G}_2$ [171] as:

$$\mathcal{G}_{k,2} = \frac{1}{\sqrt{2}} \begin{bmatrix} s_{k,n_1} & s_{k,n_2} \\ -s_{k,n_2}^* & s_{k,n_1}^* \end{bmatrix}. \tag{7.3}$$

Hence, after the STC and spreading, we have a $(2N \times 2)$-dimensional transmit signal matrix $\boldsymbol{X}_k$ expressed as

$$\begin{aligned} \boldsymbol{X}_k =& \frac{1}{\sqrt{2}} \left[\boldsymbol{c}_{k1} \quad \boldsymbol{c}_{k2} \right] \begin{bmatrix} s_{k,n_1} & s_{k,n_2} \\ -s_{k,n_2}^* & s_{k,n_1}^* \end{bmatrix} \\ =& \left[\boldsymbol{x}_{k,n_1} \quad \boldsymbol{x}_{k,n_2} \right], \end{aligned} \tag{7.4}$$

where $\boldsymbol{x}_{k,n_1}$ and $\boldsymbol{x}_{k,n_2}$ are transmitted by the n_1-th and n_2-th TAs, respectively.

Additionally, the transmit signal of user k in a further generalized GSM/SSTFS system employing t $(t \geq 2)$ active TAs over D symbol durations can be expressed as

$$\begin{aligned} \boldsymbol{X}_k =& \left[\boldsymbol{c}_{k1} \quad \boldsymbol{c}_{k2} \quad \cdots \quad \boldsymbol{c}_{kD} \right] \mathcal{G}_t^{(k)} \\ =& \left[\boldsymbol{x}_{k,n_1} \quad \boldsymbol{x}_{k,n_2} \quad \cdots \quad \boldsymbol{x}_{k,n_t} \right], \end{aligned} \tag{7.5}$$

where the design of $[\boldsymbol{c}_{k1}, \cdots, \boldsymbol{c}_{kt}]$ is discussed in [103] and $\mathcal{G}_t^{(k)}$ represents a STC constructed by a block of symbols transmitted by the k-th user, as shown in [177].

7.2.2 Receiver Model

The channel impulse response (CIR) between the n_i-th TA ($n_i = 1, 2, \cdots, N_T$) of the k-th user ($k = 1, 2, \cdots, K$) and the u-th RA ($u = 1, 2, \cdots, U$) of the BS is denoted by:

$$\boldsymbol{h}_{k,n_i}^{(u)} = [h_{k,n_i,1}^{(u)}, h_{k,n_i,2}^{(u)}, \cdots, h_{k,n_i,L}^{(u)}]^T, \tag{7.6}$$

where $\boldsymbol{h}_{k,n_i}^{(u)}$ is independent identically distributed (iid) in terms of k, n_i, and u, and obeys the complex Gaussian distribution with zero mean and a variance of $0.5/L$ per dimension. Then, the corresponding FD channel transfer function (FD-CHTF) experienced by the N subcarriers can be expressed as [103]

$$\hat{\boldsymbol{h}}_{k,n_i}^{(u)} = \boldsymbol{\mathcal{F}}\boldsymbol{\Phi}_L \boldsymbol{h}_{k,n_i}^{(u)}, \tag{7.7}$$

where $\boldsymbol{\Phi}_L$ having a dimension of $(N \times L)$ is formed by the first L columns of an identity matrix $\boldsymbol{I}_N$, while $\boldsymbol{\mathcal{F}}$ represents the FFT having the property of $\boldsymbol{\mathcal{F}}\boldsymbol{\mathcal{F}}^H = \boldsymbol{\mathcal{F}}^H\boldsymbol{\mathcal{F}} = N\boldsymbol{I}_N$.

Following the assumptions routinely exploited in STS and STC [177], in the GSM-SSTFS system having $t = 2$ we assume that the CIR $\boldsymbol{h}_{k,n_i}^{(u)}$ remains constant for two consecutive symbols.

Therefore, the observations received at the u-th RA over the 2 symbol durations of a GSM-SSTFS system can be expressed as

$$\begin{bmatrix} \boldsymbol{y}_u^{(1)} \\ \boldsymbol{y}_u^{(2)} \end{bmatrix} = \sum_{k=1}^{K} \left(\mathrm{diag}\{\boldsymbol{x}_{k,n_1}\} \begin{bmatrix} \hat{\boldsymbol{h}}_{k,n_1}^{(u)} \\ \hat{\boldsymbol{h}}_{k,n_1}^{(u)} \end{bmatrix} + \mathrm{diag}\{\boldsymbol{x}_{k,n_2}\} \begin{bmatrix} \hat{\boldsymbol{h}}_{k,n_2}^{(u)} \\ \hat{\boldsymbol{h}}_{k,n_2}^{(u)} \end{bmatrix} \right) + \begin{bmatrix} \boldsymbol{n}_u^{(1)} \\ \boldsymbol{n}_u^{(2)} \end{bmatrix}, \tag{7.8}$$

where $\boldsymbol{n}_u^{(i)}$ is additive white Gaussian noise (AWGN) with zero-mean and a covariance matrix of $2\sigma^2\boldsymbol{I}_N$, expressed as $\mathcal{CN}(0, 2\sigma^2\boldsymbol{I}_N)$, where $\sigma^2 = 1/(2\gamma)$, $\gamma = b\gamma_0$ denotes the signal-to-noise ratio (SNR) per symbol, while γ_0 is the SNR per bit.

After assembling $\boldsymbol{y}_u^{(1)}$, which is the conjugate of $\boldsymbol{y}_u^{(2)}$ into a vector, the received $\left[\left(\boldsymbol{y}_u^{(1)}\right)^T, \left(\boldsymbol{y}_u^{*(2)}\right)^T \right]^T$ can be expressed as

$$\underbrace{\begin{bmatrix} \boldsymbol{y}_u^{(1)} \\ \boldsymbol{y}_u^{*(2)} \end{bmatrix}}_{\boldsymbol{y}} = \sum_{k=1}^{K} \frac{1}{2} \underbrace{\begin{bmatrix} \boldsymbol{C}_k & \boldsymbol{C}_k \\ \boldsymbol{C}_k & -\boldsymbol{C}_k \end{bmatrix} \begin{bmatrix} \hat{\boldsymbol{h}}_{k,n_1}^{(u)} & \hat{\boldsymbol{h}}_{k,n_2}^{(u)} \\ \hat{\boldsymbol{h}}_{k,n_2}^{*(u)} & -\hat{\boldsymbol{h}}_{k,n_1}^{*(u)} \end{bmatrix}}_{\boldsymbol{H}_{m_k}} \underbrace{\begin{bmatrix} s_{k,n_1} \\ s_{k,n_2} \end{bmatrix}}_{\boldsymbol{s}_k} + \underbrace{\begin{bmatrix} \boldsymbol{n}_u^{(1)} \\ \boldsymbol{n}_u^{*(2)} \end{bmatrix}}_{\boldsymbol{n}}. \tag{7.9}$$

where $\boldsymbol{C}_k = \mathrm{diag}\{\boldsymbol{c}_k\}$ and $\boldsymbol{H}_{m_k}$ represents the channel matrix between the t active TAs of user k selected by the GSM symbol m_k and the receiver. Hence we have obtained the MIMO equation for our GSM-SSTFS system. Next, our JMPA detector is conceived in Section 7.3.2.

7.3 Joint Message Passing-Aided Detection

Let us first express the symbols $\boldsymbol{s}_k = [s_{k,n_1}, \cdots, s_{k,n_t}]$, $s_{k,n_t} \in \mathcal{M}_2$, $n_i = n_1, \cdots, n_t$, transmitted by the t active TAs of user k in the form of a combined constellation symbol set defined as $\mathcal{M} = \underbrace{\mathcal{M}_2 \otimes \cdots \otimes \mathcal{M}_2}_{t} = \{g_1, g_2, \cdots, g_{M_2^t}\}$, which has a size of M_2^t. More explicitly, $g_1, g_2, \cdots, g_{M_2^t}$ represent the combinations of t QAM symbols. In the case of $t = 2$ and $\mathcal{M}_2 = \{0, 1\}$, we have $\mathcal{M} = \mathcal{M}_2 \otimes \mathcal{M}_2 = \{00, 01, 10, 11\}$. Then the GSM-QAM symbols transmitted by the k-th user employing t active TAs can be expressed as $z_k = m_k | g_k$, where $m_k \in \mathcal{M}_1$, $g_k \in \mathcal{M}$ and $z_k \in \mathcal{M}_1 \otimes \mathcal{M}$. Therefore, the GSM-QAM symbols transmitted by all K users can be defined as $\boldsymbol{z} = [z_1, \ldots, z_K]$.

Let us now assume that the BS perfectly knows both the CIRs and the spreading sequences. Then, the maximum-likelihood detection (MLD) finds the estimate of $\boldsymbol{z}$ by solving the optimization problem of

$$\begin{aligned}\hat{\boldsymbol{z}} =& [\hat{z}_1, \ldots, \hat{z}_K] \\ =& [\hat{m}_1 | \hat{g}_1, \cdots, \hat{m}_K | \hat{g}_K] \\ =& \underset{\substack{\tilde{m}_1, \cdots, \tilde{m}_K \in \mathcal{M}_1 \\ \tilde{g}_1, \cdots, \tilde{g}_K \in \mathcal{M}}}{\arg\min} \left\{ \left\| \boldsymbol{y} - \sum_{k=1}^{K} \boldsymbol{H}_{\tilde{m}_k} \tilde{g}_k \right\|^2 \right\}, \end{aligned} \tag{7.10a}$$

where the legitimate combinations of $\boldsymbol{H}_{\tilde{m}_k}$ and $\tilde{g}_k$ represent all possible candidates $\tilde{z}_k$. Explicitly, the MLD has to visit all possible candidate symbols in the symbol set $\mathcal{M} \otimes \mathcal{M}_1$ of all users, which has a detection complexity on the order of $\mathcal{O}\left[(M_1 M_2^t)^K\right]$. This excessive-complexity MLD is unsuitable for practical GSM/SSTFS systems.

Therefore, a low-complexity JMPA detection algorithm is proposed in this section, which jointly detects the GSM-QAM symbol based on the message-passing principle. Hence, in Section 7.3.1, we first design a factor graph for reduced-complexity signal detection, followed by our JMPA detector conceived in Section 7.3.2.

7.3.1 Factor Graph Design

Conventionally, a factor graph can be employed by a NOMA system for representing the connections between the users' transmitted symbols and the resource units transmitting these symbols. However, in a GSM/SSTFS system, a user's signal is transmitted by both the classic QAM symbols and the TAs activated from the N_T available TAs. Naturally, the receiver does not have the knowledge of the active TA indices before the detection. Hence, the corresponding factor graph has to be constructed to show the connections

between the K users' integrated symbols in the form of $m_k|g_k$ and the N subcarriers, so that joint STF-domain detection can be performed.

As an example, the factor graph of a GSM/SSTFS system having $N = 4$, $t = 2$, $N_T = 4$, $d_x = 2$ and $d_c = 3$, supporting $K = 6$ users is illustrated in Fig. 7.4. Explicitly, the variable node (VN) $j^{(l)}$ represents the combined QAM symbol g_j transmitted by the legitimate TA combination associated with the spatial symbol $m_j \in \mathcal{M}_1$ of user j in the l-th symbol duration, which is determined by the activated TAs of user j. By contrast, the check node (CN) i $(1 \leq i \leq N)$ represents the i-th subcarrier transmitting the signals of d_c users.

Let us define the connections with the VNs and those with the CNs as

$$\begin{aligned} \mathcal{X}_j &= \{i : 1 \leqslant i \leqslant N, e_{j,i} \neq 0\}, j = 1, \cdots, K \\ \mathcal{C}_i &= \{j : 1 \leqslant j \leqslant K, e_{j,i} \neq 0, \}, i = 1, \cdots, N, \end{aligned} \tag{7.11}$$

where $e_{j,i}$ represents the connection between the VN j and the CN i. To elaborate a little further, $\mathcal{X}_i$ collects all the CNs connected to the VN j and $\mathcal{C}_i$ contains all the VNs connected to the CN i.

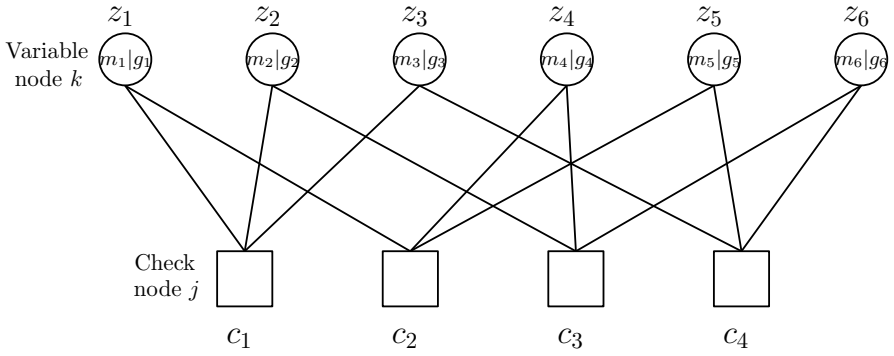

FIGURE 7.4: An example of the factor graph representation of the GSM/SSTFS system using regular sparse sequences and the parameters of $N = 4$, $n_a = 2$, $d_x = 2$, $d_c = 3$ and $K = 6$.

7.3.2 Joint Message Passing-Aided Detection

As shown in Fig. 7.4, information can be conveyed via the edge $e_{j,i}$ upward from the CN i to the VN j. By contrast, information is conveyed from the VN j to the CN i. The probability $\delta_{j,i}^{a_m,t}$, $a_m \in \mathcal{M}_1 \otimes \mathcal{M}$ is the information conveyed from the CN i to the VN j during the t-th iteration. More explicitly, $\delta_{j,i}^{a_m,t}$ represents the probability of $z_j = a_m, a_m \in \mathcal{M}_1 \otimes \mathcal{M}$, given the probabilities received by the CN i from all the connected VNs, but excluding j. Similarly, the information forwarded from the VN j to the CN i in the t-th iteration is denoted by $\eta_{j,i}^{a_m,t}$, which is defined as the probability of $z_j = a_m$, given the probabilities received by the VN j from all the connected CNs, but excluding j. Then the JMPA detector performs the following steps.

$$P(y_{ui}^{(1)}|\boldsymbol{z}_{[i]}) = \frac{1}{2\pi\sigma^2} \times \exp\left(-\frac{\left\|y_{ui}^{(1)} - \frac{1}{2}\sum_{j\in\mathcal{C}_i}\left\{c_{ji}\left[\hat{h}_{j,n_1,i}^{(u)}(s_{j,n_1} - s_{j,n_2}^*) + \hat{h}_{j,n_2,i}^{(u)}(s_{j,n_2} + s_{j,n_1}^*)\right]\right\}\right\|^2}{2\sigma^2}\right), \tag{7.13}$$

$$P(y_{ui}^{(2)}|\boldsymbol{z}_{[i]}) = \frac{1}{2\pi\sigma^2} \times \exp\left(-\frac{\left\|y_{ui}^{(2)} - \frac{1}{2}\sum_{j\in\mathcal{C}_i}\left\{c_{ji}\left[\hat{h}_{j,n_1,i}^{(u)}(s_{j,n_1} + s_{j,n_2}^*) + \hat{h}_{j,n_2,j}^{(u)}(s_{j,n_2} - s_{j,n_1}^*)\right]\right\}\right\|^2}{2\sigma^2}\right). \tag{7.14}$$

First, $\eta_{j,i}^{a_m,0}$ is initialised to $1/(M_1M_2^a)$ for all $a_m \in \mathcal{M}_1 \otimes \mathcal{M}$, and any $e_{j,i} \neq 0$. Then, at the t-th iteration, $\delta_{j,i}^{a_m,t}$ for $j \in \mathcal{X}_j$, and $j \in \mathcal{C}_j$ can be updated as

$$\delta_{j,i}^{a_m,t} = \sum_{\boldsymbol{z}_{[j]}\in(\mathcal{M}_1\otimes\mathcal{M})^{d_c-1}, z_j=a_m} \left(\prod_{z_v\in\boldsymbol{z}_{[j]}\setminus z_j} \eta_{j,i}^{z_v,i}\right) \times \prod_{u=1}^{U}\prod_{t=1}^{T} p(y_{uj}^{(l)}|\boldsymbol{z}_{[j]}, z_j = a_m), \tag{7.12}$$

where $\prod_{z_v\in\boldsymbol{z}_{[j]}\setminus z_j} \eta_{j,i}^{z_v,i}$ is the *a priori* probability of a given $\boldsymbol{z}_{[j]}$ with $z_j = a_m$. For the GSM/SSTFS having $t = 2$ TAs, when $\boldsymbol{z}_{[j]}$ is given, the PDF of $P(y_{uj}^{(l)}|\boldsymbol{z}_{[j]})$ at the $l = 1$-st and $l = 2$-nd symbol duration can be expressed in (7.13) and (7.14), respectively.

Observe from (7.12) that the information conveyed by the CN i to the VN j is the product of the information gleaned from all the other edges connected to the CN i. The total information conveyed to the VN j is the sum of the information arriving from all the CNs connected to the VN j.

Next, at the $(t+1)$-st iteration, the values $\delta_{j,i}^{a_m,t}$ obtained in the t-th iteration are used for updating $\eta_{j,i}^{a_m,t+1}$ for $i \in \mathcal{X}_j$ and $j \in \mathcal{C}_i$ as follows

$$\eta_{j,i}^{a_m,t+1} = \varphi_{j,i} \prod_{v\in\mathcal{X}_j\setminus j} \delta_{j,v}^{a_m,t}, \tag{7.15}$$

where $\varphi_{j,i}$ is the normalisation factor ensuring that $\sum_{a_m\in\mathcal{M}_1\otimes\mathcal{M}} \eta_{j,i}^{a_m,t+1} = 1$.

Finally, after I iterations, the symbol transmitted by the j-th user can be expressed as

$$\hat{z}_j = \hat{m}_j|\hat{g}_j = \underset{a_m \in \mathcal{M}_1 \otimes \mathcal{M}}{\arg\max} \prod_{v \in \mathcal{X}_j} \delta_{j,v}^{a_m,t}, \; j = 1, 2, \ldots, K. \tag{7.16}$$

Observe from (7.12) that the computational complexity is primarily determined by the upward information transition of Fig. 7.4 and, in particular, by the number of multiplications in (7.12). Therefore, the size of $\boldsymbol{z}_{[j]}$ is employed to represent the complexity order of the JMPA detector, which comprises $(M_1 M_2^t)^{d_c-1}$ legitimate combinations in $(\mathcal{M}_1 \otimes \mathcal{M})^{d_c-1}$. Hence, the complexity order of the JMPA detector can be expressed as $\mathcal{O}\left[(M_1 M_2^t)^{d_c-1}\right]$.

7.4 Performance Results

In this section, we quantify the BER performance of the proposed GSM/SSTFS scheme for transmission over frequency-selective Rayleigh fading channels having different number of CIR taps. Then we will compare the proposed GSM/SSTFS scheme both to the SSTFS scheme operating without GSM and to the MIMO-SCMA systems of [149] integrated with GSM. The number of active TAs is fixed to $t = 2$, as in the 5G NR, and each user spreads the signal over $d_x = 2$ subcarriers. Furthermore, the number of JMPA detection iterations is fixed to $I = 15$, since usually the BER of the proposed GSM/SSTFS system no longer improves beyond $I = 10$ iterations.

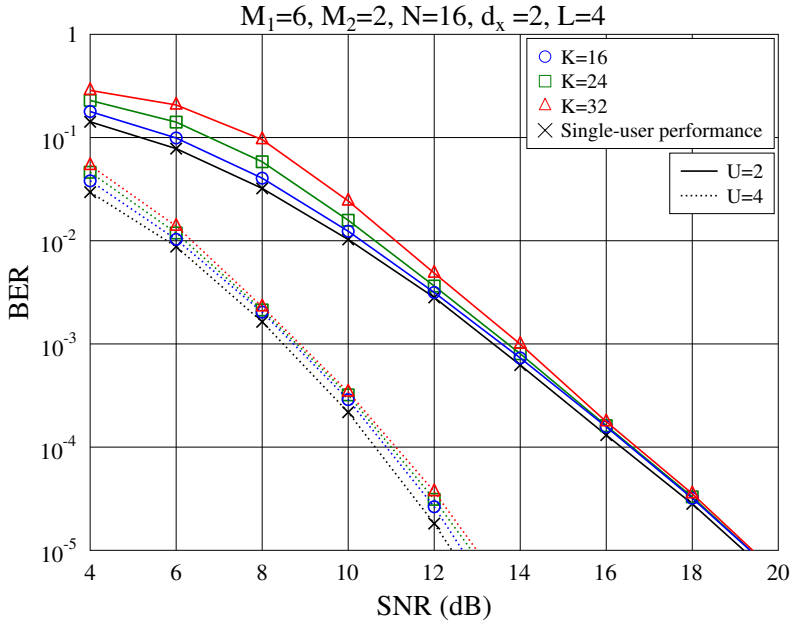

FIGURE 7.5: BER performance of the GSM/SSTFS systems supporting $K = 16, 24$ and 32 users within $N = 16$ resource slots employing $U = 2, 4$ RAs over frequency-selective fading channels having $L = 4$ CIR taps.

Firstly, the BER performance of the GSM/SSTFS system supporting the normalized user loads of up to $\frac{K}{N} = 200\%$ is shown in Fig. 7.5 for transmission over frequency-selective fading channels having $L = 4$ paths, $N = 16$ subcarriers, $N_T = 6$ TAs and binary phase shift keying (BPSK) modulation. The BER of the GSM/SSTFS system supporting a single user is also included as a benchmark. At the receiver, $U = 2$ or $U = 4$ receive antennas (RAs) are employed, which demonstrate a beneficial diversity gain at the receiver. Observe from Fig. 7.5 that the GSM/SSTFS system having a 200% user load shows a slight performance loss of about 1 dB compared to that of the 100% user load at a BER level of 10^{-2}. However, this BER performance loss becomes insignificant in higher signal-to-noise ratios (SNR), where the BER of the GSM/SSTFS systems supporting $K = 16, 24$ and 32 users converge to that of the single-user scenario. Therefore, it can be concluded that with the aid of transmit diversity, the proposed GSM/SSTFS system becomes capable of supporting up to 200% user load at a near-single-user BER in heavily-loaded next-generation systems.

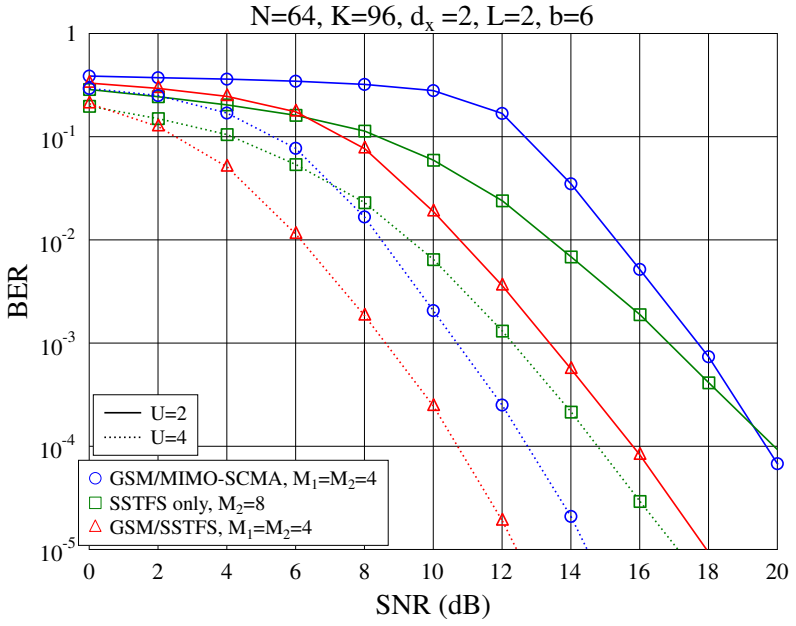

FIGURE 7.6: BER comparison of the GSM/SSTFS, SSTFS, and GSM/MIMO-SCMA systems with $U = 2, 4$ RAs supporting $K = 96$ users within $N = 64$ resource slots over frequency-selective fading channels having $L = 2$ CIR taps.

Furthermore, we compare the BER performance of the GSM/SSTFS system to that of 1) SSTFS operating without GSM, and 2) the MIMO-SCMA system of [20] amalgamated with GSM at an identical data rate of $b = 6$ bps, when communicating over frequency-selective Rayleigh fading channels having $L = 2$ or $L = 16$ channel impulse response (CIR) taps, as shown in Figs. 7.6 and 7.7, respectively. In both figures, a total of $N = 64$ subcarriers are employed for supporting $K = 96$ users, giving a normalized user load of $\frac{K}{N} = 150\%$. It can be observed from both Figs. 7.6 and 7.7 that the proposed GSM/SSTFS system achieves the best BER among the three candidate schemes considered. More specifically, for the SSTFS system dispensing with GSM, the 6-bit

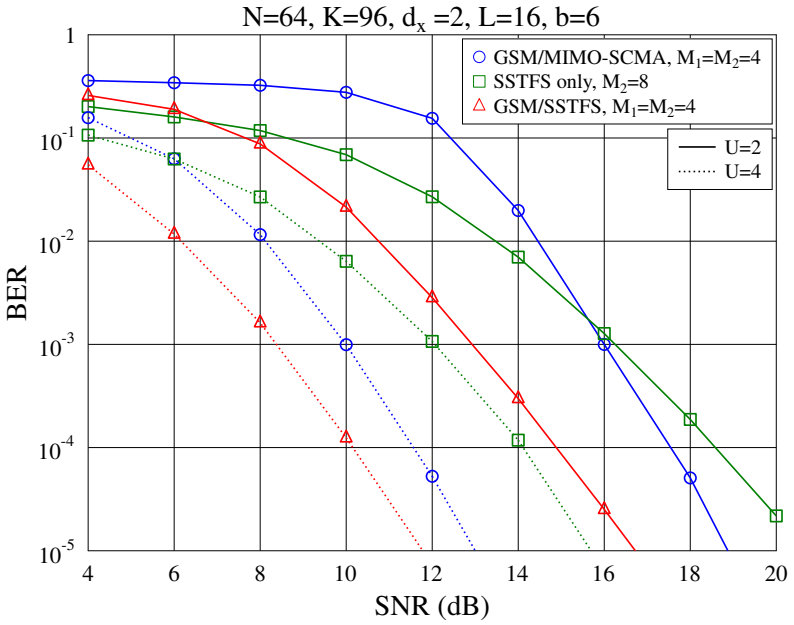

FIGURE 7.7: BER comparison of the GSM/SSTFS, SSTFS, and GSM/MIMO-SCMA systems with $U = 2, 4$ RAs supporting $K = 96$ users within $N = 64$ resource slots over frequency-selective fading channels having $L = 16$ CIR taps.

information is transmitted by only a pair of $M_2 = 8$-QAM symbols, whereas the proposed GSM/SSTFS scheme exploits the extra resource of the spatial domain, which maps the 6-bit information bits into a single 2-bit GSM symbol and a pair of $M_2 = 4$-QAM symbols. This achieves 4 dB gain at a BER level of 10^{-4}, when communicating over frequency-selective fading channels having $L = 16$ CIR taps and $U = 2$ RAs are employed at the receiver, as shown in Fig. 7.6.

By contrast, as shown in Fig. 7.7, in the case of a 150% user load and $U = 2$ RAs, the GSM/SSTFS system achieves up to 2.5 dB SNR gain at a BER of 10^{-4} over the GSM-aided MIMO-SCMA system of [20] in the frequency-selective Rayleigh fading channels having $L = 16$ CIR taps, which is achieved by the beneficial exploitation of STF-domain spreading. Hence, the GSM/SSTFS scheme may find promising application in large-scale access scenarios, where a large number of users access a single access point (AP) via limited spectral resources. Additionally, by comparing Figs. 7.6 and 7.7, we can see the advantageous frequency diversity gain of MC communications for transmission over frequency-selective channels, where all the systems achieve superior BER performance.

7.5 Conclusions

TABLE 7.2: Main conclusions of Chapter 7.

System	SM/MC-SCDMA system	
Example	$M_1 = M_2 = 4$, $U = 2$ $L = 2$	
SNR at a BER of 10^{-3}	$N = 16$, $K = 24$	$N = 64$, $K = 96$
	10.6 dB	10.0 dB
Complexity order	MLD	JMPA
	$\mathcal{O}\left[(M_1 M_2^a)^K\right]$	$\mathcal{O}\left[(M_1 M_2^a)^{d_c-1}\right]$

Based on the STC/GSM-SCMA system introduced in Chapter 6, we have further exploited the transmit diversity and proposed a GSM/SSTFS scheme, which relies on the STF-domain spreading. The main conclusions of this chapter are summarized in Table 7.2.

Specifically, in the GSM/SSTFS system employing two active TAs, each user spreads its signal over two symbol durations, two active TAs and multiple subcarriers. Extra information bits are embedded in the TA indices with the aid of GSM. Hence, the GSM/SSTFS scheme allows each user to transmit at a relatively high data rate, in addition to supporting large-scale access at a high normalized user-load. Furthermore, our JMPA detector imposes a low complexity. Our simulation results show that compared to the conventional MIMO-NOMA scheme, the proposed GSM/SSTFS system is capable of achieving a 5-dB SNR gain at 6 bpcu and at a BER of 10^{-5}, in the case of $N = 64$ and $K = 96$, i.e. at a normalized loading factor of 150%.

Chapter 8

Conclusions and Future Research

As shown in Figure 8.1, this thesis has concentrated on spatial modulation-aided non-orthogonal multiple access (SM-NOMA) schemes conceived for supporting massive machine-type communications (mMTC) and IoT for next generation communications. Firstly, the conclusions of each chapter are summarized in Section 8.1. Following this, future research interests are proposed in Section 8.3.

8.1 Chapter Conclusions

8.1.1 Chapter 1

Our discussions were commenced by reviewing the milestone contributions to the literature on SM and SM-aided multiuser communications. Specifically, Section 1.1 reviewed

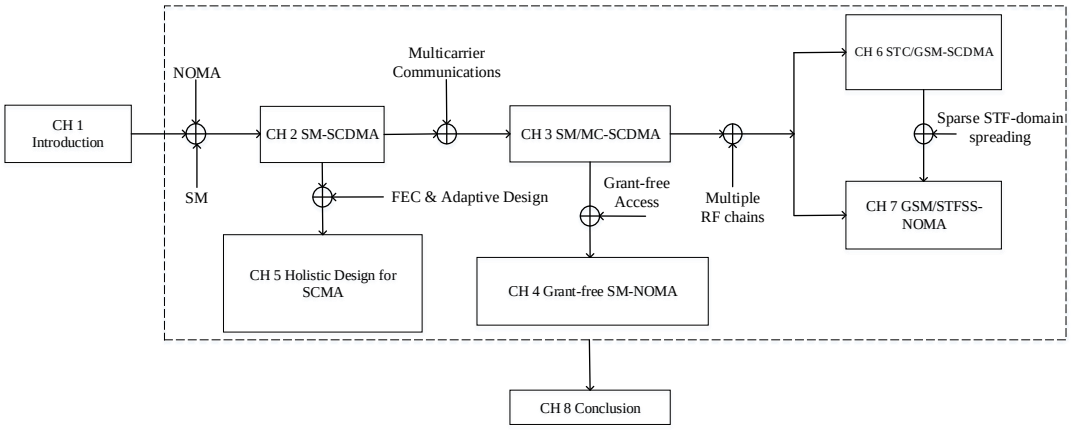

FIGURE 8.1: Thesis structure.

the family of SM schemes, which were summarized in Table 1.1. Then, SM-assisted orthogonal multiple access (OMA) and NOMA techniques were surveyed in Sections 1.2 and 1.3. Later in Section 1.4, the grant-free multiple access concepts were introduced, with the relevant research literature summarized in Table 1.4. Finally, Section 1.5 highlighted the organization as well as the main findings of this thesis.

8.1.2 Chapter 2

In this chapter, SM-aided sparse code division multiple access (SM-SCDMA) is proposed and analysed, which jointly adopts the nonorthogonal approaches for supporting heavily-loaded multiuser communications and employs SM for reducing the number of radio-frequency (RF) transceivers. Firstly, SM-SCDMA is detailed in Section 2.2. Explicitly, each user of the SM-SCDMA system employs several transmit antennas (TAs) for supporting the SM, while the base station (BS) employs several receive antennas for enhancing the detection reliability, where multiple access (MA) is supported with the aid of SCDMA. Since our SM-SCDMA relies on the principle of NOMA, it has the potential of supporting MA transmission, where the number of (active) users is higher than the total number of chips in the spreading codes.

Secondly, Section 2.3 addresses the detection of SM-SCDMA signals. We first consider the optimal maximum likelihood detector (MLD) in Section 2.3.1 in order to study the best possible potential of the SM-SCDMA scheme. Then, we derive a maximum *a-posteriori* detector (MAPD) in Section 2.3.2, based on which we develop a reduced complexity message passing-aided detector (MPAD) that is suitable for SM-SCDMA systems in Section 2.3.3, which employs SM and exploits receiver diversity.

Then in Section 2.4, we mathematically analyzed the error correction performance of SM-SCDMA systems by first deriving the single-user bit error rate (BER) bound and then analyzing the approximate BER of multi-user SM-SCDMA systems. By exploiting the specific structure of SM-SCDMA, a range of formulas were derived, which allowed us to estimate the BER performance of SM-SCDMA systems having an arbitrary dimension.

Following the theoretical analysis of Section 2.4, Section 2.5 characterized the performance of SM-SCDMA systems both by Monte-Carlo simulations and by evaluating the formulas derived. Based on SM-SCDMA systems having a relatively small dimension, we first verified the formulas derived by simulation and quantified their range of validity in this section. Then, the performance of relatively large-scale SM-SCDMA systems was investigated based on the numerical evaluation of our formulas derived. Furthermore, we addressed the impact of the related parameters on the BER performance attained, and demonstrated the efficiency of the MPAD. Additionally, in this section, we proposed a novel 8-ary quadrature amplitude modulation (QAM) scheme. When communicating over Gaussian channels, it outperformed all the existing 8QAM schemes in the relatively

low signal-to-noise (SNR) (≤ 10 dB) region, while achieving a similar BER performance to the best existing 8QAM schemes in the relatively high-SNR region. By contrast, when communicating over Rayleigh fading channels, it outperformed all the existing 8QAM schemes within the SNR region considered.

8.1.3 Chapter 3

Chapter 3 extended the work of Chapter 2 to multi-carrier (MC) communications and proposed a SM/MC-SCDMA system. To start with, the transceiver structure of an uplink SM/MC-SCDMA system has been introduced in detail in Section 3.2. In contrast to the SM-SCDMA scheme of Chapter 2, our SM/MC-SCDMA arrangement employed MC signalling to combat frequency-selective fading. Sparse spreading has been employed for the sake of facilitating low-complexity detection, whilst significantly alleviating the PAPR problem of MC systems. Secondly, three detectors were developed for the SM/MC-SCDMA system in Section 3.3, including the optimal MLD, the MAP and the low-complexity MPAD.

Following this, the analysis of the single-user BER bound of our SM/MC-SCDMA system was provided in Section 3.4, when assuming that the signals experience frequency-selective fading, whilst taking into account the correlation among the subcarriers. Based on the single-user BER bound, we proposed tangible design guidelines for the system. Furthermore, we conceived a sparse code allocation technique for achieving a high diversity gain.

Finally, Section 3.5 characterizes the BER performance of our SM/MC-SCDMA systems using MPAD in different scenarios both by Monte-Carlo simulations and by our analytical results. Additionally, the SM/MC-SCDMA scheme is generalized to a novel SM/MC aided sparse code multiple access (SCMA) arrangement for the sake of obtaining extra shaping gain. Furthermore, the BER performance of both SM/MC-SCDMA and SM/MC-SCMA is compared to that of other related legacy MIMO schemes in this section.

8.1.4 Chapter 4

Grant-free access scenarios were considered in Chapter 4, while relaxing the assumption of Chapters 2 and 3 that all users are active in each symbol duration in the system. An uplink grant-free SM/MC-NOMA scheme is proposed in this chapter, where users transmit in a sporadic pattern at a low rate. Section 4.2 describes the system model of the proposed grant-free SM/MC-NOMA scheme, which gleans diversity gains from the often independently-fading frequency- and spatial-domains. SM is employed for reducing the number of RF chains, while nonorthogonal frequency-domain (FD) spreading is harness

for attaining FD diversity gains for MC transmission over frequency-selective fading channels.

In order to identify the active users and detect their transmitted data, a pair of detection algorithms were detailed in Sections 4.4 and 4.5, after a brief overview of the CS-based multiuser detectors in Section 4.3. More specifically, an iterative Joint Multiuser Matching Pursuit (JMuMP) detector was first proposed in Section 4.4, which exploited the sparsity of both the user activity and of SM in the antenna domain. The number of active users was estimated by our JMuMP detector before the detection of data conveyed by the classic space-shift keying (SSK) and amplitude-phase modulation (APM) symbols, where the SSK information detection was intrinsically integrated into the active user identification process. Furthermore, an improved symbol mapping approach is also proposed and integrated into the JMuMP detector. Following the JMuMP detector, an Adaptive MuMP (AMuMP) detector was conceived in Section 4.5, which did not require the perfect *a priori* knowledge of the user activity at the receiver, and yet further improved the BER performance of the SM/MC-NOMA system employing the JMuMP detector. In the proposed AMuMP detector, both the active users as well as their data are iteratively recovered, until both the active users and their data are deemed to be reliably detected. This is more realistic, but also more challenging than the JMuMP philosophy of assuming that the number of users identified in each iteration remains unchanged.

Finally, Section 4.6 characterized the system performance in terms of its BER vs. computational complexity, when employing the JMuMP, AMuMP and several benchmark detectors. We demonstrated that the AMuMP scheme provided more reliable detection than the JMuMP detector, even when the user activation probability was as high as $p = 0.3$, albeit at the cost of a higher detection complexity and latency. Furthermore, design guidelines were provided by taking into account the BER vs complexity trade-off.

8.1.5 Chapter 5

In Chapter 5, we extended our focus to the holistic design of SCMA systems and conceive an EXtrinsic Information Transfer (EXIT)-chart-aided hybrid detection and decoding (HDD) algorithm for turbo-coded sparse code multiple access (SCMA) systems, which reduced the complexity of the conventional joint detection and decoding (JDD), without degrading its BER performance. Section 5.2 described the transmitter and receiver schematics of the turbo-coded SCMA system. Following this, the state-of-the-art review of separate detection and decoding was offered, while the JDD scheme advocated was discussed in Section 5.3. Finally, we detailed the iterative extrinsic logarithmic likelihood ratio (LLR) exchange between the MPA detector and the Logarithmic Bahl-Cocke-Jelinek-Raviv (Log-BCJR) turbo decoder.

By analysing the convergence behaviour of our system by EXIT charts in Section 5.4, we proposed a HDD aided turbo-coded SCMA system, which maintains the BER performance, but achieves a beneficial complexity reduction. To be more specific, we optimize the activation order of detection and decoding scheduling for achieving the early termination of iterations with the aid of EXIT chart analysis. In this way, the detection and decoding latency can be significantly reduced at a similar BER to that of HDD. Additionally, the proposed HDD achieves a complexity reduction of up to 25% with the aid of our early-termination philosophy.

Then, Section 5.5 proposed a near-instantaneously adaptive turbo-coded system design example along with characterizing the adaptive system's performance employing HDD. In the proposed adaptive turbo-coded system, the transmitter selects the most appropriate transmission mode according to the prevalent near-instantaneous channel conditions. More explicitly, our adaptive turbo-coded SCMA system configures itself in the most appropriate mode of operation by jointly selecting the user load, coding rate as well as modulation order by maintaining the data rate at the target BER. Our adaptive system design principle can be readily extended to diverse SCMA systems in combination with other popular channel coding schemes.

8.1.6 Chapter 6

In this chapter, we further expanded our research scope for conceiving transmit diversity aided SM-NOMA systems and proposed a space-time-coded generalized SM-aided SCDMA (STC/GSM-SCDMA) system, which achieved transmit diversity in both the spatial- and frequency-domain (STD).

Firstly, Section 6.2 introduced the STC/GSM-SCDMA system model for supporting heavily-loaded uplink multiuser (MU) MC communications, which achieved transmit diversity in the SFD. In our STC/GSM-SCDMA system, GSM was employed both for reducing the number of RF chains and for transmitting extra information bits via the active TA indices, while STC is employed for gleaning spatial domain diversity. By employing LDS in the FD, MC signalling can also be activated for combatting frequency-selective fading. Furthermore, in contrast to the conventional orthogonal MU systems, where 'only' up to 100% normalized user-load can be attained, each orthogonal FD resource unit in the proposed STC/GSM-SCDMA system is capable of supporting more than a single user, hence supporting a higher normalized user-load.

Secondly, Section 6.3 conceived a pair of detection algorithms. Specifically, Section 6.3.1 first designed a joint factor graph for representing the connections of the proposed STC/GSM-SCDMA system, based on which our bespoke MPA detection relying on the proposed joint factor graph. Then, a 3-dimensional (3D) factor graph is designed in Section 6.3.2, where the connections between users and TAs as well as those between

subcarriers and RAs are separately illustrated. Based on this unique relationship, a low-complexity approximate message passing (AMP) detector is proposed. the theoretical single-user performance bound is derived for the proposed STC/GSM-SCDMA system for transmission over frequency-selective Rayleigh fading channels, which is employed as the benchmark of our multiuser STC/GSM-SCDMA systems.

Furthermore, the single-user performance bound of our proposed STC/GSM-SCMA system over the frequency selective channels was derived in Section 6.4 as the system benchmark. Finally, our BER vs. complexity simulation results were provided in Section 6.5. The results also showed that our STC/GSM-SCDMA system outperformed the multiple-input multiple-output (MIMO) NOMA systems of [29, 110].

8.1.7 Chapter 7

Chapter 7 proposed an alternative technique of achieving transmit diversity based on the concept of GSM-aided sparse space-time-frequency spreading (GSM/SSTFS) assisted NOMA systems. Firstly, Section 7.2 describes the transmitter and receiver of the proposed GSM/SSTFS system. More specifically, in the GSM/SSTFS system relying on two active TAs, each user spreads its signal over two symbol durations, two active TAs, and multiple subcarriers by a unique pre-assigned sparse code, before transmitting the signal over the channel. Furthermore, with the aid of GSM, extra information bits are embedded in the TA indices.

Following this, Section 7.3 designs a joint factor graph, which is eminently suitable for visualizing the message-propagation by the STF-domain spreading. Based on the connections of the proposed joint factor graph, we conceived the low-complexity joint message passing algorithm (JMPA) detection for the GSM/SSTFS-NOMA.

Finally, our BER performance results have demonstrated that the proposed GSM/SSTFS scheme achieves superior BER over the conventional MIMO-NOMA schemes of [29, 110] at the same data rate in terms of bits per symbol (BPS). Quantitatively, the proposed GSM/SSTFS system is capable of achieving a 5-dB SNR gain at 6 bpcu and at a BER of 10^{-5}, in the case of $N = 64$ and $K = 96$, i.e. at a normalized loading factor of 150% MIMO-NOMA system of [110].

8.2 Design Guidelines

Fig. 8.2 shows our guidelines for a typical system design with the aim of meeting particular requirements, which comprises 6 steps for designing and optimizing a communication system.

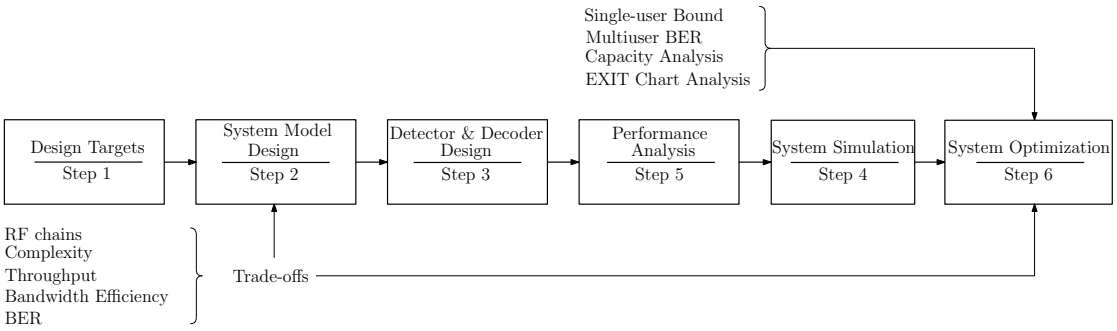

FIGURE 8.2: Design guidelines based on the thesis.

- **Step 1:** the first step is to identify and define the performance requirements. In the case of the mMTC scenario considered in this treatise, our design targets included having a small number of RF chains, a low detection complexity, a high throughput as well as a low BER, as shown in Fig. 8.2. These requirements guide the design and determine the overall system characteristics.

- **Step 2:** Given the explicit performance targets, a system model meeting the requirements is designed in Step 2. For example, in order to support rank-deficient multiuser communications at a low complexity and a high throughput, Chapter 2 proposed a SM-SCDMA scheme, which jointly exploited the benefits of SM and NOMA for supporting up to 200% normalized user load.

- **Step 3:** Following the system design, a complete receiver, including for example a joint detector and decoder design, has to be developed to examine whether the resultant system will be capable of satisfying the requirements identified in Step 1. For instance, a hybrid detector and decoder was designed in Chapter 5 for our turbo-coded SCMA system for improving the BER and reducing detection complexity.

- **Step 4:** Once the system architecture has been finalized, its performance may be evaluated theoretically, as shown in Step 5 of Fig. 8.2. The performance metrics may include the BER, throughput, delay or latency, while one of the most potent tools is constituted by EXIT chart analysis. For example, in chapter 5 the convergence behavior of turbo decoding and SCMA detection characterized by EXIT charts may be employed to guide the activation order of the detection and decoding components of turbo-coded SCMA systems.

- **Step 5:** Then in Step 5, the Mont-Carlo simulations may be employed for quantifying the characteristics such as the BER, throughput, delay vs. complexity, etc., which allows a convenient comparison with state-of-the-art solutions. An example of this step may be constituted by the BER simulations of Chapter 7, where different benchmark systems such as MIMO-NOMA and SM-NOMA were compared.

- **Step 6:** In general, not all the targets and requirements will be fulfilled in the first attempt. Therefore, Step 6 optimises the algorithmic and architectural design in order to fill the gap between the simulation results and the design targets.

8.3 Future Work

Potential research interests inspired by our work presented in this thesis are introduced in this section.

8.3.1 Non-Coherent Detection of Spatial Modulation-Aided Non-Orthogonal Multiple Access

The SM-NOMA systems proposed in this thesis are all based on coherent detection approaches, which requires accurate channel state information (CSI) at the receiver. However, in practical communication systems, the wireless channel may experience time-varing fading, where abrupt changes of the CSI may be observed such those in air-to-air (A2A) or air-to-ground (A2G) communications, for example, where the airplane velocity is extremely high.

The transceiver structure of the uplink differential SM-NOMA system is demonstrated in Fig. 8.3, where differential modulation is employed at the transmitter and non-coherent detection is performed at the receiver. In this case, the CSI is no longer required at the base station (BS), facilitating the support of high-speed communication scenarios.

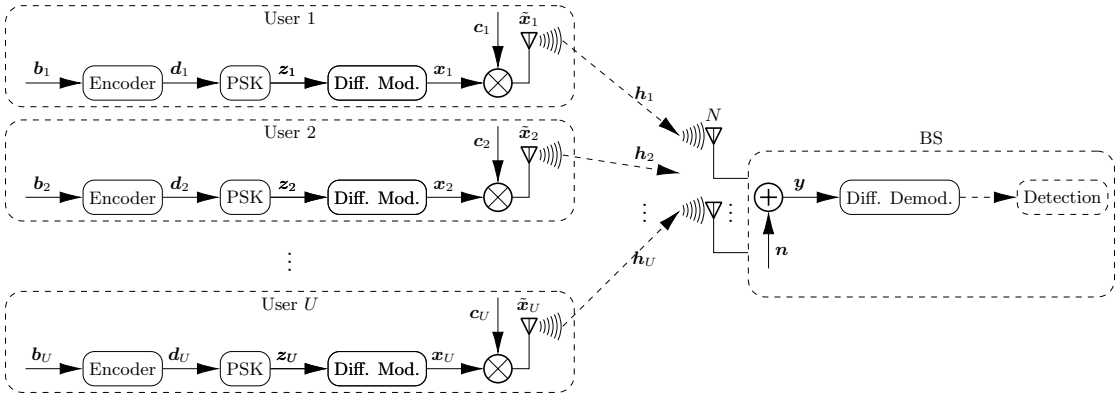

FIGURE 8.3: The transceiver schematic of the the non-coherent SM-NOMA system.

8.3.2 Physical-Layer Security Design of Spatial Modulation-Aided Non-Orthogonal Multiple Access

This thesis focused on the system design of SM-NOMA systems for supporting mMTC or IoT networks. However, the SM-NOMA systems can be further employed for enhancing the physical layer security (PLS), when L data streams are transmitted with N ($L \geq N$) limited resource units. A potential system model of SM-SCMA for PLS is shown in Fig. 8.4, where the channel quality indicator (CQI) is adopted to guide the SM-SCMA scheme's bit-to-symbol mapping, enabling secure transmission between the transmitter and the desired receiver.

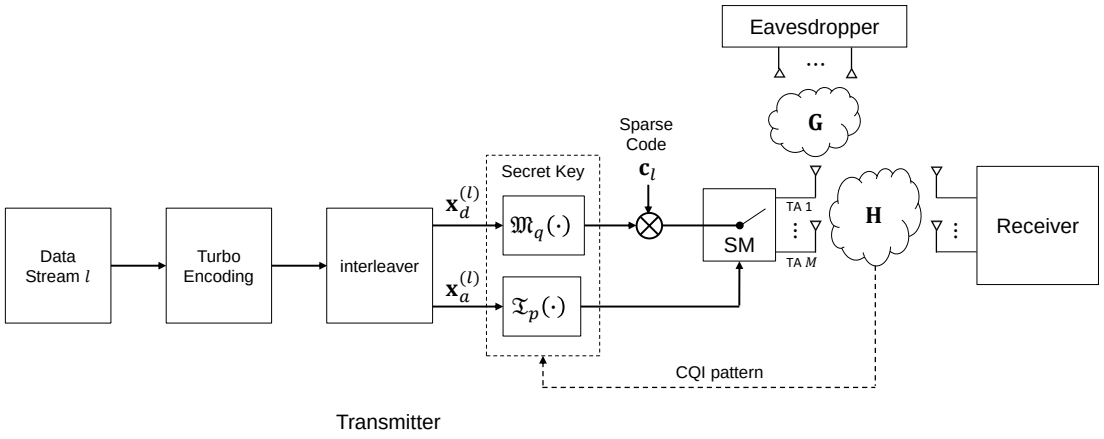

FIGURE 8.4: The CQI-mapped SM-SCMA with turbo encoding for the l-th data stream delivered from the transmitter to the desired receiver and the eavesdropper.

8.3.3 Deep-Learning-Aided Grant-Free Non-Orthogonal Multiple Access

The grant-free SM-NOMA scheme investigated in Chapter 4 relies on the assumption that perfect CSI knowledge is available at the receiver. However, in practical communication scenarios, the CSI has to be estimated by relying on the pilot symbols. Hence, joint channel estimation, user activity and signal detection may be conceived for grant-free SM-NOMA.

Additionally, as summarized in Table 1.4, machine learning-aided approaches have been envisioned as a promising technique of solving the joint user and data detection problem in grant-free NOMA [99–101], albeit they are less mature compared to conventional CS-based solutions [87–94].

Fortunately, with the aid of the autoencoder concept, joint transmitter and receiver optimization can be attained, which would further improve the attainable system performance in a data-driven pattern.

Glossary

3D	Three-Dimensional
3GPP	Third Generation Partnership Project
5G	Fifth Generation
ABER	Average Bit Error Rate
ADC	Analog-to-Digital Convertor
AMP	Approximate Message Passing
AMuMP	Adaptive Multiuser Matching Pursuit
APM	Amplitude-Phase Modulation
ASER	Average Symbol Error Rate
AWGN	Additive White Gaussian Noise
BER	Bit Error Rate
BPS	Bits per Symbol
BS	Base Station
CDMA	Code Division Multiple Access
CHTF	Channel Transfer Function
CIR	Channel Impulse Response
CN	Check Node
CoSaMP	Compressive Sampling Matching Pursuit
CP	Cyclic Prefix
CS	Compressive Sensing
DCS	Dynamic Compressive Sensing
DL	Downlink
DQSM	Differential Quadrature Spatial Modulation
DSM	Differential Spatial Modulation
EM	Expectation Maximization
ETU	Extended Typical Urban
EXIT	EXtrinsic Information Transfer
FD	Frequency Domain
FER	Frame Error Rate
FFT	Fast Fourier Transform
FLOP	Floating Point Operation

GSM	Generalized Spatial Modulation
HDD	Hybrid Detection and Decoding
IFFT	Inverse Fast Fourier Transform
IoT	Internet-of-Things
ISI	Inter-Symbol Interference
iSNR	Instantaneous Signal-to-Noise Ratio
IUI	Inter-User Interference
JDD	Joint Detection and Decoding
JMPA	Joint Message Passing-aided
JMuMP	Joint Multiuser Matching Pursuit
LDPC	Low-Density Parity-Check
LDS	Low Density Signature
LLR	Logarithmic Likelihood Ratio
Log-BCJR	Logarithmic Bahl-Cocke-Jelinek-Raviv
LS	Least Square
LTE	Long Term Evolution
MA	Multiple Access
MAPD	Maximum *a-posteriori* Detector
MC	Multicarrier
MF	Matched Filtering
MGF	Moment Generation Function
MI	Mutual Information
MIMO	Multiple-Input Multiple-Output
ML	Maximum-Likelihood
MLD	Maximum-Likelihood Detection
mMTC	massive Machine-Type Communications
MPA	Massage Passing Algorithm
MPAD	Message Passing-aided Detector
MUI	Multiuser Interference
NOMA	Non-Orthogonal Multiple Access
NR	New Radio
OFDM	Orthogonal Frequency Division Multiplexing
OMA	Orthogonal Multiple Access
OMP	Orthogonal Matching Pursuit
OP	Outage Probability
P/S	Parallel-to-Serial
PAPR	Peak-to-Average power ratio
PAR	Peak-to-Average Ratio
PDF	Probability Density Function
PEP	Pairwise Error Probability
PSM	Precoded Spatial Modulation

QAM	Quadrature Amplitude Modulation
QSM	Quadrature Spatial Modulation
RA	Receive Antenna
RDSM	Rectangular Differential Spatial Modulation
RF	Radio Frequency
RIP	Restricted Isometry Property
RSM	Receive Spatial Modulation
SCDMA	Sparse Code Division Multiple Access
SCMA	Sparse Code Multiple-Access
SD	Symbol Duration
SDD	Separate Detection and Decoding
SDMA	Space Division Multiple Access
SFD	Spatial- and Frequency-Domain
SIC	Successive Interference Cancellation
SM	Spatial Modulation
SNR	Signal-to-Noise Ratio
SP	Subspace Pursuit
SSK	Space-Shift Keying
SSTFS	Sparse Space-Time-Frequency Spreading
STBC	Space-Time Block Coding
STC	Space-Time-Coding
STFD	Space-, Time-, and Frequency-Domain
STS	Space-Time Spreading
STSK	Space-Time Shift Keying
TA	Transmit Antenna
TAS	Transmit Antenna Selection
TC	Trellis Coding
TD	Time Domain
UL	Uplink
URLLC	Ultra-Reliable Low-Latency Communication
VN	Variable Node

Bibliography

[1] L. Liu and W. Yu, "Massive connectivity with massive MIMO - part I: Device activity detection and channel estimation," *IEEE Transactions on Signal Processing*, vol. 66, no. 11, pp. 2933–2946, 2018.

[2] L. Tello-Oquendo, V. Pla, I. Leyva-Mayorga, J. Martinez-Bauset, V. Casares-Giner, and L. Guijarro, "Efficient random access channel evaluation and load estimation in LTE-A with massive MTC," *IEEE Transactions on Vehicular Technology*, vol. 68, no. 2, pp. 1998–2002, 2018.

[3] W. Shao, S. Zhang, H. Li, N. Zhao, and O. A. Dobre, "Angle-domain noma over multicell millimeter wave massive MIMO networks," *IEEE Transactions on Communications*, vol. 68, no. 4, pp. 2277–2292, 2020.

[4] L. Hanzo, M. Münster, B. Choi, and T. Keller, *OFDM and MC-CDMA for broadband multi-user communications, WLANs and broadcasting.* John Wiley & Sons, 2005.

[5] L. Dai, B. Wang, Z. Ding, Z. Wang, S. Chen, and L. Hanzo, "A survey of non-orthogonal multiple access for 5G," *IEEE Communications Surveys & Tutorials*, vol. 20, no. 3, pp. 2294–2323, 2018.

[6] M. Moltafet, N. M. Yamchi, M. R. Javan, and P. Azmi, "Comparison study between PD-NOMA and SCMA," *IEEE Transactions on Vehicular Technology*, vol. 67, no. 2, pp. 1830–1834, 2017.

[7] X. Li, J. Li, Y. Liu, Z. Ding, and A. Nallanathan, "Residual transceiver hardware impairments on cooperative noma networks," *IEEE Transactions on Wireless Communications*, vol. 19, no. 1, pp. 680–695, 2019.

[8] H. Liu, T. A. Tsiftsis, K. J. Kim, K. S. Kwak, and H. V. Poor, "Rate splitting for uplink NOMA with enhanced fairness and outage performance," *IEEE Transactions on Wireless Communications*, vol. 19, no. 7, pp. 4657–4670, 2020.

[9] Y. Liu, Z. Qin, M. Elkashlan, Z. Ding, A. Nallanathan, and L. Hanzo, "Nonorthogonal multiple access for 5G and beyond," *Proceedings of the IEEE*, vol. 105, no. 12, pp. 2347–2381, 2017.

[10] R. Hoshyar, F. P. Wathan, and R. Tafazolli, "Novel low-density signature for synchronous CDMA systems over AWGN channel," *IEEE Transactions on Signal Processing*, vol. 56, no. 4, pp. 1616–1626, 2008.

[11] D. Guo and C.-C. Wang, "Multiuser detection of sparsely spread CDMA," *IEEE Journal on Selected Areas in Communications*, vol. 26, no. 3, pp. 421–431, 2008.

[12] R. Razavi, A.-I. Mohammed, M. A. Imran, R. Hoshyar, and D. Chen, "On receiver design for uplink low density signature OFDM (LDS-OFDM)," *IEEE Transactions on Communications*, vol. 60, no. 11, pp. 3499–3508, 2012.

[13] H. Nikopour and H. Baligh, "Sparse code multiple access," in *Annual International Symposium on Personal, Indoor, and Mobile Radio Communications (PIMRC)*, pp. 332–336, 2013.

[14] S. Chen, B. Ren, Q. Gao, S. Kang, S. Sun, and K. Niu, "Pattern division multiple access-a novel nonorthogonal multiple access for fifth-generation radio networks," *IEEE Transactions on Vehicular Technology*, vol. 66, no. 4, pp. 3185–3196, 2016.

[15] Z. Ding, R. Schober, and H. V. Poor, "A general MIMO framework for NOMA downlink and uplink transmission based on signal alignment," *IEEE Transactions on Wireless Communications*, vol. 15, no. 6, pp. 4438–4454, 2016.

[16] Z. Yang, Z. Ding, P. Fan, and N. Al-Dhahir, "A general power allocation scheme to guarantee quality of service in downlink and uplink NOMA systems," *IEEE Transactions on Wireless Communications*, vol. 15, no. 11, pp. 7244–7257, 2016.

[17] R. Mesleh, H. Haas, C. W. Ahn, and S. Yun, "Spatial modulation-a new low complexity spectral efficiency enhancing technique," in *First International Conference on Communications and Networking in China*, pp. 1–5, 2006.

[18] R. Y. Mesleh, H. Haas, S. Sinanovic, C. W. Ahn, and S. Yun, "Spatial modulation," *IEEE Transactions on Vehicular Technology*, vol. 57, no. 4, pp. 2228–2241, 2008.

[19] M. Di Renzo, H. Haas, and P. M. Grant, "Spatial modulation for multiple-antenna wireless systems: A survey," *IEEE Communications Magazine*, vol. 49, no. 12, 2011.

[20] M. Di Renzo, H. Haas, A. Ghrayeb, S. Sugiura, and L. Hanzo, "Spatial modulation for generalized MIMO: Challenges, opportunities, and implementation," *Proceedings of the IEEE*, vol. 102, no. 1, pp. 56–103, 2014.

[21] P. Yang, M. Di Renzo, Y. Xiao, S. Li, and L. Hanzo, "Design guidelines for spatial modulation," *IEEE Communications Surveys & Tutorials*, vol. 17, no. 1, pp. 6–26, 2015.

[22] M. Wen, B. Zheng, K. J. Kim, M. Di Renzo, T. A. Tsiftsis, K.-C. Chen, and N. Al-Dhahir, "A survey on spatial modulation in emerging wireless systems: Research progresses and applications," *IEEE Journal on Selected Areas in Communications*, vol. 37, no. 9, pp. 1949–1972, 2019.

[23] Y. Chen, L. Wang, Y. Ai, B. Jiao, and L. Hanzo, "Performance analysis of NOMA-SM in vehicle-to-vehicle massive MIMO channels," *IEEE Journal on Selected Areas in Communications*, vol. 35, no. 12, pp. 2653–2666, 2017.

[24] Z. Wang, J. Cao, *et al.*, "NOMA-based spatial modulation," *IEEE Access*, vol. 5, pp. 3790–3800, 2017.

[25] R. F. Siregar, F. W. Murti, and S. Y. Shin, "Combination of spatial modulation and non-orthogonal multiple access using hybrid detection scheme," in *Ubiquitous and Future Networks (ICUFN) Conference*, pp. 476–481, 2017.

[26] Y. Liu, L. Yang, and L. Hanzo, "Spatial modulation aided sparse code-division multiple access," *IEEE Transactions on Wireless Communications*, vol. 17, pp. 1474–1487, March 2018.

[27] C. Zhong, X. Hu, X. Chen, D. W. K. Ng, and Z. Zhang, "Spatial modulation assisted multi-antenna non-orthogonal multiple access," *IEEE Wireless Communications*, vol. 25, no. 2, pp. 61–67, 2018.

[28] Z. Pan, J. Luo, J. Lei, L. Wen, and C. Tang, "Uplink spatial modulation SCMA system," *IEEE Communications Letters*, vol. 23, no. 1, pp. 184–187, 2018.

[29] Y. Liu, L.-L. Yang, P. Xiao, H. Haas, and L. Hanzo, "Spatial modulated multicarrier sparse code-division multiple access," *IEEE Transactions on Wireless Communications*, 2019.

[30] I. Al-Nahhal, O. A. Dobre, E. Basar, and S. Ikki, "Low-cost uplink sparse code multiple access for spatial modulation," *IEEE Transactions on Vehicular Technology*, vol. 68, no. 9, pp. 9313–9317, 2019.

[31] Q. Li, M. Wen, E. Basar, H. V. Poor, and F. Chen, "Spatial modulation-aided cooperative NOMA: Performance analysis and comparative study," *IEEE Journal of Selected Topics in Signal Processing*, vol. 13, no. 3, pp. 715–728, 2019.

[32] Q. Si, M. Jin, Y. Chen, N. Zhao, and X. Wang, "Performance analysis of spatial modulation aided NOMA with full-duplex relay," *IEEE Transactions on Vehicular Technology*, vol. 69, no. 5, pp. 5683–5687, 2020.

[33] Y. Liu, L.-L. Yang, and L. Hanzo, "Sparse space-time-frequency-domain spreading for large-scale non-orthogonal multiple access," *IEEE Transactions on Vehicular Technology*, 2020.

[34] Z. Hong, G. Li, Y. Xu, and X. Zhou, "User grouping and power allocation for downlink NOMA-based quadrature spatial modulation," *IEEE Access*, vol. 8, pp. 38136–38145, 2020.

[35] Y. A. Chau and S.-H. Yu, "Space modulation on wireless fading channels," in *Vehicular Technology Conference Fall,*, vol. 3, pp. 1668–1671, 2001.

[36] J. Jeganathan, A. Ghrayeb, L. Szczecinski, and A. Ceron, "Space shift keying modulation for MIMO channels," *IEEE Transactions on Wireless Communications*, vol. 8, no. 7, pp. 3692–3703, 2009.

[37] R. Mesleh, M. Di Renzo, H. Haas, and P. M. Grant, "Trellis coded spatial modulation," *IEEE Transactions on Wireless Communications*, vol. 9, no. 7, pp. 2349–2361, 2010.

[38] E. Başar, U. Aygölü, E. Panayirci, and H. V. Poor, "Space-time block coded spatial modulation," *IEEE Transactions on Communications*, vol. 59, no. 3, pp. 823–832, 2010.

[39] S. Sugiura, S. Chen, and L. Hanzo, "Coherent and differential space-time shift keying: A dispersion matrix approach," *IEEE Transactions on Communications*, vol. 58, no. 11, pp. 3219–3230, 2010.

[40] L.-L. Yang, "Transmitter preprocessing aided spatial modulation for multiple-input multiple-output systems," in *Vehicular Technology Conference Spring*, pp. 1–5, 2011.

[41] J. Wang, S. Jia, and J. Song, "Generalised spatial modulation system with multiple active transmit antennas and low complexity detection scheme," *IEEE Transactions on Wireless Communications*, vol. 11, no. 4, pp. 1605–1615, 2012.

[42] R. Zhang, L.-L. Yang, and L. Hanzo, "Generalised pre-coding aided spatial modulation," *IEEE Transactions on Wireless Communications*, vol. 12, no. 11, pp. 5434–5443, 2013.

[43] Y. Bian, X. Cheng, M. Wen, L. Yang, H. V. Poor, and B. Jiao, "Differential spatial modulation," *IEEE Transactions on Vehicular Technology*, vol. 64, no. 7, pp. 3262–3268, 2014.

[44] R. Mesleh, S. S. Ikki, and H. M. Aggoune, "Quadrature spatial modulation," *IEEE Transactions on Vehicular Technology*, vol. 64, no. 6, pp. 2738–2742, 2014.

[45] R. Mesleh, S. Althunibat, and A. Younis, "Differential quadrature spatial modulation," *IEEE Transactions on Communications*, vol. 65, no. 9, pp. 3810–3817, 2017.

[46] N. Ishikawa and S. Sugiura, "Rectangular differential spatial modulation for open-loop noncoherent massive-MIMO downlink," *IEEE Transactions on Wireless Communications*, vol. 16, no. 3, pp. 1908–1920, 2017.

[47] L. Xiao, P. Xiao, Y. Xiao, I. Hemadeh, A. Mohamed, and L. Hanzo, "Bayesian compressive sensing assisted space–time block coded quadrature spatial modulation," *IEEE Transactions on Vehicular Technology*, vol. 67, no. 10, pp. 10044–10048, 2018.

[48] C. Wu, Y. Xiao, L. Xiao, P. Yang, X. Lei, and W. Xiang, "Space-time block coded rectangular differential spatial modulation: System design and performance analysis," *IEEE Transactions on Communications*, vol. 67, no. 9, pp. 6586–6597, 2019.

[49] L. Xiao, Y. Xiao, C. Xu, X. Lei, P. Yang, S. Li, and L. Hanzo, "Compressed-sensing assisted spatial multiplexing aided spatial modulation," *IEEE Transactions on Wireless Communications*, vol. 17, no. 2, pp. 794–807, 2017.

[50] E. Basar, U. Aygolu, E. Panayirci, and H. V. Poor, "Space-time block coded spatial modulation," *IEEE Transactions on Communications*, vol. 59, no. 3, pp. 823–832, 2010.

[51] M. Di Renzo and H. Haas, "Bit error probability of space-shift keying MIMO over multiple-access independent fading channels," *IEEE Transactions on Vehicular Technology*, vol. 60, no. 8, pp. 3694–3711, 2011.

[52] N. Serafimovski, S. Sinanović, M. Di Renzo, and H. Haas, "Multiple access spatial modulation," *EURASIP Journal on Wireless Communications and Networking*, vol. 2012, no. 1, p. 299, 2012.

[53] T. L. Narasimhan, P. Raviteja, and A. Chockalingam, "Large-scale multiuser SM-MIMO versus massive MIMO," in *Information Theory and Applications Workshop (ITA)*, pp. 1–9, 2014.

[54] S. Wang, Y. Li, and J. Wang, "Multiuser detection in massive spatial modulation MIMO with low-resolution ADCs," *IEEE Transactions on Wireless Communications*, vol. 14, no. 4, pp. 2156–2168, 2014.

[55] S. Narayanan, M. J. Chaudhry, A. Stavridis, M. Di Renzo, F. Graziosi, and H. Haas, "Multi-user spatial modulation MIMO," in *IEEE Wireless Communications and Networking Conference (WCNC)*, pp. 671–676, 2014.

[56] T. L. Narasimhan, P. Raviteja, and A. Chockalingam, "Generalized spatial modulation in large-scale multiuser MIMO systems," *IEEE Transactions on Wireless Communications*, vol. 14, no. 7, pp. 3764–3779, 2015.

[57] A. Garcia-Rodriguez and C. Masouros, "Low-complexity compressive sensing detection for spatial modulation in large-scale multiple access channels," *IEEE Transactions on Communications*, vol. 63, pp. 2565–2579, July 2015.

[58] Z. Gao, L. Dai, Z. Wang, S. Chen, and L. Hanzo, "Compressive-sensing-based multiuser detector for the large-scale SM-MIMO uplink," *IEEE Transactions on Vehicular Technology*, vol. 65, no. 10, pp. 8725–8730, 2015.

[59] M. Maleki, H. R. Bahrami, and A. Alizadeh, "Layered spatial modulation for multiuser communications," *IEEE Transactions on Wireless Communications*, vol. 15, no. 10, pp. 7143–7159, 2016.

[60] L. He, J. Wang, J. Song, and L. Hanzo, "On the multi-user multi-cell massive spatial modulation uplink: How many antennas for each user?," *IEEE Transactions on Wireless Communications*, vol. 16, pp. 1437–1451, March 2017.

[61] X. Meng, S. Wu, L. Kuang, D. Huang, and J. Lu, "Multi-user detection for spatial modulation via structured approximate message passing," *IEEE Communications Letters*, vol. 20, no. 8, pp. 1527–1530, 2016.

[62] R. Rajashekar, K. Hari, and L. Hanzo, "Transmit antenna subset selection for single and multiuser spatial modulation systems operating in frequency selective channels," *IEEE Transactions on Vehicular Technology*, vol. 67, no. 7, pp. 6156–6169, 2018.

[63] M. Maleki, K. Mohamed-Pour, and M. Soltanalian, "Large-system mutual information analysis of receive spatial modulation in correlated multi-cell massive MIMO networks," *IEEE Transactions on Communications*, vol. 67, no. 9, pp. 6071–6084, 2019.

[64] P. Pan and L.-L. Yang, "Spatially modulated code-division multiple-access for high-connectivity multiple access," *IEEE Transactions on Wireless Communications*, vol. 18, no. 8, pp. 4031–4046, 2019.

[65] F. R. Castillo-Soria, E. Basar, J. Cortez, and M. Cardenas-Juarez, "Quadrature spatial modulation based multiuser MIMO transmission system," *IET Communications*, vol. 14, no. 7, pp. 1147–1154, 2020.

[66] Y. Cai, Z. Qin, F. Cui, G. Y. Li, and J. A. McCann, "Modulation and multiple access for 5G networks," *IEEE Communications Surveys & Tutorials*, vol. 20, no. 1, pp. 629–646, 2018.

[67] K. Yang, N. Yang, N. Ye, M. Jia, Z. Gao, and R. Fan, "Non-orthogonal multiple access: Achieving sustainable future radio access," *IEEE Communications Magazine*, vol. 57, no. 2, pp. 116–121, 2018.

[68] M. Morales-Céspedes, O. Dobre, and A. García-Armada, "Semi-blind interference aligned NOMA for downlink MU-MISO systems," *IEEE Transactions on Communications*, vol. 68, no. 3, pp. 1852–1865, 2020.

[69] X. Mu, Y. Liu, L. Guo, and J. Lin, "Non-orthogonal multiple access for air-to-ground communication," *IEEE Transactions on Communications*, vol. 68, no. 5, pp. 2934–2949, 2020.

[70] X. Chen, D. W. K. Ng, W. Yu, E. G. Larsson, N. Al-Dhahir, and R. Schober, "Massive access for 5G and beyond," *arXiv preprint arXiv:2002.03491*, 2020.

[71] S. Ali, N. Rajatheva, and W. Saad, "Fast uplink grant for machine type communications: Challenges and opportunities," *IEEE Communications Magazine*, vol. 57, no. 3, pp. 97–103, 2019.

[72] S. K. Sharma and X. Wang, "Towards massive machine type communications in ultra-dense cellular IoT networks: Current issues and machine learning-assisted solutions," *IEEE Communications Surveys & Tutorials*, 2019.

[73] Z. Ding, X. Lei, G. K. Karagiannidis, R. Schober, J. Yuan, and V. K. Bhargava, "A survey on non-orthogonal multiple access for 5G networks: Research challenges and future trends," *IEEE Journal on Selected Areas in Communications*, vol. 35, no. 10, pp. 2181–2195, 2017.

[74] F. R. Kschischang, B. J. Frey, and H.-A. Loeliger, "Factor graphs and the sum-product algorithm," *IEEE Transactions on Information Theory*, vol. 47, no. 2, pp. 498–519, 2001.

[75] F. R. Kschischang, "Codes defined on graphs," *IEEE Communications Magazine*, vol. 41, no. 8, pp. 118–125, 2003.

[76] H. Mu, Z. Ma, M. Alhaji, P. Fan, and D. Chen, "A fixed low complexity message pass algorithm detector for up-link SCMA system," *IEEE Wireless Communications Letters*, vol. 4, no. 6, pp. 585–588, 2015.

[77] A. Bayesteh, H. Nikopour, M. Taherzadeh, H. Baligh, and J. Ma, "Low complexity techniques for SCMA detection," in *IEEE Globecom Workshops (GC Wkshps)*, pp. 1–6, 2015.

[78] L. Yang, Y. Liu, and Y. Siu, "Low complexity message passing algorithm for SCMA system," *IEEE Communications Letters*, vol. 20, no. 12, pp. 2466–2469, 2016.

[79] W. Yuan, N. Wu, Q. Guo, Y. Li, C. Xing, and J. Kuang, "Iterative receivers for downlink MIMO-SCMA: Message passing and distributed cooperative detection," *IEEE Transactions on Wireless Communications*, vol. 17, no. 5, pp. 3444–3458, 2018.

[80] Y. Du, B. Dong, Z. Chen, X. Wang, and P. Gao, "Improved serial scheduling-based detection for sparse code multiple access systems," *IEEE Wireless Communications Letters*, vol. 6, no. 5, pp. 570–573, 2017.

[81] X. Ma, L. Yang, Z. Chen, and Y. Siu, "Low complexity detection based on dynamic factor graph for SCMA systems," *IEEE Communications Letters*, vol. 21, no. 12, pp. 2666–2669, 2017.

[82] Z. Na, Y. Liu, J. Shi, C. Liu, and Z. Gao, "UAV-supported clustered NOMA for 6G-enabled Internet of things: Trajectory planning and resource allocation," *IEEE Internet of Things Journal*, 2020.

[83] M. Mohammadkarimi, M. A. Raza, and O. A. Dobre, "Signature-based nonorthogonal massive multiple access for future wireless networks: Uplink massive connectivity for machine-type communications," *IEEE Vehicular Technology Magazine*, vol. 13, no. 4, pp. 40–50, 2018.

[84] S. Han, X. Xu, S. Fang, Y. Sun, Y. Cao, X. Tao, and P. Zhang, "Energy efficient secure computation offloading in NOMA-based mMTC networks for IoT," *IEEE Internet of Things Journal*, vol. 6, no. 3, pp. 5674–5690, 2019.

[85] A. Hoglund, J. Bergman, X. Lin, O. Liberg, A. Ratilainen, H. S. Razaghi, T. Tirronen, and E. A. Yavuz, "Overview of 3GPP Release 14 further enhanced MTC," *IEEE Communications Standards Magazine*, vol. 2, pp. 84–89, JUNE 2018.

[86] D. L. Donoho *et al.*, "Compressed sensing," *IEEE Transactions on Information Theory*, vol. 52, no. 4, pp. 1289–1306, 2006.

[87] H. Zhu and G. B. Giannakis, "Exploiting sparse user activity in multiuser detection," *IEEE Transactions on Communications*, vol. 59, no. 2, pp. 454–465, 2011.

[88] C. Bockelmann, H. F. Schepker, and A. Dekorsy, "Compressive sensing based multi-user detection for machine-to-machine communication," *Transactions on Emerging Telecommunications Technologies*, vol. 24, no. 4, pp. 389–400, 2013.

[89] B. Wang, L. Dai, Y. Zhang, T. Mir, and J. Li, "Dynamic compressive sensing-based multi-user detection for uplink grant-free NOMA," *IEEE Communications Letters*, vol. 20, no. 11, pp. 2320–2323, 2016.

[90] Y. Du, B. Dong, Z. Chen, X. Wang, Z. Liu, P. Gao, and S. Li, "Efficient multi-user detection for uplink grant-free NOMA: Prior-information aided adaptive compressive sensing perspective," *IEEE Journal on Selected Areas in Communications*, vol. 35, no. 12, pp. 2812–2828, 2017.

[91] T. Wang, S. Liu, F. Yang, J. Wang, J. Song, and Z. Han, "Generalized spatial modulation-based multi-user and signal detection scheme for terrestrial return

channel with NOMA," *IEEE Transactions on Broadcasting*, vol. 64, no. 2, pp. 211–219, 2017.

[92] Y. Du, B. Dong, W. Zhu, P. Gao, Z. Chen, X. Wang, and J. Fang, "Joint channel estimation and multiuser detection for uplink grant-free NOMA," *IEEE Wireless Communications Letters*, vol. 7, pp. 682–685, Aug 2018.

[93] Y. Du, C. Cheng, B. Dong, Z. Chen, X. Wang, J. Fang, and S. Li, "Block-sparsity-based multiuser detection for uplink grant-free NOMA," *IEEE Transactions on Wireless Communications*, vol. 17, no. 12, pp. 7894–7909, 2018.

[94] Y. Zhang, Q. Guo, Z. Wang, J. Xi, and N. Wu, "Block sparse Bayesian learning based joint user activity detection and channel estimation for grant-free NOMA systems," *IEEE Transactions on Vehicular Technology*, vol. 67, no. 10, pp. 9631–9640, 2018.

[95] J. A. Tropp and A. C. Gilbert, "Signal recovery from random measurements via orthogonal matching pursuit," *IEEE Transactions on Information Theory*, vol. 53, no. 12, pp. 4655–4666, 2007.

[96] W. Dai and O. Milenkovic, "Subspace pursuit for compressive sensing signal reconstruction," *IEEE Transactions on Information Theory*, vol. 55, no. 5, pp. 2230–2249, 2009.

[97] D. Needell and J. A. Tropp, "CoSaMP: Iterative signal recovery from incomplete and inaccurate samples," *Applied and Computational Harmonic Analysis*, vol. 26, no. 3, pp. 301–321, 2009.

[98] J. Zhang, Y. Pan, and J. Xu, "Compressive sensing for joint user activity and data detection in grant-free NOMA," *IEEE Wireless Communications Letters*, vol. 8, no. 3, pp. 857–860, 2019.

[99] S. Jiang, X. Yuan, X. Wang, C. Xu, and W. Yu, "Joint user identification, channel estimation, and signal detection for grant-free NOMA," *IEEE Transactions on Wireless Communications*, 2020.

[100] N. Ye, X. Li, H. Yu, A. Wang, W. Liu, and X. Hou, "Deep learning aided grant-free NOMA toward reliable low-latency access in tactile internet of things," *IEEE Transactions on Industrial Informatics*, vol. 15, no. 5, pp. 2995–3005, 2019.

[101] W. Kim, Y. Ahn, and B. Shim, "Deep neural network-based active user detection for grant-free NOMA systems," *IEEE Transactions on Communications*, vol. 68, no. 4, pp. 2143–2155, 2020.

[102] J. Zhang, X. Tao, H. Wu, N. Zhang, and X. Zhang, "Deep reinforcement learning for throughput improvement of uplink grant-free NOMA system," *IEEE Internet of Things Journal*, 2020.

[103] L.-L. Yang, *Multicarrier Communications*. Chichester, United Kingdom: John Wiley, 2009.

[104] A. Goldsmith, *Wireless Communications*. Cambridge University Press, 2005.

[105] W. Abdessamad, Y. Nasser, K. Y. Kabalan, and O. Bazzi, "On the performance evaluation of MIMO-SCMA systems," in *Ultra Modern Telecommunications and Control Systems and Workshops (ICUMT)*, pp. 135–140, 2016.

[106] J. Bao, Z. Ma, G. K. Karagiannidis, M. Xiao, and Z. Zhu, "Joint multiuser detection of multidimensional constellations over fading channels," *IEEE Transactions on Communications*, vol. 65, no. 1, pp. 161–172, 2016.

[107] S.-C. Lim, N. Kim, and H. Park, "Uplink SCMA system with multiple antennas," *IEEE Transactions on Vehicular Technology*, vol. 66, no. 8, pp. 6982–6992, 2017.

[108] D. Cai, P. Fan, and P. T. Mathiopoulos, "A tight lower bound for the symbol error performance of the uplink sparse code multiple access," *IEEE Wireless Communications Letters*, vol. 6, no. 2, pp. 190–193, 2017.

[109] X. Wang, J. Wang, L. He, and J. Song, "Spectral efficiency analysis for downlink NOMA aided spatial modulation with finite alphabet inputs," *IEEE Transactions on Vehicular Technology*, vol. 66, no. 11, pp. 10562–10566, 2017.

[110] Z. Pan, W. Liu, J. Lei, J. Luo, L. Wen, and C. Tang, "Multi-dimensional space-time block coding aided downlink MIMO-SCMA," *IEEE Transactions on Vehicular Technology*, vol. 68, no. 7, pp. 6657–6669, 2019.

[111] L. Dai, B. Wang, Y. Yuan, S. Han, I. Chih-Lin, and Z. Wang, "Non-orthogonal multiple access for 5G: solutions, challenges, opportunities, and future research trends," *IEEE Communications Magazine*, vol. 53, no. 9, pp. 74–81, 2015.

[112] A. Graham, "Kronecker products and matrix calculus: With applications.," *JOHN WILEY & SONS, INC., 605 THIRD AVE., NEW YORK, NY 10158, 1982, 130*, 1982.

[113] R. Gallager, "Low-density parity-check codes," *IRE Transactions on Information Theory*, vol. 8, no. 1, pp. 21–28, 1962.

[114] M. C. Davey and D. MacKay, "Low-density parity check codes over GF(q)," *IEEE Communications Letters*, vol. 2, pp. 165–167, June 1998.

[115] W. Ryan and S. Lin, *Channel codes: classical and modern*. Cambridge University Press, 2009.

[116] M. D. Renzo and H. Haas, "Bit error probability of SM-MIMO over generalized fading channels," *IEEE Transactions on Vehicular Technology*, vol. 61, pp. 1124–1144, March 2012.

[117] R. Zhang, L. L. Yang, and L. Hanzo, "Generalised pre-coding aided spatial modulation," *IEEE Transactions on Wireless Communications*, vol. 12, pp. 5434–5443, November 2013.

[118] M. K. Simon and M.-S. Alouini, *Digital Communication over Fading Channels*. New York: John Wiley & Sons, 2 ed., 2005.

[119] J. G. Proakis, *Digital Communications*. McGraw Hill, 5 ed., 2007.

[120] M.-S. Alouini and A. J. Goldsmith, "A unified approach for calculating error rates of linearly modulated signals over generalized fading channels," *IEEE Transactions on Communications*, vol. 47, pp. 1324–1334, September 1999.

[121] L.-L. Yang and L. Hanzo, "Performance of generalized multicarrier DS-CDMA over Nakagami-m fading channels," *IEEE Transactions on Communications*, vol. 50, pp. 956 – 966, June 2002.

[122] I. Gradshteyn and I. Ryzhik, *Table of Integrals, Series, and Products*. New York, London: Academic Press, Inc, 7 ed., 2007.

[123] L. Hanzo, S. X. Ng, W. Webb, and T. Keller, *Quadrature amplitude modulation: From basics to adaptive trellis-coded, turbo-equalised and space-time coded OFDM, CDMA and MC-CDMA systems*. IEEE Press-John Wiley, 2004.

[124] A. J. Goldsmith and S.-G. Chua, "Variable-rate variable-power MQAM for fading channels," *IEEE Transactions on communications*, vol. 45, no. 10, pp. 1218–1230, 1997.

[125] A. Younis, N. Serafimovski, R. Mesleh, and H. Haas, "Generalised spatial modulation," in *Signals, Systems and Computers (ASILOMAR), Conference* , pp. 1498–1502, 2010.

[126] T. J. Richardson and R. L. Urbanke, "The capacity of low-density parity-check codes under message-passing decoding," *IEEE Ttransactions on Information Theory*, vol. 47, no. 2, pp. 599–618, 2001.

[127] K. Abend and B. D. Fritchman, "Statistical detection for communication channels with intersymbol interference," *Proceedings of the IEEE*, vol. 58, no. 5, pp. 779–785, 1970.

[128] G. Shafer *et al.*, *A mathematical theory of evidence*, vol. 1. Princeton university press Princeton, 1976.

[129] J. Bao, Z. Ma, M. Xiao, and Z. Zhu, "Error performance of sparse code multiple access networks with joint ML detection," in *Vehicular Technology Conference Spring*, pp. 1–5, 2016.

[130] J. Bao, Z. Ma, M. Xiao, Z. Ding, and Z. Zhu, "Performance analysis of uplink SCMA with receiver diversity and randomly deployed users," *IEEE Transactions on Vehicular Technology*, vol. 67, no. 3, pp. 2792–2797, 2018.

[131] M. D. Renzo and H. Haas, "Bit error probability of space-shift keying MIMO over multiple-access independent fading channels," *IEEE Transactions on Vehicular Technology*, vol. 60, pp. 3694–3711, Oct 2011.

[132] G. Taricco and E. Biglieri, "Exact pairwise error probability of space-time codes," *IEEE Transactions on Information Theory*, vol. 48, no. 2, pp. 510–513, 2002.

[133] T. A. Lamahewa, M. K. Simon, R. A. Kennedy, and T. D. Abhayapala, "Performance analysis of space-time codes in realistic propagation environments: A moment generating function-based approach," *Journal of Communications and Networks*, vol. 7, no. 4, pp. 450–461, 2005.

[134] P. Pan, L.-L. Yang, and Y. Zhang, "Statistics and error performance of orthogonal frequency-division multiplexing over Nakagami-m fading channels," 2011.

[135] M. Taherzadeh, H. Nikopour, A. Bayesteh, and H. Baligh, "SCMA codebook design," in *Vehicular Technology Conference Fall*, pp. 1–5, 2014.

[136] E. Telatar, "Capacity of multi-antenna Gaussian channels," *European Transactions on Telecommunications*, vol. 10, no. 6, pp. 585–595, 1999.

[137] C. Bockelmann, N. Pratas, H. Nikopour, K. Au, T. Svensson, C. Stefanovic, P. Popovski, and A. Dekorsy, "Massive machine-type communications in 5G: Physical and MAC-layer solutions," *IEEE Communications Magazine*, vol. 54, no. 9, pp. 59–65, 2016.

[138] E. J. Candes and T. Tao, "Near-optimal signal recovery from random projections: Universal encoding strategies?," *IEEE Transactions on Information Theory*, vol. 52, no. 12, pp. 5406–5425, 2006.

[139] F. Monsees, M. Woltering, C. Bockelmann, and A. Dekorsy, "Compressive sensing multi-user detection for multicarrier systems in sporadic machine type communication," in *Vehicular Technology Conference Spring*, pp. 1–5, 2015.

[140] T. T. Do, L. Gan, N. Nguyen, and T. D. Tran, "Sparsity adaptive matching pursuit algorithm for practical compressed sensing," in *Signals, Systems and Computers Asilomar Conference*, pp. 581–587, 2008.

[141] M. Arakawa, "Computational workloads for commonly used signal processing kernels," tech. rep., MASSACHUSETTS INST OF TECH LEXINGTON LINCOLN LAB, 2006.

[142] J. Choi, J. J. Dongarra, L. S. Ostrouchov, A. P. Petitet, D. W. Walker, and R. C. Whaley, "Design and implementation of the ScaLAPACK LU, QR, and Cholesky factorization routines," *Scientific Programming*, vol. 5, no. 3, pp. 173–184, 1996.

[143] Y. Wu, S. Zhang, and Y. Chen, "Iterative multiuser receiver in sparse code multiple access systems," in *IEEE International Conference on Communications (ICC)*, pp. 2918–2923, 2015.

[144] B. Xiao, K. Xiao, S. Zhang, Z. Chen, B. Xia, and H. Liu, "Iterative detection and decoding for SCMA systems with LDPC codes," in *Wireless Communications & Signal Processing (WCSP) Conference*, pp. 1–5, 2015.

[145] K. Han, Z. Zhang, J. Hu, and J. Chen, "A high performance joint detection and decoding scheme for LDPC coded SCMA system," in *IEEE Globecom Workshops (GC Wkshps)*, pp. 1–6, 2016.

[146] J. Dai, K. Niu, Z. Si, C. Dong, and J. Lin, "Polar-coded non-orthogonal multiple access," *IEEE Transactions on Signal Processing*, vol. 66, no. 5, pp. 1374–1389, 2017.

[147] Z. Pan, E. Li, L. Zhang, J. Lei, and C. Tang, "Design and optimization of joint iterative detection and decoding receiver for uplink polar coded SCMA system," *IEEE Access*, vol. 6, pp. 52014–52026, 2018.

[148] L. Yuan, J. Pan, N. Yang, Z. Ding, and J. Yuan, "Successive interference cancellation for LDPC coded nonorthogonal multiple access systems," *IEEE Transactions on Vehicular Technology*, vol. 67, no. 6, pp. 5460–5464, 2018.

[149] J. Dai, K. Niu, and J. Lin, "Iterative Gaussian-approximated message passing receiver for MIMO-SCMA system," *IEEE Journal of Selected Topics in Signal Processing*, vol. 13, no. 3, pp. 753–765, 2019.

[150] Z. B. K. Egilmez, L. Xiang, R. G. Maunder, and L. Hanzo, "The development, operation and performance of the 5G polar codes," *IEEE Communications Surveys & Tutorials*, 2019.

[151] L. Xiang, M. F. Brejza, R. G. Maunder, B. M. Al-Hashimi, and L. Hanzo, "Arbitrarily parallel turbo decoding for ultra-reliable low latency communication in 3GPP LTE," *IEEE Journal on Selected Areas in Communications*, vol. 37, no. 4, pp. 826–838, 2019.

[152] B. Tahir, S. Schwarz, and M. Rupp, "BER comparison between convolutional, turbo, LDPC, and polar codes," in *International Conference on Telecommunications (ICT)*, pp. 1–7, 2017.

[153] M. A. Lema, A. Laya, T. Mahmoodi, M. Cuevas, J. Sachs, J. Markendahl, and M. Dohler, "Business case and technology analysis for 5G low latency applications," *IEEE Access*, vol. 5, pp. 5917–5935, 2017.

[154] J. Sachs, L. A. Andersson, J. Araújo, C. Curescu, J. Lundsjö, G. Rune, E. Steinbach, and G. Wikström, "Adaptive 5G low-latency communication for tactile Internet services," *Proceedings of the IEEE*, vol. 107, no. 2, pp. 325–349, 2018.

[155] L. Hanzo, L.-L. Yang, E.-L. Kuan, and K. Yen, *Single-and multi-carrier DS-CDMA: multi-user detection, space-time spreading, synchronisation, standards and networking*. John Wiley & Sons, 2003.

[156] T. Keller and L. Hanzo, "Adaptive multicarrier modulation: A convenient framework for time-frequency processing in wireless communications," *Proceedings of the IEEE*, vol. 88, no. 5, pp. 609–640, 2000.

[157] L. Hanzo, T. Liew, B. Yeap, R. Tee, and S. X. Ng, *Turbo coding, turbo equalisation and space-time coding: EXIT-chart-aided near-capacity designs for wireless channels*, vol. 22. John Wiley & Sons, 2011.

[158] R. G. Maunder, "A fully-parallel turbo decoding algorithm," *IEEE Transactions on Communications*, vol. 63, no. 8, pp. 2762–2775, 2015.

[159] J. H. Van Lint, R. M. Wilson, and R. M. Wilson, *A course in combinatorics*. Cambridge university press, 2001.

[160] S. X. Ng and L. Hanzo, "On the MIMO channel capacity of multidimensional signal sets," *IEEE Transactions on Vehicular Technology*, vol. 55, no. 2, pp. 528–536, 2006.

[161] W. C. Lee, "Estimate of channel capacity in Rayleigh fading environment," *IEEE Transactions on Vehicular Technology*, vol. 39, no. 3, pp. 187–189, 1990.

[162] M. El-Hajjar and L. Hanzo, "EXIT charts for system design and analysis," *IEEE Communications Surveys & Tutorials*, vol. 16, no. 1, pp. 127–153, 2013.

[163] A. Svensson, "An introduction to adaptive QAM modulation schemes for known and predicted channels," *Proceedings of the IEEE*, vol. 95, no. 12, pp. 2322–2336, 2007.

[164] E. U. T. R. Access, "User equipment (UE) radio transmission and reception," *3GPP TS*, vol. 36, p. V10, 2011.

[165] R. Steele and L. Hanzo, *Mobile radio communications: Second and third generation cellular and WATM systems: 2nd*. IEEE Press-John Wiley, 1999.

[166] Q. Ni, "Performance analysis and enhancements for IEEE 802.11 e wireless networks," *IEEE network*, vol. 19, no. 4, pp. 21–27, 2005.

[167] 3GPP Technical Report 21.916, "Release 16 description; summary of Rel-16 work items," *3rd Generation Partnership Project*, 2019.

[168] H. Holma, A. Toskala, and T. Nakamura, *5G Technology: 3GPP New Radio*. John Wiley & Sons, 2020.

[169] M. Khani, M. Alizadeh, J. Hoydis, and P. Fleming, "Adaptive neural signal detection for massive MIMO," *IEEE Transactions on Wireless Communications*, vol. 19, no. 8, pp. 5635–5648, 2020.

[170] M. Toka and O. Kucur, "Non-orthogonal multiple access with Alamouti space–time block coding," *IEEE Communications Letters*, vol. 22, no. 9, pp. 1954–1957, 2018.

[171] S. M. Alamouti, "A simple transmit diversity technique for wireless communications," *IEEE Journal on Selected Areas in Communications*, vol. 16, no. 8, pp. 1451–1458, 1998.

[172] D. L. Donoho, A. Maleki, and A. Montanari, "Message-passing algorithms for compressed sensing," *Proceedings of the National Academy of Sciences*, vol. 106, no. 45, pp. 18914–18919, 2009.

[173] S. Wu, L. Kuang, Z. Ni, J. Lu, D. Huang, and Q. Guo, "Low-complexity iterative detection for large-scale multiuser MIMO-OFDM systems using approximate message passing," *IEEE Journal of Selected Topics in Signal Processing*, vol. 8, no. 5, pp. 902–915, 2014.

[174] J. P. Vila and P. Schniter, "Expectation-maximization Gaussian-mixture approximate message passing," *IEEE Transactions on Signal Processing*, vol. 61, no. 19, pp. 4658–4672, 2013.

[175] T. Van Erven and P. Harremos, "Rényi divergence and Kullback-Leibler divergence," *IEEE Transactions on Information Theory*, vol. 60, no. 7, pp. 3797–3820, 2014.

[176] Z. Tang, J. Wang, J. Wang, and J. Song, "A low-complexity detection algorithm for uplink NOMA system based on Gaussian approximation," in *IEEE Wireless Communications and Networking Conference (WCNC)*, pp. 1–6, 2017.

[177] L.-L. Yang and L. Hanzo, "Performance of broadband multicarrier DS-CDMA using space-time spreading-assisted transmit diversity," *IEEE Transactions on Wireless Communications*, vol. 4, no. 3, pp. 885–894, 2005.

Subject Index

Adaptive system design 120
Adaptive Turbo-coded SCMA System 119–123
Analysis of Approximate Bit Error Rate 29–35
Analysis of Single-User Average Bit Error Rate 26–29
Analysis of Single-User Average Bit Error Ratio 55–60
Analysis of the Single-User Performance and its Discussion 55–61
Approximated Message Passing (AMP) Detection 135–140

BER Performance 143–147

Capacity 110–111
Chapter Conclusions 165–170
Chapter Summary and Conclusions 42–43, 70–71, 123, 149–150
CN update 134, 137–139
Complexity 147–149
Complexity Analysis 119
Conclusions 163
Conclusions and Future Research 165–173

Deep-learning-aided grant-free NOMA 173
Design Guidelines 170–172
Detection Algorithms 132–140
Discussions 60–61

Error correction performance .. 111–112
EXtrinsic Information Transfer (EXIT) chart analysis 114–115

Factor Graph Design 157–158
Final iteration 139–140
Future Work 172–173

GSM/SSTFS for Large-Scale NOMA 151–163

Hybrid Iterative Detection and Decoding of Near-Instantaneously Adaptive Turbo-Coded Sparse Code Multiple Access (SCMA) 99–123

Improved scheduling of detection and decoding: HDD 115–119
Initialisation 133, 136
Introduction ... 18–19, 45–47, 100–103, 125–128, 151–152

Joint Message Passing-Aided Detection 158–160
Joint signal detection and decoding 109

Maximum *A-Posteriori* Detection 23–24, 52–53
Maximum-Likelihood Detection . 22–23, 51–52
Message Passing Algorithm Aided Detection 24–25, 53–55
Message Passing-Aided (MPA) Detection 132–135

Non-coherent detection of SM-NOMA 172

Performance Analysis 25–35
Performance of the adaptive turbo-coded SCMA system 121–123
Performance Results 35–42, 61–70, 143–149, 160–163
Physical-layer security of SM-NOMA 173

Receiver Model 21, 49–50, 104–105, 130–132, 156

Separate signal detection and decoding 105–108
Signal Detection 21–25, 50–55
Signal detection and decoding .105–109
Single-User Performance Analysis 141–143
SM/MC-SCDMA System Model .47–50
Space-Time-Coded Generalized SM for SCDMA (STC/GSM-SCDMA) 125–150
Spatial Modulation-Aided Multicarrier SCDMA 45–71
Spatial Modulation-Aided Sparse Code Division Multiple Access 17–43
Symbol mapping 135, 140
System Model 19–21, 103–105, 128–132, 153–156
System performance and hybrid detection and decoding 110–119

Transmitter Model 19–21, 48–49, 103–104, 128–130, 153–155

VN update 133–134, 136–137

Author Index

3GPP Technical Report 21.916 167

Abdessamad, Wissam 105

Abend, Kenneth 127

Abhayapala, Thushara D 133

Access, Evolved Universal Terrestrial Radio 164

Aggoune, Hadi M 44

Ahn, Chang Wook 17, 18

Ahn, Yongjun 101

Ai, Yutong 23

Al-Dhahir, Naofal 16, 22, 70

Al-Hashimi, Bashir M 151

Al-Nahhal, Ibrahim 30

Alamouti, Siavash M 171

Alhaji, Mahamuda 76

Ali, Samad 71

Alizadeh, Ardalan 59

Alizadeh, Mohammad 169

Alouini, Mohamed-Slim 118, 120

Althunibat, Saud 45

Andersson, Lars AA 154

Arakawa, Masahiro 141

Araújo, José 154

Au, Kelvin 137

Aygolu, Umit 50

Azmi, Paeiz 6

Bahrami, Hamid Reza 59

Baligh, Hadi 13, 77, 135

Bao, Jinchen 106, 129, 130

Basar, Ertugrul 30, 31, 50, 65

Bayesteh, Alireza 77, 135

Bazzi, Oussama 105

Bergman, J. 85

Bhargava, Vijay K 73

Bian, Yuyang 43

Biglieri, Ezio 132

Bockelmann, Carsten 88, 137, 139

Brejza, Matthew F 151

Cai, Donghong 108

Cai, Yunlong 66

Candes, Emmanuel J 138

Cao, Jianfei 24

Cao, Yue 84

Cardenas-Juarez, Marco 65

Casares-Giner, Vicente 2

Castillo-Soria, Francisco Ruben 65

Ceron, Andres 36

Chau, Yawgeng A 35

Chaudhry, Marium Jalal 55

Chen, Dageng 12, 76

Chen, Fangjiong 31

Chen, Jienan 145

Chen, Kwang-Cheng 22
Chen, S. 5
Chen, Shanzhi 14
Chen, Sheng 39, 58
Chen, Xiaoming 27, 70
Chen, Yan 143
Chen, Yingyang 23
Chen, Yunfei 32
Chen, Z. 92
Chen, Zhi 80, 81, 90, 93
Chen, Zhiyong 144
Cheng, Cong 93
Cheng, Xiang 43
Chih-Lin, I 111
Chockalingam, A 53, 56
Choi, Byungcho 4
Choi, Jaeyoung 142
Chua, Soon-Ghee 124
Cortez, Joaquín 65
Cuevas, Maria 153
Cui, Fangyu 66
Curescu, Calin 154

Dai, Jincheng 146, 149
Dai, L. 89
Dai, Linglong 58, 111
Dai, Wei 96
Davey, M. C. 114
Dekorsy, Armin 88, 137, 139
Di Renzo, Marco 19–22, 37, 51, 52, 55
Ding, Z. 5
Ding, Zhiguo 7, 9, 15, 16, 73, 130, 148
Do, Thong T 140
Dobre, Octavia 68
Dobre, Octavia A 3, 30, 83
Dohler, Mischa 153
Dong, B. 92
Dong, Binhong 80, 90, 93
Dong, Chao 146
Dongarra, Jack J 142
Donoho, David L 86, 172
Du, Y. 92
Du, Yang 80, 90, 93

Egilmez, Zeynep B Kaykac 150
El-Hajjar, Mohammed 162
Elkashlan, Maged 9

Fan, Pingzhi 16, 76, 108
Fan, Rongfei 67
Fang, J. 92
Fang, Jun 93
Fang, Sisai 84
Fleming, Phil 169
Frey, Brendan J 74
Fritchman, Bruce D 127

Gallager, Robert 113
Gan, Lu 140
Gao, P. 92
Gao, Pengyu 80, 90
Gao, Qiubin 14
Gao, Zhen 58, 67
Gao, Zihe 82
García-Armada, Ana 68
Garcia-Rodriguez, A. 57
Ghrayeb, Ali 20, 36
Giannakis, Georgios B 87
Gilbert, Anna C 95
Goldsmith, A. 104
Goldsmith, Andrea J 124

Gradshteyn, I.S. 122
Graham, Alexander 112
Grant, Peter M 19, 37
Graziosi, Fabio 55
Guijarro, Luis 2
Guo, Dongning 11
Guo, Li 69
Guo, Qinghua 79, 94, 173

Haas, H. 116, 131
Haas, Harald 17–20, 29, 37, 51, 52, 55, 125
Han, Kaining 145
Han, Shuangfeng 111
Han, Shujun 84
Han, Zhu 91
Hanzo, Lajos 4, 5, 9, 20, 21, 23, 26, 29, 33, 39, 42, 47, 49, 58, 60, 62, 117, 121, 123, 150, 151, 155–157, 160, 162, 165, 177
Hari, KVS 62
Harremos, Peter 175
He, L. 60
He, Longzhuang 109
Hemadeh, Ibrahim 47
Hoglund, A. 85
Holma, Harri 168
Hong, Zijie 34
Hoshyar, Reza 10, 12
Hou, Xiaolin 100
Hoydis, Jakob 169
Hu, Jianhao 145
Hu, Xiaoling 27
Huang, Defeng 61, 173

Ikki, Salama 30
Ikki, Salama S 44
Imran, Muhammad Ali 12
Ishikawa, Naoki 46

Javan, Mohammad Reza 6
Jeganathan, Jeyadeepan 36
Jia, Min 67
Jia, Shuyun 41
Jiang, Shuchao 99
Jiao, Bingli 23, 43
Jin, Minglu 32

Kabalan, Karim Y 105
Kang, Shaoli 14
Karagiannidis, George K 73, 106
Keller, T 123
Keller, Thomas 4, 156
Kennedy, Rodney A 133
Khani, Mehrdad 169
Kim, Kyeong Jin 8, 22
Kim, Namshik 107
Kim, Wonjun 101
Kschischang, Frank R 74, 75
Kuan, Ee-Lin 155
Kuang, Jingming 79
Kuang, Linling 61, 173
Kucur, Oğuz 170
Kwak, Kyung Sup 8

Lamahewa, Tharaka A 133
Larsson, Erik G 70
Laya, Andres 153
Lee, William CY 161
Lei, Jing 28, 110, 147
Lei, Xia 48, 49
Lei, Xianfu 73
Lema, Maria A 153
Leyva-Mayorga, Israel 2
Li, Erbao 147

Li, Geoffrey Ye 66
Li, Guoquan 34
Li, Hongyan 3
Li, J. 89
Li, Jingjing 7
Li, Qiang 31
Li, Shaoqian 21, 49, 90, 93
Li, Xiangming 100
Li, Xingwang 7
Li, Yonghui 79
Li, Yunzhou 54
Liberg, O. 85
Liew, TH 157
Lim, Seung-Chan 107
Lin, Jiaru 69, 146, 149
Lin, Shu 115
Lin, X. 85
Liu, Chungang 82
Liu, Hongwu 8
Liu, Hui 144
Liu, Liang 1
Liu, Sicong 91
Liu, Wei 110
Liu, Wenjia 100
Liu, Yuanwei 7, 9, 69
Liu, Yue 82
Liu, Yunyun 78
Liu, Yusha 26, 29, 33
Liu, Zeyuan 90
Loeliger, H-A 74
Lu, Jianhua 61, 173
Lundsjö, Johan 154
Luo, Junshan 28, 110

Ma, Jianglei 77
Ma, Xinying 81
Ma, Zheng 76, 106, 129, 130
MacKay, D. 114
Mahmoodi, Toktam 153
Maleki, Arian 172
Maleki, Marjan 63
Maleki, Mehdi 59
Markendahl, Jan 153
Martinez-Bauset, Jorge 2
Masouros, C. 57
Mathiopoulos, P Takis 108
Maunder, Robert G 150, 151, 158
McCann, Julie A 66
Meng, Xiangming 61
Mesleh, Raed 37, 44, 45, 125
Mesleh, Raed Y 18
Mesleh, Read 17
Milenkovic, Olgica 96
Mir, T. 89
Mohamed, Abdelrahim 47
Mohamed-Pour, Kamal 63
Mohammadkarimi, Mostafa 83
Mohammed, AL-Imari 12
Moltafet, Mohammad 6
Monsees, Fabian 139
Montanari, Andrea 172
Morales-Céspedes, Máximo 68
Mu, Hang 76
Mu, Xidong 69
Münster, Matthias 4
Murti, Fahri Wisnu 25

Na, Zhenyu 82
Nakamura, Takehiro 168
Nallanathan, Arumugam 7, 9

Narasimhan, T Lakshmi 53, 56
Narayanan, Sandeep 55
Nasser, Youssef 105
Needell, Deanna 97
Ng, Derrick Wing Kwan 27, 70
Ng, Soon Xin 123, 157, 160
Nguyen, Nam 140
Ni, Qiang 166
Ni, Zuyao 173
Nikopour, Hosein 13, 77, 135, 137
Niu, Kai 14, 146, 149

Ostrouchov, L Susan 142

Pan, Jie 148
Pan, Peng 64, 134
Pan, Yongping 98
Pan, Zhipeng 28, 110, 147
Panayirci, Erdal 38, 50
Park, Hyuncheol 107
Petitet, Antoine P 142
Pla, Vicent 2
Poor, H Vincent 8, 15, 31, 38, 43, 50
Popovski, Petar 137
Pratas, Nuno 137
Proakis, John G. 119

Qin, Zhijin 9, 66

Rajashekar, Rakshith 62
Rajatheva, Nandana 71
Ratilainen, A. 85
Raviteja, Patchava 53, 56
Raza, Muhammad Ahmad 83
Razaghi, H. S. 85
Razavi, Razieh 12
Ren, Bin 14
Renzo, M. Di 116, 131
Richardson, Thomas J 126
Rune, Göran 154
Rupp, Markus 152
Ryan, William 115
Ryzhik, I.M. 122

Saad, Walid 71
Sachs, Joachim 153, 154
Schepker, Henning F 88
Schniter, Philip 174
Schober, Robert 15, 70, 73
Schwarz, Stefan 152
Serafimovski, Nikola 52, 125
Shafer, Glenn 128
Shao, Weidong 3
Sharma, Shree Krishna 72
Shi, Jingcheng 82
Shim, Byonghyo 101
Shin, Soo Young 25
Si, Qintuya 32
Si, Zhongwei 146
Simon, Marvin K 133
Sinanović, Sinan 52
Siregar, Rahmat Faddli 25
Siu, Yunming 78, 81
Soltanalian, Mojtaba 63
Song, J. 60
Song, Jian 41, 91, 109, 176
Stavridis, Athanasios 55
Steele, Raymond 165
Stefanovic, Cedomir 137
Steinbach, Eckehard 154
Sugiura, Shinya 20, 39, 46
Sun, Shaohui 14

Sun, Yan 84
Svensson, Arne 163
Svensson, Tommy 137
Szczecinski, Leszek 36

Tafazolli, Rahim 10
Taherzadeh, Mahmoud 77, 135
Tahir, Bashar 152
Tang, Chaojing 28, 110, 147
Tang, Zihan 176
Tao, Terence 138
Tao, Xiaofeng 84, 102
Taricco, Giorgio 132
Tee, RYS 157
Telatar, Emre 136
Tello-Oquendo, Luis 2
Tirronen, T. 85
Toka, Mesut 170
Toskala, Antti 168
Tran, Trac D 140
Tropp, Joel A 95, 97
Tsiftsis, Theodoros A 8, 22

Urbanke, Rüdiger L 126

Van Erven, Tim 175
Van Lint, Jacobus Hendricus 159
Vila, Jeremy P 174

Walker, David W 142
Wang, Aihua 100
Wang, B. 89
Wang, Bichai 111
Wang, Chih-Chun 11
Wang, J. 60
Wang, Jing 54
Wang, Jintao 41, 91, 109, 176
Wang, Jun 176
Wang, Li 23
Wang, Shengchu 54
Wang, Tengjiao 91
Wang, X. 92
Wang, Xianbin 32, 72
Wang, Xiaodong 80, 90, 93
Wang, Xin 99
Wang, Xuesi 109
Wang, Z. 5
Wang, Zhaocheng 24, 58, 111
Wang, Zhongyong 94
Wathan, Ferry P 10
Webb, WT 123
Wen, Lei 28, 110
Wen, Miaowen 22, 31, 43
Whaley, R Clint 142
Wikström, Gustav 154
Wilson, Richard Michael 159
Woltering, Matthias 139
Wu, Chaowu 48
Wu, Huici 102
Wu, Nan 79, 94
Wu, Sheng 61, 173
Wu, Yiqun 143

Xi, Jiangtao 94
Xia, Bin 144
Xiang, Luping 150, 151
Xiang, Wei 48
Xiao, Baicen 144
Xiao, Kexin 144
Xiao, Lixia 47–49
Xiao, Ming 106, 129, 130
Xiao, Pei 29, 47

Xiao, Yue 21, 47–49
Xing, Chengwen 79
Xu, Chao 49
Xu, Chongbin 99
Xu, Jie 98
Xu, Xiaodong 84
Xu, Yongjun 34

Yamchi, Nader Mokari 6
Yang, Fang 91
Yang, Kai 67
Yang, Lie-Liang 26, 29, 33, 40, 42, 64, 103, 117, 121, 134, 155, 177
Yang, Lin 78, 81
Yang, Liuqing 43
Yang, Nan 67, 148
Yang, Ping 21, 48, 49
Yang, Zheng 16
Yavuz, E. A. 85
Ye, Neng 67, 100
Yeap, BL 157
Yen, Kai 155
Younis, Abdelhamid 45, 125
Yu, Hanxiao 100
Yu, Shi-Hong 35
Yu, Wei 1, 70, 99
Yuan, Jinhong 73, 148
Yuan, Lei 148
Yuan, Weijie 79
Yuan, Xiaojun 99
Yuan, Yifei 111
Yun, Sangboh 17, 18

Zhang, Jiazhen 102
Zhang, Jun 98
Zhang, Lei 147
Zhang, Ning 102
Zhang, Ping 84
Zhang, R. 117
Zhang, Rong 42
Zhang, Shun 3
Zhang, Shunqing 143
Zhang, Shutian 144
Zhang, Xuefei 102
Zhang, Y. 89
Zhang, Youguang 134
Zhang, Yuanyuan 94
Zhang, Zhaoyang 27
Zhang, Zhenbing 145
Zhao, Nan 3, 32
Zheng, Beixiong 22
Zhong, Caijun 27
Zhou, Xiangyun 34
Zhu, Hao 87
Zhu, W. 92
Zhu, Zhongliang 106, 129, 130